International Journal of
Molecular Sciences

Oligonucleotide, Therapy, and Applications

Edited by
Luis Sendra and Salvador F. Aliño

Printed Edition of the Special Issue Published in
International Journal of Molecular Sciences

www.mdpi.com/journal/ijms

MDPI

Oligonucleotide, Therapy, and Applications

Oligonucleotide, Therapy, and Applications

Editors

Luis Sendra
Salvador F. Aliño

MDPI • Basel • Beijing • Wuhan • Barcelona • Belgrade • Manchester • Tokyo • Cluj • Tianjin

Editors

Luis Sendra
Pharmacogenetics and Gene Therapy
Instituto de Investigación Sanitaria La Fe
Valencia
Spain

Salvador F. Aliño
Gene Therapy & Pharmacogenomic Group
Department of Pharmacology
Universitat de València
Valencia
Spain

Editorial Office
MDPI
St. Alban-Anlage 66
4052 Basel, Switzerland

This is a reprint of articles from the Special Issue published online in the open access journal *International Journal of Molecular Sciences* (ISSN 1422-0067) (available at: www.mdpi.com/journal/ijms/special_issues/oligonucleotide).

For citation purposes, cite each article independently as indicated on the article page online and as indicated below:

LastName, A.A.; LastName, B.B.; LastName, C.C. Article Title. *Journal Name* **Year**, *Volume Number*, Page Range.

ISBN 978-3-0365-3057-4 (Hbk)
ISBN 978-3-0365-3056-7 (PDF)

Contents

International Journal of
Molecular Sciences

MDPI

Article

Foxp3 Silencing with Antisense Oligonucleotide Improves Immunogenicity of an Adjuvanted Recombinant Vaccine against *Sporothrix schenckii*

Alexander Batista-Duharte [1,*], Luis Sendra [2,3,*], Maria José Herrero [2,3], Deivys Leandro Portuondo [1], Damiana Téllez-Martínez [1], Gladys Olivera [3], Manuel Fernández-Delgado [4], Beatriz Javega [5], Guadalupe Herrera [2], Alicia Martínez [6], Paulo Inacio Costa [1], Iracilda Zeppone Carlos [1] and Salvador Francisco Aliño [2,3,7]

1 Department of Clinical Analysis, School of Pharmaceutical Sciences, São Paulo State University (UNESP), Araraquara 14800-903, São Paulo, Brazil; deivysleandro@gmail.com (D.L.P.); damianatellezm@gmail.com (D.T.-M.); costapi.unesp@gmail.com (P.I.C.); iracilda.zeppone@unesp.br (I.Z.C.)
2 Pharmacology Department, Faculty of Medicine, Universitat de Valencia, 46010 Valencia, Spain; Maria.Jose.Herrero@uv.es (M.J.H.); gherreramartin@gmail.com (G.H.); salvador.f.alino@uv.es (S.F.A.)
3 Pharmacogenetics Unit, Instituto de Investigación Sanitaria La Fe, 46026 Valencia, Spain; gladysmjiv@hotmail.com
4 Service of Hematology and Hemotherapy, Hospital General Universitario de Castellón, 12004 Castelló de la Plana, Spain; mfdezdm@gmail.com
5 Cytometry Unit, Faculty of Medicine, Universitat de Valencia, 46010 Valencia, Spain; beatriz.javega@uv.es
6 Cytomics Unit, Centro de Investigación Príncipe Felipe, 46012 Valencia, Spain; amartinez@cipf.es
7 Unit of Clinical Pharmacology, Medicine Clinical Area, Hospital Universitario y Politécnico La Fe, 46026 Valencia, Spain
* Correspondence: batistaduhartea@gmail.com (A.B.-D.); luis.sendra@uv.es (L.S.)

check for updates

Citation: Batista-Duharte, A.; Sendra, L.; Herrero, M.J.; Portuondo, D.L.; Téllez-Martínez, D.; Olivera, G.; Fernández-Delgado, M.; Javega, B.; Herrera, G.; Martínez, A.; et al. Foxp3 Silencing with Antisense Oligonucleotide Improves Immunogenicity of an Adjuvanted Recombinant Vaccine against *Sporothrix schenckii*. *Int. J. Mol. Sci.* **2021**, *22*, 3470. https://doi.org/10.3390/ijms22073470

Academic Editor: Marek Drozdzik

Received: 6 March 2021
Accepted: 25 March 2021
Published: 27 March 2021

Publisher's Note: MDPI stays neutral with regard to jurisdictional claims in published maps and institutional affiliations.

Abstract: Background: In recent years, there has been great interest in developing molecular adjuvants based on antisense oligonucleotides (ASOs) targeting immunosuppressor pathways with inhibitory effects on regulatory T cells (Tregs) to improve immunogenicity and vaccine efficacy. We aim to evaluate the immunostimulating effect of 2′OMe phosphorothioated Foxp3-targeted ASO in an antifungal adjuvanted recombinant vaccine. Methods: The uptake kinetics of Foxp3 ASO, its cytotoxicity and its ability to deplete Tregs were evaluated in murine splenocytes in vitro. Groups of mice were vaccinated with recombinant enolase (Eno) of *Sporothix schenckii* in Montanide Gel 01 adjuvant alone or in combination with either 1 µg or 8 µg of Foxp3 ASO. The titers of antigen-specific antibody in serum samples from vaccinated mice (male C57BL/6) were determined by ELISA (enzyme-linked immunosorbent assay). Cultured splenocytes from each group were activated in vitro with Eno and the levels of IFN-γ and IL-12 were also measured by ELISA. The results showed that the anti-Eno antibody titer was significantly higher upon addition of 8 µM Foxp3 ASO in the vaccine formulation compared to the standard vaccine without ASO. In vitro and in vivo experiments suggest that Foxp3 ASO enhances specific immune responses by means of Treg depletion during vaccination. Conclusion: Foxp3 ASO significantly enhances immune responses against co-delivered adjuvanted recombinant Eno vaccine and it has the potential to improve vaccine immunogenicity.

Keywords: antisensense oligonucleotide; Foxp3; regulatory T cells; vaccine immunogenicity; *Sporothrix schenckii*

1. Introduction

Regulatory T cells (Tregs) are a subset of CD4+ T-cells that play a suppressive role in the immune system. Tregs control the immune response to self and foreign antigens, helping to prevent over-inflammation and autoimmune disease [1–3]. On the other hand, a great deal of evidence shows that Tregs are often involved in the failure of anti-infectious defense [4–8] and effective vaccination [9–13].

In recent years, there has been great interest in developing molecular adjuvants with inhibitory effects on Tregs, aiming to improve the immunogenicity and vaccine efficacy [14,15] against deleterious foreign antigens. One of the newer strategies for depletion/inhibition of Tregs in vaccines has been the use of antisense oligonucleotides (ASOs) targeting important immunosuppressor pathways or immune checkpoints [16]. ASOs are small-sized (around 20 nucleotides) single-stranded oligonucleotides designed to bind specifically to the RNA or DNA target, based on their sequence homology, and bring about gene silencing [17]. Several ASOs have already been approved by the United States Food and Drug Administration (FDA) and many others to treat cardiovascular, metabolic, endocrine, neurological, neuromuscular, inflammatory, and infectious diseases [18] are under study in clinical trials.

Foxp3 (forkhead box P3), also known as the scurfin protein, is a member of the forkhead transcription factor family that is mainly expressed in Tregs. Foxp3 acts as a transcription activator for several genes, such as CD25, Cytotoxic T-Lymphocyte Antigen 4 (CTLA-4), glucocorticoid-induced TNF receptor family gene (GITR), and folate receptor 4. The regulation of Foxp3 expression in Tregs occurs through the concerted action of transcription factors, epigenetic control mechanisms, and post-translational modifications that modulate Foxp3 function [19]. Vaccination of mice with dendritic cells transfected with Foxp3 mRNA promoted selective depletion of Foxp3+ Tregs and stimulated specific cytotoxic T lymphocytes (CTL) with enhanced vaccine-induced protective immunity [20]. An improvement of vaccine immunogenicity and Foxp3 targeting efficacy has been reported using other strategies, including a chimeric Foxp3-Fc(IgG) fusion construct/protein to stimulate the immune responses against Tregs [21], as well as synthetic peptides with the ability to inhibit Foxp3 function [22–24].

In a previous study by our group, therapeutic vaccination was combined with either Foxp3 or CTLA4 gene silencing to enhance the antitumor response following B16 tumor cell transplantation. Either 2′-O-methyl phosphorotioate-modified oligonucleotides (2′-OMe-PS-ASOs) or polypurine reverse Hoogsteen hairpins (PPRHs) were used for Foxp3 or CTLA4 gene silencing. Combining the therapeutic vaccine with Foxp3 ASO achieved a greater survival rate (50%) than with CTLA4 ASO (20%), associated with Treg depletion. In that study, both ASOs were injected intraperitoneally, and the pharmacological effects were observed only at the higher doses [25]. Thus, the high cost and the potential risk of off-target effects and toxicity limited this strategy [26].

In this study, we evaluated whether a low dose of ASO Foxp3 as part of the vaccine formulation could improve vaccine immunogenicity. We studied the kinetics of Foxp3 ASO access into CD4+ T cells. The functional effects of the ASO on Treg depletion, cytotoxicity, and its ability to enhance the immunogenicity of an antifungal adjuvanted vaccine against sporotrichosis [27] were also evaluated.

2. Results

2.1. Primary Sequence of the Foxp3 Gene in FASTA Format and Target Region for Foxp3 Silencing

The target sequence of the ASO used for silencing the Foxp3 gene was located in intron 1 of the last update of NCBI (Supplement Figure S1). This location allowed us to estimate that its possible site of action could be at the pre-RNA level, still containing the non-coding sequences. Therefore, the probable silencing mechanism could occur through the action of an RNAse-H, which cleaves the heterodimer, or also by a steric hindrance mechanism and splicing inhibition [16].

2.2. Oligonucleotide (ON) Uptake Kinetics in Murine Splenocytes

Before the in vivo studies, the optimal conditions for the ON uptake were determined with a size-range study that encompassed those normally used for gene silencing, such as the anti-Foxp3 ASO used in this study. The ability of two fluorescent ONs with different sizes (13-mer and 20-mer) to enter splenocytes was evaluated. Fluorescence was determined by means of flow cytometry at different times between 0 and 120 min, employing different concentrations (0.5, 1.0, 2.0, and 4.0 μM). As shown in Figure 1, after 10 min of

incubation, most of the ONs could be detected in the cells. From that time on, although the entry of ONs into the cells continued to increase at concentrations of 0.5, 1, and 2 μM, at concentrations of 4 and 10 μM from 10 min of incubation no greater absorption of ONs was observed. Regarding the sizes of the ONs, no differences were observed between the 13 and 20 mer ONs, and splenocytes and lymphocytes showed a similar pattern of uptake. This result coincides with other studies carried out in our laboratory using human blood in which similar absorption patterns were observed (results not-shown); thus, both mouse splenocytes and human blood models can be used for studies of ON uptake kinetics.

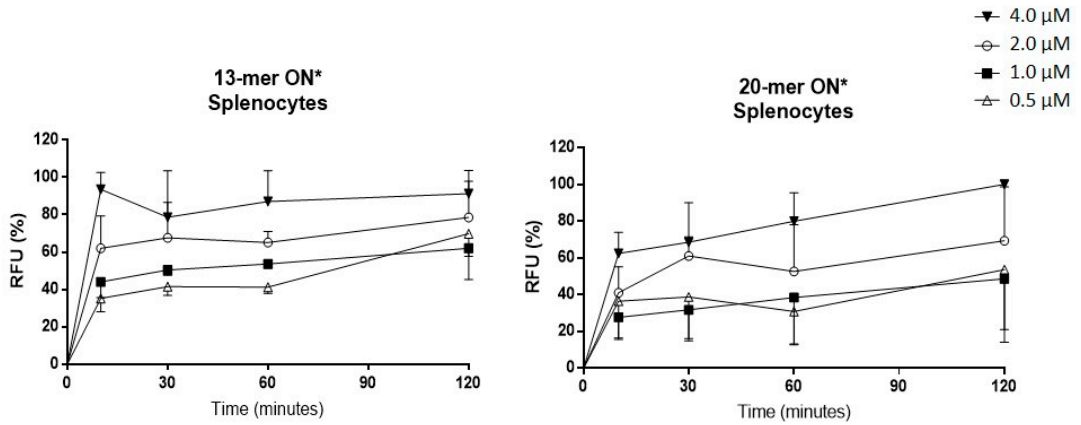

Figure 1. Labeled oligonucleotide (ON) absorption kinetics in splenocytes. Labeled ONs with sizes of 13 or 20 mer were cultured at different times and concentrations in the presence of C57BL6 mouse splenocytes. The fluorescent ONs of either 13 or 20 mer, labeled with Cy5 or FITC, were incubated independently at concentrations of 0.5, 1, 2, and 4 μM at 37 °C at 0, 10, 30, 60, and 120 min. At each time, the splenocytes were analyzed by means of flow cytometry to measure the ON uptake and the % of ONs was calculated with respect to maximal relative fluorescence unit (RFU) values achieved. ON* refers to fluorescent oligonucleotide.

To determine the possible cellular location of the labeled ONs, an imaging study was carried out using InCell equipment. As shown in Figure 2, the presence of lymphocytes with labeled ONs in their cellular structure was confirmed, although it was not possible to precisely define their cellular location.

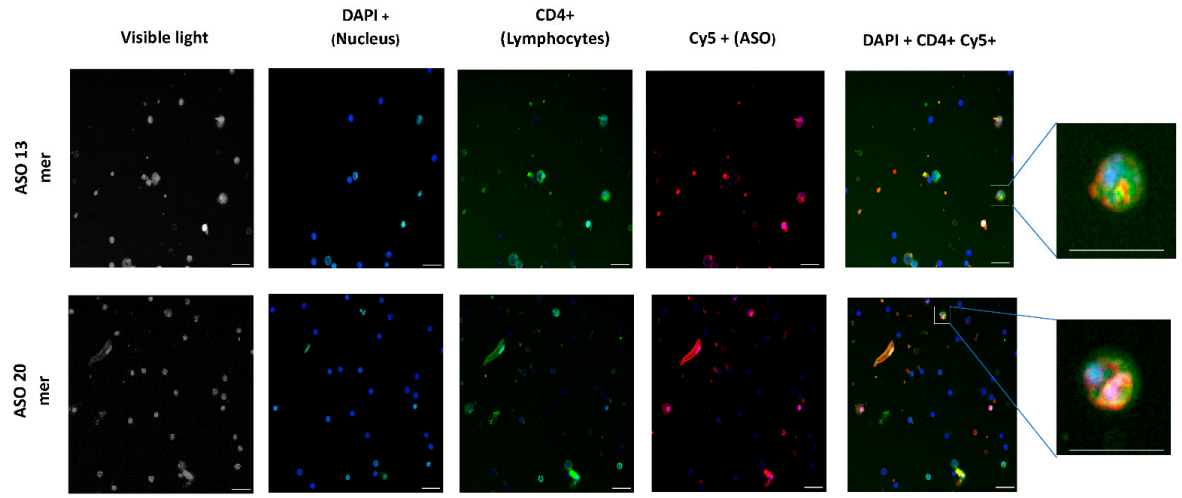

Figure 2. Location of fluorescent ONs in splenic lymphocytes. Splenocytes were treated with Cy5-labeled ONs and incubated for 1 h at 4 μM. Then, the cells were marked with anti-mouse CD4 FITC, fixed with 4% formaldehyde in phosphate buffered saline (PBS) solution and analyzed using an InCell analyzer 2200 system to observe the uptake of ONs in CD4+ lymphocytes. Scale bar represents 10 μm.

2.3. Biological Activity of the ASO Foxp3

To confirm the silencing effect of the anti-Foxp3 ASO on this transcription factor, B16 cells from murine melanoma, which constitutively express high levels of Foxp3, were cultured and incubated with anti-Foxp3 or Scrambled ONs. Considering the results of the previous studies, it was determined to use a concentration of 2 μM and incubate it for 1 h. After incubation, a 1:4 dilution with complete RPMI (Roswell Park Memorial Institute) medium was performed and cells were kept in culture for 48 h at 37 °C and 5% CO_2. Under these conditions, Foxp3 mRNA expression was silenced by about 70%. Moreover, mouse splenocytes were cultured with either anti-Foxp3 or scrambled ASO and the presence of CD4 + CD25 + Foxp3 cells was measured. A significant reduction from ~3% to ~1% of Tregs ($p < 0.05$) was observed with Foxp3 ASO treatment, as evidence of Treg depletion in the culture (Figure 3).

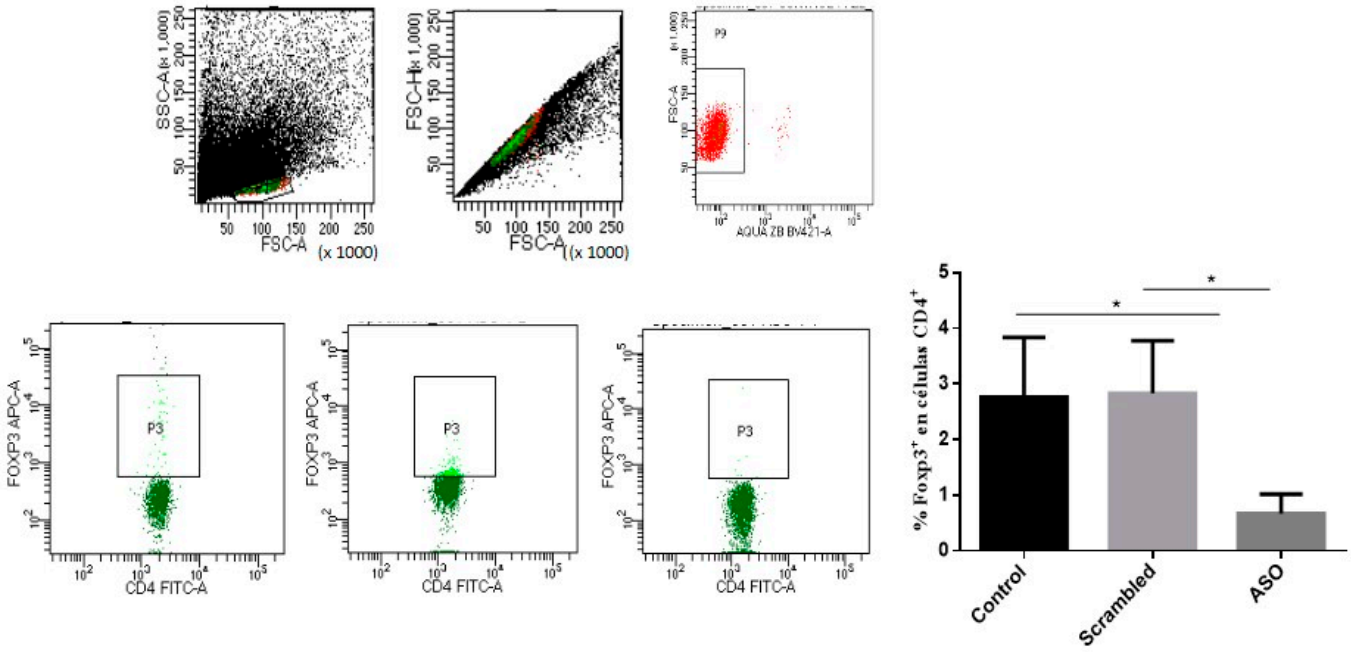

Figure 3. Biological activity of the anti-Foxp3 antisense oligonucleotide (ASO). Effect of anti-Foxp3 ASO in mouse splenocytes on CD4 + Foxp3 + cell populations. The upper panel represents the strategy of gates and the confirmation of the viability of the cells studied. The lower panel shows representative images of the reduction of CD4+ Foxp3+ population (as %) in the cells treated with anti Foxp3 ASO. A one-way analysis of variance (ANOVA) with Tukey's post-hoc test was used. The confidence interval was established at 95% for all tests. The level of significance and *p*-values are shown as * ($p < 0.05$).

2.4. Cellular Viability

Next, the cytotoxicity of Eno, anti-Foxp3 ASO, and its scrambled control alone or in combination was evaluated. The concentrations used were the same as those employed in the functional studies and were incubated for 48 h as well. Cell viability was analyzed using a combination of PI/Annexin V-FITC to determine the presence of necrosis (PI+ Annexin V−), late apoptosis (PI+ Annexin V+) and living cells (PI− Annexin V− or PI− Annexin V+). Late apoptosis cells (PI+ Annexin V+) suffer irreversible damage, whereas PI− Annexin V+ cells are in early apoptosis, which can be reversible. As shown in Figure 4, live cells (both PI− Annexin V− and PI− Annexin V+) accounted for more than 90% in all cells treated with Eno, ASO anti-Foxp3, scrambled or in their combinations. This result showed that the direct cytotoxicity of both molecules at the concentrations employed is low, and that they can be used in in vitro studies.

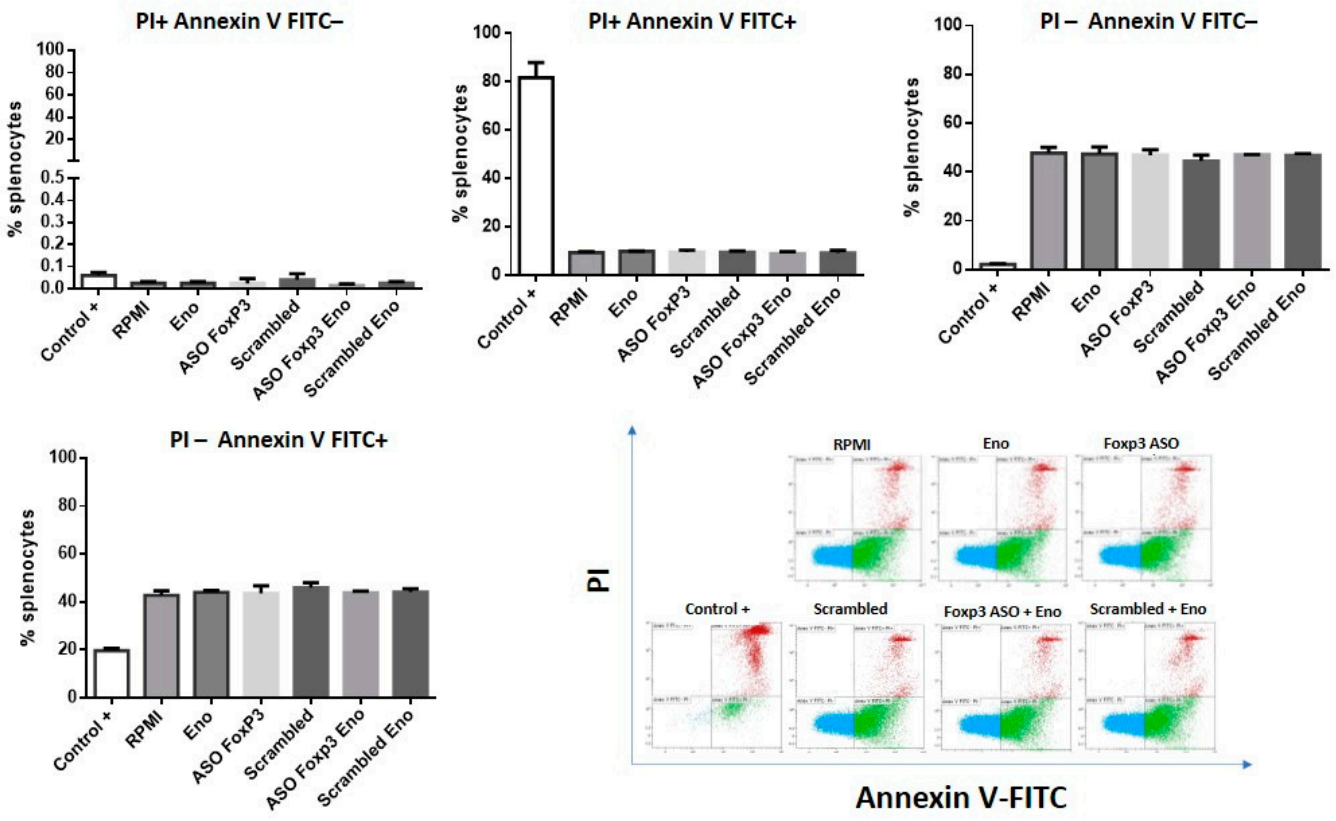

Figure 4. Analysis of variance (ANOVA) with Tukey's post-hoc test was used. The confidence interval was established at 95% for all tests. There were no significant differences between the experimental groups. A positive heat-killed cell control was used by means of incubation at 56 °C for 30 min.

2.5. Immunogenicity Study

With these initial results, an experimental study to evaluate the effect of the administration of anti-Foxp3 ASO on the immunogenicity of an experimental vaccine against *Sporothrix schenckii* previously developed in our laboratory [27,28] was carried out. We used the same experimental design previously described but including the anti-Foxp3 ASO within the formulation to determine its effect on the specific immune response. Two doses of anti-Foxp3 ASO, 1 or 8 μg per mouse and dose, were used to evaluate a possible dose-response effect.

2.5.1. Anti-Eno Antibodies

To evaluate the antibody response, the serum was extracted from the animals' blood samples and the titers of total IgG, IgG1, and specific IgG2a were quantified. As can be seen in Figure 5, the groups immunized with the vaccine using adjuvant and ASO at 8 μg presented higher titers of specific IgG and IgG1 antibodies. In the case of IgG1, a dose-response trend could be observed. For IgG2a, significant differences between the groups with and without ASO were not observed.

This result shows that anti Foxp3 ASO mediated greater stimulation of the immune response, suggesting that the inhibition of the suppressive effect of Tregs could have helped to achieve a greater immunogenicity of enolase. Other authors have obtained similar results using other ASOs targeting Tregs [29–32]. Further studies will be necessary to confirm these findings.

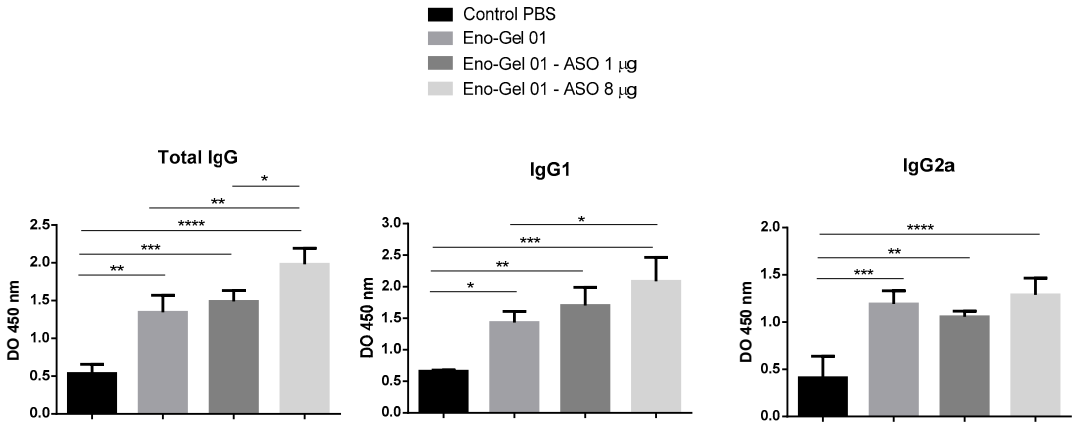

Figure 5. Specific antienolase antibodies. Mice (C57BL/6) were immunized on days 0 and 14. Specific antibodies to *S. schenckii* enolase in serum were evaluated on day 21 by means of ELISA. A one-way analysis of variance (ANOVA) with Tukey's post hoc test was used. The confidence interval was established at 95% for all tests. The level of significance and *p*-values are shown as * ($p < 0.05$); ** ($p < 0.01$); *** ($p < 0.001$); **** ($p < 0.0001$).

2.5.2. CD4+ CD25+ Foxp3 T Cells

To evaluate the effect of the different immunization regimens on Tregs, splenocytes were cultured for 48 h in the presence of Eno or Eno+ anti-Foxp3 ASO. As shown in Figure 6, the vaccinated groups exhibited a higher presence of Tregs after stimulation in vitro than non-vaccinated groups. However, there were no differences between the group vaccinated with Eno-Gel 01 and the groups treated with Eno and ASOs. Similarly, cells cultured with Eno + ASO showed Treg reductions compared to cells that were only stimulated with Eno, although this reduction was lower in the group immunized with the highest dose of ASO anti-Foxp3.

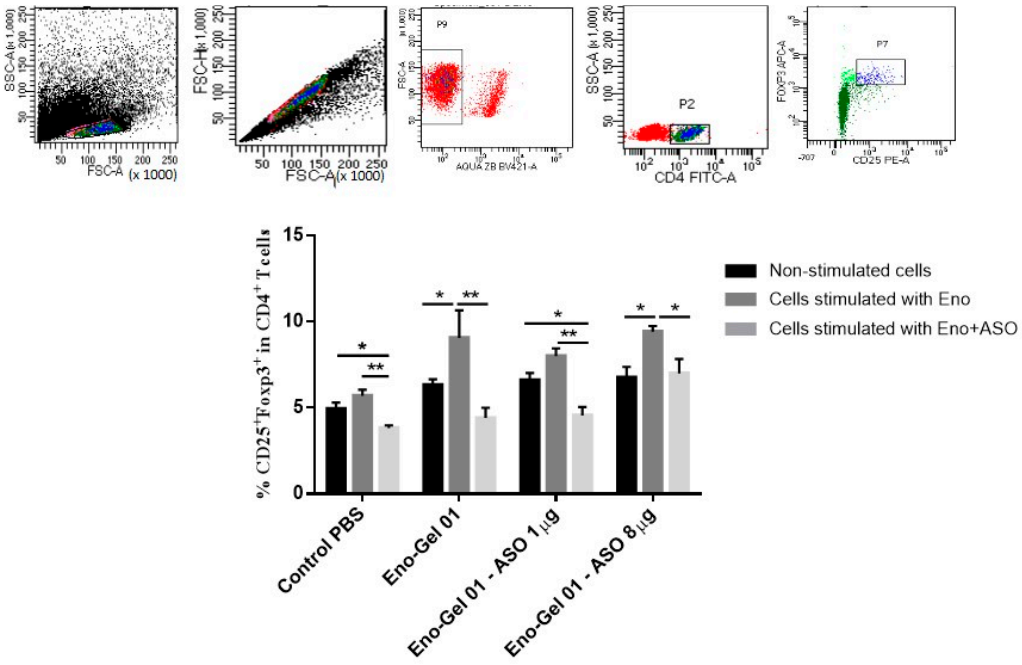

Figure 6. CD4+ CD25+ Foxp3 T cells in mouse spleens. Splenocytes were extracted on day 21 after immunization, then they were stimulated for 48 with Eno of *S. schenckii* or with Eno + ASO anti-Foxp3. Treg % was evaluated by means of flow cytometry. Top panel shows the gates strategy used in the study. A one-way analysis of variance (ANOVA) with Tukey's post hoc test was used. The confidence interval was established at 95% for all tests. The level of significance and *p*-values are shown as * ($p < 0.05$); ** ($p < 0.01$).

2.5.3. IFN-γ and IL-12 Production

To evaluate the effect of immunization using anti-Foxp3 ASO on the production of Th1 cytokines, we measured the production of IFN-γ and IL-12 in Eno-stimulated splenocytes. These cytokines are importantly involved in the defense against *S. schenckii* [33,34]. As can be seen in Figure 7, the mouse cells immunized with the vaccine formulation containing 8 μg ASO showed greater production of these cytokines than the rest of the groups. However, when stimulation was produced with Eno + anti-Foxp3 ASO, no differences were observed in cytokine production when compared to cells stimulated in vitro with Eno alone. In this case, we expected that the reduction of Tregs would have a positive influence, causing greater production of IFN-γ and IL-12.

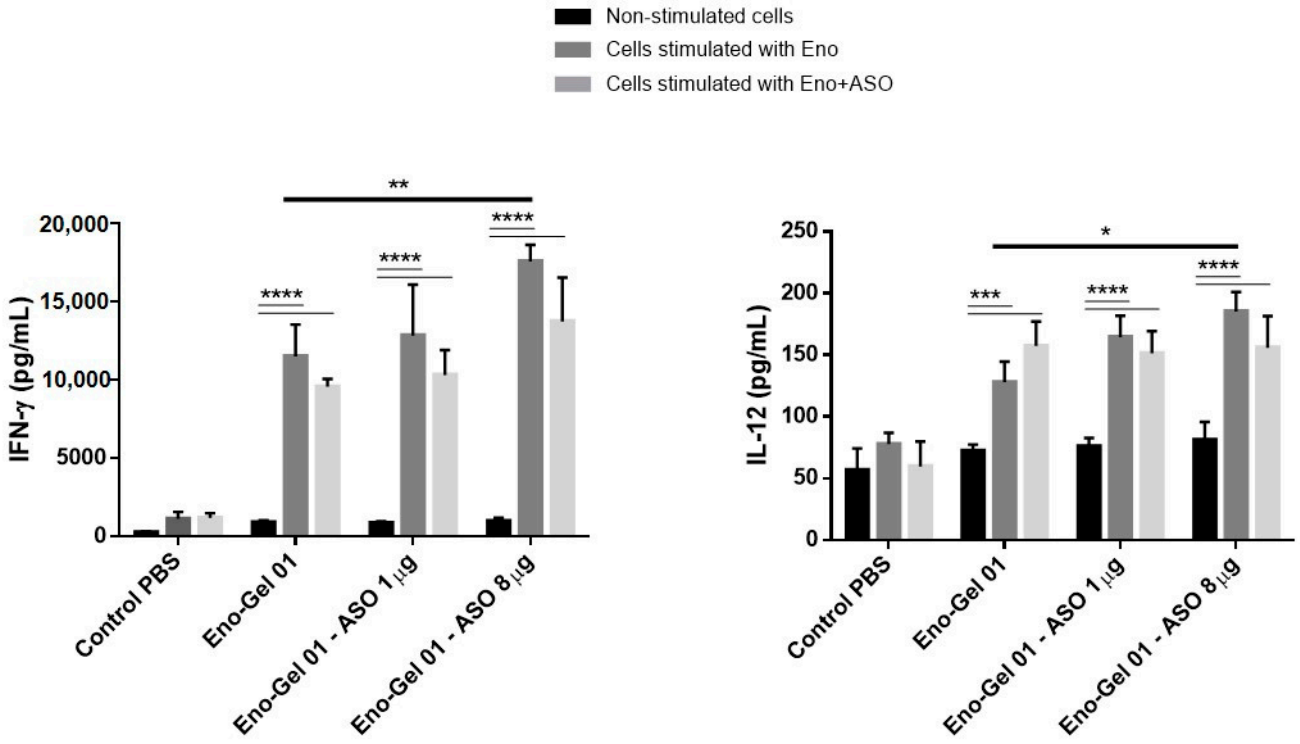

Figure 7. IFN-γ and IL-12 cytokines in the spleen. The spleen cells were extracted on day 21, then incubated for 48 h with Eno of *S. schenckii* or with Eno+ ASO anti-Foxp3. The cytokines IFN-γ and IL-12 were evaluated by means of ELISA. A one-way analysis of variance (ANOVA) with Tukey's post hoc test was used. The confidence interval was established at 95% for all tests. The level of significance and *p* values are shown as * ($p < 0.05$); ** ($p < 0.01$); *** ($p < 0.001$); **** ($p < 0.0001$).

3. Discussion

In the last decade, there has been growing interest in the rational design of vaccines using defined molecules with well-characterized cellular and molecular mechanisms of action. Given the known deleterious effects of Tregs in vaccine immunogenicity and efficacy, one of the current directions of this approach is the development of subunit vaccines and molecular adjuvants targeting immune regulatory networks to improve vaccine immunogenicity [15]. The use of ASOs targeting important regulatory mechanisms is one of the most promising molecular adjuvants for vaccine improvement [16]. Several ASOs have been designed against immunomodulatory components, such as cytokines [29,30], immune checkpoints [31,32], or transcription factors [25]. Recently, indoleamine 2,3-dioxygenase (IDO), which is involved in Treg activation, has also been targeted by silencing strategies [35]. In all cases, they showed a relevant activity enhancing vaccine immunogenicity.

Foxp3 transcription is induced in Tregs by T cell receptor (TCR) signaling. Upon its expression, an autoregulatory transcriptional circuit stabilizes Foxp3 gene expression to

consolidate Treg differentiation and activate the suppressive function [36]. The block of Foxp3 elicits Treg depletion and it promotes enhanced stimulation of effector immune mechanisms [37]. Foxp3 blocking has been used for vaccine improvement using different methods, including interfering with Foxp3 mRNA-transfected dendritic cells [20], synthetic peptides [22–24], and ASOs [25].

In this study, we used an anti-Foxp3 ASO, selected according to the results of a previous study, in which several ASOs were evaluated to improve an anti-tumor vaccine. The selected ASO showed the best Foxp3 silencing and immunostimulating activity [25]. Although several characterizations were made in that study, additional in vitro tests were included herein to deepen our understanding of its mechanisms of action. We first evaluated the capture kinetics of the ASO in murine splenocytes. This test allowed us to assess the phenomenon that occurs in vivo in the target cells. We also used two ASOs with different sizes (13 and 20 mer), and we observed that ONs in this size range can reach cells in a noticeably short time under culture conditions, barely 10 min. The highest concentrations in cells were achieved after two hours of incubation. Similar results were reported by other authors using different cells such as RAW264.7 cells [30] and lymph node cells from naïve ICR mice [31]. A parallel test was developed in human leucocytes from peripheral blood (CD45+) and the same results were observed.

The target of our anti-Foxp3 ASO was located in intron 1 of Foxp3 gene, so it is estimated that its site of action could lie at the preRNA level. In this way, the Foxp3 silencing effect and Treg depletion were evidenced in B16 cells and splenocytes, respectively. Although the microscopic images in splenocytes did not reveal the exact localization of the ONs, the heterogeneous distribution of the fluorescence suggests that they reached different intracellular regions. However, the best evidence that the ONs accessed the cell was the demonstration of the biologic effect evidenced by Foxp3 silencing and depletion of CD4 + CD25 + Foxp3 cells in vitro. In addition, under the experimental conditions used, the ONs used in this study were not cytotoxic, as previously reported [25].

The experimental vaccine used in this study was designed for the prevention of sporotrichosis, a worldwide emergent subcutaneous mycosis caused by pathogenic species of the genus *S. schenckii*. The recombinant-Enolase vaccine tested in this study was recently developed by our group and was suggested to be protective against experimental infection in mice [27,29]. Administration of anti-Foxp3 ASO as part of the vaccine formulation induced a considerable upregulation of the Th1-type cytokines IFN-γ and IL-12 in immunized mice. Moreover, it was also associated with enhanced production of specific antibodies. Interestingly, when the Tregs were quantified in the splenocytes of vaccinated mice, no differences between groups stimulated with enolase and those not stimulated were observed. The lack of differences in the presence of Tregs between the vaccinated groups may be because samples were taken 1 week after the second immunization. Thus, Treg depletion by the vaccine formulations with ASOs may not have been detected due to their being clonal and transitory. However, once again the stimulation of splenocytes with Eno plus ASO reduced the presence of Tregs in all groups.

Most of the adverse effects associated with Treg depletion occur when using products that are systematically administered [38–40]. Instead, the use of ASOs targeting Tregs as part of vaccine formulations could reduce off-target effects and toxicity manifestations. In this sense, the use of appropriate ASO delivery systems could help to optimize the adjuvant effect in a safer way [41]. More studies are necessary to consider the use of different delivery systems with vaccine models, including tissue distribution, pharmacokinetics, and stability analysis.

4. Materials and Methods

4.1. Oligonucleotides (ONs)

To study the Foxp3 interfering activity, ON sequences were as follows: ASO Foxp3: 5′-GGGGGAAGCACGGAAGGG′ (18 bp); scrambled: 5′-AGGAGGACAGGAGAGAGA-3′ (18 bp). The sequence of Foxp3 ASO is complementary to a region located in intron

1 preserved regions of the Foxp3 gene of *Mus musculus*, strain C57BL/6J chromosome X, GRCm38.p4 C57BL/6J (Accession NC_000086 Region: 7579676.7595243 VERSION NC_000086.7) in the US National Center for Biotechnology Information (NCBI) Nucleotide Database). Herein, we used the anti-Foxp3 2′-OMe-PS-ASO (ASO) and the control (Scrambled), as previously reported [25]. All these nucleic acids were purchased from Integrated DNA Technologies (Coralville, IA USA).

4.2. ON Uptake Kinetics in Murine Splenocytes

Spleens from 12-week-old male C57BL6 mice were aseptically removed and a suspension of splenocytes was prepared as previously described [42]. Two oligonucleotides (ONs) of 13- and 20-mer sizes with phosphorothioated, backbone labeled with either cyanine-5 (Cy-5) or fluorescein-5-isothiocyanate (FITC), and were used to evaluate the ON uptake kinetics in murine splenocytes. Labeled ONs of either 13 or 20 mer were incubated independently at concentrations of 0.5, 1, 2, and 4 μM at 37 °C for 0, 10, 30, 60, and 120 min with a of 1×10^7 cells/mL suspension of splenocytes in RPMI 1640 medium (Merck KGaA, Darmstadt, Germany), supplemented with 10% Fetal Bovine Serum. At each time and for each cell concentration, 50 μL of cell suspension were taken, properly dissolved in phosphate buffer saline (PBS pH 7.4), and analyzed by means of flow cytometry to measure the relative fluorescence (as RFU). A Gallios cytometer (Beckman Coulter, Brea, CA, USA) was used in all analyses.

Several samples of splenocytes treated with Cy5-labeled ONs and incubated for 1 h at 4 μM, from the experiment above, were also marked with anti-mouse CD4 FITC antibody (RM4–5) (Thermofisher Scientific, Waltham, MA, USA) and fixed with 4% formalin. Images of labeled cells were acquired by the high-content screening (HCS) InCell analyzer 2200 system (Cytiva, UK) to observe the uptake of ONs in CD4+ lymphocytes.

4.3. Biological Activity of the ASO Foxp3

The silencing effect of the anti-foxp3 ASO was confirmed in the murine melanoma cell line B16, which expresses high concentrations of this transcription factor. These cells are syngeneic with the C57BL/6 mice (Charles River Laboratories, Wilmington, MA, USA) employed. Cells were incubated with 2 μM ASO for 48 h. To quantify the Foxp3 mRNA, RNA was extracted from cultured cells using a commercial kit (NuceloSpin® RNA-Blood, (Machery-Nagel, Bethlehem, PA, USA) according to the manufacturer's instructions. RNA was retrotranscribed into complementary DNA (cDNA) using random hexamers and the enzyme reverse transcriptase High capacity cDNA reverse transcription kit, (Applied Biosystems, Foster City, CA, USA). The mRNA copy number of the gene was quantified by means of quantitative real time PCR using the 7900HT Fast Real-Time PCR System (Applied Biosystems, Foster City, CA, USA). TaqMan probes to amplify Foxp3 were obtained from Applied Biosystems (Foster City, CA, USA). The silencing efficiency was obtained by comparing the number of mRNA copies of these genes in the treated groups with cells treated with a respective control (scrambled), plotting the results on a standard curve prepared with a known amount of Foxp3 copy number.

The activity on Treg depletion was evaluated in splenocytes cultured with 2 μM of anti-Foxp3 ASO or a respective control scrambled ON for 48 h. The presence of CD4+ CD25+ Foxp3+ lymphocytes was quantified by means of flow cytometry using the eBioscience™ Mouse Regulatory T Cell Staining Kit #3 (Thermo Fisher Scientific, Waltham, MA, USA).

4.4. Recombinant Sporothrix schenckii Enolase

Recombinant *S. schenckii* enolase (Eno) used as the antigen in this study was obtained and characterized as previously described [27].

4.5. Cytotoxicity of ASO Foxp3 and Eno

The cytotoxicity of Eno (10 μg/mL) alone or in combination with the anti-Foxp3 or the scrambled control ASO (2 μM) was evaluated after 48 h incubation. These concentrations

were the same as those used in the following studies. Cell viability was analyzed by flow cytometry using the combination of PI/Annexin V-FITC (Thermo Fisher Scientific, Waltham, MA, USA) to determine the presence of necrosis (PI+ Annexin V−), late apoptosis (PI+ Annexin V+), early apoptosis (PI− Annexin V+), and living cells (PI− Annexin V−).

4.6. Adjuvants and Vaccine Formulation

The vaccine formulations were prepared as follows (Table 1):

Table 1. Vaccines composition.

Vaccine Formulations/100 µL/Mouse
PBS (Control)
100 µg of Eno in PBS
100 µg of Eno in PBS + 5% Montanide Gel 01 adjuvant (Gel 01) kindly provided by Seppic (Paris, France).
100 µg of Eno in PBS + 5% Gel 01 + ASO anti-Foxp3, 1 µg
100 µg of Eno in PBS + 5% Gel 01 + ASO anti-Foxp3, 8 µg.

4.7. Immunization Schedule

Male C57BL6 mice (n = 7) between 6 and 8 weeks of age received the subcutaneous (sc) administration of the vaccine (on days 0 for priming and 14 for boosting) on the back of the neck, with one of the vaccine formulations described above. One week after boosting, mice were sacrificed under anesthesia and bled by cardiac puncture to obtain serum, which was aliquoted and stored at −20 °C until use. The experimental procedure (Code: 2019/VSC/PEA/0279, 15 January 2020) was approved by the Biological Research Committee of the University of Valencia, Spain) and followed the European and Spanish directives for animal care 63/2010 and RD 53/2013, respectively.

4.8. Quantification of Anti-Eno Antibody Response by ELISA

The titration of IgG, IgG1, and IgG2A types of anti-Eno antibodies was carried out as described previously [27]. Briefly, a 96-well ELISA plate (Costar™, Thermo Fisher Scientific, Waltham, MA, USA) was coated with 5 µg Eno/mL in PBS at 4 °C (overnight). The plate was washed with washing buffer (0.1% Tween 20) and then blocked with 1% PBS-BSA for 1 h at room temperature and washed again. Specific IgG antibodies (total and 1 and 2A subclasses) against *S. schenckii* Eno, induced by the vaccine, were made in the serum of the vaccinated animals and controls. Serum samples were diluted in PBS-BSA 1% -Tween 20 (0.1%), at a 1/1000 ratio to determine total IgG and the IgG1 subclass and 1/100 for the IgG2a subclass, and were added to the ELISA plate. These samples were incubated at room temperature for 3 h. Antibodies were detected with total goat anti-IgG (Biocheck, South San Francisco, CA, USA) at 1/10,000 dilution and with anti-mouse IgG subclasses at 1/1000 dilution (Mouse monoclonal isotyping reagents; Sigma-Aldrich, St. Louis. MO, USA), followed by a 1/5000 dilution of biotinylated rabbit anti-goat IgG (Sigma, Sigma-Aldrich, St. Louis. MO, USA) and streptavidin coupled to horseradish peroxidase (Merck KGaA, Darmstadt, Germany). The plates were finally developed with a mixture of 30 mg/mL orthophenylenediamine (OPD) (Merck KGaA, Darmstadt, Germany) and hydrogen peroxide. The reaction was stopped with 1 N HCl to read the absorbance at 492 nm.

4.9. Quantification of IFN-γ and IL-12 in Splenocyte Culture Supernatant

Splenocytes from immunized and non-immunized mice were cultured as described above and stimulated with 10 µg/mL Eno or 10 µg/mL Eno+ 2 µM of ASO for 24 h. The levels of both IFN-γ and IL-12 were measured by means of ELISA in the culture supernatant, after stimulation, according to the manufacturer's instructions (Pharmingen, BD Biosciences, Diego, CA, USA).

4.10. Statistical Analysis

Statistical analysis was performed with Prism software ver. 6.01 (GraphPad, San Diego, CA, USA). One-way analysis of variance (ANOVA) with Tukey's test of comparisons was used. The confidence interval was established at 95% for all tests. The level of significance and the p values are shown as * ($p < 0.05$); ** ($p < 0.01$); *** ($p < 0.001$); **** ($p < 0.0001$).

5. Conclusions

In summary, the Foxp3 ASO used in this study is a safe and stable molecule that is suitable for improving the immunogenicity of adjuvanted vaccines as part of the vaccine formulation. Treg depletion seems to be the main mechanism of immunostimulation. Future studies will contribute to unraveling other mechanisms of ASO anti-Foxp3-induced immunostimulation and its safety profile. Another issue that is being evaluated is whether ASO can act alone as a vaccine adjuvant in different formulations and by different routes of administration.

Supplementary Materials: The following are available online at https://www.mdpi.com/article/10.3390/ijms22073470/s1.

Author Contributions: Conceptualization, A.B.-D., L.S., M.J.H., and S.F.A.; methodology, A.B.-D., L.S., M.J.H., and S.F.A.; validation, A.B.-D., L.S., M.J.H., and S.F.A.; formal analysis A.B.-D., L.S., M.J.H., and S.F.A.; investigation, A.B.-D., L.S., M.J.H., D.L.P., D.T.-M., G.O., M.F.-D., B.J., G.H., A.M., P.I.C., and S.F.A.; resources, A.B.-D.,S.F.A.; data curation, A.B.-D., L.S., M.J.H., and S.F.A.; writing—original draft preparation, A.B.-D., L.S., D.T.-M., and S.F.A.; writing—review and editing, A.B.-D., L.S., and S.F.A.; visualization, A.B.-D., L.S., and S.F.A.; supervision, I.Z.C. and S.F.A.; project administration, A.B.-D., I.Z.C., and S.F.A.; funding acquisition, A.B.-D. and I.Z.C. All authors have read and agreed to the published version of the manuscript.

Funding: This work was supported by Fundacão de Amparo à Pesquisa do Estado de São Paulo (FAPESP, grant No. 2018/15187-2).

Institutional Review Board Statement: The experimental procedure (Code: 2019/VSC/PEA/0279, 15 January 2020) was approved by the Biological Research Committee of the University of Valencia, Spain) and followed the European and Spanish directives for animal care 63/2010 and RD 53/2013, respectively.

Informed Consent Statement: Not applicable.

Data Availability Statement: No new data were created or analyzed in this study. Data sharing is not applicable to this article.

Conflicts of Interest: The authors declare no conflict of interest. The funders had no role in the design of the study; in the collection, analyses, or interpretation of data; in the writing of the manuscript, or in the decision to publish the results.

References

1. Brunkow, M.E.; Jeffery, E.W.; Hjerrild, K.A.; Paeper, B.; Clark, L.B.; Yasayko, S.A.; Wilkinson, J.E.; Galas, D.; Ziegler, S.F.; Ramsdell, F. Disruption of a new forkhead/winged-helix protein, scurfin, results in the fatal lymphoproliferative disorder of the scurfy mouse. *Nat. Genet.* **2001**, *27*, 68–73. [CrossRef]
2. Hori, S.; Nomura, T.; Sakaguchi, S. Control of regulatory T cell development by the transcription factor Foxp3. *Science* **2003**, *299*, 1057–1061. [CrossRef]
3. Fontenot, J.D.; Gavin, M.A.; Rudensky, A.Y. Foxp3 programs the development and function of CD4+CD25+ regulatory T cells. *Nat. Immunol.* **2003**, *4*, 330–336. [CrossRef] [PubMed]
4. Netea, M.G.; Sutmuller, R.; Hermann, C.; Van der Graaf, C.A.; Van der Meer, J.W.; van Krieken, J.H.; Hartung, T.; Adema, G.; Kullberg, B.J. Toll-like receptor 2 suppresses immunity against Candida albicans through induction of IL-10 and regulatory T cells. *J. Immunol.* **2004**, *172*, 3712–3718. [CrossRef]
5. Felonato, M.; Pina, A.; de Araujo, E.F.; Loures, F.V.; Bazan, S.B.; Feriotti, C.; Calich, V.L. Anti-CD25 treatment depletes Treg cells and decreases disease severity in susceptible and resistant mice infected with *Paracoccidioides brasiliensis*. *PLoS ONE* **2012**, *7*, e51071. [CrossRef]

6. Galdino, N.; Loures, F.V.; de Araújo, E.F.; da Costa, T.A.; Preite, N.W.; Calich, V. Depletion of regulatory T cells in ongoing paracoccidioidomycosis rescues protective Th1/Th17 immunity and prevents fatal disease outcome. *Sci. Rep.* **2018**, *8*, 16544. [CrossRef]
7. Whibley, N.; Maccallum, D.M.; Vickers, M.A.; Zafreen, S.; Waldmann, H.; Hori, S.; Gaffen, S.L.; Gow, N.A.; Barker, R.N.; Hall, A.M. Expansion of Foxp3(+) T-cell populations by *Candida albicans* enhances both Th17-cell responses and fungal dissemination after intravenous challenge. *Eur. J. Immunol.* **2014**, *44*, 1069–1083. [CrossRef] [PubMed]
8. Batista-Duharte, A.; Téllez-Martínez, D.; de Andrade, C.R.; Polesi, M.C.; Portuondo, D.L.; Carlos, I.Z. Transient Foxp3(+) regulatory T-cell depletion enhances protective Th1/Th17 immune response in murine sporotrichosis caused by *Sporothrix schenckii*. *Immunobiology* **2020**, *225*, 151993. [CrossRef] [PubMed]
9. Chakraborty, N.G.; Chattopadhyay, S.; Mehrotra, S.; Chhabra, A.; Mukherji, B. Regulatory T-cell response and tumor vaccine-induced cytotoxic T lymphocytes in human melanoma. *Hum. Immunol.* **2004**, *65*, 794–802. [CrossRef] [PubMed]
10. Klages, K.; Mayer, C.T.; Lahl, K.; Loddenkemper, C.; Teng, M.W.; Ngiow, S.F.; Smyth, M.J.; Hamann, A.; Huehn, J.; Sparwasser, T. Selective depletion of Foxp3+ regulatory T cells improves effective therapeutic vaccination against established melanoma. *Cancer Res.* **2010**, *70*, 7788–7799. [CrossRef]
11. Li, J.; Tan, D.; Liu, H.; Li, K. CD4(+) CD25(+) FoxP3(+) T regulatory cells in subjects responsive or unresponsive to hepatitis B vaccination. *Zhong Nan da Xue Xue Bao. Yi Xue Ban* **2011**, *36*, 1046–1051. [CrossRef]
12. Stein, P.; Weber, M.; Prüfer, S.; Schmid, B.; Schmitt, E.; Probst, H.C.; Waisman, A.; Langguth, P.; Schild, H.; Radsak, M.P. Regulatory T cells and IL-10 independently counterregulate cytotoxic T lymphocyte responses induced by transcutaneous immunization. *PLoS ONE* **2011**, *6*, e27911. [CrossRef]
13. Espinoza Mora, M.R.; Steeg, C.; Tartz, S.; Heussler, V.; Sparwasser, T.; Link, A.; Fleischer, B.; Jacobs, T. Depletion of regulatory T cells augments a vaccine-induced T effector cell response against the liver-stage of malaria but fails to increase memory. *PLoS ONE* **2014**, *9*, e104627. [CrossRef]
14. Mousavi Niri, N.; Memarnejadian, A.; Pilehvar-Soltanahmadi, Y.; Agha Sadeghi, M.; Mahdavi, M.; Kheshtchin, N.; Arab, S.; Namdar, A.; Jadidi, F.; Zarghami, N.; et al. Improved anti-treg vaccination targeting Foxp3 efficiently decreases regulatory T cells in mice. *J. Immunother.* **2016**, *39*, 269–275. [CrossRef] [PubMed]
15. Batista-Duharte, A.; Téllez-Martínez, D.; Fuentes, D.; Carlos, I.Z. Molecular adjuvants that modulate regulatory T cell function in vaccination: A critical appraisal. *Pharmacol. Res.* **2018**, *129*, 237–250. [CrossRef] [PubMed]
16. Batista-Duharte, A.; Sendra, L.; Herrero, M.J.; Téllez-Martínez, D.; Carlos, I.Z.; Aliño, S.F. Progress in the use of antisense oligonucleotides for vaccine improvement. *Biomolecules* **2020**, *10*, 316. [CrossRef]
17. Crooke, S.T. Molecular mechanisms of antisense oligonucleotides. *Nucleic Acid Ther.* **2017**, *27*, 70–77. [CrossRef] [PubMed]
18. Dhuri, K.; Bechtold, C.; Quijano, E.; Pham, H.; Gupta, A.; Vikram, A.; Bahal, R. Antisense oligonucleotides: An emerging area in drug discovery and development. *J. Clin. Med.* **2020**, *9*, 2004. [CrossRef]
19. Lu, L.; Barbi, J.; Pan, F. The regulation of immune tolerance by FOXP3. *Nat. Rev. Immunol.* **2017**, *17*, 703–717. [CrossRef] [PubMed]
20. Nair, S.; Boczkowski, D.; Fassnacht, M.; Pisetsky, D.; Gilboa, E. Vaccination against the forkhead family transcription factor Foxp3 enhances tumor immunity. *Cancer Res.* **2007**, *67*, 371–380. [CrossRef]
21. Mousavi Niri, N.; Memarnejadian, A.; Hadjati, J.; Aghasadeghi, M.R.; Shokri, M.; Pilehvar-Soltanahmadi, Y.; Akbarzadeh, A.; Zarghami, N. Construction and production of Foxp3-Fc (IgG) DNA vaccine/fusion protein. *Avicenna J. Med. Biotechnol.* **2016**, *8*, 57–64.
22. Casares, N.; Rudilla, F.; Arribillaga, L.; Llopiz, D.; Riezu-Boj, J.I.; Lozano, T.; López-Sagaseta, J.; Guembe, L.; Sarobe, P.; Prieto, J.; et al. A peptide inhibitor of FOXP3 impairs regulatory T cell activity and improves vaccine efficacy in mice. *J. Immunol.* **2010**, *185*, 5150–5159. [CrossRef] [PubMed]
23. Lozano, T.; Villanueva, L.; Durántez, M.; Gorraiz, M.; Ruiz, M.; Belsúe, V.; Riezu-Boj, J.I.; Hervás-Stubbs, S.; Oyarzábal, J.; Bandukwala, H.; et al. Inhibition of FOXP3/NFAT interaction enhances T cell function after TCR stimulation. *J. Immunol.* **2015**, *195*, 3180–3189. [CrossRef] [PubMed]
24. Lozano, T.; Soldevilla, M.M.; Casares, N.; Villanueva, H.; Bendandi, M.; Lasarte, J.J.; Pastor, F. Targeting inhibition of Foxp3 by a CD28 2′-Fluro oligonucleotide aptamer conjugated to P60-peptide enhances active cancer immunotherapy. *Biomaterials* **2016**, *91*, 73–80. [CrossRef] [PubMed]
25. Miguel, A.; Sendra, L.; Noé, V.; Ciudad, C.J.; Dasí, F.; Hervas, D.; Herrero, M.J.; Aliño, S.F. Silencing of Foxp3 enhances the antitumor efficacy of GM -CSF genetically modified tumor cell vaccine against B16 melanoma. *Onco Targets Ther.* **2017**, *10*, 503–514. [CrossRef]
26. Hagedorn, P.H.; Pontoppidan, M.; Bisgaard, T.S.; Berrera, M.; Dieckmann, A.; Ebeling, M.; Møller, M.R.; Hudlebusch, H.; Jensen, M.L.; Hansen, H.F.; et al. Identifying and avoiding off-target effects of RNase H-dependent antisense oligonucleotides in mice. *Nucleic Acids Res.* **2018**, *46*, 5366–5380. [CrossRef] [PubMed]
27. Portuondo, D.L.; Dores-Silva, P.R.; Ferreira, L.S.; de Oliveira, C.S.; Téllez-Martínez, D.; Marcos, C.M.; de Aguiar Loesch, M.L.; Guzmán, F.; Gava, L.M.; Borges, J.C.; et al. Immunization with recombinant enolase of *Sporothrix* spp. (rSsEno) confers effective protection against sporotrichosis in mice. *Sci. Rep.* **2019**, *9*, 17179. [CrossRef]
28. Téllez-Martínez, D.; Leandro Portuondo, D.; Loesch, M.L.; Batista-Duharte, A.; Zeppone Carlos, I. A Recombinant enolase-Montanide™ PetGel a vaccine promotes a protective Th1 immune response against a highly virulent *Sporothrix schenckii* by toluene exposure. *Pharmaceutics* **2019**, *11*, 144. [CrossRef]

29. Ripple, M.J.; You, D.; Honnegowda, S.; Giaimo, J.D.; Sewell, A.B.; Becnel, D.M.; Cormier, S.A. Immunomodulation with IL-4Rα antisense oligonucleotide prevents respiratory syncytial virus-mediated pulmonary disease. *J. Immunol.* **2010**, *185*, 4804–4811. [CrossRef]
30. Zhang, J.; Liu, N.; Lu, Y.; Huang, Z.; Zang, Y.; Chen, J.; Zhang, J.; Ding, Z. Phosphorothioated antisense oligodeoxynucleotide suppressing interleukin-10 is a safe and potent vaccine adjuvant. *Vaccine* **2019**, *37*, 4081–4088. [CrossRef] [PubMed]
31. Li, X.; Yang, L.; Zhao, P.; Yao, Y.; Lu, F.; Tu, L.; Liu, J.; Li, Z.; Yu, Y.; Wang, L. Adjuvanticity of a CTLA-4 3′ UTR complementary oligonucleotide for emulsion formulated recombinant subunit and inactivated vaccines. *Vaccine* **2017**, *35*, 2379–2389. [CrossRef] [PubMed]
32. Li, Z.; Song, Y.; Cui, C.; Lan, Y.; Li, X.; Liu, Y.; Lu, F.; Zhang, Y.; Yu, Y.; Wang, L. A LAG3-interfering oligonucleotide acts as an adjuvant to enhance the antibody responses induced by recombinant protein vaccines and inactivated influenza virus vaccines. *Appl. Microbiol. Biotechnol.* **2019**, *103*, 6543–6557. [CrossRef] [PubMed]
33. Maia, D.C.; Sassá, M.F.; Placeres, M.C.; Carlos, I.Z. Influence of Th1/Th2 cytokines and nitric oxide in murine systemic infection induced by *Sporothrix schenckii*. *Mycopathologia* **2006**, *161*, 11–19. [CrossRef]
34. Batista-Duharte, A.; Téllez-Martínez, D.; Roberto de Andrade, C.; Portuondo, D.L.; Jellmayer, J.A.; Polesi, M.C.; Carlos, I.Z. *Sporothrix brasiliensis* induces a more severe disease associated with sustained Th17 and regulatory T cells responses than *Sporothrix schenckii sensu stricto* in mice. *Fung. Biol.* **2018**, *122*, 1163–1170. [CrossRef] [PubMed]
35. Liu, Y.; Xu, P.; Liu, H.; Fang, C.; Guo, H.; Chen, X.; Tan, M.; Zhang, Y.; Min, W. Silencing IDO2 in dendritic cells: A novel strategy to strengthen cancer immunotherapy in a murine lung cancer model. *Int. J. Oncol.* **2020**, *57*, 587–597. [CrossRef]
36. Colamatteo, A.; Carbone, F.; Bruzzaniti, S.; Galgani, M.; Fusco, C.; Maniscalco, G.T.; Di Rella, F.; de Candia, P.; De Rosa, V. Molecular mechanisms controlling Foxp3 expression in health and autoimmunity: From epigenetic to post-translational regulation. *Front. Immunol.* **2020**, *10*, 3136. [CrossRef]
37. Lahl, K.; Sparwasser, T. *In vivo* depletion of FoxP3+ Tregs using the DEREG mouse model. *Methods Mol. Biol.* **2011**, *707*, 157–172. [CrossRef]
38. van Elsas, A.; Sutmuller, R.P.; Hurwitz, A.A.; Ziskin, J.; Villasenor, J.; Medema, J.P.; Overwijk, W.W.; Restifo, N.P.; Melief, C.J.; Offringa, R.; et al. Elucidating the autoimmune and antitumor effector mechanisms of a treatment based on cytotoxic T lymphocyte antigen-4 blockade in combination with a B16 melanoma vaccine: Comparison of prophylaxis and therapy. *J. Exp. Med.* **2001**, *194*, 481–489. [CrossRef]
39. Kähler, K.C.; Hassel, J.C.; Heinzerling, L.; Loquai, C.; Thoms, K.M.; Ugurel, S.; Zimmer, L.; Gutzmer, R. Side effect management during immune checkpoint blockade using CTLA-4 and PD-1 antibodies for metastatic melanoma—An update. *J. Dtsch. Dermatol. Ges.* **2020**, *18*, 582–609. [CrossRef]
40. Corsello, S.M.; Barnabei, A.; Marchetti, P.; De Vecchis, L.; Salvatori, R.; Torino, F. Endocrine side effects induced by immune checkpoint inhibitors. *J. Clin. Endocrinol. Metab.* **2013**, *98*, 1361–1375. [CrossRef]
41. Ferreira, L.S.; Gonçalves, A.C.; Portuondo, D.L.; Maia, D.C.; Placeres, M.C.; Batista-Duharte, A.; Carlos, I.Z. Optimal clearance of *Sporothrix schenckii* requires an intact Th17 response in a mouse model of systemic infection. *Immunobiology* **2015**, *220*, 985–992. [CrossRef] [PubMed]
42. Roberts, T.C.; Langer, R.; Wood, M.J.A. Advances in oligonucleotide drug delivery. *Nat. Rev. Drug Discov.* **2020**, *19*, 673–694. [CrossRef] [PubMed]

International Journal of
Molecular Sciences

MDPI

Article

Proof-of-Concept: Antisense Oligonucleotide Mediated Skipping of Fibrillin-1 Exon 52

Jessica M. Cale [1], Kane Greer [1], Sue Fletcher [1,2,3] and Steve D. Wilton [1,2,*]

[1] Centre for Molecular Medicine and Innovative Therapeutics, Health Futures Institute, Murdoch University, Murdoch, WA 6150, Australia; jessica.cale@murdoch.edu.au (J.M.C.); K.Greer@murdoch.edu.au (K.G.); S.Fletcher@murdoch.edu.au (S.F.)
[2] Centre for Neuromuscular and Neurological Disorders, Perron Institute for Neurological and Translational Science, The University of Western Australia, Nedlands, WA 6009, Australia
[3] PYC Therapeutics, Nedlands, WA 6009, Australia
* Correspondence: s.wilton@murdoch.edu.au; Tel.: +61-8-9360-2305

Abstract: Marfan syndrome is one of the most common dominantly inherited connective tissue disorders, affecting 2–3 in 10,000 individuals, and is caused by one of over 2800 unique *FBN1* mutations. Mutations in *FBN1* result in reduced fibrillin-1 expression, or the production of two different fibrillin-1 monomers unable to interact to form functional microfibrils. Here, we describe in vitro evaluation of antisense oligonucleotides designed to mediate exclusion of *FBN1* exon 52 during pre-mRNA splicing to restore monomer homology. Antisense oligonucleotide sequences were screened in healthy control fibroblasts. The most effective sequence was synthesised as a phosphorodiamidate morpholino oligomer, a chemistry shown to be safe and effective clinically. We show that exon 52 can be excluded in up to 100% of *FBN1* transcripts in healthy control fibroblasts transfected with PMO52. Immunofluorescent staining revealed the loss of fibrillin 1 fibres with ~50% skipping and the subsequent re-appearance of fibres with >80% skipping. However, the effect of exon skipping on the function of the induced fibrillin-1 isoform remains to be explored. Therefore, these findings demonstrate proof-of-concept that exclusion of an exon from *FBN1* pre-mRNA can result in internally truncated but identical monomers capable of forming fibres and lay a foundation for further investigation to determine the effect of exon skipping on fibrillin-1 function.

Keywords: Marfan syndrome; fibrillin-1; antisense oligonucleotides; exon skipping; splice-switching

Citation: Cale, J.M.; Greer, K.; Fletcher, S.; Wilton, S.D. Proof-of-Concept: Antisense Oligonucleotide Mediated Skipping of Fibrillin-1 Exon 52. *Int. J. Mol. Sci.* **2021**, *22*, 3479. https://doi.org/10.3390/ijms22073479

Academic Editors: Salvador F. Aliño and Luis Sendra

Received: 10 February 2021
Accepted: 25 March 2021
Published: 27 March 2021

1. Introduction

Marfan syndrome (MFS, MIM 154700) is one of the most common dominantly inherited connective tissue diseases, affecting an estimated 2–3 in 10,000 individuals [1,2], in a family of disorders called the type-1 fibrillinopathies [3]. Marfan syndrome is characterised by extreme height with disproportionate limb and digit length in comparison to the torso, coupled with a myriad of other skeletal, ocular, skin and cardiovascular abnormalities [4]. However, it is the progressive growth of the aorta often eventuating into aortic dissection and rupture that is the most common cause of death [5].

Marfan syndrome was linked in the early 1990s to mutations in the, then recently discovered [6], fibrillin-1 gene (*FBN1*) [7,8]. Since then, over 2800 disease-causing mutations have been reported [9]. Fibrillin-1 encodes a large 350 kDa glycoprotein of the same name that is secreted from the cell and deposited into the extracellular matrix (ECM) [6]. In a healthy individual, fibrillin-1 monomers aggregate into multimer units within the first few hours after secretion [10]. Fibrillin-1 multimers form the backbone of microfibrils [6] that are essential in the majority of connective tissues and to which many microfibril associated proteins bind [11]. It is in the microfibril form that fibrillin-1 exerts its structural and regulatory roles, providing a backbone for microfibrils [12], maintaining the stability of elastic

fibres [13], and regulating the bioavailability of signalling proteins such as transforming growth factor-beta (TGF-β) [14,15].

In a Marfan syndrome patient, the disease-causing *FBN1* mutation results in a lack of functional microfibrils, in turn leading to instability of the ECM that is further compounded by the dysregulation of TGF-β [12,16]. An increase in bioavailable TGF-β activates a signalling cascade resulting in, among other outcomes, increased expression of matrix metalloproteinase [15] that degrade fibrillin-1 and other matrix proteins leading to further destabilisation of the ECM [15,17]. The initial loss of functional microfibrils is theorised to depend on the type of mutation. In general, missense mutations, which do not affect a conserved cysteine, as well as splicing mutations are thought to exert dominant negative effects. Such mutations result in the production of a dominant aberrant monomer that disrupts the assembly of the wild-type protein into microfibrils [18]. In contrast, many nonsense and frameshifting mutations are associated with haploinsufficiency [19,20]. This haploinsufficiency is the result of transcript instability that leads to degradation and thus reduced fibrillin-1 expression [21]. A small subgroup of nonsense and frameshift mutations that affect the C-terminal region can produce stable transcripts that are translated into protein rather than being degraded [22,23]. Such mutations have been associated with intracellular retention of fibrillin-1, the outcome of which is a similar lack of microfibrils in the ECM [20,22].

The most common type of mutations are missense mutations that result in the disruption of a cysteine residue [9,24]. The fibrillin-1 protein has several repeated domains including 47 epidermal growth factor (EGF)-like domains, 43 of which are involved in calcium-binding (cbEFG-like), seven TGF-β binding protein-like (TB) domains and two hybrid domains [25,26]. Each of these domains are cysteine-rich with six to eight conserved cysteine residues that play a critical role in the folding and stability of the fibrillin-1 protein [25,27]. Mutations affecting a conserved cysteine have been shown to either increase the susceptibility of fibrillin-1 to proteolysis [28,29] or disrupt the folding and secretion of fibrillin-1 leading to intracellular retention [30]. The outcome of either scenario is a similar decreased microfibril stability and abundance.

Following the discovery that mutations in fibrillin-1 result in TGF-β dysregulation, a research area emerged focussing on the antagonism of TGF-β as a therapeutic strategy [31,32]. However, no breakthroughs have yet been made in the field and treatment of MFS patients remains heavily focused on symptom management. The current standard of care includes surgical correction of scoliosis, ectopia lentis, pectus deformities and aortic dilatation, as well as pain management and the use of β-Blockers [33–35] or more recently angiotensin II receptor type 1 blockers [1,31,36] to slow aortic growth. Here, we propose that personalised medicines using antisense oligonucleotides (AO) to alter *FBN1* exon selection during the splicing process, may be an appropriate therapeutic approach for some individuals with Marfan syndrome.

Antisense oligonucleotides (AO) are short sequences, generally between 15 and 30 bases in length, that are single-stranded analogues of nucleic acids. An AO is designed to be complementary to the region of interest binding to the target RNA or DNA through Watson-Crick base pairing. When bound to the target sequence and depending upon the chemistry, AOs can alter transcripts through two main mechanisms; recruiting RNase-H to cleave the target leading to degradation [37,38] or physically blocking the binding of regulatory factors or machinery of the transcription [39], translation [40] or splicing [41,42] processes. Several studies have outlined the potential of AOs in the treatment of genetic diseases. Several notable examples—eteplirsen [43,44], nusinersen [45,46] and more recently golodirsen [47], viltolarsen [48] and casimersen [49]—have now been approved by the United States Food and drug authority (FDA). All four drugs are a class of AO commonly referred to as splice switching. Splice switching AOs function by blocking the splicing machinery or regulatory features, altering the normal splicing process.

Splicing is an essential process for all multi-exon genes; removing the non-coding introns and re-joining the coding exons, before the transcript can be translated. The splicing

process is, therefore, tightly regulated by several *cis*- and *trans*-acting elements. The majority of multi-exon genes, however, also undergo a process called alternative splicing [50]. Alternative splicing allows the production of multiple transcripts, and thus proteins, from a single gene, significantly increasing genetic complexity and diversity. To maintain the precise removal of introns, as well as supporting alternative splicing, the regulation of these processes is multi-layered and complex while maintaining a level of flexibility in the definition of an exon. Utilising the inherent flexibility of exon definition AOs can be targeted to motifs involved in exon recognition and processing, such as the acceptor and donor splice sites, as well as hotspots for splicing enhancers either in the intron or exon. Targeting enhancer sites can block the binding of positive splicing factors, thus decreasing the definition and recognition of an exon sufficiently to result in its exclusion [51,52]. Contrariwise, targeting exonic splicing silencer or intronic splicing silencer sequences can inhibit the binding of negative splicing factors, increasing exon recognition leading to inclusion [52,53].

The affinity, specificity, efficiency, stability and tolerance of an AO can be increased by modifying the chemical structure of the monomers and the backbone. Two widely used chemistries were utilised in this study. First of which has 2′-O-methyl (2′OMe) ribose ring modifications on a negatively charged phosphorothioate (PS) backbone. The resulting 2′OMe-PS compounds are robust RNase-H independent AOs that are nuclease resistant and relatively cost-effective to synthesise. The second chemistry is the phosphorodiamidate morpholino oligomer (PMO) that completely replaces the ribose sugar moiety with a morpholine ring and has phosphorodiamidate linkages [54]. The PMO chemistry is RNase-H independent, and has a neutral charge that precludes interaction with proteins, greatly reducing the possibility of off-target effects [55,56]. While the PMO chemistry is both more technically challenging and costly to synthesise than 2′OMe-PS AOs, PMOs are generally recognised as both safe and effective in a clinical setting, making it a promising chemistry for drug development [43,57].

As described previously, fibrillin-1 monomers are secreted from the cell and rapidly aggregated into multimer units to form the backbone of fibrillin-1 microfibrils [10]. Mutations in *FBN1* disrupt the formation of microfibrils, ultimately leading to a disease phenotype; either Marfan syndrome or another type-1 fibrillinopathy. Therefore, we propose that removal of a mutation-associated exon from all *FBN1* transcripts during the splicing process could result in the production of fibrillin-1 proteins that are able to form functional microfibrils, restoring ECM stability. To assess the viability of this hypothesis, we addressed three preliminary questions using *FBN1* exon 52 as a model. (1) Can an exon be specifically removed from *FBN1* pre-mRNA using antisense oligonucleotides, (2) Can sufficient exon skipping be achieved, and (3) can the internally truncated fibrillin-1 protein form microfibrils.

2. Results

2.1. The FBN1 Transcript and Antisense Oligonucleotide Design

The fibrillin-1 transcript (LRG_778t1; NM_000138.4) contains 11,695 bases separated into 66 exons, 65 of which encode the 350 kDa fibrillin-1 protein (Figure 1a). Exon 52 of *FBN1* encodes a total of 22 amino acids and makes up a portion of the sixth, of seven TB domains. Over 20 disease-causing mutations have been reported to affect exon 52, the majority of which result, or are predicted to result, in aberrant exon 52 splicing [9,24]. To excise exon 52, along with the flanking introns during the splicing process, five AOs were designed to target the acceptor, and donor splice sites as well as exonic splice enhancer (ESE) and intronic splice enhancer (ISE) sites across exon 52, predicted using the webtool SpliceAid [58] (Figure 1c). SpliceAid examines the exonic and intronic sequence of interest and determines associated silencer and enhancer sites. Each site is given a score of 1 to 10 that indicates the strength of the site, with the value closest to 10 being the strongest ESE sites.

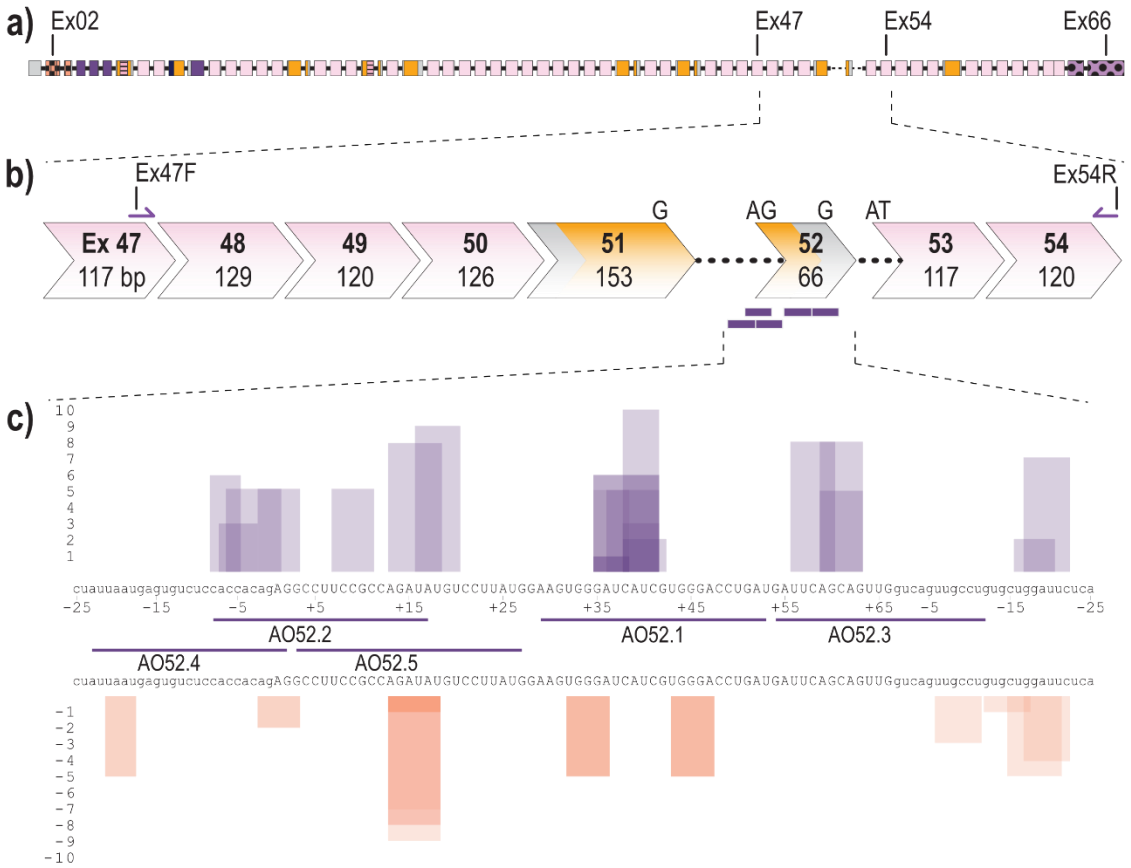

Figure 1. Schematic of *FBN1* pre-mRNA highlighting the region between exons 47 and 54 as well as AO binding sites (**a**) Full fibrillin-1 pre-mRNA transcript with each box representing an exon. The solid black line represents introns (not to scale); (**b**) highlighting the region between exons 47 and 54; showing forward and reverse primers and antisense oligonucleotide binding sites (purple bars). Chevron sides indicate exons bounded by partial codons. Pink and yellow fill indicate regions encoding cbEGF-like and TB domains, respectively. The black dotted line indicates partial introns 51 and 52.; (**c**) Antisense oligonucleotide binding sites and the regulatory motifs they target predicted using spliceAid [58]. Each box represents a predicted enhancer (purple) or silencer (orange) site. The height of the box represents the strength of the site with 1 being the weakest and 10 being the strongest. Exonic and intronic sequences are shown in upper- and lower-case, respectively.

2.2. Evaluation of AOs to Induce Exon 52 Skipping from FBN1 Transcripts

Initial AO screening was performed using AOs composed of 2′OMe-PS molecules. An unrelated control AO that does not anneal to any transcript was included in all transfections as a sham treatment to observe any chemistry or delivery related effects on cell health and transcript abundance. A complete list of AOs can be found in Table 1.

All 2′OMe-PS AOs were transfected into fibroblasts, derived from a healthy control subject, at three concentrations (200 nM, 100 nM and 50 nM) and incubated for 24 h before collection for RNA extraction and RT-PCR analysis to assess exon skipping efficiencies. The 24-h transfection incubation period was chosen after a time course of 24, 48 and 72 h revealed negligible differences in skipping efficiency over time (data not shown). However, treated cells, in particular those treated with the higher AO concentration, showed changes in morphology and began to die after 48 h (data not shown).

Table 1. Antisense oligonucleotide binding coordinates and sequences.

Nomenclature (FBN1 H . . .)	Name	Sequence (5′-3′)	Chemistry
52A(+29+53)N	AO52.1^{n}	AUC AGG UCC CAC GAU GAU CCC ACU U ATC AGG TCC CAC GAT GAT CCC ACT T	2′OMe-PS PMO
52A(+29+53)M	AO52.1^{m}	AUC AGG UCC CAC AAU GAU CCC ACU U	2′OMe-PS
52A(−08+17)	AO52.2	UAU CUG GCG GAA GGC CUC UGU GGU G	2′OMe-PS
52D(+13-12)	AO52.3	CAG GCA ACU GAC CAA CUG CUG AAU C	2′OMe-PS
52A(−23+02)	AO52.4	CUC UGU GGU GGA GAC ACU CAU UAA U	2′OMe-PS
52A(+03+27)	AO52.5	CAU AAG GAC AUA UCU GGC GGA AGG C	2′OMe-PS
Control AO	Ctrl	GGA UGU CCU GAG UCU AGA CCC UCC G	2′OMe-PS
GeneTools Control	GTC	CCT CTT ACC TCA GTT ACA ATT TAT A	PMO

Analysis of PCR amplicons revealed the presence of two products in several samples; the expected full length (FL) product between exon 47 forward and exon 54 reverse primers, as well as a smaller product corresponding to the expected size after skipping of exon 52 (Δ52) (Figure 2a). The identity of the amplicons was confirmed by band purification and Sanger sequencing, confirming the precise removal of all 66 bases of exon 52 (Figure 2b,c).

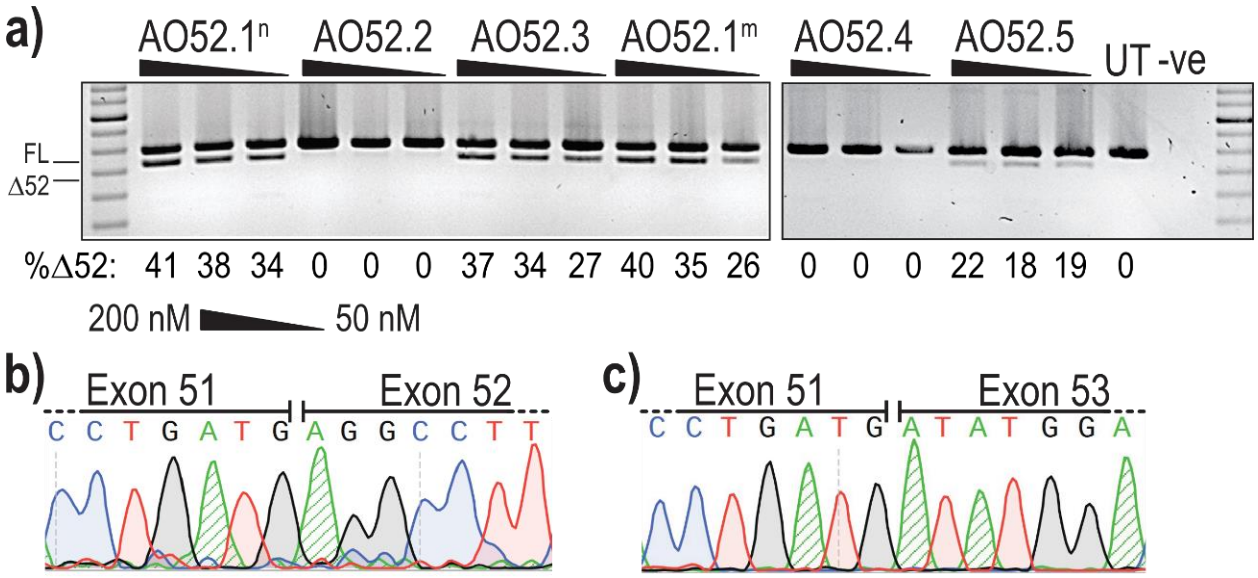

Figure 2. Evaluation of AOs designed to induce *FBN1* exon 52 skipping. (**a**) Screening of 2′OMe-PS AOs targeting exon 52. Healthy control fibroblasts were transfected with AOs as lipoplexes at three concentrations, 200, 100 and 50 nM. The values below each gel image indicate the percentage of exon 52 skipped (Δ52) transcripts in each sample. Ctrl: an unrelated sequence used as a sham treatment, UT: untreated control, -ve: RT-PCR negative control. 100 bp molecular marker used for size reference. The gels were cropped for presentation. Full gel images are presented in Figure S1; (**b**) Sanger sequencing analysis showing the junction between exons 51 and 52 in full-length transcripts (FL, 859 bp); (**c**) Sanger sequencing analysis showing the junction between exon 51 and 53 exon 52-skipped transcripts (Δ52, 793 bp).

The most efficient exon 52 skipping was induced by AO52.1^{n}, with 41% of transcripts lacking exon 52 after transfection at 200 nM (Figure 2a). However, three other sequences, AO52.1^{m}, AO52.3 and AO52.5 were also relatively efficient, inducing up to 40%, 37% and 22% skipping, respectively (Figure 2a). The remaining two sequences did not induce any measurable exon 52 skipping. The sequences AO52.1^{n} and AO52.1^{m} differ by a single base, with each being an exact complementary pair for the wild-type and a known Marfan syndrome patient cell line, respectively. This AO was designed in the hopes of understanding the mechanism behind the mutation that is known to cause mis-splicing of

exon 52. The one base-pair mismatch did not greatly reduce the efficiency of AO52.1^{m} in healthy control cells.

Following initial AO screening, removal of exon 52 was deemed an appropriate option. In an attempt to further enhance exon exclusion, two AOs targeting *FBN1* exon 52 were combined into cocktails and evaluated. This method has previously been shown to boost skipping efficiency through synergy between the two AOs [59]. Six of the eight cocktails tested, induced between 23% and 42% exon 52 skipping, suggestive of an additive or baseline effect, similar to that achieved with a single AO. The combination of AO52.1^{n} with AO52.2 or AO52.3 was antagonistic resulting in no measurable exon skipping (Figure S2). No synergistic cocktails were identified, therefore AO52.1^{n} was chosen as the most promising candidate and the sequence was synthesised as a PMO for further analysis (Table 1).

2.3. PMO52 Induces Efficient Exon 52 Skipping and an Increase in Fibrillin-1 Microfibrils Determined by Immunofluorescent Staining

To both confirm the efficiency of the AO52.1^{n} sequence as a PMO, and to assess the effect of exon 52 skipping on fibrillin-1 microfibril formation, PMO52 was transfected into healthy control fibroblasts. An electroporation-based transfection method, nucleofection, was used to deliver PMO52 into control cells at two concentrations, 250 and 50 μM, as calculated in a 20 μL cuvette. Transfected cells were plated either directly into 24 well plates or onto coverslips and incubated for 72 h before cells were collected for RNA analysis and coverslips fixed for immunofluorescent staining.

Representative results of healthy control cells treated with PMO52 are presented in Figure 3a. These representative RT-PCR results reflect exon 52 removal from approximately 100% of transcripts, with no measurable FL product remaining. The lower AO concentration was observed to induce approximately 50% skipping, with no endogenous exon 52 skipping observed in either the control or untreated samples (Figure 3a). Analysis of RT-PCR amplicons across four replicates revealed relatively consistent dose-dependent exon 52 skipping. On average Δ52 transcripts constituted 91% of total *FBN1* transcripts from cells transfected at the higher concentration and 55% at the lower concentration (Figure 3b). The lowest skipping efficiency at the highest concentration was 74%; in the same experiment, the lower concentration maintained the average 55% skipping efficiency (Figure 3b).

Fibrillin-1 protein was detected through immunofluorescent staining using a fibrillin-1 specific primary antibody and a fluorescently tagged secondary. Staining of the untreated sample revealed the long-thin extracellular fibre-like formations expected of fibrillin-1 (Figure 3c iii). Notably, the morphology of fibres in the sample with more than 90% skipping is trending toward those seen in the untreated healthy control (Figure 3c i,iii). The abundance of fibrillin-1 staining, as well as the abundance of fibre-like formations is, however, noticeably reduced in the 250 μM-treated samples. In contrast to the fibre formation in both untreated and high concentration of PMO52, healthy control cells treated with 50 μM of PMO52, present with a complete loss of fibrillin-1 fibres and an overall reduction in fibrillin-1 staining (Figure 3c ii).

Following successful exon 52 skipping in healthy control fibroblasts, PMO52 was further assessed in fibroblasts derived from an individual with Marfan syndrome obtained from the NIGMS Human Genetic Cell Repository at the Coriell Institute for Medical Research. The patient fibroblasts (MFS$^{\Delta 52}$) were reported to harbour a silent c.6354C > T, p.(Ile2118Ile) mutation in *FBN1* that was found to result in the in-frame skipping of exon 52 [60]. PMO52 was nucleofected into the MFS$^{\Delta 52}$ and healthy control fibroblasts and collected for RNA and protein analysis after 4 days. The PMO52 sequence resulted in robust skipping in both cell lines and a strong dose response was observed. Treatment with 50 μM resulted in 64% and 41% exon 52 skipping in MFS$^{\Delta 52}$ and healthy control fibroblasts, respectively (Figure 4a). Increasing the concentration to 250 μM resulted in 92% skipping in both cell lines (Figure 4a).

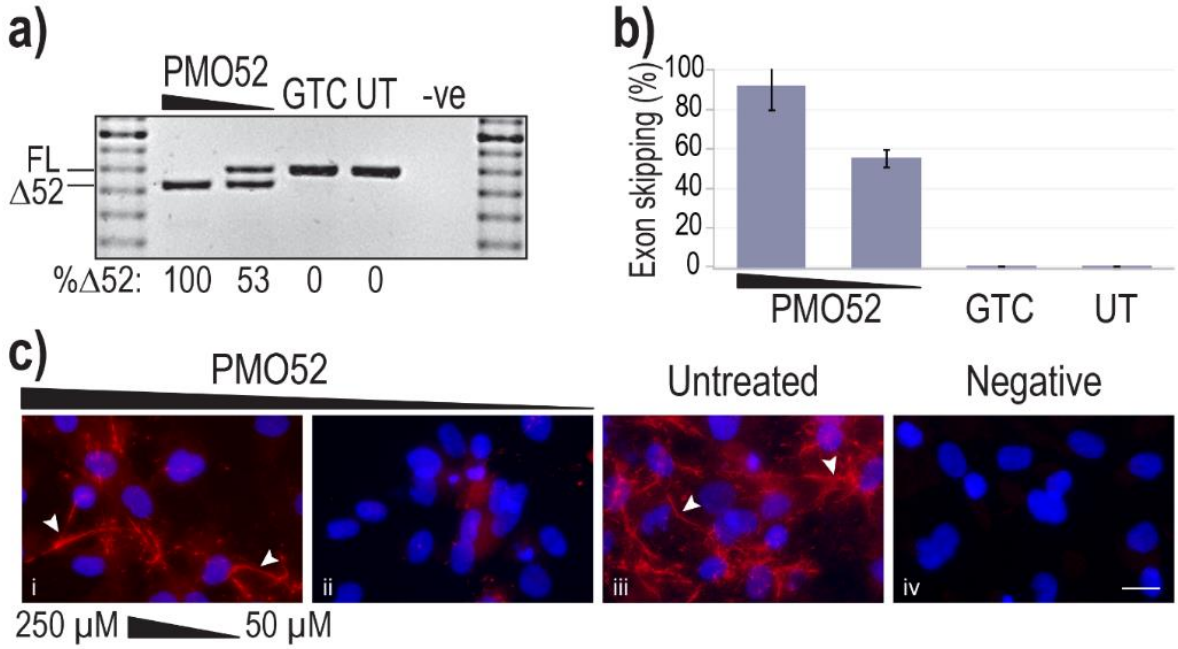

Figure 3. Efficiency and effect of PMO52. Healthy control fibroblasts were harvested for protein and RNA analysis, 72 h after nucleofection with PMO52 at concentrations of 250 μM and 50 μM; calculated in a 20 μL cuvette. (**a**) Agarose gel fractionation of *FBN1* exons 47 to 54 amplicons showing full-length (FL, 859 bp) and exon 52-skipped (Δ52, 793 bp) transcripts. The values below the gel image indicate the percentage of Δ52 transcripts. GTC: Gene Tools control PMO, UT: Untreated control, -ve: RT-PCR negative control, 100 bp molecular marker used as a size reference. The gels were cropped for presentation. Full gel images are presented in Figure S1 (**b**) The percentage of full-length transcript relative to total *FBN1* transcript across four biological replicates (means plus error bars. Error bars = standard deviation, $n = 4$). (**c**) Fibrillin-1 protein analysed via immunofluorescent staining. Merged fluorescence images of Hoechst staining of the nucleus (blue) and fibrillin-1 (red) with 'healthy' fibre-like morphology of fibrillin-1 indicated by white arrowheads. Negative: no primary antibody added, to control for non-specific binding of the secondary antibody. Untreated: no PMO added. Scale bar = 20 μm. The images were cropped for presentation. Full images are presented in Figure S3.

Immunofluorescence once again revealed the strong fibre-like structures formed by fibrillin-1 in the untreated, and GTC treated, healthy control fibroblasts. These fibres were completely lost when 41% skipping was induced (Figure 4b vi). The staining pattern mirrored that observed in the untreated MFS$^{\Delta 52}$ fibroblasts with no fibre formation and minimal diffuse fibrillin-1 staining (Figure 4b iv). The minor increase in the proportion of skipped products after treatment of MFS$^{\Delta 52}$ fibroblasts with 50 μM of PMO52, did not alter the fibrillin-1 staining pattern (Figure 4b ii). In both cell lines, treatment with 250 μM of PMO52 resulted in the formation of fibrillin-1 fibres. In the healthy control cells, these fibres, while of high staining intensity, were fragmented and reduced in abundance compared to the untreated healthy control sample (Figure 4b v,viii). However, in MFS$^{\Delta 52}$ cells treated with the 250 μM, fibrillin-1 fibres had a continuous, non-fragmented morphology trending toward those seen in the untreated healthy control (Figure 4b i,viii). The fibres are also relatively abundant filling the majority of the field-of-view; however, they are not as plentiful as those seen in the untreated healthy control that form a multi-layered lattice (Figure 4b i,viii). Similar staining patterns were seen across multiple biological replicates representative images of one replicate are presented in Figure S4.

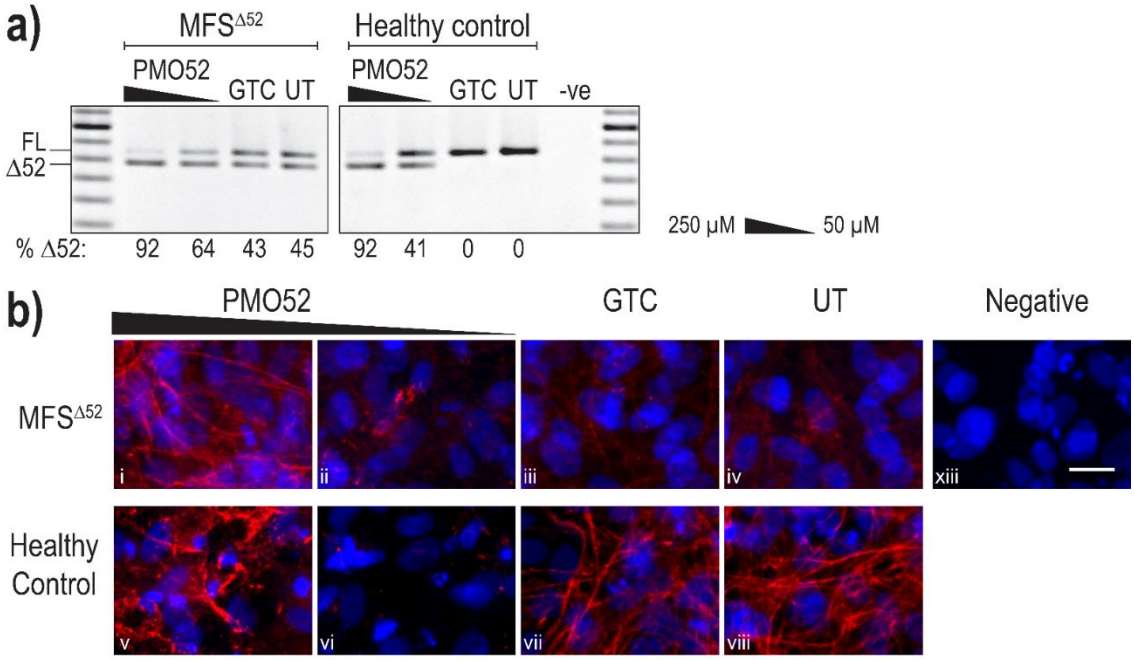

Figure 4. Evaluation of PMO52 in MFS$^{\Delta 52}$ fibroblasts. Healthy control and MFS$^{\Delta 52}$ patient fibroblasts were transfected with PMO52 (250 μM and 50 μM), GTC or left untreated. Cells were collected 4 days post-transfection. (**a**) RT-PCR analysis of *FBN1* exons 47 to 54 amplicons showing full-length (FL, 859 bp) and exon 52-skipped (Δ52, 793 bp) transcripts. The relative abundance (%) of Δ52 amplicons are shown below each gel image. GTC: Gene Tools control PMO, UT: untreated control, -ve: RT-PCR negative control, 100 bp molecular marker used as a size reference. The gels were cropped for presentation. Full gel images are presented in Figure S1 (**b**) Representative images showing fibrillin-1 (red) and nuclei (blue) in MFS$^{\Delta 52}$ or healthy control fibroblasts treated with (**i,v**) 250 μM of PMO52, (**ii,vi**) 50 μM of PMO52, (**iii,vii**) 250 μM of GTC or (**iv,viii**) left untreated. (**xiii**) negative control with no primary antibody added. Scale bar = 20 μm. The images were cropped for presentation. Full images are presented in Figure S3.

3. Discussion

Although Marfan syndrome is well established as an inherited connective tissue disorder caused by mutations in the fibrillin-1 gene, the exact mechanism of pathogenesis has not been fully resolved. Current understanding suggests that the pathogenesis is dependent on the mutation type with an overarching basis that a lack of functional fibrillin-1 microfibrils leads to *TGF-β* dysregulation, further compounding ECM destabilisation [15,61]. Therefore, we propose that removal of a mutation-associated exon from all *FBN1* transcripts could result in the production of internally truncated fibrillin-1 proteins that retain some function and are able to form microfibrils. We addressed this hypothesis by designing antisense oligonucleotides to induce exon 52 exclusion from unaffected *FBN1* pre-mRNA. We suggest that many fibrillin-1 gene lesions will be amenable to the removal of the affected exon for two main reasons. Firstly, fibrillin-1 is highly repetitive suggesting the possibility of functional redundancy. Secondly, excluding exons 2, 3, 64, 65 and 66, the majority of fibrillin-1 exons are in-frame, and therefore can be removed without disrupting the reading frame.

Here, we describe evidence for the efficient removal of *FBN1* exon 52. Of the five 2′OMe-PS AOs tested three were found to induce exon 52 skipping. Earlier dystrophin screening studies similarly found that two out of three AOs induced some skipping, albeit at different efficiencies [59]. The different delivery methods, concentration and length of incubation that were used when assessing the 2′OMe-PS and PMO sequences, make it impossible to directly compare their efficiencies. However, our data show that the proportion of Δ52 transcripts induced is greater when using the PMO sequence, this is likely in-part because a higher PMO concentration and longer incubation period could be used without a large decrease in cell viability. A higher concentration is generally re-

quired for the PMOs as the neutral charge of the chemistry hinders cellular uptake [62,63]. Immunofluorescent staining of fibrillin-1 in treated cells supports the hypothesis that fibrillin-$1^{\Delta 52}$ proteins can interact to form multimers. We observed fibre formation, mirroring that of the untreated control cells, when more than 92% exon 52 skipping was induced in either the healthy control or $MFS^{\Delta 52}$ patient fibroblasts. We also established that inducing approximately 50% exon 52 skipping results in a complete loss of fibrillin-1 fibre staining in healthy control fibroblasts mimicking the disease-like state caused by splicing mutations. Together, these results demonstrate proof-of-concept that the internally truncated fibrillin-$1^{\Delta 52}$ proteins produced through efficient exon 52 skipping are able to form multimers.

Of particular interest, is the total loss of microfibril formation that results from the induction of a combination of wild-type and *FBN1*$^{\Delta 52}$ transcripts after sub-optimal levels of PMO-induced exon skipping. This finding demonstrates the inability of the heterogenous population of Δ52 fibrillin-1 proteins to form microfibrils, supporting the dominant-negative pathogenic mechanism [64]. We observed a similar lack of extracellular fibrillin-1 as that reported by Liu et al. [65] resulting from the c.6354C > T mutation that leads to 41% fibrillin-1 synthesis and only 5% deposition of fibrillin-1 in the extracellular matrix. However, this finding also has relevance to mapping of amenable *FBN1* exons that could be targeted in a splice intervention therapy. The elimination of microfibrils and subsequent formation with increased skipping efficiency could prove to be an invaluable tool in optimisation of fibrillin-1 AO sequences as well as identification of potential target exons for therapeutic intervention. Importantly, being able to induce a disease-like state would allow the use of healthy control cells, rather than specific patient cells, for the identification of exons that when removed do not affect the expression or function of fibrillin-1. Furthermore the occurrence and severity of dominant negative effects depend on the mutation type and location [66]. For example, duplications causing a mouse model of tight skin syndrome, result in a larger fibrillin-1 protein that has been shown to only form microfibrils in the presence of wild-type fibrillin-1 [67]. While the co-polymerisation of the two fibrillin-1 isoforms forms functionally deficient microfibrils, the outcome is a mild phenotype lacking vascular involvement [67]. Identification of such naturally occurring co-polymerisation events that lead to a mild phenotype could reveal potential therapeutic strategies to assess in the future.

We predict that the AOs reported here can manipulate *FBN1* splicing such that, at lower skipping efficiencies disease characteristics can be induced in unaffected cells and upon increased efficiency, sufficient skipping can be induced to reduce the key phenotype of MFS. This prediction is based on the dominant-negative model that suggests that in the presence of two protein isoforms, the aberrant protein disrupts the formation of microfibrils by the wild-type protein [18]. It is unknown exactly what ratio of wild-type to aberrant proteins would negate the dominant negative effects. However, the results presented here suggest that this tolerable threshold may be approximately 95%. We demonstrate that fibrillin-1 fibres can be formed when exon 52 skipping is sufficient, likely >90% skipping, such that more than 95% of total multimers that are formed would be of the fibrillin-$1^{\Delta 52}$-fibrillin-$1^{\Delta 52}$ structure. We also note, however, that *FBN1* mutations resulting in haploinsufficiency lead to disease. Therefore, we believe that the abundance of microfibrils has to be maintained, as a minimum, above that observed in haploinsufficiency patients [19,21]. It is also important to note that while this exon skipping strategy relies on excluding the target exon from both the mutation-harbouring and healthy *FBN1* transcripts, the exon skipping is at the mRNA level, and therefore not permanent as would be the case for other techniques such as gene therapy.

While we demonstrated efficient and consistent exon skipping using PMO52, the concentrations used are relatively high, when compared to similar studies targeting other genes [59,68]. One of the possible explanations for the high concentration required is the abundance of fibrillin-1 transcripts. Fibrillin-1 RNA is expressed in the vast majority of cell types and is maintained at relatively high levels throughout the body [69]. We

noted the efficient PCR amplification of *FBN1* transcripts; requiring 20 or fewer rounds of amplification coupled with the need for very low template concentrations (25 ng). While the in vitro PMO transfection concentrations used seem relatively high, we noticed no changes in morphology or health of cell cultures up to four days post-transfection with PMO52. The PMO chemistry is generally considered to be safe with no off-target effects nor toxicity [43,57,62]. Nevertheless, while the PMO chemistry may be safe and a higher concentration required due to the level of fibrillin-1 expression, there are still several ways in which the efficiency of an AO can be improved, including optimisation of AO delivery, sequence, length and chemistry. Further optimisation could allow for the use of a significantly lower dosage that in turn would not only reduce the possibility of off-target effects or toxicity but also lower the cost of treatment.

The fibrillin-1 protein produced by excising exon 52 is predicted to be internally truncated, fibrillin-$1^{\Delta 52}$, and lack the last seven amino acids of the sixth TB domain. This isoform has only been reported in the context of exon 52 mutations, where it is known to act in a dominant-negative manner against the wild-type protein and result in a severe lack of functional microfibrils [60,65]. Liu et al. [65] also reported that an exon 52 splicing mutation leads to reduced fibrillin-1 synthesis, less than 50% of that observed in healthy controls, while the mutant mRNA levels remain unchanged, suggesting that the fibrillin-$1^{\Delta 52}$ proteins are unstable. Liu et al. [65] suggests this instability may result from the partial deletion of a TB domain that leads to misfolding of the fibrillin-1 protein increasing its susceptibility to proteolysis. If this is the case then attempts to induce exon skipping of other exons encoding partial TB domains; 10, 11, 17, 18, 38, 39, 42, 43 and 51, would likely face the same issue. It is possible that removal of the two exons encoding the TB domain as a pair could solve this problem. However, our findings suggest that the fibrillin$1^{\Delta 52}$ proteins produced through exon 52 skipping are able to be synthesised, secreted from the cell and form fibre-like structures in both healthy control and MFS$^{\Delta 52}$ patient fibroblasts. Nevertheless, the synthesis, deposition and function of fibrillin-$1^{\Delta 52}$, especially in the absence of wild-type fibrillin-1, needs to be investigated further.

Here, we illustrate that when fibrillin-$1^{\Delta 52}$ is the predominant product it is able to be both synthesised and secreted from the cell, with no evidence of intracellular staining. We also demonstrate that fibrillin-$1^{\Delta 52}$ proteins can form fibres, provided that *FBN1*$^{\Delta 52}$ transcripts make up more than 90% of total *FBN1* transcripts. These results suggest that the fibrillin-$1^{\Delta 52}$ protein is at least partially functional, although further protein analysis is required to assess if the fibres formed can interact with the microfibril associated proteins with which fibrillin-1 naturally interacts. The ability of fibrillin-$1^{\Delta 52}$ proteins to sequester TGF-β also needs to be assessed. If removal of exon 52 disrupts the regulation of TGF-β, then regardless of the high skipping efficiency and fibre formation that is observed, symptoms such as aortic growth would continue to progress with no benefit from this treatment. To assess the effect of *FBN1* exon skipping and the function of the induced fibrillin-1 isoform especially the impacts on TGF-β signalling, surrogate markers such as the phosphorylation of Smad2 can be analysed [70,71]. The level of active and total TGF-β can similarly be assessed as a measure of functionality [61,71,72]. Such assays were outside the scope of the current study and will be the focus of further research.

As previously noted, our results support the hypothesis that fibrillin-$1^{\Delta 52}$ can form fibres. However, while the morphology of fibres is superficially similar to that of the untreated, healthy control, their abundance is reduced. The reduction in abundance could be the result of the experimental design and protocols. For example, nucleofection can cause cell stress potentially reducing fibrillin-1 expression, or the transfection incubation time could be insufficient to allow more efficient formation of microfibrils after treatment. However, it is likely that, as reported by Liu et al. [65], fibrillin-$1^{\Delta 52}$ synthesis is reduced in comparison to the wild-type. Western blotting analysis of intracellular and extracellular fibrillin-1 was attempted, however, due to poor signal and resolution in samples from healthy control fibroblasts we were unable to confirm any changes in fibrillin-1 abundance. Further optimisation of the Western blot protocol to produce reliable results is required

before the effect of *FBN1* exon skipping on the abundance of fibrillin-1 can be assessed. While restoring microfibril abundance and function to a 'normal' state would be ideal, this may not be possible. We believe that any increase in functional microfibrils could provide a therapeutic benefit by reducing disease progression and severity.

As discussed earlier, the current standard of care for individuals living with MFS relies heavily on invasive surgical interventions and the lifelong use of medicines such as β-adrenergic receptor blockades that slow the progression of aortic dilation [33–35]. These interventions have proven lifesaving, as well as life-extending [5,73]. However, the burden of MFS on quality of life, and the economic stress, for both patients and their families, remains substantial [74,75]. In more recent years major efforts have been made to discover and develop therapeutics for MFS [31–33,76]. Research has focused on slowing aortic growth as well as a continued improvement upon current treatment strategies for the main symptoms of MFS. With FDA approval of AO therapeutics to restore gene function in spinal muscular atrophy [45] and Duchenne muscular dystrophy [77–79], we suggest that antisense oligonucleotide-mediated splice switching as described here could be an appropriate direction for the development of therapies for Marfan syndrome.

In conclusion, this study assessed the ability of a suite of AOs to induce targeted exon 52 skipping from full-length *FBN1* mRNA transcripts expressed in healthy control fibroblasts. The most efficient sequence, and the consequences of splice modification, was further evaluated in both healthy control and MFS$^{\Delta 52}$ patient fibroblasts. We showed in vitro, that AO52.1^{n}, AO52.1^{m} and AO52.3 as well as PMO52 induced dose-dependent exon 52 skipping. Encouragingly the presence of more than 90% of one transcript type; wild-type or *FBN1*$^{\Delta 52}$, corresponded with the formation of fibrillin-1 fibres in both cell lines. In contrast, a mixed transcript pool resulted with the complete loss of fibrillin-1 fibres, mimicking the disease-like state.

While this study is a preliminary, in vitro investigation, our candidate PMO consistently induces efficient exon 52 exclusion while maintaining fibrillin-1$^{\Delta 52}$ fibre formation. With increasing numbers of AO therapeutics being approved for clinical use, our results suggest that PMO52 may be an attractive therapeutic option for the treatment of Marfan syndrome caused by mutations in fibrillin-1 exon 52. This study provides proof-of-concept and a foundation for the further development of antisense oligonucleotide therapies for Marfan syndrome.

4. Materials and Methods

4.1. Design and Synthesis of Antisense Oligonucleotides

Antisense oligonucleotides were designed to target splicing regulatory motifs at the exon-intron junctions as well as exonic splicing enhancer sequences predicted using the SpliceAid web tool [58]. AO sequences were also analysed using NCBI nucleotide BLAST (NCBI, Bethesda, MD, USA) [80] to identify any possible off-target annealing. Antisense oligonucleotides with 2′OMe-PS chemistry were purchased from TriLink biotechnologies (Maravai LifeSciences, San Diego, CA, USA), and PMOs were purchased from GeneTools LLC (Philomath, OR, USA). The nomenclature of AOs is based on that described by Mann et al. [42] and provides information on the gene, exon, annealing co-ordinates and species. A full list of AOs used in this study are provided in Table 1. The *FBN1* exon nomenclature was determined with respect to the NCBI Reference Sequence NM_000138.4, in which the translation start codon is in the second of 66 exons.

4.2. Cell Culture and Transfection

Fibroblasts were originally sourced from a dermal biopsy derived from a healthy volunteer with informed consent. The following cell line was obtained from the NIGMS Human Genetic Cell Repository at the Coriell Institute for Medical Research: GM21941 (Camden, NJ, USA). The use of human cells for this research was approved by the Murdoch University Human Ethics Committee, approval numbers 2013_156 (25 October 2013) and 2017_101 (12 May 2017) and The University of Western Australia Human Research Ethics

Committee, approval number RA/4/1/2295 (21 April 2009). Healthy control fibroblasts were maintained in Dulbecco's Modified Essential Medium (DMEM, Gibco; Thermo Fisher Scientific, Melbourne, Australia) supplemented with 10% foetal bovine serum (FBS, Scientifix, Melbourne, Australia). The $MFS^{\Delta 52}$ patient fibroblasts were maintained in DMEM supplemented with 15% FBS (Scientifix, Melbourne, Australia) and 1% glutaMax (Gibco; Thermo Fisher Scientific, Melbourne, Australia). Both cell lines were maintained at 37 °C with 5% CO_2.

Antisense oligonucleotides (2′OMe-PS chemistry) used for target site screening were transfected into healthy control fibroblasts using Lipofectamine 3000 (L3K, Life Technologies, Melbourne, Australia). Transfections were prepared by incubating the AO with 3 µL of L3K, at room temperature in 50 µL of Opti-MEM (Gibco; Thermo Fisher Scientific, Melbourne, Australia), according to manufacturer's protocol. The transfection mixture was then diluted to the desired AO concentration in a final volume of 1 mL and applied to cells. Transfected cells were incubated for 24 h before collection.

The PMO was delivered using the 4D-Nucleofector™ and P3 nucleofection kits (Lonza, Melbourne, Australia). One microliter of stock PMO (5 mM), either undiluted (250 µM) or diluted 1:4 in sterilised water (50 µM), was added into a cuvette along with 300,000 fibroblasts resuspended in 19 µL of pre-warmed transfection solution. The mixture of fibroblasts and PMO was subsequently nucleofected using the pulse code, CA 137, previously optimised in our laboratory for dermal fibroblasts. Nucleofected fibroblasts were maintained in DMEM supplemented with 5% FBS before collection after 3 or 4 days.

4.3. RNA Extraction and RT-PCR Analysis

Total RNA was extracted using MagMax™ nucleic acid isolation kits (Thermo Fisher Scientific, Melbourne, Australia) as per the manufacturer's protocol. Total RNA concentration and purity were determined using a Nanodrop 1000 spectrophotometer (Thermo Fisher Scientific, Melbourne, Australia). Transcripts were amplified using one-step SuperScript® III reverse transcriptase (Thermo Fisher Scientific, Melbourne, Australia) with 25 ng of total RNA as a template. To assess exon 52 skipping, *FBN1* transcripts were amplified using exon 47 Forward (5′-GGTTTCATCCT-TTCTCACAAC-3′) and exon 54 Reverse (5′-TCACATGTCATCATTGGACC-3′) primers (Integrated DNA Technologies, Sydney, Australia). The cycling conditions were as follows; 55 °C for 30 min, 94 °C for 2 min followed by 20 cycles of 94 °C for 30 s, 55 °C for 30 s and 68 °C for 1 min. The PCR amplicons were fractionated on 2% agarose gels in Tris-Acetate-EDTA buffer. Relative exon skipping efficiency was estimated through densitometric analysis of images using ImageJ (version 1.8.0_112) imaging software (NIH, Bethesda, MD, USA) [81] and reported as the proportion of FL or Δ52 transcript products relative to the sum of products.

4.4. Immunofluorescence

Immediately after nucleofection, 100,000 fibroblasts were seeded into each well of a 24-well plate lined with a 13 mm #0 round uncoated glass coverslip. Cells were incubated for 72 h before being fixed in ice-cold acetone: methanol (1:1, *v*:*v*) and allowed to air dry. Fixed cells were washed once with PBS to rehydrate before blocking with 10% goat serum in PBS for 1 h at room temperature. The primary antibody, Anti-fibrillin-1 antibody clone 26 (Merck Millipore, Sydney, Australia), was applied at a dilution of 1:100 in 1% goat serum-PBS and incubated overnight at 4 °C. Secondary antibody; AlexaFluor568 anti-mouse IgG (Thermo Fisher Scientific, VIC, Australia) was applied, 1:400, for 1 h at room temperature, and co-stained with Hoechst 33,342 (Sigma-Aldrich, Sydney, Australia) for nuclei detection (1 mg/mL diluted, 1:125). Coverslips were mounted using ProLong™ Gold antifade mountant (Thermo Fisher Scientific, Melbourne, Australia). Fibrillin-1 was detected using a Nikon 80i microscope with NIS-Elements software (Nikon, Adelaide, Australia). The brightness and contrast of individual channel images were altered equally for each image, then merged. The merged image was cropped from the original

1280 × 1024 pixel image using Adobe Photoshop CC. A 20 μm scale bar was added using ImageJ software (NIH, Bethesda, MD, USA) [81].

Supplementary Materials: The following are available online at https://www.mdpi.com/article/10.3390/ijms22073479/s1, Figure S1: Full gel images for figures listed, Figure S2: Evaluation of AO cocktails designed to induce *FBN1* exon 52 skipping, Figure S3: Full immunofluorescence staining images for figures listed, Figure S4: Additional evaluation of PMO52.

Author Contributions: Conceptualization, J.M.C. and S.D.W.; methodology, J.M.C. and K.G.; formal analysis, J.M.C.; investigation, J.M.C. and K.G.; writing—original draft preparation, J.M.C.; writing—review and editing, J.M.C., K.G., S.F. and S.D.W.; visualization, J.M.C.; supervision, S.F., S.D.W.; funding acquisition, S.D.W. All authors have read and agreed to the published version of the manuscript.

Funding: This research was funded by NHMRC, grant number APP 1144791. J.C. received a Research Training Program scholarship from Murdoch University. This work was conducted in Perth, Australia.

Institutional Review Board Statement: Primary dermal fibroblasts derived from a healthy volunteer after informed consent. The MFS$^{\Delta 52}$ patient fibroblasts were obtained from the NIGMS Human Genetic Cell Repository at the Coriell Institute for Medical Research (Cat#: GM21941). The use of human cells for this research was approved by the Murdoch University Human Ethics Committee, approval numbers 2013_156 (25 October 2013) and 2017_101 (12 May 2017) and The University of Western Australia Human Research Ethics Committee, approval number RA/4/1/2295 (21 April 2009).

Informed Consent Statement: Informed consent was obtained from all subjects involved in the study.

Data Availability Statement: Not applicable.

Conflicts of Interest: The authors declare no conflict of interest.

References

1. Ammash, N.M.; Sundt, T.M.; Connolly, H.M. Marfan Syndrome-Diagnosis and Management. *Curr. Probl. Cardiol.* **2008**, *33*, 7–39. [CrossRef] [PubMed]
2. Pyeritz, R.E. Recent Progress in Understanding the Natural and Clinical Histories of the Marfan Syndrome. *Trends Cardiovasc. Med.* **2016**, *26*, 423–428. [CrossRef]
3. Collod-Béroud, G.; Boileau, C. Marfan Syndrome in the Third Millennium. *Eur. J. Hum. Genet.* **2002**, *10*, 673–681. [CrossRef]
4. Loeys, B.L.; Gerber, E.E.; Riegert-Johnson, D.; Iqbal, S.; Whiteman, P.; McConnell, V.; Chillakuri, C.R.; Macaya, D.; Coucke, P.J.; De Paepe, A.; et al. Mutations in Fibrillin-1 Cause Congenital Scleroderma: Stiff Skin Syndrome. *Sci. Transl. Med.* **2010**, *2*, 23ra20. [CrossRef]
5. Murdoch, J.L.; Walker, B.A.; Halpern, B.L.; Kuzma, J.W.; McKusick, V.A. Life Expectancy and Causes of Death in the Marfan Syndrome. *N. Engl. J. Med.* **1972**, *286*, 804–808. [CrossRef]
6. Sakai, L.Y.; Keene, D.R.; Engvall, E. Fibrillin, a New 350-KD Glycoprotein, Is a Component of Extracellular Microfibrils. *J. Cell Biol.* **1986**, *103*, 2499–2509. [CrossRef]
7. Dietz, H.C.; Cutting, G.R.; Pyeritz, R.E.; Maslen, C.L.; Sakai, L.Y.; Corson, G.M.; Puffenberger, E.G.; Hamosh, A.; Nanthakumar, E.J.; Curristin, S.M. Marfan Syndrome Caused by a Recurrent de Novo Missense Mutation in the Fibrillin Gene. *Nature* **1991**, *352*, 337–339. [CrossRef]
8. Hollister, D.W.; Godfrey, M.; Sakai, L.Y.; Pyeritz, R.E. Immunohistologic Abnormalities of the Microfibrillar-Fiber System in the Marfan Syndrome. *N. Engl. J. Med.* **1990**, *323*, 152–159. [CrossRef]
9. Stenson, P.D.; Mort, M.; Ball, E.V.; Chapman, M.; Evans, K.; Azevedo, L.; Hayden, M.; Heywood, S.; Millar, D.S.; Phillips, A.D.; et al. The Human Gene Mutation Database (HGMD®): Optimizing Its Use in a Clinical Diagnostic or Research Setting. *Hum. Genet.* **2020**. [CrossRef] [PubMed]
10. Reinhardt, D.P.; Gambee, J.E.; Ono, R.N.; Bächinger, H.P.; Sakai, L.Y. Initial Steps in Assembly of Microfibrils. Formation of Disulfide-Cross-Linked Multimers Containing Fibrillin-1. *J. Biol. Chem.* **2000**, *275*, 2205–2210. [CrossRef] [PubMed]
11. Gibson, M.A. *Microfibril-Associated Glycoprotein-1 (MAGP-1) and Other Non-Fibrillin Macromolecules Which May Possess a Functional Association with the 10 Nm Microfibrils*; Landes Bioscience: Austin, TX, USA, 2013.
12. Sengle, G.; Sakai, L.Y. The Fibrillin Microfibril Scaffold: A Niche for Growth Factors and Mechanosensation? *Matrix Biol.* **2015**, *47*, 3–12. [CrossRef]
13. Kielty, C.M.; Shuttleworth, C.A. Fibrillin-Containing Microfibrils: Structure and Function in Health and Disease. *Int. J. Biochem. Cell Biol.* **1995**, *27*, 747–760. [CrossRef]

14. Isogai, Z.; Ono, R.N.; Ushiro, S.; Keene, D.R.; Chen, Y.; Mazzieri, R.; Charbonneau, N.L.; Reinhardt, D.P.; Rifkin, D.B.; Sakai, L.Y. Latent Transforming Growth Factor β-Binding Protein 1 Interacts with Fibrillin and Is a Microfibril-Associated Protein. *J. Biol. Chem.* **2003**, *278*, 2750–2757. [CrossRef] [PubMed]
15. Ramachandra, C.J.A.; Mehta, A.; Guo, K.W.Q.; Wong, P.; Tan, J.L.; Shim, W. Molecular Pathogenesis of Marfan Syndrome. *Int. J. Cardiol.* **2015**, *187*, 585–591. [CrossRef] [PubMed]
16. Doyle, J.J.; Gerber, E.E.; Dietz, H.C. Matrix-Dependent Perturbation of TGFβ Signaling and Disease. *FEBS Lett.* **2012**, *586*, 2003–2015. [CrossRef] [PubMed]
17. Ikonomidis, J.S.; Jones, J.A.; Barbour, J.R.; Stroud, R.E.; Clark, L.L.; Kaplan, B.S.; Zeeshan, A.; Bavaria, J.E.; Gorman, J.H.; Spinale, F.G.; et al. Expression of Matrix Metalloproteinases and Endogenous Inhibitors Within Ascending Aortic Aneurysms of Patients With Marfan Syndrome. *Circulation* **2006**, *114*, I-365. [CrossRef]
18. Dietz, H.C.; McIntosh, I.; Sakai, L.Y.; Corson, G.M.; Chalberg, S.C.; Pyeritz, R.E.; Francomano, C.A. Four Novel FBN1 Mutations: Significance for Mutant Transcript Level and EGF-like Domain Calcium Binding in the Pathogenesis of Marfan Syndrome. *Genomics* **1993**, *17*, 468–475. [CrossRef]
19. de Vries, B.B.A.; Pals, G.; Odink, R.; Hamel, B.C.J. Homozygosity for a FBN1 Missense Mutation: Clinical and Molecular Evidence for Recessive Marfan Syndrome. *Eur. J. Hum. Genet.* **2007**, *15*, 930–935. [CrossRef]
20. Aoyama, T.; Francke, U.; Dietz, H.C.; Furthmayr, H. Quantitative Differences in Biosynthesis and Extracellular Deposition of Fibrillin in Cultured Fibroblasts Distinguish Five Groups of Marfan Syndrome Patients and Suggest Distinct Pathogenetic Mechanisms. *J. Clin. Invest.* **1994**, *94*, 130–137. [CrossRef]
21. Aubart, M.; Gross, M.-S.; Hanna, N.; Zabot, M.-T.; Sznajder, M.; Detaint, D.; Gouya, L.; Jondeau, G.; Boileau, C.; Stheneur, C. The Clinical Presentation of Marfan Syndrome Is Modulated by Expression of Wild-Type FBN1 Allele. *Hum. Mol. Genet.* **2015**, *24*, 2764–2770. [CrossRef] [PubMed]
22. Jensen, S.A.; Aspinall, G.; Handford, P.A. C-Terminal Propeptide Is Required for Fibrillin-1 Secretion and Blocks Premature Assembly through Linkage to Domains CbEGF41-43. *Proc. Natl. Acad. Sci. USA* **2014**, *111*, 10155–10160. [CrossRef]
23. Graul-Neumann, L.M.; Kienitz, T.; Robinson, P.N.; Baasanjav, S.; Karow, B.; Gillessen-Kaesbach, G.; Fahsold, R.; Schmidt, H.; Hoffmann, K.; Passarge, E. Marfan Syndrome with Neonatal Progeroid Syndrome-like Lipodystrophy Associated with a Novel Frameshift Mutation at the 3′ Terminus of the FBN1-Gene. *Am. J. Med. Genet. A* **2010**, *152A*, 2749–2755. [CrossRef]
24. Collod-Béroud, G.; Le Bourdelles, S.; Ades, L.; Ala-Kokko, L.; Booms, P.; Boxer, M.; Child, A.; Comeglio, P.; De Paepe, A.; Hyland, J.C.; et al. Update of the UMD-FBN1 Mutation Database and Creation of an FBN1 Polymorphism Database. *Hum. Mutat.* **2003**, *22*, 199–208. [CrossRef] [PubMed]
25. Jensen, S.A.; Iqbal, S.; Lowe, E.D.; Redfield, C.; Handford, P.A. Structure and Interdomain Interactions of a Hybrid Domain: A Disulphide-Rich Module of the Fibrillin/LTBP Superfamily of Matrix Proteins. *Structure* **2009**, *17*, 759–768. [CrossRef] [PubMed]
26. Pereira, L.; D'Alessio, M.; Ramirez, F.; Lynch, J.R.; Sykes, B.; Pangilinan, T.; Bonadio, J. Genomic Organization of the Sequence Coding for Fibrillin, the Defective Gene Product in Marfan Syndrome. *Hum. Mol. Genet.* **1993**, *2*, 961–968. [CrossRef] [PubMed]
27. Jensen, S.A.; Robertson, I.B.; Handford, P.A. Dissecting the Fibrillin Microfibril: Structural Insights into Organization and Function. *Structure* **2012**, *20*, 215–225. [CrossRef]
28. Reinhardt, D.P.; Ono, R.N.; Sakai, L.Y. Calcium Stabilizes Fibrillin-1 against Proteolytic Degradation. *J. Biol. Chem.* **1997**, *272*, 1231–1236. [CrossRef] [PubMed]
29. Ramirez, F.; Gayraud, B.; Pereira, L. Marfan Syndrome: New Clues to Genotype-Phenotype Correlations. *Ann. Med.* **1999**, *31*, 202–207. [CrossRef]
30. Schrijver, I.; Liu, W.; Brenn, T.; Furthmayr, H.; Francke, U. Cysteine Substitutions in Epidermal Growth Factor-like Domains of Fibrillin-1: Distinct Effects on Biochemical and Clinical Phenotypes. *Am. J. Hum. Genet.* **1999**, *65*, 1007–1020. [CrossRef] [PubMed]
31. Habashi, J.P.; Judge, D.P.; Holm, T.M.; Cohn, R.D.; Loeys, B.L.; Cooper, T.K.; Myers, L.; Klein, E.C.; Liu, G.; Calvi, C.; et al. Losartan, an AT1 Antagonist, Prevents Aortic Aneurysm in a Mouse Model of Marfan Syndrome. *Science* **2006**, *312*, 117–121. [CrossRef]
32. Gao, L.; Chen, L.; Fan, L.; Gao, D.; Liang, Z.; Wang, R.; Lu, W. The Effect of Losartan on Progressive Aortic Dilatation in Patients with Marfan's Syndrome: A Meta-Analysis of Prospective Randomized Clinical Trials. *Int. J. Cardiol.* **2016**, *217*, 190–194. [CrossRef] [PubMed]
33. Rossi-Foulkes, R.; Roman, M.J.; Rosen, S.E.; Kramer-Fox, R.; Ehlers, K.H.; O'Loughlin, J.E.; Davis, J.G.; Devereux, R.B. Phenotypic Features and Impact of Beta Blocker or Calcium Antagonist Therapy on Aortic Lumen Size in the Marfan Syndrome. *Am. J. Cardiol.* **1999**, *83*, 1364–1368. [CrossRef]
34. Shores, J.; Berger, K.R.; Murphy, E.A.; Pyeritz, R.E. Progression of Aortic Dilatation and the Benefit of Long-Term Beta-Adrenergic Blockade in Marfan's Syndrome. *N. Engl. J. Med.* **1994**, *330*, 1335–1341. [CrossRef]
35. Judge, D.P.; Dietz, H.C. Marfan's Syndrome. *Lancet* **2005**, *366*, 1965–1976. [CrossRef]
36. Franken, R.; den Hartog, A.W.; Radonic, T.; Micha, D.; Maugeri, A.; van Dijk, F.S.; Meijers-Heijboer, H.E.; Timmermans, J.; Scholte, A.J.; van den Berg, M.P.; et al. Beneficial Outcome of Losartan Therapy Depends on Type of FBN1 Mutation in Marfan Syndrome. *Circ. Cardiovasc. Genet.* **2015**, *8*, 383–388. [CrossRef] [PubMed]
37. Shuttleworth, J.; Colman, A. Antisense Oligonucleotide-Directed Cleavage of MRNA in Xenopus Oocytes and Eggs. *EMBO J.* **1988**, *7*, 427–434. [CrossRef] [PubMed]

38. Dash, P.; Lotan, I.; Knapp, M.; Kandel, E.R.; Goelet, P. Selective Elimination of MRNAs in Vivo: Complementary Oligodeoxynucleotides Promote RNA Degradation by an RNase H-like Activity. *Proc. Natl. Acad. Sci. USA* **1987**, *84*, 7896–7900. [CrossRef]
39. Bielinska, A.; Shivdasani, R.A.; Zhang, L.Q.; Nabel, G.J. Regulation of Gene Expression with Double-Stranded Phosphorothioate Oligonucleotides. *Science* **1990**, *250*, 997–1000. [CrossRef]
40. Boiziau, C.; Kurfurst, R.; Cazenave, C.; Roig, V.; Thuong, N.T.; Toulmé, J.J. Inhibition of Translation Initiation by Antisense Oligonucleotides via an RNase-H Independent Mechanism. *Nucleic Acids Res.* **1991**, *19*, 1113–1119. [CrossRef]
41. Dominski, Z.; Kole, R. Restoration of Correct Splicing in Thalassemic Pre-MRNA by Antisense Oligonucleotides. *Proc. Natl. Acad. Sci. USA* **1993**, *90*, 8673–8677. [CrossRef]
42. Mann, C.J.; Honeyman, K.; Cheng, A.J.; Ly, T.; Lloyd, F.; Fletcher, S.; Morgan, J.E.; Partridge, T.A.; Wilton, S.D. Antisense-Induced Exon Skipping and Synthesis of Dystrophin in the Mdx Mouse. *Proc. Natl. Acad. Sci. USA* **2001**, *98*, 42–47. [CrossRef]
43. Mendell, J.R.; Rodino-Klapac, L.R.; Sahenk, Z.; Roush, K.; Bird, L.; Lowes, L.P.; Alfano, L.; Gomez, A.M.; Lewis, S.; Kota, J.; et al. Eteplirsen for the Treatment of Duchenne Muscular Dystrophy. *Ann. Neurol.* **2013**, *74*, 637–647. [CrossRef]
44. FDA Grants Accelerated Approval to First Drug for Duchenne Muscular Dystrophy. Available online: https://www.fda.gov/news-events/press-announcements/fda-grants-accelerated-approval-first-drug-duchenne-muscular-dystrophy (accessed on 29 October 2020).
45. Rigo, F.; Chun, S.J.; Norris, D.A.; Hung, G.; Lee, S.; Matson, J.; Fey, R.A.; Gaus, H.; Hua, Y.; Grundy, J.S.; et al. Pharmacology of a Central Nervous System Delivered 2′-O-Methoxyethyl–Modified Survival of Motor Neuron Splicing Oligonucleotide in Mice and Nonhuman Primates. *J. Pharmacol. Exp. Ther.* **2014**, *350*, 46–55. [CrossRef]
46. FDA Approves First Drug for Spinal Muscular Atrophy. Available online: https://www.fda.gov/news-events/press-announcements/fda-approves-first-drug-spinal-muscular-atrophy (accessed on 11 February 2021).
47. FDA Grants Accelerated Approval to First Targeted Treatment for Rare Duchenne Muscular Dystrophy Mutation. Available online: https://www.fda.gov/news-events/press-announcements/fda-grants-accelerated-approval-first-targeted-treatment-rare-duchenne-muscular-dystrophy-mutation (accessed on 29 October 2020).
48. FDA Approves Targeted Treatment for Rare Duchenne Muscular Dystrophy Mutation. Available online: https://www.fda.gov/news-events/press-announcements/fda-approves-targeted-treatment-rare-duchenne-muscular-dystrophy-mutation (accessed on 27 January 2021).
49. FDA Approves Targeted Treatment for Rare Duchenne Muscular Dystrophy Mutation. Available online: https://www.fda.gov/news-events/press-announcements/fda-approves-targeted-treatment-rare-duchenne-muscular-dystrophy-mutation-0 (accessed on 4 March 2021).
50. Pan, Q.; Shai, O.; Lee, L.J.; Frey, B.J.; Blencowe, B.J. Deep Surveying of Alternative Splicing Complexity in the Human Transcriptome by High-Throughput Sequencing. *Nat. Genet.* **2008**, *40*, 1413–1415. [CrossRef]
51. Cartegni, L.; Chew, S.L.; Krainer, A.R. Listening to Silence and Understanding Nonsense: Exonic Mutations That Affect Splicing. *Nat. Rev. Genet.* **2002**, *3*, 285–298. [CrossRef] [PubMed]
52. Ward, A.J.; Cooper, T.A. The Pathobiology of Splicing. *J. Pathol.* **2010**, *220*, 152–163. [CrossRef]
53. Singh, N.K.; Singh, N.N.; Androphy, E.J.; Singh, R.N. Splicing of a Critical Exon of Human Survival Motor Neuron Is Regulated by a Unique Silencer Element Located in the Last Intron. *Mol. Cell Biol.* **2006**, *26*, 1333–1346. [CrossRef]
54. Summerton, J.E.; Weller, D.D. Uncharged Morpolino-Based Polymers Having Phosphorous Containing Chiral Intersubunit Linkages. U.S. Patent No 5,185,444A, 9 February 1993.
55. Summerton, J.E. Morpholino, SiRNA, and S-DNA Compared: Impact of Structure and Mechanism of Action on off-Target Effects and Sequence Specificity. *Curr. Top. Med. Chem.* **2007**, *7*, 651–660. [CrossRef]
56. Moulton, J.D.; Jiang, S. Gene Knockdowns in Adult Animals: PPMOs and Vivo-Morpholinos. *Molecules* **2009**, *14*, 1304–1323. [CrossRef] [PubMed]
57. Iversen, P.L.; Arora, V.; Acker, A.J.; Mason, D.H.; Devi, G.R. Efficacy of Antisense Morpholino Oligomer Targeted to C-Myc in Prostate Cancer Xenograft Murine Model and a Phase I Safety Study in Humans. *Clin. Cancer Res.* **2003**, *9*, 2510–2519. [PubMed]
58. Piva, F.; Giulietti, M.; Nocchi, L.; Principato, G. SpliceAid: A Database of Experimental RNA Target Motifs Bound by Splicing Proteins in Humans. *Bioinformatics* **2009**, *25*, 1211–1213. [CrossRef] [PubMed]
59. Adams, A.M.; Harding, P.L.; Iversen, P.L.; Coleman, C.; Fletcher, S.; Wilton, S.D. Antisense Oligonucleotide Induced Exon Skipping and the Dystrophin Gene Transcript: Cocktails and Chemistries. *BMC Mol. Biol.* **2007**, *8*, 57. [CrossRef]
60. Liu, W.; Qian, C.; Francke, U. Silent Mutation Induces Exon Skipping of Fibrillin-1 Gene in Marfan Syndrome. *Nat. Genet.* **1997**, *16*, 328–329. [CrossRef]
61. Neptune, E.R.; Frischmeyer, P.A.; Arking, D.E.; Myers, L.; Bunton, T.E.; Gayraud, B.; Ramirez, F.; Sakai, L.Y.; Dietz, H.C. Dysregulation of TGF-Beta Activation Contributes to Pathogenesis in Marfan Syndrome. *Nat. Genet.* **2003**, *33*, 407–411. [CrossRef] [PubMed]
62. Amantana, A.; Iversen, P.L. Pharmacokinetics and Biodistribution of Phosphorodiamidate Morpholino Antisense Oligomers. *Curr. Opin. Pharmacol.* **2005**, *5*, 550–555. [CrossRef] [PubMed]
63. Iversen, P.L.; Aird, K.M.; Wu, R.; Morse, M.M.; Devi, G.R. Cellular Uptake of Neutral Phosphorodiamidate Morpholino Oligomers. *Curr. Pharm. Biotechnol.* **2009**, *10*, 579–588. [CrossRef] [PubMed]
64. Dietz, H. Marfan Syndrome. In *GeneReviews®*; Adam, M.P., Ardinger, H.H., Pagon, R.A., Wallace, S.E., Bean, L.J., Stephens, K., Amemiya, A., Eds.; University of Washington, Seattle: Seattle, WA, USA, 1993.

65. Liu, W.; Schrijver, I.; Brenn, T.; Furthmayr, H.; Francke, U. Multi-Exon Deletions of the FBN1 Gene in Marfan Syndrome. *BMC Med. Genet.* **2001**, *2*, 11. [CrossRef]
66. Faivre, L.; Collod-Beroud, G.; Loeys, B.L.; Child, A.; Binquet, C.; Gautier, E.; Callewaert, B.; Arbustini, E.; Mayer, K.; Arslan-Kirchner, M.; et al. Effect of Mutation Type and Location on Clinical Outcome in 1,013 Probands with Marfan Syndrome or Related Phenotypes and FBN1 Mutations: An International Study. *Am. J. Hum. Genet.* **2007**, *81*, 454–466. [CrossRef] [PubMed]
67. Gayraud, B.; Keene, D.R.; Sakai, L.Y.; Ramirez, F. New Insights into the Assembly of Extracellular Microfibrils from the Analysis of the Fibrillin 1 Mutation in the Tight Skin Mouse. *J. Cell Biol.* **2000**, *150*, 667–680. [CrossRef] [PubMed]
68. McIntosh, C.S.; Aung-Htut, M.T.; Fletcher, S.; Wilton, S.D. Removal of the Polyglutamine Repeat of Ataxin-3 by Redirecting Pre-MRNA Processing. *Int. J. Mol. Sci.* **2019**, *20*, 5434. [CrossRef]
69. Uhlén, M.; Fagerberg, L.; Hallström, B.M.; Lindskog, C.; Oksvold, P.; Mardinoglu, A.; Sivertsson, Å.; Kampf, C.; Sjöstedt, E.; Asplund, A.; et al. Proteomics. Tissue-Based Map of the Human Proteome. *Science* **2015**, *347*, 1260419. [CrossRef]
70. Lin, M.; Zhao, S.; Liu, G.; Huang, Y.; Yu, C.; Zhao, Y.; Wang, L.; Zhang, Y.; Yan, Z.; Wang, S.; et al. Identification of Novel FBN1 Variations Implicated in Congenital Scoliosis. *J. Hum. Genet.* **2020**, *65*, 221–230. [CrossRef] [PubMed]
71. Le Goff, C.; Mahaut, C.; Wang, L.W.; Allali, S.; Abhyankar, A.; Jensen, S.; Zylberberg, L.; Collod-Beroud, G.; Bonnet, D.; Alanay, Y.; et al. Mutations in the TGFβ Binding-Protein-like Domain 5 of FBN1 Are Responsible for Acromicric and Geleophysic Dysplasias. *Am. J. Hum. Genet.* **2011**, *89*, 7–14. [CrossRef] [PubMed]
72. Chaudhry, S.S.; Cain, S.A.; Morgan, A.; Dallas, S.L.; Shuttleworth, C.A.; Kielty, C.M. Fibrillin-1 Regulates the Bioavailability of TGFβ1. *J. Cell Biol.* **2007**, *176*, 355–367. [CrossRef] [PubMed]
73. Silverman, D.I.; Burton, K.J.; Gray, J.; Bosner, M.S.; Kouchoukos, N.T.; Roman, M.J.; Boxer, M.; Devereux, R.B.; Tsipouras, P. Life Expectancy in the Marfan Syndrome. *Am. J. Cardiol.* **1995**, *75*, 157–160. [CrossRef]
74. Achelrod, D.; Blankart, C.R.; Linder, R.; von Kodolitsch, Y.; Stargardt, T. The Economic Impact of Marfan Syndrome: A Non-Experimental, Retrospective, Population-Based Matched Cohort Study. *Orphanet J. Rare Dis.* **2014**, *9*, 90. [CrossRef]
75. Blankart, C.R.; Milstein, R.; Rybczynski, M.; Schüler, H.; von Kodolitsch, Y. Economic and Care Considerations of Marfan Syndrome. *Expert Rev. Pharmacoecon. Outcomes Res.* **2016**, *16*, 591–598. [CrossRef]
76. Mullen, M.; Jin, X.Y.; Child, A.; Stuart, A.G.; Dodd, M.; Aragon-Martin, J.A.; Gaze, D.; Kiotsekoglou, A.; Yuan, L.; Hu, J.; et al. Irbesartan in Marfan Syndrome (AIMS): A Double-Blind, Placebo-Controlled Randomised Trial. *Lancet* **2019**, *394*, 2263–2270. [CrossRef]
77. Lim, K.R.Q.; Maruyama, R.; Yokota, T. Eteplirsen in the Treatment of Duchenne Muscular Dystrophy. *Drug Des. Dev. Ther.* **2017**, *11*, 533–545. [CrossRef]
78. Anwar, S.; Yokota, T. Golodirsen for Duchenne Muscular Dystrophy. *Drugs Today* **2020**, *56*, 491–504. [CrossRef]
79. Roshmi, R.R.; Yokota, T. Viltolarsen for the Treatment of Duchenne Muscular Dystrophy. *Drugs Today* **2019**, *55*, 627–639. [CrossRef] [PubMed]
80. Altschul, S.F.; Gish, W.; Miller, W.; Myers, E.W.; Lipman, D.J. Basic Local Alignment Search Tool. *J. Mol. Biol.* **1990**, *215*, 403–410. [CrossRef]
81. Schneider, C.A.; Rasband, W.S.; Eliceiri, K.W. NIH Image to ImageJ: 25 Years of Image Analysis. *Nat. Methods* **2012**, *9*, 671–675. [CrossRef] [PubMed]

International Journal of
Molecular Sciences

MDPI

Article

Covalent Bi-Modular Parallel and Antiparallel G-Quadruplex DNA Nanocostructs Reduce Viability of Patient Glioma Primary Cell Cultures

Valeria Legatova [1], Nadezhda Samoylenkova [2], Alexander Arutyunyan [3], Vadim Tashlitsky [3], Elena Zavyalova [1], Dmitry Usachev [2], Galina Pavlova [2,4,5,*] and Alexey Kopylov [1,*]

1 Chemistry Department, Lomonosov Moscow State University, 119991 Moscow, Russia; legatovav.chem.msu@gmail.com (V.L.); zlenka2006@gmail.com (E.Z.)
2 Burdenko Neurosurgical Institute, 125047 Moscow, Russia; samoylenkova.n@gmail.com (N.S.); dousachev@nsi.ru (D.U.)
3 Belozersky Research Institute of Physical Chemical Biology, Lomonosov Moscow State University, 119991 Moscow, Russia; ararut@belozersky.msu.ru (A.A.); tashlitsky@belozersky.msu.ru (V.T.)
4 Institute of Higher Nervous Activity and Neurophysiology, Russian Academy of Sciences, 117485 Moscow, Russia
5 Department of Medical Genetics, Sechenov First Moscow State Medical University, 119991 Moscow, Russia
* Correspondence: author: lkorochkin@mail.ru (G.P.); kopylov@rnp-group.genebee.msu (A.K.); Tel.: +7-495-939-31-49 (G.P. & A.K.); Fax: +7-495-939-31-81 (G.P. & A.K.)

Abstract: G-quadruplex oligonucleotides (GQs) exhibit specific anti-proliferative activity in human cancer cell lines, and they can selectively inhibit the viability/proliferation of cancer cell lines vs. non-cancer ones. This ability could be translated into a cancer treatment, in particular for glioblastoma multiform (GBM), which currently has a poor prognosis and low-efficiency therapeutic treatments. A novel bi-modular GQ, bi-(AID-1-T), a twin of the previously described three-quartet AID-1-T, was designed and studied in terms of both its structure and function. A covalent conjugation of two AID-1-Ts via three thymidine link, TTT, did not interfere with its initial GQ structure. A comparison of bi-(AID-1-T) with its mono-modular AID-1-T, mono-modular two-quartet HD1, and bi-modular bi-HD1, as well as conventional two-quartet AS1411, was made. Among the five GQs studied, bi-(AID-1-T) had the highest anti-proliferative activity for the neural cancer cell line U87, while not affecting the control cell line, human embryonic fibroblasts. GQs, for the first time, were tested on several primary glioma cultures from patient surgical samples. It turned out that the sensitivity of the patient primary glioma cultures toward GQs varied, with an apparent IC_{50} of less than 1 μM for bi-(AID-1-T) toward the most sensitive G11 cell culture (glioma, Grade III).

Keywords: G-quadruplexes; covalent dimer construct; anti-proliferative activity; primary cell culture of human glioma

Citation: Legatova, V.; Samoylenkova, N.; Arutyunyan, A.; Tashlitsky, V.; Zavyalova, E.; Usachev, D.; Pavlova, G.; Kopylov, A. Covalent Bi-Modular Parallel and Antiparallel G-Quadruplex DNA Nanocostructs Reduce Viability of Patient Glioma Primary Cell Cultures. *Int. J. Mol. Sci.* **2021**, *22*, 3372. https://doi.org/10.3390/ijms22073372

Academic Editors: Salvador F. Aliño and Luis Sendra

Received: 27 February 2021
Accepted: 22 March 2021
Published: 25 March 2021

1. Introduction

G-quadruplex DNAs (GQs) have been well-known anti-proliferative agents since the beginning of the millennium [1]. A straightforward hypothesis, which could explain this effect, assumes that some regulatory regions of genomic DNA have GQ structures that are involved in the regulation of cell proliferation [2]. Therefore, after cellular uptake, GQ could bind with regulatory proteins (GQ-binding proteins), competing with regulatory GQ DNA regions, and therefore providing pleiotropic effects; anti-proliferation included. Knowing a target DNA regulatory region, a rational approach for a functional GQ design has been developed: GQ DNA decoys. For example, oligonucleotides mimicking a particular GQ motif in the KRAS promoter were found to compete with DNA–protein complexes between non-homologous end joining (NHE) and a nuclear extract from pancreatic cancer cells [3].

Moreover, a current approach is the screening of random GQs [1], no matter which way the GQ was originated. Both GQ DNA structures and the type of sensitive cells vary, therefore requiring the application of empirical approaches for screening the activity of different GQs toward different types of cells to establish an effective "corresponding pair" to study further in more detail. Additional studies will be required to answer the question of whether and how the GQ structures of oligonucleotides contribute to their cellular uptake and anti-proliferative activity [4]. Here are three the most successful examples:

The first example of anti-proliferative GQ is AS1411, developed by Bates et al. since 2009 [5] as the first-in-class anti-cancer GQ. A tumor-targeting aptamer AS1411 is a 26-mer DNA oligonucleotide that has a polymorphic GQ structure, and binds to nucleolin, which is preferentially expressed on the surface of cancer cells [6]. AS1411 provides cancer cell cytotoxicity [7] by causing methuosis, a novel type of non-apoptotic cell death, via nucleolin stimulated Rac1 activation, and massive vacuolization in the cytoplasm [8]. Therefore, AS1411 potentially serves as an anti-cancer therapeutic agent. AS1411 has been evaluated in phase II clinical trials for acute myeloid leukemia and renal cell carcinoma [9]. It exhibited a good safety profile, but the trial was terminated because of poor pharmacokinetics, requiring the enhancement of stability in circulation for a further translation [6]. In addition, it could serve as a tumor-targeting agent. For example, recently a novel targeted drug delivery system (TDDS) with practical application potential for colon cancer treatment has been developed. The TDDS was built by loading docetaxel in albumin nanoparticles that were functionalized with AS1411 [10].

Conformational polymorphism could be a negative factor for successful translation [11]. To reduce polymorphism, a new AS1411 derivative, AT11, has been synthesized with a unique GQ conformation. It turned out that it has two covalently conjugated propeller-type parallel-stranded two-tetrad modules [4] (Figure 1). AT11 has an anti-proliferative activity, like AS1411, for human lung cancer cell line, and does not affect the normal cell lines.

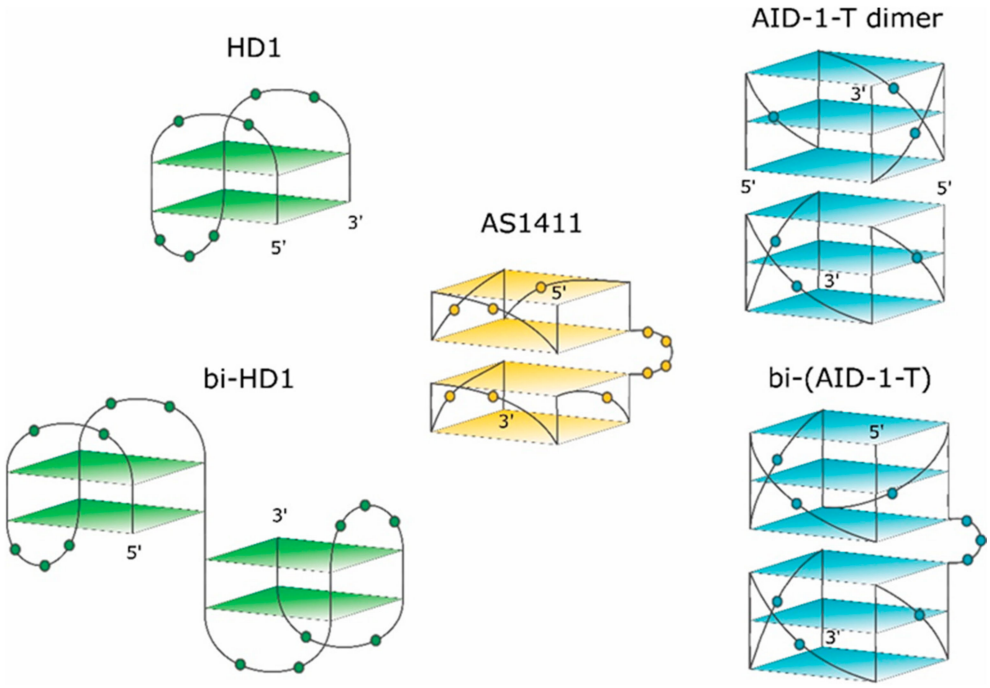

Figure 1. Schematic pictures of putative structures of the GQs under study. The 3-D structure of HD1 is known. 5′- and 3′-ends are indicated. Nucleotides are shown in the loops only.

Recently, some more derivatives of AS1411 with anti-proliferative activity toward MCF-7 cells have been developed [12]. GQs with three-tetrad structures were 10 times more active than the initial AS1411 with two-tetrad GQ.

The second example of an anti-proliferative GQ is HD1, which came from a different area. Originally, 15-mer DNA GQ HD1 (Figure 1) was discovered in 1991 as a thrombin binding aptamer via selection by conventional SELEX [13]. As HD1 has a typical GQ structure, it exhibits anti-proliferative activity like some other GQs [1,14,15].

The third example of an anti-proliferative GQ is a T-series GQ DNA, which has simple repeating sequences like $(G3T)_4$ for T30923 [16] (Figure 1) for $(G3T)_4$ -T), and $(G3C)_4$ for T40214 [17].

Recently, some rational designs for making anti-proliferative GQ have been developed by us. Attempting to enhance the anti-proliferative activity, two single GQ DNA modules were covalently conjugated to make a bi-modular, "twin" molecule (see also [18]). Certainly, a simple covalent joining of two single GQ modules does not necessarily yield a perfect "twin" molecule with a double anti-proliferative activity, because extensions at both the 3′- and 5′-ends could affect the GQ stability and functioning [19]. For instance, HD1 could be covalently conjugated via a single T nucleotide; yielding bi-HD1 (Figure 1), which retains anti-proliferative activity [14].

This paper pursued this approach to make twin molecules and to explore their specific properties. The paper describes some structural and functional properties of a constructed, bi-(AID-1-T), bi-modular anti-proliferative GQ twin molecule, which was made by conjugating two modules of $(G3T)_3GGG$ via three T nucleotides (Figure 1).

2. Results

2.1. Topology of GQs and Bi-GQs

The topology of G-quadruplex oligonucleotides (GQs) was analyzed by characteristic circular dichroism (CD) spectroscopy. The CD spectrum of a parallel GQ had a huge positive band at 260 nm, a relatively shallow negative band at 240 nm, and another large positive band at 210 nm. The CD spectrum of an antiparallel quadruplex had a typical positive band at 295 nm, two other smaller ones at 240 and 210 nm, and a negative band at 260 nm [20–23].

AS1411, 26-mer GGTGGTGGTGGTTGTGGTGGTGGTGG, could form both monomolecular and bimolecular GQs. The 3-D structure of AS1411 was highly polymorphic in solution, with at least eight different GQs structures detected by chromatography and NMR [11,24]. The structure of AT11, 28-mer, with a close but mutated sequence (underlined) TGGTGGTGGTTGTTGTGGTGGTGGTGGT, turned out to have a single GQ conformation, and exhibited a similar anti-proliferative activity to AS1411. The solution structure of AT11, solved by NMR, revealed two GQs; each GQ is a propeller-type parallel-stranded two-tetrad module (Figure 1). The covalent conjugation supports stacking via the 3′-5′ interface [4].

HD1, 15-mer GGTTGGTGTGGTTGG, folds into antiparallel GQ with chair-like conformation (Figure 1, for rev. [13]).

The exact 3-D structure of AID-1-T, 15-mer GGGTGGGTGGGTGGG [25], is not yet known. AID-1, a close counterpart of AID-1-T (also coined as T30923), has an additional T at the 3′-end; its derivative, J19, with the single replacement G2I, GIGTGGGTGGGTGGGT, could form a noncovalent dimer: two identical propeller-type parallel-stranded three-tetrad GQ modules stacked via the 5′-5′ interface (Figure 1) [16].

The 3-D structures of the covalent dimers discussed in the text, the twin molecules, are not known yet. The idea that, after covalent joining of two GQ modules, the twins have to keep the original structure of the initial modules is not obvious. On the contrary, it was shown that just the single stranded oligonucleotide extensions at both the 3′- and 5′-ends of GQ of HD1 could affect the GQ properties [19]. Indeed, for the simplest case, bi-HD1, it seems that the two GQ modules are not equal, being covalently conjugated via single T ([14], and refs therein). Indeed, the molar ellipticity of CD spectrum at 295 nm of bi-HD1 is not exactly twice as for HD1, but just 1.5 times (Figure 2A).

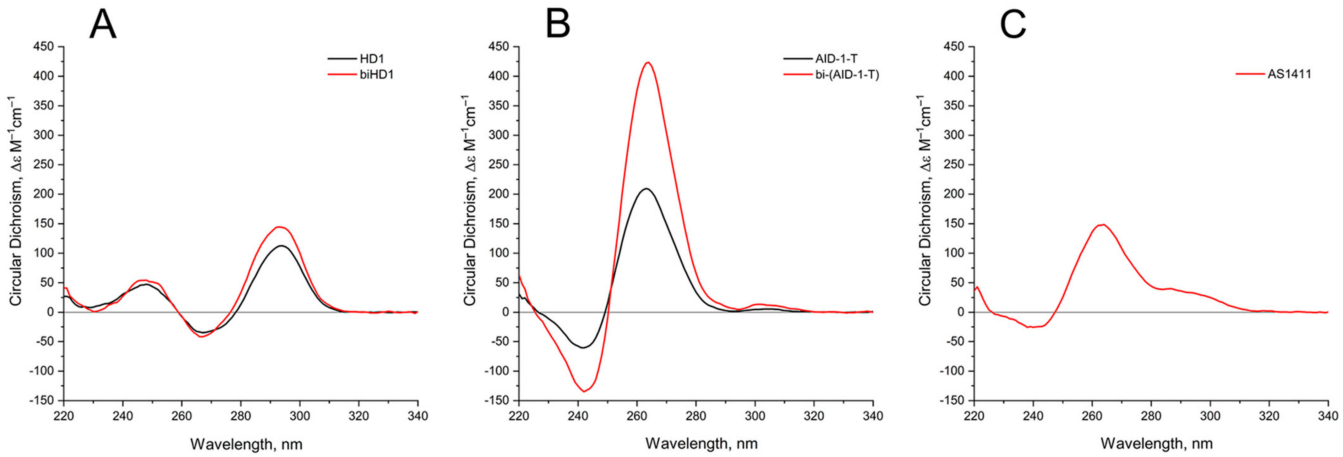

Figure 2. Circular dichroism (CD) spectra of the GQs under study in the buffer B (140 mM NaCl and 10 mM KCl) at 20 °C: (**A**) HD1 (black), bi-HD1 (red); (**B**) AID-1-T (black), bi-(AID-1-T) (red); (**C**) AS1411.

Continuing to explore the structural and functional properties of twin molecules, we made another twin, a novel bi-modular GQ, bi-(AID-1-T), a covalent dimer of AID-1-T module [25], connected with a TTT linker (Figure 1).

Comparing the spectra of mono-modular AID-1-T and covalent bi-modular GQ, bi-(AID-1-T), it is clear, that bi-GQ retains a topology of parallel GQ (Figure 2B). Moreover, the molar ellipticity of the covalent twin molecule is two times the ellipticity of the mono-modular one, despite the fact that AID-1-T does exist as a non-covalent dimer in the solution (see the next Section); therefore both molecules are dimers, either non-covalent AID-1-T or covalent bi-(AID-1-T). Though a striking difference is the following: Non-covalent dimerization of AID-1-T in solution happens via 5′-5′ stacking interactions [16], making the opposite orientation of two anti-parallel GQs, "face-to-face" (Figure 1). This is not the case for bi-(AID-1-T), where the only possibility is 5′–3′ stacking, due to the existence of the covalent link, making the same orientation of two anti-parallel GQs (Figure 1), and therefore yielding a twin with two-times higher ellipticity (Figure 2B).

As far as conformation of the reference molecule, AS1411, is concerned, it exhibits a spectrum for the mixture of conformers, as was shown before [11], with a prevailing parallel conformation (Figure 2C), which is in the vein of the suggested similarities with AT11 conformation [4].

GQ folding and stability strongly depend on the concentration and nature of the cations in a buffer [26–28]. Sodium cation Na^+ is for a shielding the phosphate charges; potassium cation K^+ is a very critical stabilizer of GQ structure, because it coordinates the octet of oxygen atoms of G-tetrads, and stabilizes GQ. Finally, barium cation Ba^{2+} is a very special coordination center, which arranges the same donors, the oxygen atoms of G, but much more strongly, and usually yielding a slightly different structure of GQ complex, unlike the one with K^+ that could be clearly detected by CD spectroscopy [29].

The behavior of the CD spectra of mono-modular anti-parallel HD1 is as described previously [29], showing increasing folding efficiency when using K^+ instead of Na^+ coordination; Ba^{2+} has a bigger effect, yielding a shift of the CD maximum from 294 nm to 302 nm (Figure 3A). As far as mono-modular parallel GQ structures are concerned, AS1411, being a mixture of conformers, shows the same tendency, with an increasing proportion of folding into the parallel structure after K^+ coordination, and almost perfect folding after Ba^{2+} coordination (Figure 3C). Not surprisingly, the folding of AID-1-T, as a perfect parallel GQ, is less affected by the nature of the cation (Figure 3D).

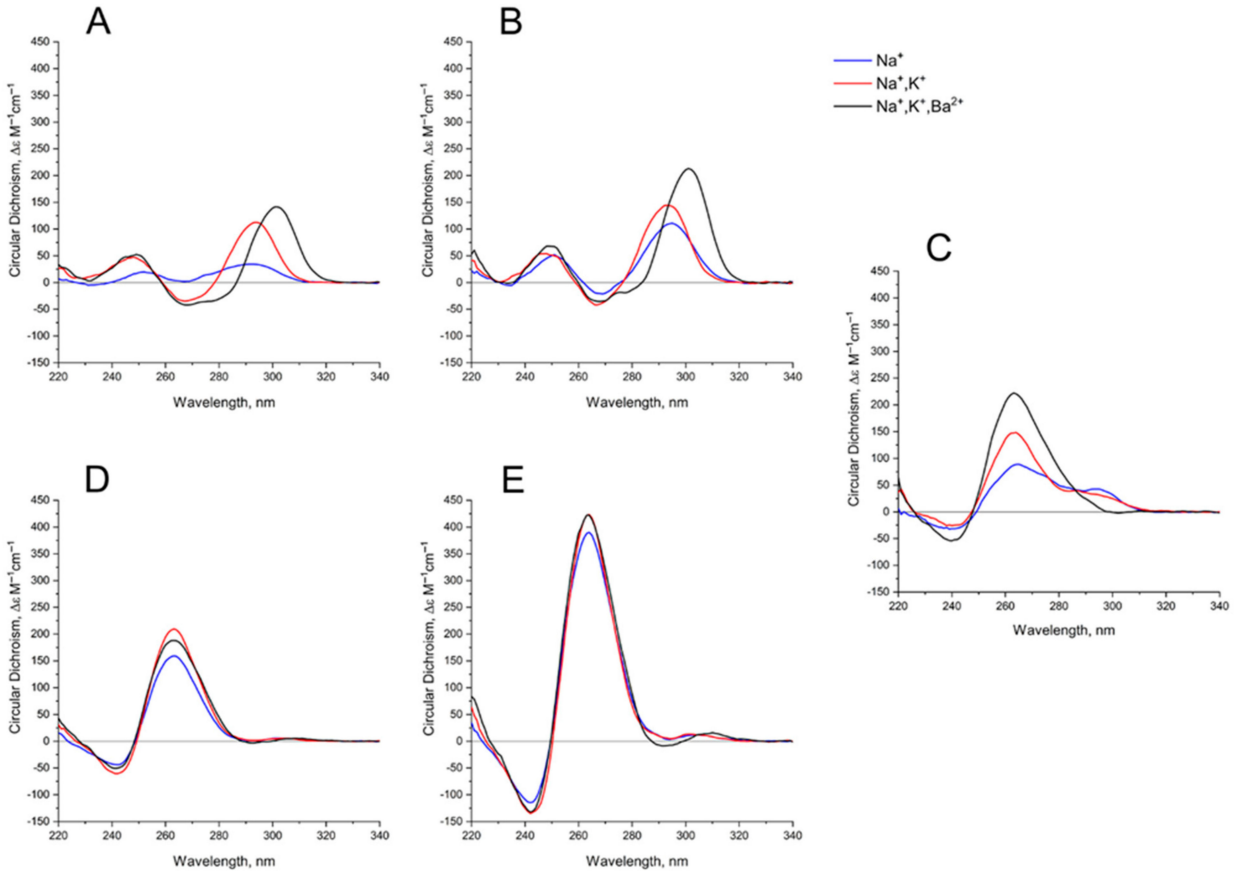

Figure 3. CD spectra GQs under study: in the buffer A (140 mM NaCl; (Na^+), blue), in the buffer B (140 mM NaCl, 10 mM KCl; (Na^+, K^+), red), in the buffer C (140 mM NaCl, 10 mM KCl, 5 mM $BaCl_2$; (Na^+, K^+, Ba^{2+}), black) at 20 °C: (**A**) HD1, (**B**) bi-HD1, (**C**) AS1411, (**D**) AID-1-T, (**E**) bi-(AID-1-T).

Bi-modular GQs are less sensitive to cation nature. Compared to HD1, bi-HD1 is folded sufficiently, even with Na^+; not mentioning that in Ba^{2+} solution it seems that both GQ modules of bi-HD1 were perfectly folded (Figure 3B). The parallel bi-modular bi-(AID-1-T) folds perfectly, with no dependence on cation nature (Figure 3E).

2.2. Thermal Stability of GQs and Bi-GQs

The thermal stability of GQs was analyzed by characteristic CD spectroscopy (Figure 4).

Table 1. List of patient glioma primary cell cultures, and brief data on patients. All samples have wt IDH1 (wild type of isocitrate dehydrogenase 1, a conventional glioma marker).

Cell Culture	Glioma Grade	Patient Gender	Patient Age
G11	III	F	33
Sus\fP2	IV	F	60
G01	IV	M	39
G23	IV	M	53
G22	IV	F	36
N1	IV	M	54

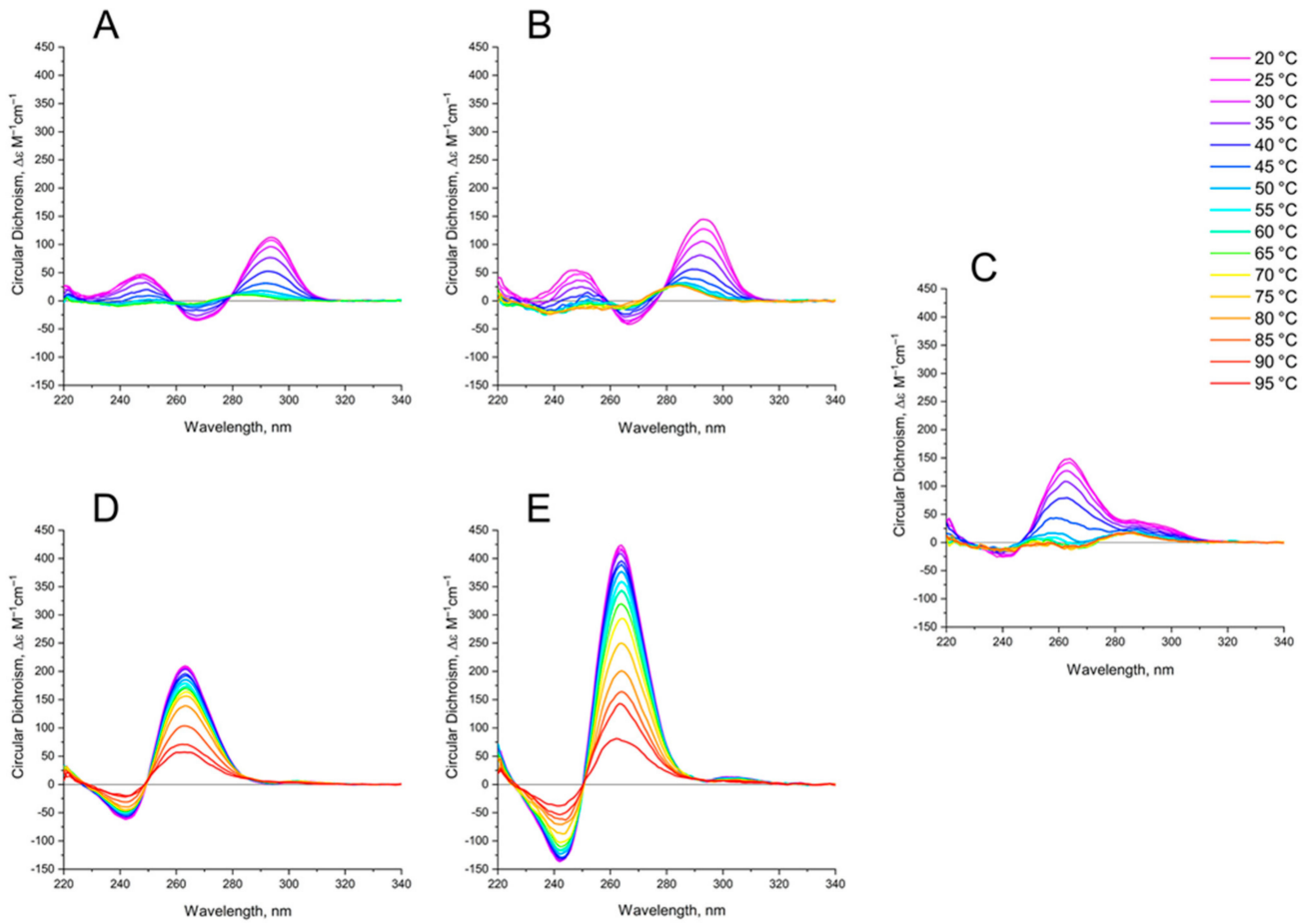

Figure 4. CD spectra of GQs under study in buffer B (140 mM NaCl and 10 mM KCl) at different Table 1. (**B**) bi-HD1; (**C**) AS1411 (**D**) AID-1-T, (**E**) bi-(AID-1-T). The color ladder on the right indicates temperatures.

The CD melting profile in the standard buffer B (140 mM and 10 mM KCl) of anti-parallel mono-modular HD1 was about the same as for bi-modular bi-HD1, as measured at 295 nm (Figure 5A). The apparent T*m* (aT*m*) were different, and about the same as those published earlier, 35 °C and 40 °C, respectively [14,30].

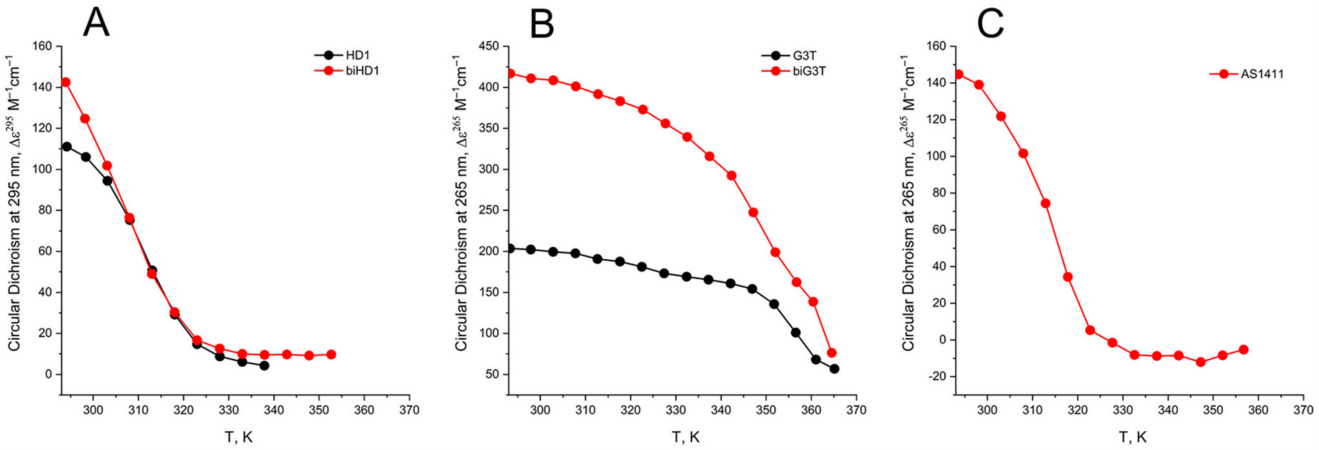

Figure 5. CD melting profile of GQs under study in buffer B (140 mM NaCl and 10 mM KCl): (**A**) HD1 (black), bi-HD1 (red); (**B**) AID-1-T (black), bi-(AID-1-T) (red); (**C**) AS1411 (red). Temperature is in kelvin (K): [°C] = [K] − 273.

The aT*m* of parallel GQs were expectedly higher than the anti-parallel GQs. The melting behavior of mono-modular AID-1-T exhibited a biphasic profile, with two distinct transitions (Figure 5B): at about 50 °C, presumably a non-covalent dimer to monomer transition (see Sub-section "size-exclusion HPLC"); and at 83 °C, the unfolding of the parallel GQ module itself. The melting profile of the covalent dimer, bi-(AID-1-T), showed a less cooperative, gradual behavior (Figure 5B), while the CD-annealing profile showed no hysteresis.

Not surprisingly, the parallel AS1411, as a mixture of conformations, and considering its two-quartet nature, had a much lower aT*m*, about 40 °C, as measured at 265 nm (Figure 5C).

Since the Ba^{2+} cation provides a very specific stabilizing effect, the melting of GQs in a buffer with Ba^{2+} was also studied (Figure A1). All tendencies of GQs melting Ba^{2+}solutions, both for mono-module and bi-modular ones, were alike for the K^+ solution, except the aT*m* were much higher.

2.3. Size-Exclusion HPLC of GQs and Bi-GQs

Size-exclusion HPLC (SE-HPLC) is a rather simple and powerful technique for the fast assessment of conformations and oligomeric forms of GQs, but it has not yet been widely applied [31] (for a review, see [32]). The separation matrix could be either polymethacrylate-based particles [32] or a silica-based one [24,33], which strongly affects the separation conditions.

Previously, we had developed conditions for silica-based SE-HPLC to perform separation with standard equipment [34,35], and applying a 10 μM concentration of GQ samples. Three different buffers were used (see CD Sub-section) to modulate the folding of GQs, and hence to estimate the conformational/oligomeric composition. It is worth mentioning that in our case, a good separation required a high salt concentration for the mobile phase; which could shift the equilibrium for dynamic conformers/oligomers if the pre-folding was made under different conditions.

Under all three conditions of pre-forming at high concentration, and with a subsequent transfer into separation conditions, AS1411 behaved as a dimer, and showing a slightly asymmetric peak (Figure 6C).

It is no surprise that the migration of bi-HD1 was much faster than mono-modular HD1. The bi-modular bi-(AID-1-T) exhibited approximately the same mobility as the non-covalent dimer of mono-modular AID-1-T; the dimerization ability of the later had also been observed before [16]. The introduction of Ba^{2+} stimulated further oligomerization of the non-covalent dimer.

2.4. Effect of GQs on the Viability of Cell Lines and Primary Glioma Cell Cultures from Patients

The focus of our study was the GBM primary cell lines from the patients, therefore the neural cancer cell line U87 was chosen as the reference, while fibroblasts from human embryo were the non-cancer controls. All GQs had no effect on the viability of fibroblasts from human embryos at all three concentrations tested: 0.1, 1, and 10 μM; whereas the effect on the viability of the reference U87 cell line strongly depended on the GQ structure (Figure 7).

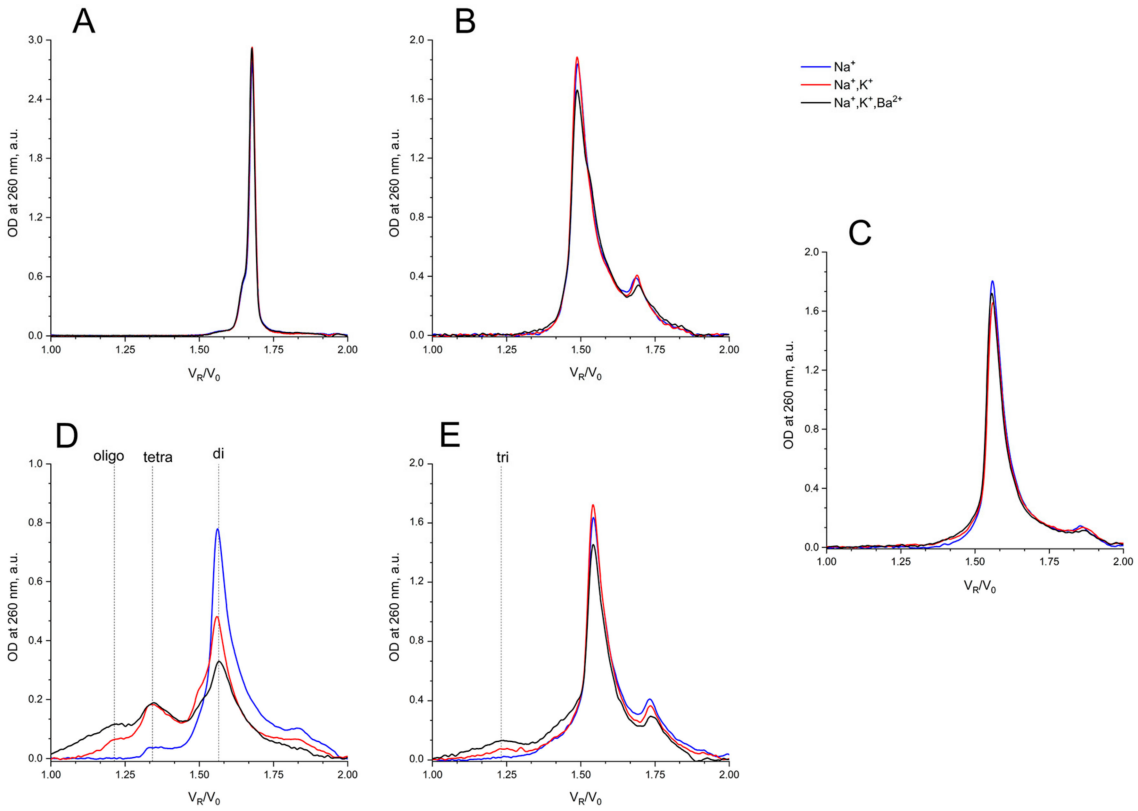

Figure 6. Size exclusion HPLC chromatography analysis of GQs under study: in buffer A (140 mM NaCl; (Na^+), blue), in buffer B (140 mM NaCl, 10 mM KCl; (Na^+, K^+), red), in buffer C (140 mM NaCl, 10 mM KCl, 5 mM $BaCl_2$; (Na^+, K^+, Ba^{2+}), black) at 20 °C: (**A**) HD1, (**B**) bi-HD1, (**C**) AS1411, (**D**) AID-1-T, (**E**) bi-(AID-1-T).

Within the range from 1 to 10 μM of GQs, only three dimeric GQs had an effect, exhibiting a gradual decrease of cell viability: the two covalent ones, bi-HD1 and bi-(AID-1-T), and the non-covalent dimer, AID-1-T.

Despite the current wide application of cell lines for studying GBM, it has become more and more evident that these results cannot be translated directly to the behavior of primary cell cultures from patient samples (for example, see [36]). Therefore, in this research, six different primary glioma cell cultures from patient samples were studied. Some patient data are listed in Table 1.

For studying the effect of GQs on the viability of cell cultures by MTT test, only twin molecules were selected, including a putative twin, the reference AS1411. Two out of six primary glioma cell cultures turned out to be sensitive toward bi-GQs treatment: G11 and Sus/fP2 (both derived from female samples) (Figure 8); and G11 was more sensitive than Sus/fP2. One other cell culture, G01, became sensitive to GQs only at a high concentration of 10 μM.

When comparing the activity of the two bi-GQs, bi-HD1 and bi-(AID-1-T), toward two sensitive cell cultures, G11 and Sus/fP2, bi-(AID-1-T) turned out to be the most active GQ, and could reduce viability twice, even at 1 μM GQ.

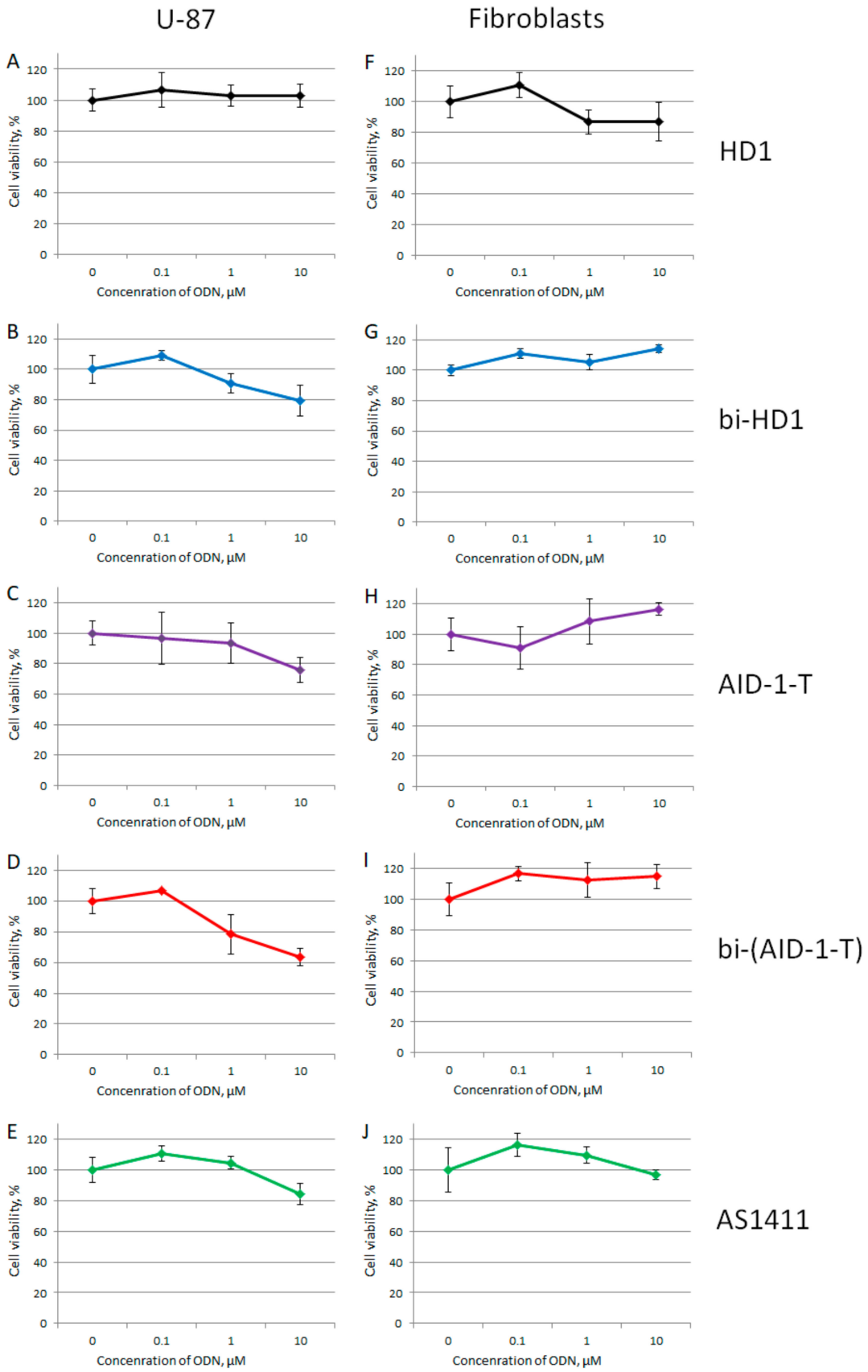

Figure 7. MTT assay data on the cell viability of two cell lines after GQ treatment with three different concentrations (0.1; 1.0, and 10 μM) for 72 h. Human cancer cell line U87 (**A**–**E**) and embryonic fibroblasts (**F**–**J**). HD1 (black), bi-HD1 (blue), AID-1-T (violet), bi-(AID-1-T) (red), AS1411 (green). Data are shown as (mean +/− S.D., standard deviation).

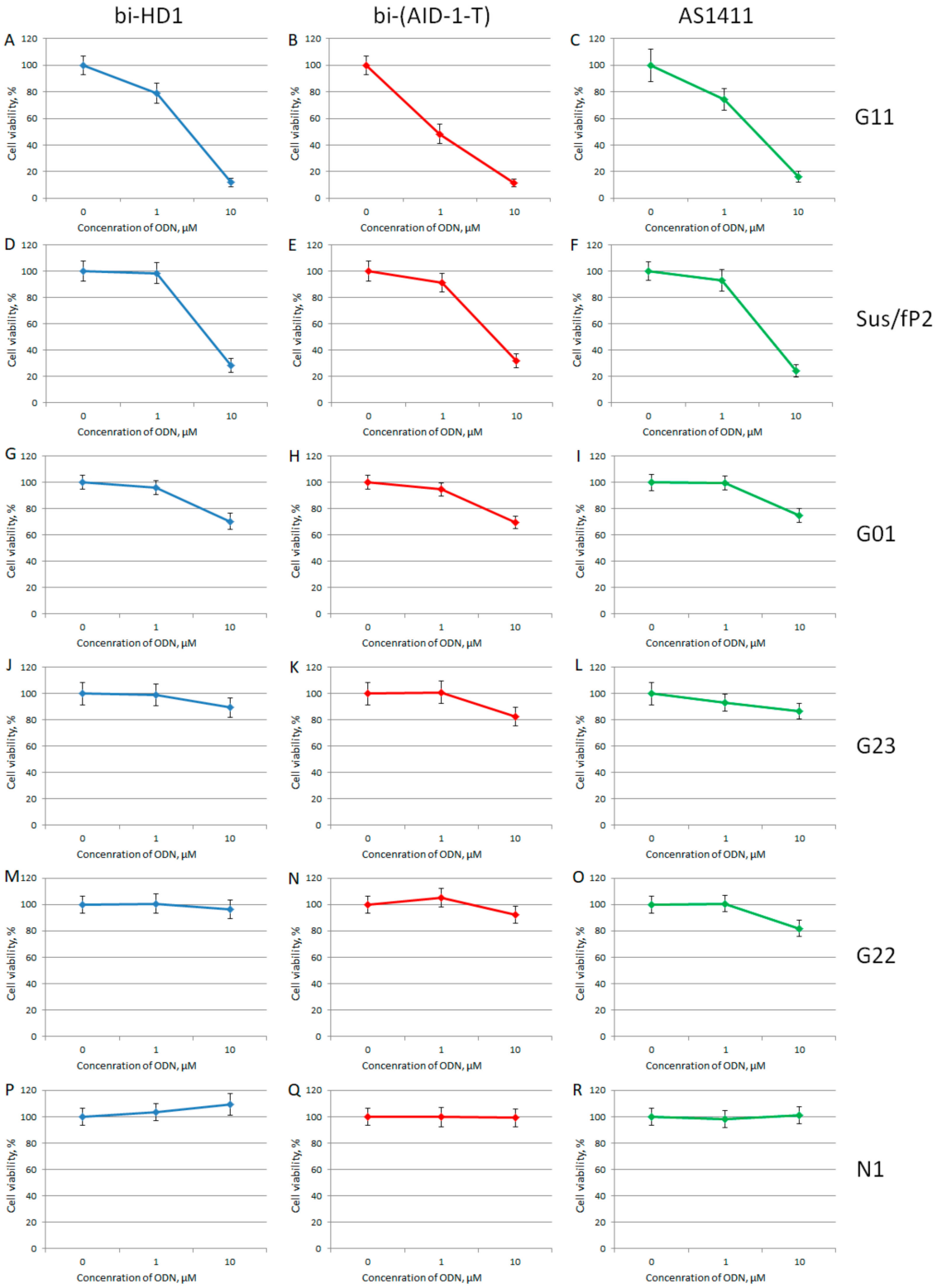

Figure 8. MTT assay data on the cell viability of six patient primary glioma cell cultures after bi-GQ treatment with three different concentrations (0.1; 1.0, and 10 μM) for 72 h. Patient primary glioma cell cultures: G11 (**A**–**C**), Sus/fP2 (**D**–**F**), G01 (**G**–**I**), G23 (**J**–**L**), G22 (**M**–**O**), N1 (**P**–**R**). bi-HD1 (blue), bi-(AID-1-T) (red), AS1411 (green). Data are shown as (mean +/− S.D.). Patient data are in the Table 1.

3. Discussion

GQs have a well-documented anti-proliferative activity [1]. Besides the numerous attempts at searching for more GQs with anti-proliferative activity, there are three established arms of research, which are based on the original mono-modular GQs, namely, AS1411, HD1, and the so called T-series.

AS1411 is a conventional GQ with anti-proliferative activity toward a variety of cell lines [6]. It is at the stage of translation, and we took it as the reference GQ. The disadvantage of AS1411 is its conformational heterogeneity, which was overcame using derivatives, like AT11 [5].

An idea for the further development of the other two arms of GQ anti-proliferative study is to conjugate known functional GQ modules, making a bi-modular twin molecule. We focused on the brain cancer, glioma. Most of the data for GQ anti-proliferative activity have been recorded using cancer cell lines, while this research was focused, for the first time, on patient glioma primary cell cultures.

Because of a lack in the literature of well-established conventional conditions for the treatment of cells with oligonucleotides, the critical point was choosing a threshold for screening. We restricted this value to 10 μM.

We have shown earlier [14] for the CNS cancer cell line, U87, that two-quartet GQ, bi-HD1, has an anti-proliferative activity; and that bi-modular constructed bi-HD1 is much more active than mono-modular HD1: GQ concentration below 10 μM GQ, for 72 h. Therefore, these GQs (Figure 1) were chosen as the reference to compare mono-modular and bi-modular GQs for anti-proliferative activity.

AID-1-T is a three-quartet GQ with an anti-proliferative activity toward a variety of cell lines [37]. Continuing the bi-modular construction, a bi-(AID-1-T) with TTT-linker in between two GQ modules was designed for the first time.

The three-dimensional structures of GQ modules are known for HD1 [38], and the derivative of AID-1, AT11 [4] (Figure 1).

It is known that any extensions from the GQ structure, like single stranded short oligonucleotides, affect the GQ internal structure, stability, and properties [19], not to mention an extension with a massive module, such as another GQ. In addition, the existence of three lateral loops could interfere with the tight packing of two GQs of HD1s joined by a short link with a single T. Indeed, a putative structure of bi-HD1 does not correspond to a sum of two initial modules; probably the structure of the second module extending from the 3′-end of the first one is slightly different from HD1 due to CD spectroscopy (Figure 2A) [14]. Therefore, the structure of bi-modular GQ constructs should be carefully studied before functional assays.

The CD spectrum of HD1 and bi-HD1 (Figure 2) correspond to a topology of anti-parallel GQ [20]. The molar CD at 294 nm for bi-HD1 with K^+ was not two times, but just 1.3 times more than that for HD1, which reflects the existence of two unequal GQs [14]. The CD spectrum of AID-1-T and bi-(AID-1-T) correspond to the topology of parallel GQ [20]. The molar ellipticity at 263 nm for bi-(AID-1-T) with K^+ was exactly two times more than that for AID-1-T, which reflects the existence of two equal GQs, unlike for bi-HD1. These structural differences of the two twins could be due to the different orientation of the two GQs within the molecule. In bi-HD1 the two GQs could not stack because of the lateral loops; on the contrary, in bi-(AID-1-T) the two GQs could perfectly stack on each other [39]. Three-quartet AID-1-T and bi-(AID-1-T) could fold more effectively than two-quartet HD1 and bi-HD1 (Figure 2). This could be due to either the number of quartets within GQ, or the stacking within the twin mentioned above, or both.

As far as the effects of cation nature on the folding are concerned, generally, bi-modular constructs were less sensitive to the nature of the cation (Figure 3). In Na^+, HD1 was, as expected, not well-folded (Figure 3A) [29], while bi-HD1 was almost folded, as it folds in favorable K^+ (Figure 3B). For AID-1-T and bi-(AID-1-T) this effect was much more pronounced (Figure 3D,E); the introduction of Ba^{2+} stressed this effect. The folding of covalently joined GQs of bi-HD1 was affected by Ba^{2+} much more strongly than a single

module of HD1 alone (Figure 3A,B), which supports the idea of unequal, imperfect GQs in bi-HD1. This was not that notable for AID-1-T and bi-(AID-1-T) because of the perfect GQ folding, and probably due to the reasons discussed above.

The thermal stability of a folded GQ strongly affected its functional activity, because most of tests were performed at 37 °C (310° K). After 35 °C (308° K) the thermal unfolding of HD1 was similar to that of bi-HD1 (Figure 5A), indicating some autonomy of GQ behavior beyond this temperature. However, an aT_m about 40 °C (313° K) could not provide totally folded molecules. Parallel GQs of AID-1-T and bi-(AID-1-T) were much more thermally stable than anti-parallel GQs, having aT_m above 75 °C (348° K), and providing almost totally folded molecules, which was firmly in favour of its applicability in exploring the anti-proliferative activity of these GQs. The difference in the thermal stability of mono- and bi-modular GQs was more pronounced. Mono-modular AID-1-T gave a non-covalent dimer via the stacking interaction of two molecules. It showed bi-phase thermal unfolding, a first gradual slow decrease of ellipticity, probably due to dissociation of dimers, and then the unfolding of the GQs themselves.

For testing the anti-proliferative activity, a rather high concentration of GQs is usually applied to cell cultures, i.e., micromole range. Therefore, an examination of the conformational/oligomeric homogeneity of GQs at these concentrations has to be carefully performed.

AS1411 behaves as a dimer, showing a slightly asymmetric peak (Figure 6C). For AS1411 the existence of a dimer fraction has been found [11], which could be due to the suggested bi-modular structure (Figure 1).

It is interesting to compare the migration of bi-HD1 with that of AS1411. The first twin, being less compact because of the lateral loops, goes faster than the putative second one, which again indirectly supports the suggested bi-modular structure of AS1411.

It is no surprize that the migration of bi-HD1 is much faster than mono-modular HD1. Bi-modular bi-(AID-1-T) exhibited approximately the same mobility as the non-covalent dimer of mono-modular AID-1-T; the dimerization ability of the later has also been observed before [16]. The introduction of Ba^{2+} stimulated further dimerization of the non-covalent dimer into a putative tetramer.

As was already mentioned, GQs have attracted a great deal of attention as potential anti-proliferative agents [1]. To increase the GQs activity, a variety of modifications have been applied, mainly attempting to improve their chemical stability in the milieu.

Aside from that trend, in this research we continued to explore an approach of constructing twin molecules by the covalent linking of identical functionally active GQ modules. Even for HD1 with lateral loops, it was shown that making a bi-modular twin molecule was effective for creating an anti-proliferative agent for the neural cancer cell line U87 (Figure 7A,B) [14].

Parallel GQs with propeller loops have the folding properties discussed above, and due to this they are more suitable for exploring anti-proliferative activity. GQ of AID-1-T is known for its ability to bind several GQ-binding proteins, like HIV integrase, and IL-6 receptor [25], but its anti-proliferative activity has not been explored toward cancer cells, nor neural cancer cells in particular.

At the beginning, all five GQs were tested toward the neural cancer cell line, U87, applying three different concentrations of GQ: 0.1, 1.0, and 10 μM, in an attempt to find the most active GQ, as well as to compare mono-modular and bi-modular constructs (Figure 7). As a control for a non-cancer cell line, human embryo fibroblasts were used. First, all GQs, except HD1, at 10 μM had a reduced U87 cell viability, and only bi-modular GQs were active at 1 μM, which stressed the value of making twin molecules. There were no effects on the human embryo fibroblast cell line at any concentration tested.

Unique results were observed when the primary glioma cell cultures from patients were tested. Brief data on patients are listed in Table 1. Six cell cultures were tested, and it turned out that the viability of just three cell cultures, G01, Sus/fP2, and G11, were affected to a very different extent (Figure 8). The IC50 for the G01 cell culture was >10 μM; the

Sus/fP2 and G11 cell cultures were 1–10 μM; and only in one case, for bi-(AID-1-T) toward G11 cell culture, the IC50 was less than 1 μM. In general, the most sensitive cell culture was G11, and the most active GQ was bi-(AID-1-T) (Figure 8B).

Therefore, the conclusion was the following: the anti-proliferative activity of different GQs toward different cell cultures was different. This ambiguity could be solved in two ways: from the GQ structure, and from the cell nature.

The specific GQ structure governs the type of action on a cancer cell line; changes in GQ conformation affect its activity: it could either reduce/abolish activity [14] or enhance activity (Figures A2–A4). The inversion of chain polarity and usage of unnatural nucleotides could increase anti-cancer activity [15,40,41], but the exact reason, like changing the conformation only, has to be established properly in each case.

The phenomenon of inter-tumor heterogeneity, in terms of the response to specific agents, like antibodies, is not surprising [36], and needs to be studied in more detail to attempt to find reasons. GQs, as crypto-aptamers, could be considered as relatively specific agents as well, though less specific than antibodies, because they can attack not a single protein, but a group of proteins, like GQ-binding proteins. This suggestion was correct in the case of AID-1-T GQ, which could interact with different proteins: the receptor IL-6R, and HIV integrase [25]. Therefore, more studies are required to find clues to the mechanism of action of its twin, bi-(AID-1-T).

At this stage of the research, some general questions could be addressed, whether this intertumor heterogeneity toward GQs is due to the very first steps of up-take, endocytosis activity, due to the status of the transport protein, like nucleolin, or due to the status of unknown receptor; or whether it reflects different inner-cell events: the pattern/status of GQ-binding proteins. Any correlations between possible histology/pathology and the molecular biology features of real patients and GQs activities remain to be established.

4. Materials and Methods

Conventional human cell lines U87 and fibroblasts from human embryo were provided from the collection of the Centre of Neurosurgery (Moscow, Russia). GBM cultures N1, G11, Sus/fP2, G22, G23, and G01 were developed in the Centre of Neurosurgery from the surgery samples of patients (Burdenko National Medical Research Centre of Neurosurgery). The data on GBM grade and some patient details are summarized in Table 1; all samples had WT IDH1 (isocitrate dehydrogenase 1). This study was approved by the Ethics Committee of Burdenko Neurosurgical Institute, Russian Academy of Medical Sciences (№_12/2020). All subjects gave written informed consent in accordance with the Declaration of Helsinki.

4.1. Materials and Reagents

NaCl and $BaCl_2$ Merck (KGaA, Darmstadt, Germany); KCl Serva (Heidelberg, Germany), HCl Bio–Rad Laboratories (Hercules, CA, United States), Tris Invitrogen (Carlsbad, CA, USA), NaH_2PO_4, $Na_2HPO_4 \cdot 2H_2O$, glycerol PanReac AppliChem (Barcelona, Spain), acetonitrile HPLC grade Sigma–Aldrich (St. Louis, MO, USA), dimethylsulfoxide PanEco (Moscow, Russia), growth medium DMEM/F–12, PBS Gibco, Thermo Fisher Scientific (Carlsbad, CA, USA), MTT–reagent CellTiter 96® Aqueous Promega (Madison, WI, USA). Solutions were made with deionized water, Milli–Q (Merck MilliPore, Burlington, MA, USA), and were filtered prior to experiments though 0.2 μm nitrocellulose filters, Sarstedt (Nümbrecht, Germany).

Buffer composition: buffer A: 20 mM Tris-HCl, pH 7.1, 140 mM NaCl; buffer B: 20 mM Tris-HCl, pH 7.1, 140 mM NaCl, 10 mM KCl; buffer C: 20 mM Tris-HCl, pH 7.1, 140 mM NaCl, 10 mM KCl, 5 mM $BaCl_2$; buffer D: 20 mM Tris-HCl, pH 7.1, 140 mM NaCl, 10 mM KCl, 1% (*v*/*v*) glycerol.

All oligonucleotides were synthesized and HPLC-purified by Evrogen Ltd. (Moscow, Russia).

The sequences of GQs are listed in Table 2. The oligonucleotides were named according to their first appearance in the literature. Four of the six oligonucleotides had been described previously. Bi-modular GQ, bi-(AID-1-T) was designed for the first time.

Table 2. List of GQ sequences of DNA oligonucleotide under study. Proposed sequences of linkers of GQ modules are underlined. References for known GQ are in the text.

GQ	DNA Sequence
AS1411	GGTGGTGGTGGTTGTGGTGGTGGTGG
HD1	GGTTGGTGTGGTTGG
bi-HD1	GGTTGGTGTGGTTGGTGGTTGGTGTGGTTGG
AID-1-T	GGGTGGGTGGGTGGG
Bi-(AID-1-T)	GGGTGGGTGGGTGGGTTTGGGTGGGTGGGTGGG

4.2. Preparation of GQ Solutions

Molar extinction coefficients of oligonucleotides were calculated using the nearest-neighbor model [42]. Optical density was measured using a UVI photometer BioPhotometer 6131 from Eppendorf (Hamburg, Germany). GQs were dissolved in buffers. All solutions were heated at 95 °C for 5 min, and cooled at room temperature.

4.3. Circular Dichroism Spectroscopy (CD)

CD spectra (as well as UV spectra) were recorded using a CD spectrometer Chirascan from Applied Photophysics (Leatherhead, UK) and a Dichrograph MARK-5 (Jobin-Yvon; Montpellier, France) equipped with a thermoelectric temperature regulator. Quartz cuvettes had a 1-cm optical path length. CD and UV spectra were measured in the wavelength range 220–340 nm, and temperatures range 20–95 °C, with a 5 °C step; the samples had a thermostatic pause for 7 min. Spectra of buffer solution were subtracted as baselines. Melting temperatures were calculated from CD melting profiles at 265 nm for parallel GQ, and at 295 nm for antiparallel GQ [43].

4.4. Size-Exclusion HPLC

Size-exclusion chromatography (SEC) was conducted as described [34,35] using an Agilent 1200 HPLC system with an autosampler and diode array detector (Agilent; Santa Clara, CA, USA). The HPLC column was a TSKgel G2000SWXL (Tosoh Bioscience; King of Prussia, PA, USA), 30 cm length, 0.78 cm diameter, 5 μm particle diameter, 12.5 nm pore diameter; the column was conventionally recommended by the manufacturer for the separation of proteins with MW (molecular weight) in the range 5–150 kDa. The developed conditions for the separation of oligonucleotides were the following: temperature 25 °C, mobile phase water/acetonitrile 9:1 v/v with potassium phosphate buffer (60 mM KH_2PO_4 and 140 mM K_2HPO_4, pH 6.9), and flow rate 0.5 mL/min. Absorption at 260 nm was registered with 10 nm bandwidth.

The column was calibrated with a set of duplexes (GeneRuler Ultra Low Range DNA Ladder from Thermo Fisher Scientific (Carlsbad, CA, USA). The linear range for log (MW) from Vr/V0 was achieved for duplexes with 10–100 base pairs (Vr—retention volume, V0—dead volume of the column, 5.64 mL). The following equation was acquired from the calibration experiment and used for further calculations of apparent molecular weights of GQ and complexes: $\log(MW) = 6.51 - 1.67 \cdot Vr/V0$.

4.5. MTT Assay

The MTT assay estimated cell viability, which was measured after adding GQ; the standard protocol was used [44]. Cells were placed in 96-well plates; 1500–2000 cells per well were supplied with 200 μL of growth medium, and cultivated for 48 h under standard conditions (37 °C, 5% CO_2, and controlled humidity). Then the growth medium was removed and 100 μL of fresh growth medium was added with GQ in the appropriate content; five repeats for each sample were made. Cells were incubated for 72 h; then growth

medium was removed; the cells were washed with PBS; 100 μL fresh growth medium and 20 μL of MTT reagent were added for 2 h. Growth medium without cells and MTT-reagent was used as a baseline sample. Optical density was measured using Infinite M200 Pro (Tecan, Switzerland) at 490 nm.

5. Conclusions

G-quadruplex DNA oligonucleotides (GQs) exhibited specific anti-proliferative activity for human cancer cell lines. This ability could be translated into the treatment of glioblastoma multiform (GBM), which has a poor prognosis and low-efficiency therapeutics. A novel bimodular GQ, bi-(AID-1-T), a covalent twin of the previously described three-quartet AID-1-T, was structurally and functionally characterized. A comparison of bi-(AID-1-T) with its module, AID-1-T, and bi-modular bi-HD1 with its module two-quartet HD1, and conventional AS1411, was made. Bi-(AID-1-T) had the highest anti-proliferative activity for neural cancer cell line U87, while not affecting the control human embryonic fibroblasts. For the first time GQs were tested toward several primary GBM cultures from patient surgical samples. The sensitivity of patient primary GBM cultures toward GQs varied, with an apparent IC50 less than 1 μM for bi-(AID-1-T) toward the most sensitives G11 cell culture (GBM, Grade III).

Author Contributions: A.K., G.P.; methodology, V.L., N.S., A.A., V.T., E.Z.; software, A.K.; validation, A.K., E.Z., D.U., G.P.; investigation, A.K., G.P.; resources, A.K., D.U.; data curation, A.K.; writing—original draft preparation, V.L., A.K., G.P.; writing—review and editing, A.K., G.P.; visualization, V.L., N.S., A.A., V.T.; project administration, A.K., D.U.; funding acquisition, A.K., G.P., D.U. All authors have read and agreed to the published version of the manuscript.

Funding: This research was funded by the Ministry of Education and Science of Russia Foundation, grant number № 075-15-2020-809 (13.1902.21.0030) and by the Russian Foundation for Basic Research, grants number №17-00-00160, №17-00-00157 (17-00-00162 K) and №18-015-00279 A.

Institutional Review Board Statement: The study was conducted according to the guidelines of the Declaration of Helsinki, and was approved by the Local Ethics Committee of Burdenko Neurosurgery Center (protocol code №12/2020, 15.12.2020).

Informed Consent Statement: Informed consent was obtained from all subjects involved in the study.

Data Availability Statement: The data presented in this study are available on request from the corresponding author. The data are not publicly available due to the reason that some of the generated data is not published.

Acknowledgments: We appreciate the collaboration of Anastasiya Bizayeva and Eva Dominik with the additional CD folding-unfolding experiment, and preparation of Figures.

Conflicts of Interest: The authors declare no conflict of interest.

Appendix A

Previously it has been shown by us, that the coordination of Ba^{2+} cation by GQ of bi-HD1 stabilized GQ and abolished its anti-proliferative activity [14].

Owing to the conformational heterogeneity of AS1411, it was suggested to stabilize a conformation of AS1411 with Ba^{2+} coordination in buffer C (Figures 3, A1 and A4), and study the anti-proliferative activity of this complex toward four primary glioma cell cultures (Figure A5). Contrary to bi-HD1, the activity of AS1411+ Ba^{2+} was increased. The most demonstrative example was the treatment of the most sensitive G11 culture with 1 μM AS1411+ Ba^{2+}, which was more effective than AS1411+K^{+} (Figure A5).

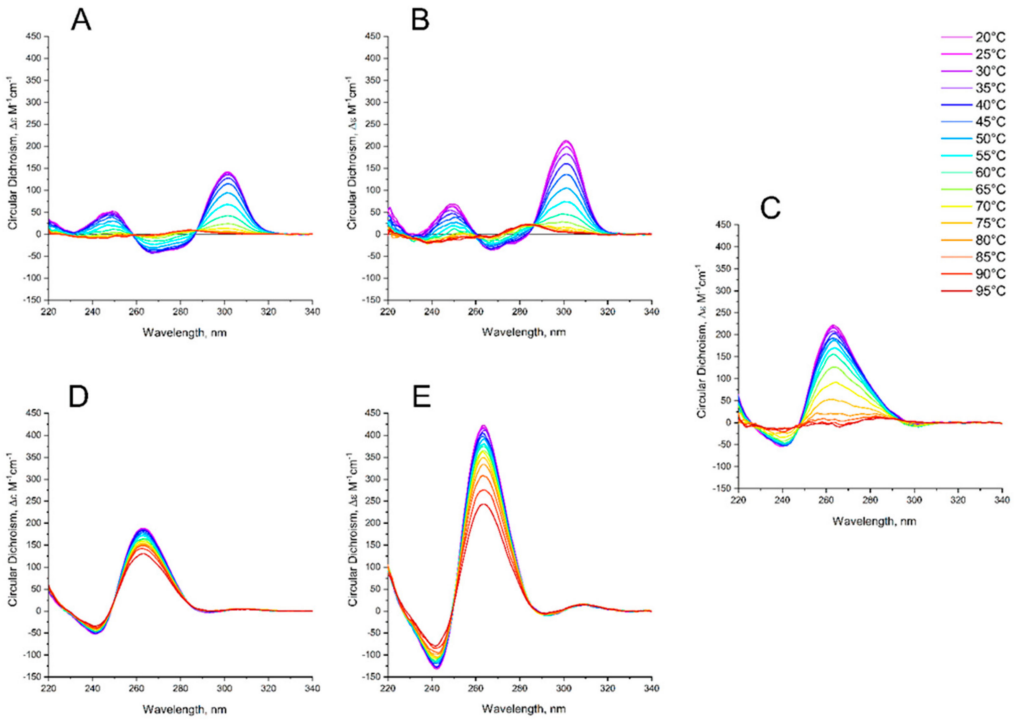

Figure A1. CD spectra of GQs under study in buffer C (140 mM NaCl, 10 mM KCl, 5 mM $BaCl_2$) at different temperatures: (**A**) HD1, (**B**) bi-HD1; (**C**) AS1411, (**D**) AID-1-T, (**E**) bi-(AID-1-T). The color ladder on the right indicates temperatures.

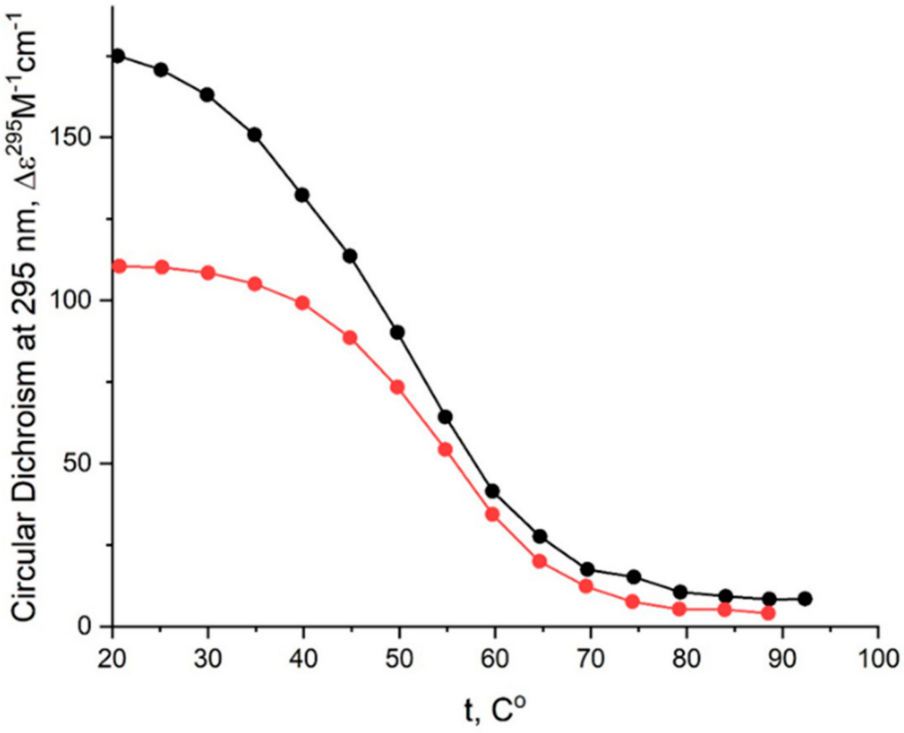

Figure A2. CD melting profile of GQs under study in the buffer C (140 mM NaCl, 10 mM KCl, 5 mM $BaCl_2$): HD1 (red), bi-HD1 (black).

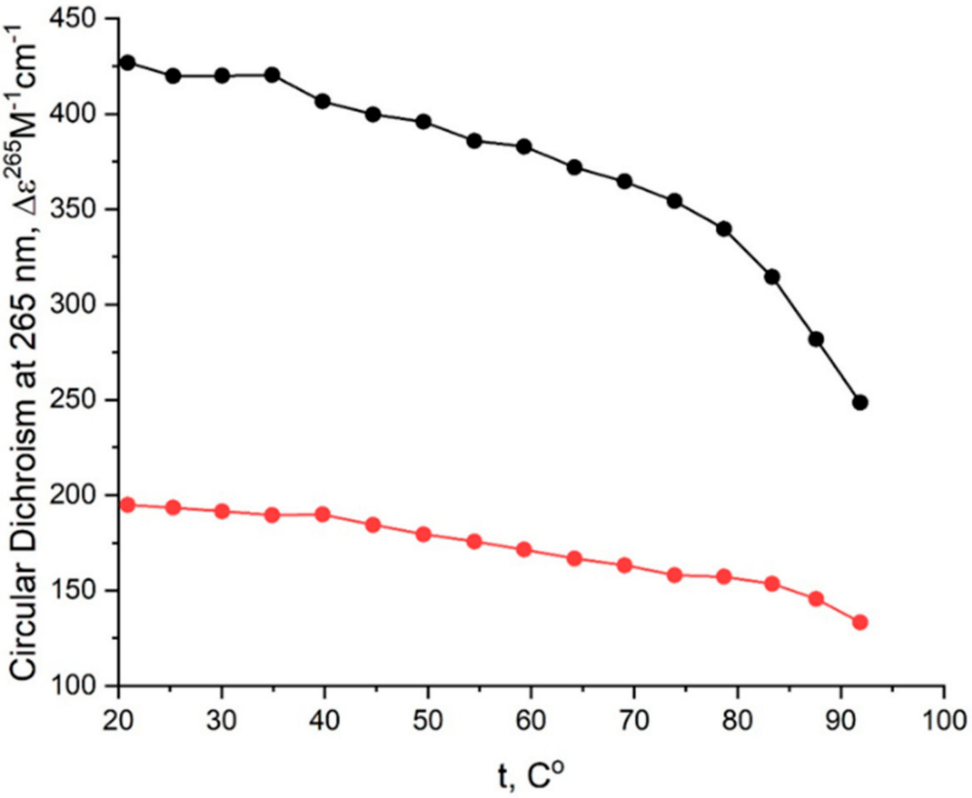

Figure A3. CD melting profile of GQs under study in the buffer C (140 mM NaCl, 10 mM KCl, 5 mM $BaCl_2$): AID-1-T (red), bi-(AID-1-T) (black).

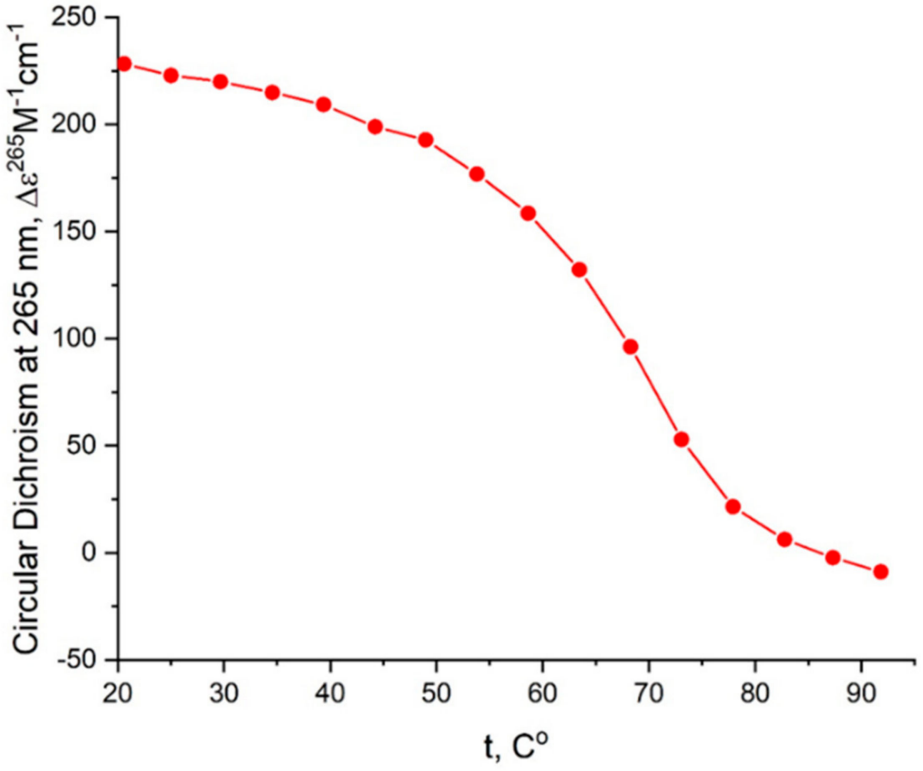

Figure A4. CD melting profile of GQs under study in buffer C (140 mM NaCl, 10 mM KCl, 5 mM $BaCl_2$): AS1411 (red).

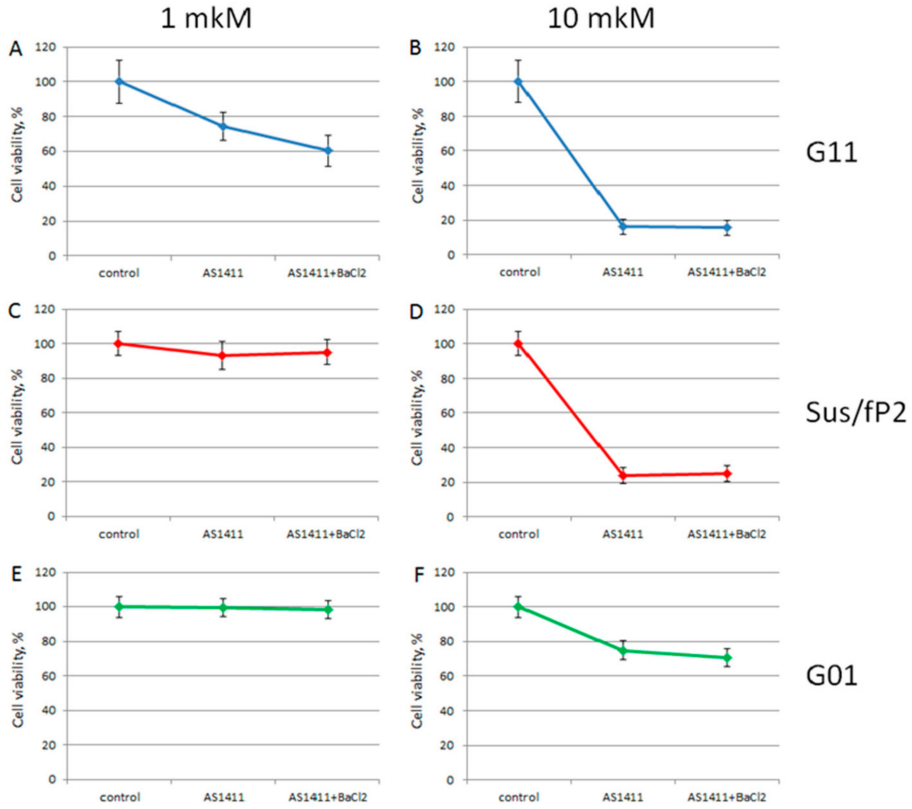

Figure A5. MTT assay data on cell viability of three patient primary glioma cell cultures after treatment with AS1411+Ba^{2+} at 1 and 10 μM, for 72 hrs. Patient primary glioma cell cultures: G11 (**A**,**B**, blue), Sus/fP2 (**C**,**D**, red), G01 (**E**,**F**, green). Data are shown as (mean +/− SD). Patient data are in Table 1.

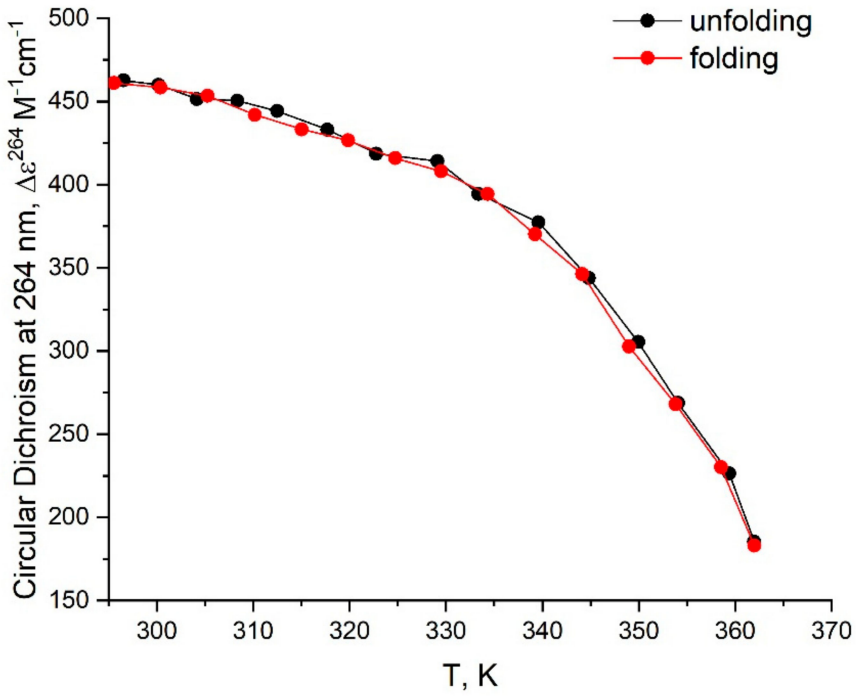

Figure A6. CD unfolding (black) and folding (red) profiles for bi-(AID-1-T) in buffer B (140 mM NaCl, 10 mM KCl; (Na^+, K^+).

References

1. Carvalho, J.; Mergny, J.-L.; Salgado, G.F.; Queiroz, J.A.; Cruz, C. G-quadruplex, Friend or Foe: The Role of the G-quartet in Anticancer Strategies. *Trends Mol. Med.* **2020**, *26*, 848–861. [CrossRef]
2. Kosiol, N.; Juranek, S.; Brossart, P.; Heine, A.; Paeschke, K. G-quadruplexes: A promising target for cancer therapy. *Mol. Cancer* **2021**, *20*, 1–18. [CrossRef]
3. Cogoi, S.; Paramasivam, M.; Filichev, V.G.; Pedersen, E.B.; Xodo, L.E. Identification of a New G-Quadruplex Motif in theKRASPromoter and Design of Pyrene-Modified G4-Decoys with Antiproliferative Activity in Pancreatic Cancer Cells. *J. Med. Chem.* **2009**, *52*, 564–568. [CrossRef] [PubMed]
4. Do, N.Q.; Chung, W.J.; Truong, T.H.A.; Heddi, B.; Phan, A.T. G-quadruplex structure of an anti-proliferative DNA sequence. *Nucleic Acids Res.* **2017**, *45*, 7487–7493. [CrossRef]
5. Bates, P.J.; Laber, D.A.; Miller, D.M.; Thomas, S.D.; Trent, J.O. Discovery and development of the G-rich oligonucleotide AS1411 as a novel treatment for cancer. *Exp. Mol. Pathol.* **2009**, *86*, 151–164. [CrossRef]
6. Bates, P.J.; Reyes-Reyes, E.M.; Malik, M.T.; Murphy, E.M.; O'Toole, M.G.; Trent, J.O. G-quadruplex oligonucleotide AS1411 as a cancer-targeting agent: Uses and mechanisms. *Biochim. Biophys. Acta* **2017**, *1861*, 1414–1428. [CrossRef] [PubMed]
7. Reyes-Reyes, E.M.; Teng, Y.; Bates, P.J. A new paradigm for aptamer therapeutic AS1411 action: Uptake by macropino-cytosis and its stimulation by a nucleolin-dependent mechanism. *Cancer Res.* **2010**, *70*, 8617–8629. [CrossRef] [PubMed]
8. Reyes-Reyes, E.M.; Šalipur, F.R.; Shams, M.; Forsthoefel, M.K.; Bates, P.J. Mechanistic studies of anticancer aptamer AS1411 reveal a novel role for nucleolin in regulating Rac1 activation. *Mol. Oncol.* **2015**, *9*, 1392–1405. [CrossRef]
9. Rosenberg, J.E.; Bambury, R.M.; Van Allen, E.M.; Drabkin, H.A.; Lara, P.N.; Harzstark, A.L.; Wagle, N.; Figlin, R.A.; Smith, G.W.; Garraway, L.A.; et al. A phase II trial of AS1411 (a novel nucleolin-targeted DNA aptamer) in metastatic renal cell carcinoma. *Investig. New Drugs* **2014**, *32*, 178–187. [CrossRef] [PubMed]
10. Yu, Z.; Li, X.; Duan, J.; Yang, X.-D. Targeted Treatment of Colon Cancer with Aptamer-Guided Albumin Nanoparticles Loaded with Docetaxel. *Int. J. Nanomed.* **2020**, *15*, 6737–6748. [CrossRef]
11. Dailey, M.M.; Miller, M.C.; Bates, P.J.; Lane, A.N.; Trent, J.O. Resolution and characterization of the structural poly-morphism of a single quadruplex-forming sequence. *Nucleic Acids Res.* **2010**, *38*, 4877–4888. [CrossRef] [PubMed]
12. Ogloblina, A.M.; Iaccarino, N.; Capasso, D.; Di Gaetano, S.; Garzarella, E.U.; Dolinnaya, N.G.; Yakubovskaya, M.G.; Pagano, B.; Amato, J.; Randazzo, A. Toward G-Quadruplex-Based Anticancer Agents: Biophysical and Biological Studies of Novel AS1411 Derivatives. *Int. J. Mol. Sci.* **2020**, *21*, 7781. [CrossRef]
13. Riccardi, C.; Napolitano, E.; Platella, C.; Musumeci, D.; Montesarchio, D. G-quadruplex-based aptamers targeting human thrombin: Discovery, chemical modifications and antithrombotic effects. *Pharmacol. Ther.* **2021**, *217*, 107649. [CrossRef] [PubMed]
14. Antipova, O.; Samoylenkova, N.; Savchenko, E.; Zavyalova, E.; Revishchin, A.; Pavlova, G.; Kopylov, A. Bimodular Antiparallel G-Quadruplex Nanoconstruct with Antiproliferative Activity. *Molecules* **2019**, *24*, 3625. [CrossRef]
15. Esposito, V.; Russo, A.; Vellecco, V.; Bucci, M.; Russo, G.; Mayol, L.; Virgilio, A.; Galeone, A. Thrombin binding aptamer analogues containing inversion of polarity sites endowed with antiproliferative and anti-motility properties against Calu-6 cells. *Biochim. Biophys. Acta* **2018**, *1862*, 2645–2650. [CrossRef] [PubMed]
16. Do, N.Q.; Lim, K.W.; Teo, M.H.; Heddi, B.; Phan, A.T. Stacking of G-quadruplexes: NMR structure of a G-rich oligonucleotide with potential anti-HIV and anticancer activity. *Nucleic Acids Res.* **2011**, *39*, 9448–9457. [CrossRef]
17. Hillion, J.; Belton, A.M.; Shah, S.N.; Turkson, J.; Jing, N.; Tweardy, D.J.; Di Cello, F.; Huso, D.L.; Resar, L.M.S. Nanoparticle delivery of inhibitory signal transducer and activator of transcription 3 G-quartet oligonucleotides blocks tumor growth inHMGA1transgenic model of T-cell leukemia. *Leuk. Lymphoma* **2014**, *55*, 1194–1197. [CrossRef]
18. Riccardi, C.; Napolitano, E.; Musumeci, D.; Montesarchio, D. Dimeric and Multimeric DNA Aptamers for Highly Effective Protein Recognition. *Molecules* **2020**, *25*, 5227. [CrossRef]
19. Buff, M.C.R.; Schäfer, F.; Wulffen, B.; Müller, J.; Pötzsch, B.; Heckel, A.; Mayer, G. Dependence of aptamer activity on opposed terminal extensions: Improvement of light-regulation efficiency. *Nucleic Acids Res.* **2009**, *38*, 2111–2118. [CrossRef] [PubMed]
20. Kejnovská, I.; Renčiuk, D.; Palacký, J.; Vorlíčková, M. CD Study of the G-Quadruplex Conformation. *Methods Mol. Biol.* **2019**, *2035*, 25–44. [CrossRef]
21. Kypr, J.; Kejnovská, I.; Renciuk, D.; Vorlícková, M. Circular dichroism and conformational polymorphism of DNA. *Nucleic Acids Res.* **2009**, *37*, 1713–1725. [CrossRef]
22. Karsisiotis, A.I.; Hessari, N.M.; Novellino, E.; Spada, G.P.; Randazzo, A.; da Silva, M.W. Topological Characterization of Nucleic Acid G-quadruplexes by UV Absorption and Circular Dichroism. *Angew. Chem. Int. Ed. Engl.* **2011**, *50*, 10645–10648. [CrossRef]
23. Del Villar-Guerra, R.; Trent, J.O.; Chaires, J.B. G-Quadruplex Secondary Structure Obtained from Circular Dichroism Spectroscopy. *Angew. Chem. Int. Ed. Engl.* **2018**, *57*, 7171–7175. [CrossRef]
24. Riccardi, C.; Musumeci, D.; Krauss, I.R.; Piccolo, M.; Irace, C.; Paduano, L.; Montesarchio, D. Exploring the conformational behaviour and aggregation properties of lipid-conjugated AS1411 aptamers. *Int. J. Biol. Macromol.* **2018**, *118*, 1384–1399. [CrossRef]
25. Magbanua, E.; Zivkovic, T.; Hansen, B.; Beschorner, N.; Meyer, C.; Lorenzen, I.; Grötzinger, J.; Hauber, J.; Torda, A.E.; Mayer, G.; et al. d(GGGT)4and r(GGGU)4are both HIV-1 inhibitors and interleukin-6 receptor aptamers. *RNA Biol.* **2013**, *10*, 216–227. [CrossRef]

26. Largy, E.; Mergny, J.-L.; Gabelica, V. Role of Alkali Metal Ions in G-Quadruplex Nucleic Acid Structure and Stability. *Metal. Ions Life Sci.* **2016**, *16*, 203–258. [CrossRef]
27. Largy, E.; Marchand, A.; Amrane, S.; Gabelica, V.; Mergny, J.-L. Quadruplex Turncoats: Cation-Dependent Folding and Stability of Quadruplex-DNA Double Switches. *J. Am. Chem. Soc.* **2016**, *138*, 2780–2792. [CrossRef] [PubMed]
28. Bhattacharyya, D.; Arachchilage, G.M.; Basu, S. Metal Cations in G-Quadruplex Folding and Stability. *Front. Chem.* **2016**, *4*, 38. [CrossRef] [PubMed]
29. Zavyalova, E.; Tagiltsev, G.; Reshetnikov, R.; Arutyunyan, A.; Kopylov, A. Cation Coordination Alters the Conformation of a Thrombin-Binding G-Quadruplex DNA Aptamer That Affects Inhibition of Thrombin. *Nucleic Acid Ther.* **2016**, *26*, 299–308. [CrossRef] [PubMed]
30. Amato, T.; Virgilio, A.; Pirone, L.; Vellecco, V.; Bucci, M.; Pedone, E.; Esposito, V.; Galeone, A. Investigating the properties of TBA variants with twin thrombin binding domains. *Sci. Rep.* **2019**, *9*, 9184. [CrossRef]
31. Riccardi, C.; Meyer, A.; Vasseur, J.-J.; Krauss, I.R.; Paduano, L.; Morvan, F.; Montesarchio, D. Fine-tuning the properties of the thrombin binding aptamer through cyclization: Effect of the 5′-3′ connecting linker on the aptamer stability and anticoagulant activity. *Bioorg. Chem.* **2020**, *94*, 103379. [CrossRef] [PubMed]
32. Largy, E.; Mergny, J.-L. Shape matters: Size-exclusion HPLC for the study of nucleic acid structural polymorphism. *Nucleic Acids Res.* **2014**, *42*, e149. [CrossRef]
33. Marzano, M.; Falanga, A.P.; D'Errico, S.; Pinto, B.; Roviello, G.N.; Piccialli, G.; Oliviero, G.; Borbone, N. New G-Quadruplex-Forming Oligodeoxynucleotides Incorporating a Bifunctional Double-Ended Linker (DEL): Effects of DEL Size and ODNs Orientation on the Topology, Stability, and Molecularity of DEL-G-Quadruplexes. *Molecules* **2019**, *24*, 654. [CrossRef]
34. Alieva, R.R.; Zavyalova, E.G.; Tashlitsky, V.N.; Kopylov, A.M. Quantitative characterization of oligomeric state of G-quadruplex antithrombin aptamers by size exclusion HPLC. *Mendeleev Commun.* **2019**, *29*, 424–425. [CrossRef]
35. Zavyalova, E.G.; Legatova, V.A.; Alieva, R.S.; Zalevsky, A.O.; Tashlitsky, V.N.; Arutyunyan, A.M.; Kopylov, A.M. Putative Mechanisms Underlying High Inhibitory Activities of Bimodular DNA Aptamers to Thrombin. *Biomolecules* **2019**, *9*, 41. [CrossRef]
36. A Greenall, S.; McKenzie, M.; Seminova, E.; Dolezal, O.; Pearce, L.; Bentley, J.; Kuchibhotla, M.; Chen, S.C.; McDonald, K.L.; Kornblum, H.; et al. Most clinical anti-EGFR antibodies do not neutralize both wtEGFR and EGFRvIII activation in glioma. *Neuro Oncol.* **2019**, *21*, 1016–1027. [CrossRef]
37. Jing, N.; Sha, W.; Li, Y.; Xiong, W.; Tweardy, D. Rational Drug Design of G-Quartet DNA as Anti-Cancer Agents. *Curr. Pharm. Des.* **2005**, *11*, 2841–2854. [CrossRef]
38. Kovačič, M.; Podbevšek, P.; Tateishi-Karimata, H.; Takahashi, S.; Sugimoto, N.; Plavec, J. Thrombin binding aptamer G-quadruplex stabilized by pyrene-modified nucleotides. *Nucleic Acids Res.* **2020**, *48*, 3975–3986. [CrossRef]
39. Kogut, M.; Kleist, C.; Czub, J. Why do G-quadruplexes dimerize through the 5′-ends? Driving forces for G4 DNA dimerization examined in atomic detail. *PLoS Comput. Biol.* **2019**, *15*, e1007383. [CrossRef]
40. Kotkowiak, W.; Lisowiec-Wachnicka, J.; Grynda, J.; Kierzek, R.; Wengel, J.; Pasternak, A. Thermodynamic, Anticoagulant, and Antiproliferative Properties of Thrombin Binding Aptamer Containing Novel UNA Derivative. *Mol. Ther. Nucleic Acids* **2018**, *10*, 304–316. [CrossRef] [PubMed]
41. Virgilio, A.; Russo, A.; Amato, T.; Russo, G.; Mayol, L.; Esposito, V.; Galeone, A. Monomolecular G-quadruplex structures with inversion of polarity sites: New topologies and potentiality. *Nucleic Acids Res.* **2017**, *45*, 8156–8166. [CrossRef] [PubMed]
42. Tataurov, A.V.; You, Y.; Owczarzy, R. Predicting ultraviolet spectrum of single stranded and double stranded deoxy-ribonucleic acids. *Biophys. Chem.* **2008**, *133*, 66–70. [CrossRef] [PubMed]
43. Mergny, J.-L.; Lacroix, L. Analysis of Thermal Melting Curves. *Oligonucleotides* **2003**, *13*, 515–537. [CrossRef]
44. Van Meerloo, J.; Kaspers, G.J.L.; Cloos, J. Cell Sensitivity Assays: The MTT Assay. *Methods Mol. Biol.* **2011**, *731*, 237–245. [PubMed]

International Journal of
Molecular Sciences

MDPI

Article

Intracerebral Administration of a Ligand-ASO Conjugate Selectively Reduces α-Synuclein Accumulation in Monoamine Neurons of Double Mutant Human A30P*A53T*α-Synuclein Transgenic Mice

Rubén Pavia-Collado [1,2,3], Valentín Cóppola-Segovia [4], Lluís Miquel-Rio [1,2,3], Diana Alarcón-Aris [1,2], Raquel Rodríguez-Aller [5,6], María Torres-López [1,2], Verónica Paz [1,2,3], Esther Ruiz-Bronchal [1,2,3], Leticia Campa [1,2,3], Francesc Artigas [1,2,3], Andrés Montefeltro [6,7], Raquel Revilla [6,7] and Analia Bortolozzi [1,2,3,*]

1 Institut d'Investigacions Biomèdiques de Barcelona (IIBB), Spanish National Research Council (CSIC), 08036 Barcelona, Spain; ruben.pavia@iibb.csic.es (R.P.-C.); lluis.miquel@iibb.csic.es (L.M.-R.); d.alarcon@keval.es (D.A.-A.); maria.torres@iibb.csic.es (M.T.-L.); veronica.paz@iibb.csic.es (V.P.); esther.ruiz@iibb.csic.es (E.R.-B.); lcmnqi@iibb.csic.es (L.C.); fapnqi@iibb.csic.es (F.A.)
2 Institut d'Investigacions Biomèdiques August Pi i Sunyer (IDIBAPS), 08036 Barcelona, Spain
3 Centro de Investigación Biomédica en Red de Salud Mental (CIBERSAM), ISCIII, 28029 Madrid, Spain
4 Laboratory of Neurobiology and Redox Pathology, Department of Basic Pathology, Federal University of Paraná (UFPR), Curitiba 81531-980, Brazil; valen.coppola@gmail.com
5 CHU de Quebec Research Center, Axe Neurosciences. Department of Molecular Medicine, Faculty of Medicine, Université Laval, Quebec City, QC G1V 4G2, Canada; raquel.rodriguez-aller.1@ulaval.ca
6 CERVO Brain Research Centre, Quebec City, QC G1J 2G3, Canada; amontefeltro@lingeamc.com (A.M.); rrevilla@cubiqfoods.com (R.R.)
7 n-Life Therapeutics, S.L., 18100 Granada, Spain
* Correspondence: analia.bortolozzi@iibb.csic.es

Abstract: α-Synuclein (α-Syn) protein is involved in the pathogenesis of Parkinson's disease (PD). Point mutations and multiplications of the α-Syn, which encodes the *SNCA* gene, are correlated with early-onset PD, therefore the reduction in a-Syn synthesis could be a potential therapy for PD if delivered to the key affected neurons. Several experimental strategies for PD have been developed in recent years using oligonucleotide therapeutics. However, some of them have failed or even caused neuronal toxicity. One limiting step in the success of oligonucleotide-based therapeutics is their delivery to the brain compartment, and once there, to selected neuronal populations. Previously, we developed an indatraline-conjugated antisense oligonucleotide (IND-1233-ASO), that selectively reduces α-Syn synthesis in midbrain monoamine neurons of mice, and nonhuman primates. Here, we extended these observations using a transgenic male mouse strain carrying both A30P and A53T mutant human α-Syn (A30P*A53T*α-Syn). We found that A30P*A53T*α-Syn mice at 4–5 months of age showed 3.5-fold increases in human α-Syn expression in dopamine (DA) and norepinephrine (NE) neurons of the substantia nigra pars compacta (SNc) and locus coeruleus (LC), respectively, compared with mouse α-Syn levels. In parallel, transgenic mice exhibited altered nigrostriatal DA neurotransmission, motor alterations, and an anxiety-like phenotype. Intracerebroventricular IND-1233-ASO administration (100 µg/day, 28 days) prevented the α-Syn synthesis and accumulation in the SNc and LC, and recovered DA neurotransmission, although it did not reverse the behavioral phenotype. Therefore, the present therapeutic strategy based on a conjugated ASO could be used for the selective inhibition of α-Syn expression in PD-vulnerable monoamine neurons, showing the benefit of the optimization of ASO molecules as a disease modifying therapy for PD and related α-synucleinopathies.

Keywords: α-synuclein; antisense oligonucleotide; dopamine neurotransmission; double mutant A30P*A53T*; motor deficits; Parkinson's disease; transgenic mouse model

Citation: Pavia-Collado, R.; Cóppola-Segovia, V.; Miquel-Rio, L.; Alarcón-Aris, D.; Rodríguez-Aller, R.; Torres-López, M.; Paz, V.; Ruiz-Bronchal, E.; Campa, L.; Artigas, F.; et al. Intracerebral Administration of a Ligand-ASO Conjugate Selectively Reduces α-Synuclein Accumulation in Monoamine Neurons of Double Mutant Human A30P*A53T*α-Synuclein Transgenic Mice. *Int. J. Mol. Sci.* **2021**, *22*, 2939. https://doi.org/10.3390/ijms22062939

Academic Editor: Salvador F. Aliño

Received: 9 February 2021
Accepted: 11 March 2021
Published: 13 March 2021

1. Introduction

In the elderly population, Parkinson's disease (PD) is the second most common neurodegenerative disease after Alzheimer's disease [1,2]. The illness is characterized by a variety of motor dysfunctions including difficulties in initiating movements, bradykinesia, rigidity, and resting tremor. These signs result from a reduction in striatal dopamine (DA) neurotransmission, which accompanies progressive degeneration of DA neurons in the substantia nigra pars compacta (SNc) [3–6]. However, PD is also characterized by a premotor phase associated with the development of neuropsychiatric symptoms, cognitive deficits, among others, involving dysfunctions of non-DA neurons, e.g., serotonin (5-HT) and norepinephrine (NE) neurons, which precedes the development of motor symptoms [7,8]. Although the causes of PD are still poorly understood, genetic studies have identified two highly penetrant mutations, A30P and A53T, in α-synuclein (α-Syn), which encodes *SNCA* gene associated with autosomal dominant inheritance of the PD [9,10]. α-Syn is a highly conserved protein made up of 140 amino acid residues that is predominantly expressed in neurons, and is abundantly localized in presynaptic terminals, which plays a significant role in the regulation of neurotransmitter release, synaptic function, and neuroplasticity [11–13].

Accumulation of α-Syn in intracytoplasmic inclusions called Lewy bodies is a neuropathological hallmark of PD. Therefore, one approach to modelling the disease is to modify the mouse genome in order to over-express wild-type human α-Syn (h-α-Syn), as well as the PD-linked α-Syn mutants A53T, A30P, and E46K, or even combinations of them [14–19]. Indeed, Richfield et al. [20] introduced a transgenic mouse model carrying a double mutant h-α-Syn gene with both A30P and A53T point mutations under the tyrosine hydroxylase (TH) promoter (A30P*A53T*α-Syn). Aged A30P*A53T*α-Syn mice (13–23 months) successfully recapitulated many important features of α-synucleinopathy, including increased α-Syn expression, which adversely induced an age-dependent DA neurodegeneration and a decrease in the DA concentration in the striatal tissue, leading to deficits in motor coordination. Moreover, A30P*A53T*α-Syn mice showed swollen, dystrophic TH^+ neurites in the SNc, as well as accumulation of oligomeric α-Syn forms at 12 months, supporting the proposal that A30P*A53T*α-Syn mice may be used as a model to test new PD-modifying therapies that reduce α-Syn expression/accumulation [21,22].

In the last decade, remarkable advances in the development of oligonucleotide therapies aimed at inhibiting α-Syn synthesis have been made [23]. Gene silencing mechanisms targeting α-Syn mRNA may reduce the intracellular protein content and stop/slow the progression of the illness. Preclinical studies in rodents and nonhuman primates have successfully shown that α-Syn can be downregulated in PD-affected brain areas after direct application of oligonucleotide therapeutics including antisense oligonucleotides (ASO), small interfering RNAs (siRNA), and microRNAs (miRNA) [24–31]. Irrespective of these potential hitches, a major limitation in the development of oligonucleotide-based therapeutics is their delivery to the brain compartment, and once there, to selected neuronal populations or cell types. In an effort to solve this problem, we successfully developed a strategy to supply in vivo oligonucleotides selectively to brainstem monoamine neurons (DA, 5-HT, and NE). This was achieved by conjugating oligonucleotides with inhibitors of monoamine transporters (MAT) showing nM affinity for MAT, such as sertraline, reboxetine, and indatraline (IND), which are exclusively expressed in monoamine neurons at high densities [32–36]. MAT inhibitors allow the selective accumulation of oligonucleotides in monoamine neurons after internalization in deep Rab-7-associated vesicles [33,35].

Recently, we reported that intracerebroventricular or intranasal administration of an indatraline-conjugated 1233-ASO (IND-1233-ASO) can effectively reduce α-Syn protein accumulation in the brainstem monoamine neurons of wild-type mice and nonhuman primates, without causing neurotoxicity [34,36]. In the present study, we extended these observations and assessed whether an IND-1233-ASO sequence designed in such a way that the target mRNA sequence displays homology with the murine, rhesus macaque, and human α-Syn is able to downregulate h-α-Syn expression in DA and NE brain areas of

transgenic A30P*A53T*α-Syn mice. Furthermore, since the A30P and A53T familial point mutations in the *SNCA* gene are a risk factor for early-onset PD [9,10,37], we also examined the anxiety-depressive phenotype and cognitive abnormalities, as well as DA function in middle-aged mice (5 months), as these features have not been assessed in previous studies using this transgenic mouse model.

2. Results

*2.1. α-Syn Expression Profile in Brain Areas of A30P*A53T*α-Syn Transgenic Mice*

We first examined the expression of h-α-Syn and murine α-Syn (m-α-Syn) mRNAs in several cortical and subcortical brain areas of non-transgenic (non-Tg) and transgenic A30P*A53T*α-Syn mice (Figure 1a and Supplemental Figure S1). Using in situ hybridization, we found that h-α-Syn mRNA levels were more than 3-fold higher than m-α-Syn mRNA levels selectively in the brainstem nuclei containing DA and NE cell bodies in brain areas such as the SNc, ventral tegmental area—VTA and locus coeruleus—LC (SNc/VTA: 316.9% ± 18.3%; LC: 377.5% ± 22.5%, respectively, versus m-α-Syn mRNA levels) (Figure 1b). The Student's t-test indicated values of $t = 10.52$, $p < 0.0001$ for SNc/VTA and $t = 11.91$, $p < 0.0001$ for LC, respectively. Moreover, m-α-Syn mRNA expression was unchanged, and comparable values were detected in cortical and subcortical brain areas of non-Tg and transgenic A30P*A53T*α-Syn mice (Supplemental Figure S1b). In parallel, A30P*A53T*α-Syn mice showed also significant reductions in murine γ-synuclein (γ-Syn) mRNA expression in the SNc/VTA and LC compared with non-Tg mice ($t = 2.838$, $p = 0.0296$; $t = 3.005$, $p = 0.0239$, Student's *t*-test, respectively) (Figure 1c,d). The increases in h-α-Syn mRNA levels in the SNc/VTA and LC were confirmed by immunohistochemistry assessment of h-α-Syn protein levels (Figure 1e).

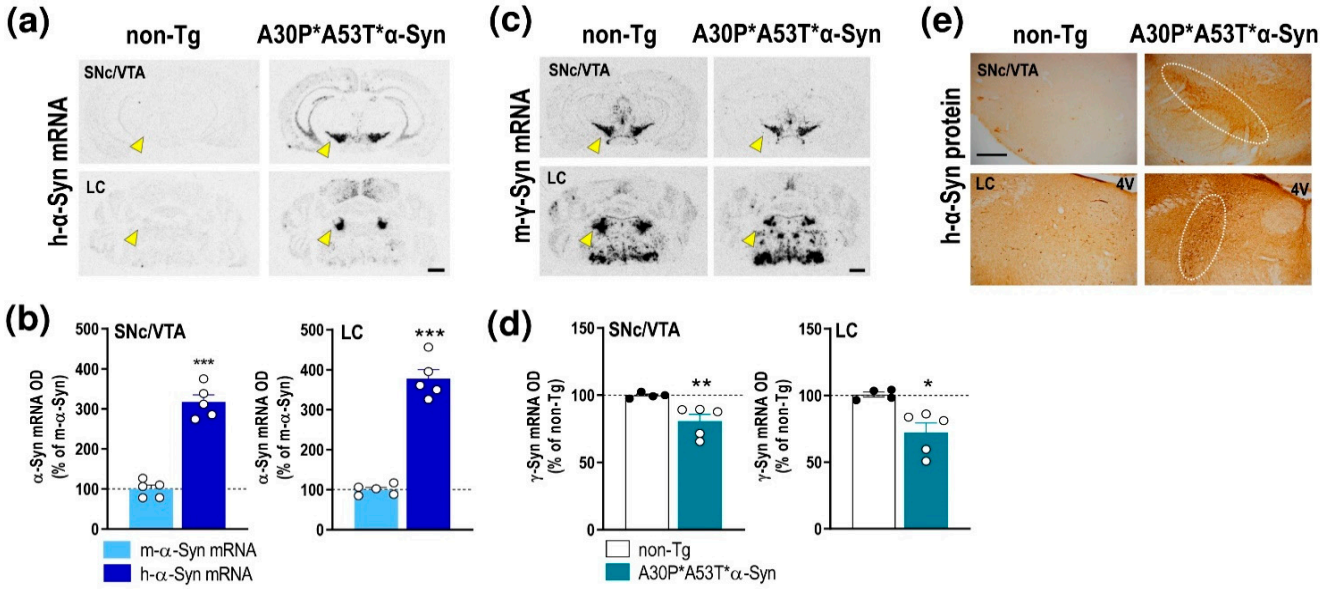

Figure 1. Profile of α-Syn expression in monoamine brain areas of A30P*A53T*α-Syn transgenic mice. (**a**) Coronal brain sections showing h-α-Syn mRNA levels in SNc/VTA assessed by in situ hybridization. Yellow arrowheads indicate the brain regions quantified in b. Scale bar: 1 mm. (**b**) Increased h-α-Syn mRNA expression in SNc/VTA and LC of A30P*A53T*α-Syn transgenic mice compared with m-α-Syn mRNA expression levels in the same mice ($n = 5$ mice/group; *** $p < 0.001$ vs. m-α-Syn mRNA levels; Student's *t*-test). (**c**) Coronal brain sections showing m-γ-Syn mRNA levels in SNc/VTA and LC assessed by in situ hybridization. Yellow arrowheads show the lower density of m-γ-Syn expression in A30P*A53T*α-Syn mice compared with non-Tg mice. Scale bar: 1 mm. (**d**) Reduced m-γ-Syn mRNA expression in SNc/VTA and LC of A30P*A53T*α-Syn transgenic mice compared with non-Tg mice ($n = 4$–5 mice/group; * $p < 0.05$, ** $p < 0.01$ versus non-Tg mice; Student's *t*-test). (**e**) Representative photomicrographs showing accumulated levels of h-α-Syn protein in SNc/VTA and LC of A30P*A53T*α-Syn transgenic mice. White frames indicate the SNc/VTA and LC brain regions. Scale bar: 200 µm. For all figures, data represent the mean ± SEM. Abbreviations: SNc, substantia nigra compacta; VTA, ventral tegmental area; LC, locus coeruleus; 4V, 4-ventricle. See also Supplemental Figure S1.

However, unlike the aged A30P*A53T*α-Syn mice (13–23 months), the middle-aged mice (5 months) did not show a loss of tyrosine hydroxylase $(TH)^+$ cells in the SNc, VTA and LC, nor were there any changes in TH density in the caudate putamen (CPu) compared with non-Tg mice (Figure 2a,b). Likewise, no alterations were found using other DA and NE neuronal markers, including the DA transporter (DAT) and NE transporter (NET) proteins, respectively. Histochemical analysis showed that the DAT density levels in SNc/VTA and CPu result in similar levels of immunoreactivity for both phenotypes (Figure 2c,d). In addition, the NET density was comparable in the LC and medial prefrontal cortex (mPFC) of A30P*A53T*α-Syn and non-Tg mice (Figure 2e,f). Altogether, these results indicate that A30P*A53T*α-Syn overexpression, and concomitant reduction in γ-Syn levels in the SNc/VTA and LC occurred in the absence of monoamine neurodegeneration, at least in middle-aged mice.

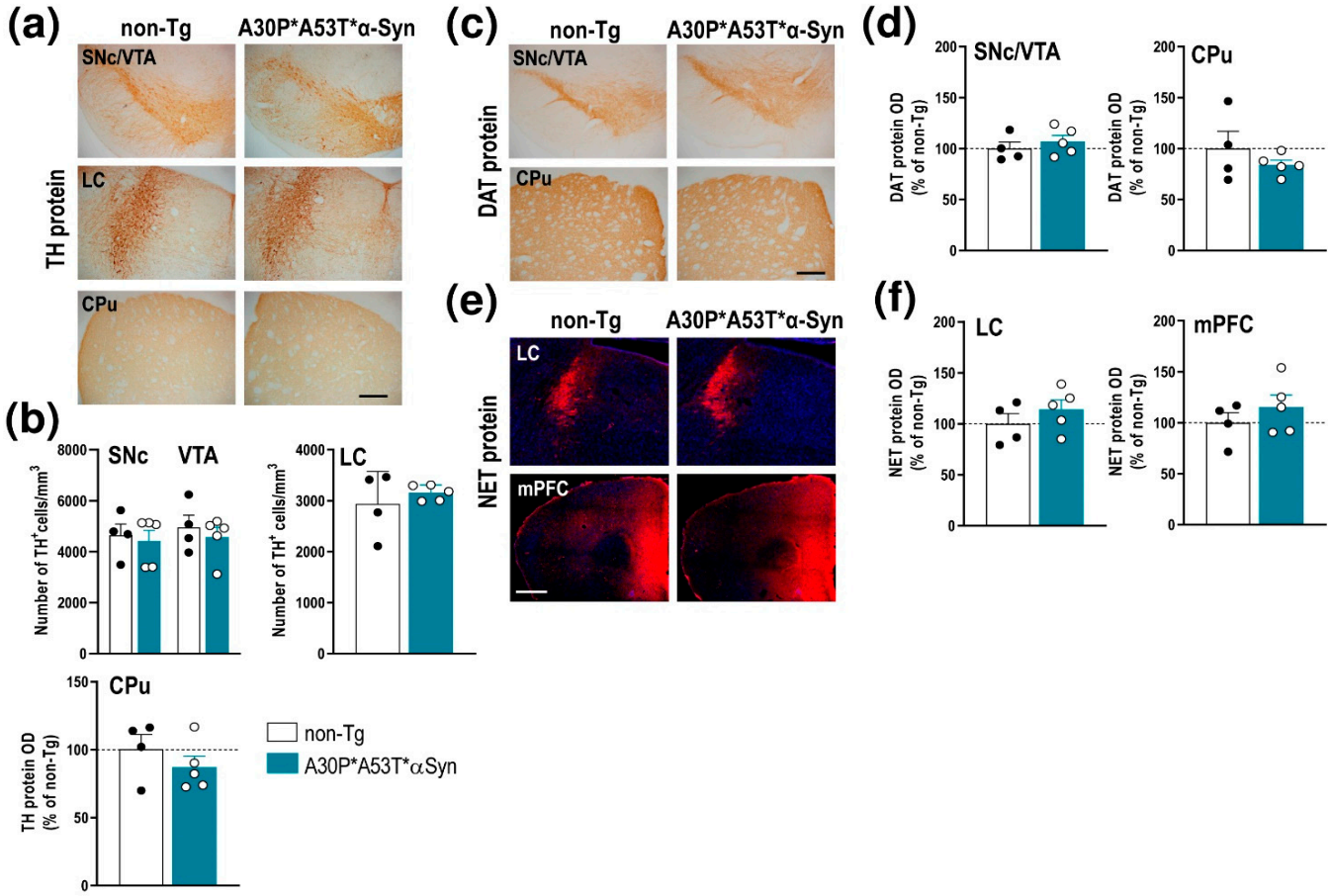

Figure 2. Integrity of DA and NE systems of middle-aged (5 months) A30P*A53T*α-Syn transgenic mice. (**a**) TH-immunostained brain sections containing SNc/VTA, LC and CPu. Scale bar: 200 µm. (**b**) No differences in the number of TH^+ neurons were found in the SNc, VTA or LC of A30P*A53T*α-Syn vs. non-Tg mice. Likewise, the density of striatal TH^+ terminals was comparable between both phenotypes. (**c**) DAT-immunostained brain sections containing SNc/VTA and CPu. Scale bar: 200 µm. (**d**) No differences in DAT protein density were found in the SNc, VTA or CPu of A30P*A53T*α-Syn vs. non-Tg mice. (**e**) Confocal images showing the NET protein density in LC and mPFC of A30P*A53T*α-Syn and non-Tg mice. Scale bar: 200 µm. (**f**) No differences in NET protein density were found in LC and mPFC of both phenotypes. Data are represented as mean ± SEM, n = 4–5 mice/group. Abbreviations: mPFC, medial prefrontal cortex; CPu, caudate putamen; HPC, hippocampus; SNc, substantia nigra compacta; VTA, ventral tegmental area; DR, dorsal raphe nucleus; LC, locus coeruleus.

*2.2. A30P*A53T*α-Syn Transgenic Mice Show Motor Deficits and an Anxiety-Like Phenotype*

To determine the functional consequences of A30P*A53T*α-Syn overexpression in SNc/VTA and LC, we performed a behavioral study assessing motor, emotional and cognitive components. Compared with non-Tg mice, A30P*A53T*α-Syn mice showed a reduced spontaneous locomotor activity as assessed in the open field test (Figure 3a,b). Differences were found between A30P*A53T*α-Syn and non-Tg mice in terms of total distance traveled, fast movements, mean speed, resting time, and vertical count. The total distance traveled and frequency of fast movements, but not slow movements, were significantly lower in A30P*A53T*α-Syn than non-Tg mice (t = 3.199, p = 0.0035; t = 2.675, p = 0.0125, Student's t-test, respectively). Likewise, A30P*A53T*α-Syn mice exhibited a reduced mean speed (t = 3.105, p = 0.0044, Student's t-test), and a longer resting time (t = 2.785, p = 0.0097, Student's t-test) compared with non-Tg mice. Vertical counts were also significantly lower in A30P*A53T*α-Syn mice than in non-Tg mice both in the open field test (Figure 3a, t = 2.91, p = 0.0074, Student's t-test) and cylinder test (Figure 3c, t = 2.397, p = 0.0247, Student's t-test). However, A30P*A53T*α-Syn mice showed no difference compared to non-Tg mice in motor asymmetry in the cylinder test as expected (Figure 3c).

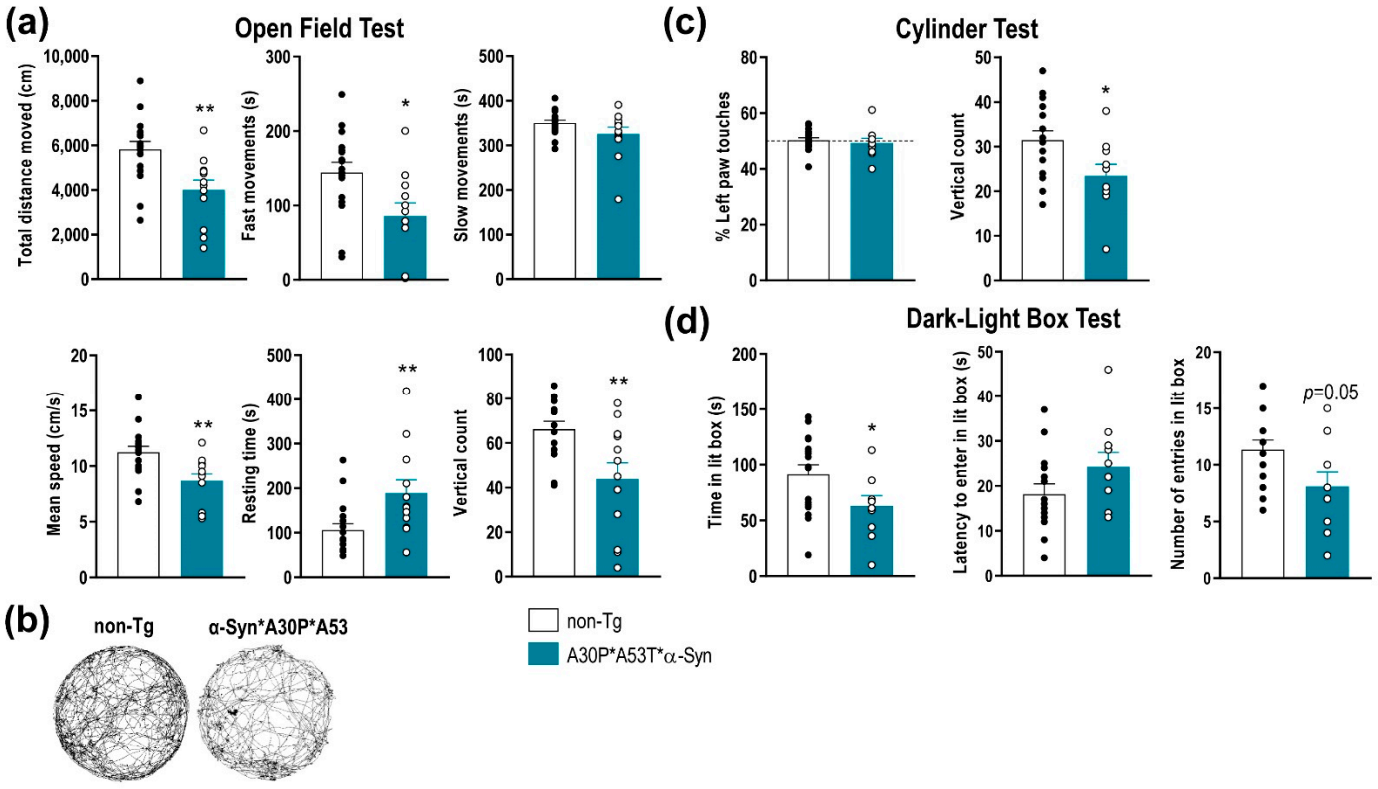

Figure 3. Impairment of motor function and anxiety-like behaviors in A30P*A53T*α-Syn transgenic mice. (**a**) Comparison of spontaneous locomotor activity between 5-month-old A30P*A53T*α-Syn and non-Tg mice in the open field test. Total distance traveled, fast movements, average speed and vertical count were significantly decreased in A30P*A53T*α-Syn mice compared with non-Tg mice. In parallel, transgenic mice showed an increased resting time compared with non-Tg mice. (**b**) Representative locomotor activity tracking was obtained from both phenotypes. (**c**) No difference in motor asymmetry examined by the use of the left paw was detected. However, A30P*A53T*α-Syn mice showed a reduced vertical count in the cylinder test compared with non-Tg mice. (**d**) In the dark-light box test, A30P*A53T*α-Syn transgenic mice evoked an anxiety-like response compared with non-Tg mice, as shown by the shorter spent time in the lit box but the marginal effects in the latency period to entering in the light box or the number of entries. Data are the mean ± SEM, n = 10–15 mice/group. Student's t-test, * $p < 0.05$, ** $p < 0.01$ compared with non-Tg mice. See also Supplemental Figure S2.

Mice were also tested using a dark-light box paradigm, a behavioral task assessing the anxiety-like phenotype (Figure 3d). The A30P*A53T*α-Syn mice showed a significant

reduction in time spent in the light box (t = 2.162, p = 0.0404, Student's t-test), and there were marginal effects on latency and the number of entries in the light box, suggesting an anxious phenotype compared with non-Tg mice. Nevertheless, no differences between both phenotypes were detected in the tail suspension test or in the novel object recognition, behavioral tasks assessing vulnerability/resilience to stress and short-term memory, respectively (Supplemental Figure S2).

2.3. A30P*A53T*α-Syn Overexpression in TH$^+$ Neurons Impairs DA Neurotransmission in the Nigrostriatal Pathway

The impact of the mutant α-Syn transgene overexpression on the nigrostriatal DA function was examined in 5-month-old A30P*A53T*α-Syn and non-Tg mice using in vivo microdialysis procedures. A30P*A53T*α-Syn transgenic mice showed no differences in baseline extracellular concentrations of DA and its 3,4-dihidroxyphenylacetic acid (DOPAC) metabolite in CPu compared with non-Tg mice (Table 1). However, infusion of the depolarizing agent veratridine (50 μM) by reverse dialysis increased extracellular DA in CPu to a lesser extend in A30P*A53T*α-Syn than in non-Tg mice (~2-fold versus ~6-fold, respectively) (Figure 4a). Two-way ANOVA followed by Tukey's post hoc test analysis showed a marginal effect of group $F_{(1,7)}$ = 3.993, p = 0.0858, and effect of time $F_{(15,105)}$ = 19.85, $p < 0.0001$ and a group-by-time interaction $F_{(15,105)}$ = 3.304, p = 0.0002.

Table 1. Baseline DA and DOPAC dialysate concentrations in the CPu of mice.

Mice	Experimental Conditions	Baseline DA	Baseline DOPAC
non-Tg	aCSF	10.3 ± 1.6 (15)	0.8 ± 0.1 (15)
	aCSF + DMSO 1%	7.2 ± 2.2 (4)	1.6 ± 0.4 (4)
A30P*A53T*α-Syn	aCSF	8.5 ± 1.2 (15)	1.1 ± 0.1 (15)
	aCSF + DMSO 1%	6.6 ± 1.7 (5)	1.8 ± 0.5 (5)

Extracellular DA and DOPAC levels are expressed as the fmol/20-min fraction. In the experiments involving the evaluation of the veratridine effect on extracellular DA and DOPAC levels, dimethyl-sulfoxide (DMSO) was added to the artificial cerebrospinal fluid (aCSF), respectively. Data are the mean ± SEM of the number of mice shown in parentheses.

Moreover, both α-Syn and γ-Syn proteins modulate membrane distribution and the reuptake function of DAT at DA terminals [19,34]. Local application of amphetamine (DA releaser and DAT inhibitor, 1–10 μM) dose-dependently elevated the dialysate DA concentration in the CPu, being significantly higher in A30P*A53T*α-Syn transgenic mice compared with non-Tg mice (Figure 4b). Two-way ANOVA showed effects of group $F_{(1,126)}$ = 7.828, p = 0.0060 and time $F_{(17,126)}$ = 6.235, $p < 0.0001$, and a marginal effect of group-by-time interaction $F_{(17,126)}$ = 1.560, p = 0.0849. However, no significant differences were observed in the extracellular DA concentration in the CPu between both phenotypes after local application of DAT inhibitor nomifensine (1–10 μM) (Figure 4c), suggesting that the greater DA elevation induced by amphetamine in A30P*A53T*α-Syn transgenic mice is not due to a differential expression/function of DAT. Two-way ANOVA showed an effect of time $F_{(17,162)}$ = 7.474, $p < 0.0001$, but not of group as well as a group-by-time interaction.

To obtain more information on the mechanisms controlling DA neurotransmission in the nigrostriatal pathways of A30P*A53T*α-Syn mice, we also examined the effect of the DA D2 receptor agonist quinpirole on DA release. Local quinpirole infusion (10 μM) by reverse dialysis comparably reduced the extracellular DA concentration in the CPu of non-Tg and A30P*A53T*α-Syn mice (Figure 4d). Two-way ANOVA showed an effect of time $F_{(17,144)}$ = 11.20, $p < 0.0001$, but not of group as well as a group-by-time interaction. No significant differences in extracellular DOPAC levels were observed between both phenotypes with the different pharmacological approaches used (data not shown) [19].

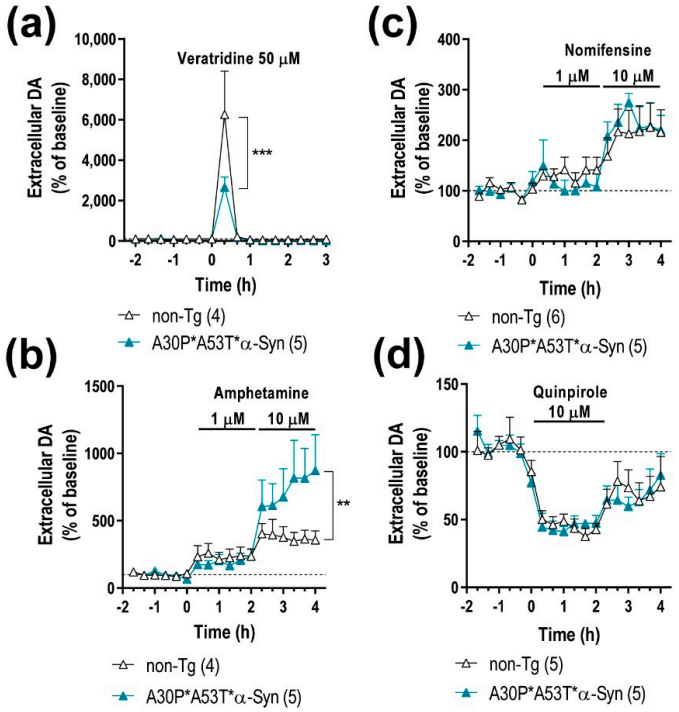

Figure 4. A30P*A53T*α-Syn overexpression in TH$^+$ neurons alters DA neurotransmission in the nigrostriatal pathway. (**a**) Local veratridine infusion (depolarizing agent; 50 µM) significantly increased DA release in the caudate putamen (CPu) of both mouse phenotypes. However, this effect was significant smaller in A30P*A53T*α-Syn mice than in non-Tg mice. (**b**) Direct application of amphetamine (DA releaser and DAT inhibitor; 1 and 10 µM) by reverse dialysis induced increases in DA release in the CPu, with the effect being significantly more pronounced in A30P*A53T*α-Syn mice than in non-Tg mice. (**c**) However, local nomifensine infusion (DAT inhibitor; 1 and 10 µM) dose-dependently increased the extracellular DA concentration in CPu, with this effect comparable being in both phenotypes. (**d**) Local activation of DA D2 receptors with quinpirole (DA D2 agonist, 10 µM) similarly decreased striatal DA release in A30P*A53T*α-Syn and non-Tg mice. Data are expressed as the mean ± SEM, n = 4–6 mice/group as indicated in the parenthesis. Two-way ANOVA and Tukey's multiple comparisons test, ** $p < 0.01$, *** $p < 0.001$ compared with non-Tg mice.

*2.4. ASO Therapy Reduces the Accumulation of Human α-Syn and Normalizes DA Neurotransmission Deficits but Not the Behavioral Phenotype in A30P*A53T*α-Syn Transgenic Mice*

Recently, we reported that IND-1233-ASO selectively reduced murine α-Syn expression in monoaminergic neurons of wild-type mice and nonhuman primates [34,36]. Likewise, the IND-1337-ASO sequence, designed specifically to target h-α-Syn in a PD-like mouse model overexpressing wild-type h-α-Syn induced by an adeno-associated viral vector, also prevented h-α-Syn accumulation in interconnected DA brain regions [36]. This specificity is due to the potent in vitro affinity and in vivo occupancy of IND for monoamine transporters [38], which allows the accumulation of the conjugated oligonucleotide in this neuronal population after intracerebroventricular or intranasal administration. Here, we extended these previous studies, and confirmed the intracellular accumulation of IND-conjugated oligonucleotides, specifically in TH$^+$ neurons of the SNc/VTA and LC of A30P*A53T*α-Syn mice after a single intracerebroventricular application of IND-1233-ASO (100 µg/mouse) (Figure 5a). In addition, IND-1233-ASO administration (100 µg/day for 28 days) significantly reduced mutant α-Syn transgene expression in the SNc/VTA and LC compared with A30P*A53T*α-Syn mice treated with a vehicle (Figure 5b). The reduction in h-α-Syn mRNA was ~54% and ~32% in the SNc/VTA and LC, respectively, compared to the level in A30P*A53T*α-Syn mice receiving a vehicle (Figure 5c). Two-way ANOVA showed an effect of treatment $F_{(1,12)} = 42.84$, $p < 0.0001$, α-Syn phenotype $F_{(1,12)} = 99.71$, $p < 0.0001$ and treatment-by- α-Syn phenotype interaction $F_{(1,12)} = 42.84$, $p < 0.0001$ for

SNc/VTA, as well as effects of treatment $F_{(1,12)} = 10.06$, $p = 0.0080$ and α-Syn phenotype $F_{(1,12)} = 157.3$, $p < 0.0001$ and a treatment-by-α-Syn phenotype interaction $F_{(1,12)} = 17.47$, $p = 0.0013$ for LC. Interestingly, IND-1233-ASO treatment did not alter m-α-Syn mRNA expression (Figure 5c). The decreased h-α-Syn mRNA level in the SNc/VTA and LC was accompanied by a significant decrease in the h-α-Syn protein level, as assessed by immunohistochemistry (SNc/VTA: $t = 3.047$, $p = 0.00226$, LC: $t = 5.812$, $p = 0.0011$, Student's t-test) (Figure 5d,e). Likewise, a lower number of h-α-Syn$^+$ cells was found in the SNc/VTA, but not in the LC, of A30P*A53T*α-Syn mice treated with IND-1233-ASO vs. those treated with the vehicle ($t = 7.163$, $p = 0.0004$, Student's t-test) (Figure 5e). Furthermore, h-α-Syn protein accumulation also decreased in brain areas with dense DA and NE innervation, such as the CPu (t = 2.809, $p = 0.0376$, Student's t-test) and mPFC ($t = 2.591$, $p = 0.0411$, Student's t-test) (Figure 5d,e).

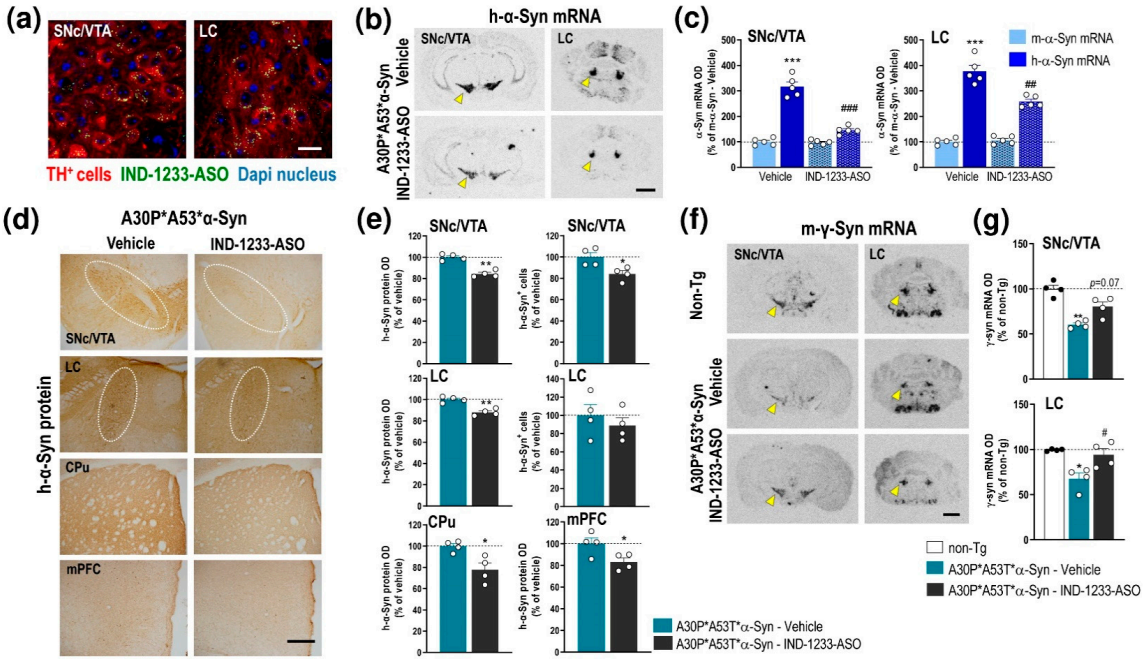

Figure 5. Intracerebroventricular IND-1233-ASO treatment selectively inhibits the expression and accumulation of h-α-Syn in interconnected DA and NE brain regions of A30P*A53T*α-Syn transgenic mice. (**a**) Confocal images showing the co-localization of A488-IND-1233-ASO (green) with TH$^+$ neurons (red) in the SNc/VTA and LC. Cell nuclei were stained with DAPI (blue). Scale bar: 10 µm. (**b**) Coronal brain sections showing reduced h-α-Syn mRNA expression in the SNc/VTA and LC of A30P*A53T*α-Syn mice treated with IND-1233-ASO (100 µg/day for 28 days), as assessed by in situ hybridization. Yellow arrowheads show h-α-Syn mRNA expression in SNc/VTA and LC. Scale bar: 1 mm. (**c**) Bar graphs showing significant reductions in h-α-Syn mRNA levels, but not m-α-Syn mRNA, in SNc/VTA and LC of IND-1233-ASO-treated A30P*A53T*α-Syn mice ($n = 5$ mice/group; *** $p < 0.001$ vs. m-α-Syn mRNA levels; $^{\#\#}$ $p < 0.01$, $^{\#\#\#}$ $p < 0.001$ vs. vehicle-treated A30P*A53T*α-Syn mice; two-way ANOVA and Tukey's multiple comparisons test). (**d**) Representative photomicrographs showing a lower h-α-Syn protein density in the SNc/VTA, LC, CPu and mPFC of IND-1233-ASO-treated A30P*A53T*α-Syn mice vs. vehicle-treated A30P*A53T*α-Syn mice. White frames indicate SNc/VTA and LC brain regions. Scale bar: 200 µm. (**e**) Bar graphs showing significant reductions in h-α-Syn protein levels in the brain areas analyzed, as well as a decreased number of h-α-Syn$^+$ cells in the SNc/VTA of IND-1233-ASO-treated A30P*A53T*α-Syn mice ($n = 4$ mice/group; * $p < 0.05$, ** $p < 0.01$ versus vehicle-treated A30P*A53T*α-Syn mice; Student's t-test). (**f**) Representative images showing increased m-γ-Syn mRNA expression in SNc/VTA and LC of A30P*A53T*α-Syn mice treated with IND-1233-ASO as assessed by in situ hybridization. Yellow arrowheads show m-γ-Syn mRNA expression in SNc/VTA and LC. Scale bar: 1 mm. (**g**) Bar graphs showing significant increases in m-γ-Syn expression in the LC and a marginal effect in the SNc/VTA of IND-1233-ASO-treated A30P*A53T*α-Syn mice ($n = 4$ mice/group; * $p < 0.05$, ** $p < 0.01$ vs. non-Tg mice; $^{\#}$ $p < 0.05$ vs. vehicle-treated A30P*A53T*α-Syn mice; one-way ANOVA). For all figures, data are the mean ± SEM. Abbreviations: mPFC, medial prefrontal cortex; CPu, caudate putamen; SNc, substantia nigra compacta; VTA, ventral tegmental area; LC, locus coeruleus. See also Supplemental Figure S3.

In parallel, the IND-1233-ASO-induced decrease in h-α-Syn expression normalized γ-Syn mRNA expression in the SNc/VTA (marginal effect) and LC of A30P*A53T*α-Syn mice compared to those mice treated with a vehicle (Figure 5f,g). One-way ANOVA showed an effect of group in SNc/VTA ($F_{(2,6)} = 14.01$, $p = 0.0055$) and LC ($F_{(2,7)} = 8.575$, $p = 0.0131$), respectively. Remarkably, IND-1233-ASO treatment did not induce any changes in TH, DAT, and NET protein levels in the SNc/VTA, or LC or in DA/NE projection brain areas, which supports the specificity and safety of the IND-1233-ASO sequence (Supplemental Figure S3). Similarly, IND-1233-ASO was well tolerated during the 4 weeks of treatment, and no changes were found in daily observed behavioral variables, such as water and food consumptions, as well as body weight in A30P*A53T*α-Syn transgenic mice compared to vehicle-treated A30P*A53T* α-Syn mice (data not shown), as previously reported [34,36].

Next, we found that A30P*A53T*α-Syn transgenic mice treated with IND-1233-ASO showed normalization of DA neurotransmission in the nigrostriatal pathway, reaching extracellular DA levels similar to those detected in non-Tg mice (Figure 4a,b and 6a,b). Local veratridine administration (50 μM) significantly increased striatal DA release in A30P*A53T*α-Syn mice treated with IND-1233-ASO compared with transgenic mice receiving a vehicle (Figures 4a and 6b). Two-way ANOVA showed an effect of time $F_{(15,80)} = 10.23$, $p < 0.0001$ and a group-by-time interaction $F_{(15,80)} = 2.021$, $p = 0.0235$, but no effect of group. Likewise, local amphetamine infusion (1–10 μM) increased extracellular DA levels to a lesser extent in the CPu of A30P*A53T*α-Syn mice treated with IND-1233-ASO compared with those treated with vehicle (Figures 4a and 6b). Two-way ANOVA showed an effect of group $F_{(1,72)} = 7.359$, $p = 0.0083$ and time $F_{(17,72)} = 4.231$, $p < 0.0001$, but no group-by-time interaction. However, despite the changes in DA neurotransmission, treatment with IND-1233-ASO for 28 days was insufficient to significantly reverse the behavioral impairments observed in A30P*A53T*α-Syn mice, and the mice exhibited motor alterations and anxiety-like behavior similar to those that received the vehicle (Figure 6c,d).

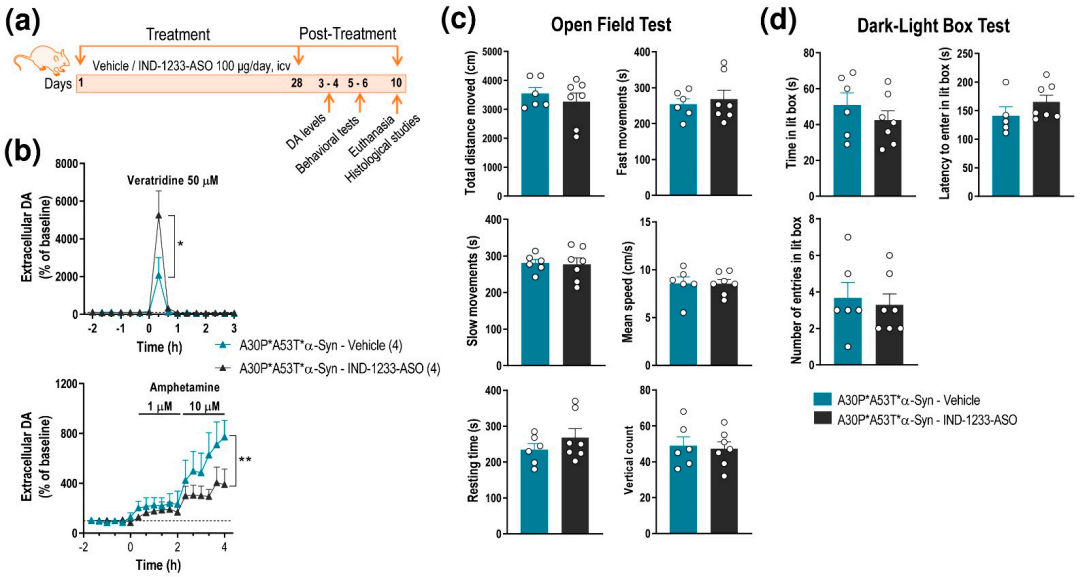

Figure 6. Intracerebroventricular IND-1233-ASO treatment recovers DA neurotransmission deficits, but not behavioral phenotype, in A30P*A53T*α-Syn transgenic mice. (**a**) Treatment timeline. A30P*A53T*α-Syn transgenic mice (4 months of age) received randomly vehicle or IND-1233-ASO (100 μg/day) into the lateral ventricle for 28 days using osmotic minipumps. In a group of mice, DA release was examined using intracerebral microdialysis at 3–4 days post-treatment, while behavioral tests were performed in an additional group at 5–6 days post-treatment. All mice were sacrificed on day 10 post-treatment. (**b**) Microdialysis approach using veratridine and amphetamine agents, as shown in Figure 3, confirmed the normalization of DA neurotransmission in the CPu of A30P*A53T*α-Syn mice treated with IND-1337-ASO (100 μg/day for 28 days) compared with transgenic mice treated with a vehicle. (**c**,**d**) No significant differences were detected in the open field test (**c**) or the dark-light box test (**d**) between both groups treated with IND-1337-ASO or a vehicle. Data are expressed as the mean ± SEM. Number of mice used in each procedure is indicated in parenthesis. Two-way ANOVA and Tukey's multiple comparisons test, * $p < 0.05$, ** $p < 0.01$ compared to A30P*A53T*α-Syn mice treated with a vehicle.

3. Discussion

The present study confirms and extends the results of previous studies on the benefit of a sustained therapy based on an IND-1233-ASO conjugate to reduce h-α-Syn expression selectively in early affected DA and NE brain areas –SNc/VTA and LC– in PD, as assessed in a transgenic mouse carrying both A30P and A53T mutant h-α-Syn. Remarkably, IND-1233-ASO also decreased h-α-Syn protein accumulation in DA/NE projection cortical and subcortical brain areas such as mPFC and CPu in the same mice. Likewise, no signs of toxicity were found in DA and NE neurons as assessed with classical DA and NE neuronal markers, in line with previous reports using wild-type mice and elderly nonhuman primates [34,36]. Human α-Syn knockdown in monoaminergic nuclei normalized the nigrostriatal DA neurotransmission in the A30P*A53T*α-Syn transgenic mice, although the current IND-1233-ASO therapy could not significantly reverse the behavioral phenotype, perhaps due to an insufficient time/dose and/or the involvement of downstream changes in relevant brain circuits not recovered by the treatment. Therefore, the current strategy of using ligand-oligonucleotide conjugates appears to have the potential for future optimization of new ligand-conjugated oligonucleotide-based therapies to treat PD and related α-synucleinopathies.

Selective reduction in h-α-Syn expression was found in the DA and NE brain regions of transgenic mice by exploiting our previous strategy, in which different oligonucleotide sequences were covalently bound to MAT inhibitors for the selective delivery of them to monoaminergic cells in vivo [32–36]. The potential use of oligonucleotide therapeutics, such as ASO, for brain illness has aroused a great deal of interest; however, delivery to the brain compartment remains a key obstacle. The issue is not simply getting oligonucleotides to the brain but getting them to specific brain cells and to intracellular sites where they actually function. Remarkably, the current IND-1233-ASO conjugate was capable to accumulate the 1233-ASO sequence in DA and NE neurons of A30P*A53T*α-Syn mice after intracerebroventricular administration, taking advantage of by the dense network of axons emerging from monoamine cell bodies containing the greatest DAT and NET densities, for which IND has a high in vitro affinity [38,39]. Both DAT and NET are subject to modulation by the α-Syn protein and, to a lesser extent, by γ-Syn in cellular trafficking models [40]. Although, the A30P*A53T*α-Syn transgenic mice showed upregulated h-α-Syn levels and concomitantly downregulated endogenous m-γ-Syn levels, with no change to m-α-Syn levels, the total density of DAT/NET in the SNc/VTA, LC, and brain projection areas was comparable to that of non-Tg mice. Likewise, DAT expression/function was similar in both phenotypes, since the DAT inhibitor nomifensine induces the same effect on DA uptake, which suggests that DAT is functionally active in transgenic mice and is capable of facilitating IND-1233-ASO accumulation in DA neurons. Indeed, our previous studies showed that a reduction in MAT expression/function by 50% still allowed ASOs/siRNAs conjugated with MAT inhibitors to be internalized efficiently into monoaminergic neurons through a Rab7-dependent endosomal mechanism [33–35].

In the present study, intracerebroventricular IND-1223-ASO treatment (100 µg/mouse/day, 28 days) prevented the accumulation of h-α-Syn mRNA and protein in the SNc/VTA and LC of transgenic mice, without affecting endogenous m-α-Syn mRNA level, unlike a previous study in which the IND-1233-ASO sequence reduced m-α-Syn expression in wild-type mice [34]. The 1233-ASO sequence was designed to efficiently target homologous α-Syn mRNAs, including those of mice, monkeys and humans, as described previously in models expressing a single α-Syn phenotype [34,36]. Therefore, it is conceivable that the 1233-ASO sequence interacts with a different binding potency against homologous α-Syn mRNAs expressed at different concentrations in the same biological system as was used here, where h-α-Syn mRNA has 3.5-fold greater expression than that of m-α-Syn mRNA. Moreover, the high efficiency of the silencing depends on the stability of the mRNA/DNA oligonucleotide hetero-duplex, perhaps higher for h-α-Syn vs. m-α-Syn mRNA, as previously reported [41].

In any case, the 30–40% decrease in h-α-Syn mRNA levels obtained after intracerebroventricular treatment did not induce DA and NE neurotoxicity nor striatal and cortical denervation as assessed by TH, DAT or NET immunohistochemistry. However, using short-hairpin RNA (shRNA) cloned in adeno-associated viral (AAV) vector to knockdown α-Syn (>80% of decrease), some reports indicated DA neurodegeneration and loss of striatal DA fibers in rats and nonhuman primates [42–45], suggesting the need to maintain a threshold for α-Syn knockdown since this protein is essential for neurotransmission homeostasis, among other biological functions. These data are important in the context of ongoing attempts to develop PD therapeutics targeting α-Syn expression. Although viral vector-mediated antisense therapies such as AAV, are useful for delivering antisense/shRNA sequences into cells; currently, they have certain issues involving (i) genome integration, (ii) the inability to be delivered repeatedly, and (iii) possible host rejection. Alternatives to viral strategies are currently being developed based on non-viral oligonucleotides (siRNA, ASO, miRNA). Non-viral approaches are biologically safer and much less immunogenic than viral vectors [46–49]. Conversely, for non-viral oligonucleotides to be effective, they must achieve delivery to affected regions or cells at appropriate concentrations. Furthermore, they must be stable requiring additional protection measures (end-blocking, base modification, etc.), and maintain efficacy over time for feasible treatment throughout the course of disease [49–51]. More recently, there is a surge of interest in the delivery of oligonucleotides to specific cell types in the brain using ligand-oligonucleotide conjugates as reported here. This cellular selectivity may be achieved by conjugating oligonucleotides to a ligand that interacts selectively with a receptor/transporter expressed in the cellular surface. Some ligand candidates that demonstrate high affinity and selectivity for brain receptors include anisamide or anandamide, ligands that bind to the sigma or cannabinoid receptors, respectively, providing effective functional delivery of ASO/siRNA to several neuronal types [52,53]. However, none of these studies allowed the delivery of oligonucleotides to specific neuronal populations. In contrast, we successfully developed a strategy to supply in vivo oligonucleotides selectively to brainstem monoamine neurons ([32–36] and present study). Therefore, although the conjugated ligand-oligonucleotide approach is still under development, it offers a promising pathway for oligonucleotide therapeutics for brain diseases.

Previous studies showed that the A30P*A53T*α-Syn transgenic mouse line on the same genetic background (C57BL/6J, α-Syn-39 line) used here exhibits significant age-dependent abnormalities in the locomotor activity from 7 months onwards [20,22]. Furthermore, the presence of the pathogenic A53T*α-Syn mutation in different lines of transgenic mice led to the development of severe motor impairment resulting in death at 8–12 months of age, while in younger animals altered motor activity and anxiety-like behaviors have also been reported [14,15,18,19]. These behavioral changes have been associated with a reduced tissue DA concentration and impaired synaptic plasticity seen within the basal ganglia prior to obvious neurodegeneration [19,54]. Our results also clearly showed that the A30P*A53T*α-Syn overexpression in the DA and NE brain areas leads to motor deficits and anxiety-like behaviors but not depressive-like phenotype nor cognitive dysfunction, in 5-month-old transgenic mice. In parallel, the A30P*A53T*α-Syn mice exhibited an altered DA neurotransmission in the nigrostriatal pathways (the effects on NE release were not assessed because of a lack of ability to perform adequate high-performance liquid chromatography-HPLC methods in our laboratory), without DA and NE neurodegeneration. These above observations emphasize the fact that the behavioral phenotype of DA deficits is not only a result of cell death and denervation, but that functionally impaired neurons contribute to the outcome and should be considered as a target for treatment. Thus, a potential attenuation of α-Syn expression/function could contribute to the reduction in deficits in DA neurotransmission, since α-Syn modulates neuronal DA activity [34]. In fact, IND-1233-ASO treatment (100 µg/mouse/day, 28 days) not only prevented h-α-Syn protein accumulation in SNc/VTA, LC, and anatomically connected brain areas but also recovered the DA neurotransmission, allowing it to reach the levels of non-Tg mice and normalize

the expression of m-γ-Syn, which is reduced in A30P*A53T*α-Syn mice. However, this was not sufficient to improve the behavioral phenotype, suggesting a need to improve the pharmacokinetic and pharmacodynamic properties of conjugated oligonucleotide-based therapies, which are still poorly known, but which have far-reaching implications for dosing regimens and clinical efficacy.

A key observation in the present study is that the overexpression of A30P*A53T*α-Syn had opposing effects on DA release in the nigrostriatal terminals after pharmacological stimulation. The depolarizing agent veratridine induced a lower increase in extracellular DA in A30P*A53T*α-Syn mice than in non-Tg mice, whereas amphetamine (DA releaser and DAT inhibitor) produced robust increases in extracellular DA levels in both groups, which were greater in A30P*A53T*α-Syn mice. The effects of veratridine on DA release are in full agreement with previous findings which indicated that nigrostriatal terminals of α-Syn-deficient mice display standard tonic DA activity after electrical stimulation with single pulses; however, they exhibited increased DA release with paired stimuli that elevated intracellular Ca^{2+} levels and vice versa in mice overexpressing α-Syn [55]. Indeed, we also demonstrated that the overexpression of wild-type h-α-Syn in the SNc using an AAV vector or in transgenic mice leads to less veratridine-dependent DA release, although the basal DA levels did not change compared with control groups [34,36].

In contrast, striatal amphetamine application significantly increased DA release in A30P*A53T*α-Syn mice compared with non-Tg mice, unlike in another wild-type α-Syn overexpression mouse models [34,36]. Given that DAT expression/function was comparable in both groups of mice (e.g., similar effect of the DAT inhibitor nomifensine), the differences between veratridine and amphetamine may be due to differences in DA releasable pools in A30P*A53T*α-Syn mice. Hence, while veratridine releases the impulse-dependent DA vesicular pool, amphetamine also releases a cytoplasmic, impulse-independent DA pool. Overall, these data suggest that there is impaired DA storage in the synaptic vesicles of A30P*A53T*α-Syn transgenic mice. This possibility is consistent with the role of α-Syn in regulating synaptic vesicle release or uptake at the monoamine terminals. In vitro studies have shown that both wild-type α-Syn and the mutant A30P*α-Syn attenuated DAT function, as well as DAT trafficking away from the plasma membrane. Interestingly, the mutant A53T*α-Syn was unable to modulate DAT function, and subsequent studies showed that this protein only very weakly interacted with the transporter [40,56,57]. Early studies also reported that the A53T* mutant can modulate the vesicular monoamine transporter (VMAT2) [56,58]. In MESC2.10 human mesencephalic cells, the presence of the A53T* mutant decreased the expression of VMAT2, accompanied by decreased potassium-induced and increased amphetamine-induced DA release, respectively [59]. These observations suggest that the A53T*α-Syn, through its effects on VMAT2, impairs vesicular DA storage and release. Altogether, this evidence supports the different in vivo effects on extracellular DA of nomifensine (DAT inhibitor) and amphetamine (DA releaser and DAT inhibitor) in A30P*A53T*α-Syn mice. In line with this observation, amphetamine-induced locomotor activity was increased in the A30P*A53T*α-Syn mouse line at 6 months of age [22].

In conclusion, the cellular selectivity and efficacy obtained with IND-1233-ASO indicate that the ligand-oligonucleotide approach has great potential to reduce wild-type and mutant human α-Syn expression specifically in monoamine neurons, with a high translational value for the treatment of PD and other α-synucleinopathies. The reduction in α-Syn synthesis did not cause monoaminergic neurodegeneration and actually improved forebrain DA neurotransmission. This study shows the benefit of optimizing conjugated ASO molecules as a disease-modifying therapy for PD, something that might be attractive in conjunction with current immunotherapy trials targeting α-Syn protein, or those with anti-aggregation agents.

4. Materials and Methods

4.1. Animals

Adult male C57BL/6J transgenic mice carrying both A30P and A53T mutant human α-Syn under TH promotor (A30P*A53T*α-Syn-39Eric/J referred to as A30P*A53T*α-Syn, 4–5 months; The Jackson Laboratory, USA) were housed under standard laboratory conditions (12 h light/dark cycle; room temperature, 23 ± 2 °C; relative humidity 50 ± 15%) with food and water available ad libitum. In addition, non-transgenic littermates with the same genetic background were used as the control group (referred to as non-Tg). We used 105 mice for the whole study. Animal procedures were conducted in accordance with standard ethical guidelines (EU directive 2010/63 of 22 September 2010) and approved by the local ethical committee (University of Barcelona).

4.2. Conjugated Antisense Oligonucleotide

The synthesis and purification of indatraline-conjugated ASO molecule targeting α-Syn (IND-1233-ASO, GenBank accession AH008229.3, NCBI, Bethesda, MD, USA) were performed by nLife therapeutics S.L., as previously reported [32,33]. ASO consistent of an antisense GapMer of 18-mer single stranded DNA molecule with four 2′-*O*-methyl RNA bases at both ends to protect the internal DNA from nuclease degradation and improve the binding to the target mRNA. The sequence of IND-1233-ASO is 5′-cuccdCdTdCdCdAdCdTdGdTdCuucu-3′, where chemical modifications of the backbone including 2′-*O*-methyl are shown in lowercase letters, while "d" indicates the presence of 2′-deoxynucleotides (Supplemental Figure S4). In brief, ASO synthesis was performed using ultra mild-protected phosphoramidites (Glen Research, Sterling, VA, USA) and an H-8 DNA/RNA automatic synthesizer (K&A Laborgeraete GbR, Schaafheim, Germany). Indatraline hydrochloride (triple blocker of monoamine transporters) was conjugated to 5′-carboxy-C10 modified oligonucleotide through an amide bond. This condensation was carried out under organic conditions (DIPEA/DMF, 24 h). Conjugated oligonucleotides were purified by high performance liquid chromatography (HPLC) using a RP-C18 column (4.6 × 150 mm, 5 μm) under a linear gradient condition of acetonitrile. The molecular weight of the oligonucleotide strands was confirmed by MALDI-TOF mass spectrometry (Ultra-flex, Bruker Daktronics, Billerica, MA, USA). The concentration of conjugated sequences was calculated based on the absorbance at a wavelength of 260 nm. In addition, to study the in vivo brain distribution and intracellular incorporation of IND-1233-ASO into DA and NE neurons, IND-1233-ASO molecules were additionally bound to fluorophore Alexa488 as previously reported [33,34]. Stock ASO solutions were prepared in RNAse-free water and stored at −20 °C until use.

4.3. Mouse Treatments

For intracerebroventricular administration, mice underwent pentobarbital anesthetization (40 mg/kg, intraperitoneal) and were placed in a stereotaxic frame. Buprenorphine (0.05 mg/kg, subcutaneous) was used as an analgesic. A micro-osmotic pump (Alzet Model 1004, Durect Corporation, Cupertino, CA, USA) was subcutaneously implanted, while the cannula (Brain Infusion Kit 3, Alzet) was implanted in the lateral ventricle (antero-posterior −0.34, medial-lateral −1.0 and dorsal-ventral −2.2 in mm) [34,60]. Micro-pumps were filled with IND-1233-ASO (37.87 mg/mL). Alzet model 1004 osmotic pumps deliver an average infusion of 0.11 μL/h (2.64 μL/day) for 28 days, providing an IND-1233-ASO dose of 100 μg/day (16.3 nmol/day). We also added a control group that received the vehicle (2.64 μL/day, artificial cerebrospinal fluid, in nM: NaCl, 125; KCl, 2.5; $CaCl_2$, 1.26 and $MgCl_2$, 1.18 with 5% glucose). The IND-1233-ASO sequence has been extensively characterized in previous studies, and the dose was chosen because it was safe without signs of neuronal and glial toxicity compared within IND-conjugated nonsense ASO sequence (IND-1227-ASO) [34,36].

To confirm the accumulation of IND-1233-ASO in DA and NE neurons, some mice (n = 3) received a single dose of IND-1233-ASO linked to Alexa488 (100 µg, 2.5 µL) in the lateral ventricle, and the mice were sacrificed 24 h later, as previously reported [33,34].

Mice were randomly assigned to treatment groups. After surgery, the animals were kept in individualization cages and the well-being of each mouse was monitored for the duration of the procedure. The body weight and general appearance of the mice were controlled according to Morton and Griffiths protocols [61].

4.4. In Situ Hybridization

Mice were killed by pentobarbital overdose and brains were rapidly removed, frozen on dry ice and stored at −80 °C. Coronal brain sections containing the SNc, VTA, LC, and projection brain areas including mPFC, hippocampus (HPC), and CPu (14 µm-thick) were obtained and processed, as described elsewhere [32,33]. Antisense oligonucleotides were complementary to bases, as follows: mouse α-Syn (m-α-Syn, 411-447 sequence, GenBank accession NM_001042451), human α-Syn (h-α-Syn, 2498-2548 sequence, NM_000345), and mouse γ-Syn (m-γ-Syn, 366-416 sequence, NM_011430 (IBA Nucleic Acids Synthesis). Oligonucleotides were individually labeled (2 pmol) at the 3′-end with ^{33}P-dATP (>2500 Ci/mmol; DuPont-NEN) using terminal deoxynucleotidyl-transferase (TdT, Calbiochem). For hybridization, the radioactively labeled probes were diluted in a solution containing 50% formamide, 4× standard saline citrate, 1× Denhardt's solution, 10% dextran sulfate, 1% sarkosyl, 20 mM phosphate buffer, pH 7.0, 250 µg/mL yeast tRNA, and 500 µg/mL salmon sperm DNA. The final concentrations of radioactive probes in the hybridization buffer were in the same range (~1.5 nM). Tissue sections were covered with hybridization solution containing the labeled probes, overlaid with para-film coverslips and, incubated overnight at 42 °C in humid boxes. Sections were washed four times (45 min each) in a buffer containing 0.6 M NaCl and 10 mM Tris-HCl (pH 7.5) at 60 °C. Hybridized sections were exposed to Biomax-MR film (Kodak, Sigma-Aldrich, Madrid, Spain) for 24–72 h with intensifying screens. For specificity control, adjacent sections were incubated with an excess (50×) of unlabeled probes. Films were analyzed and relative optical densities were evaluated in three adjacent sections in duplicate for each mouse and averaged to obtain individual values using a computer-assisted image analyzer (MCID, Mering, Germany). The MCID system was also used to acquire black and white images. Figures were prepared for publication using Adobe Photoshop software (Adobe Software, San José, CA, USA). Contrast and brightness of images were the only variables that were adjusted digitally.

4.5. Immunohistochemistry and Immunofluorescence

Mice were anaesthetized with pentobarbital and transcardially perfused with 4% paraformaldehyde (PFA) in sodium-phosphate buffer (pH 7.4). Brains were extracted, post-fixed 24 h at 4 °C in the same solution, and placed in gradient sucrose solution 10–30% for 3 days at 4 °C. After cryopreservation, serial 30 µm-thick sections were cut to obtain SNc, VTA, LC, mPFC and CPu. Brain sections were washed and incubated in a 1x PBS/Triton 0.2% solution containing normal serum from the secondary antibody host. Primary antibodies for h-α-Syn (anti-h-α-Syn clone Syn211, 1:1350; ref.: MA1-12874, Thermo Fisher Scientific, Waltham, MA, USA), DAT (anti-DAT, 1:2500 for SNc/VTA and 1:5000 for CPu; ref.: MAB369, Millipore, Burlington, MA, USA), and TH (anti-TH, 1:5000; ref.: AB112, Abcam, Cambridge, UK) were used. Briefly, primary antibodies were incubated overnight at 4 °C, followed by incubation with the corresponding biotinylated anti-mouse IgG1 (1:200, ref.: A-10519, Life Technologies, Carlsbad, CA, USA) for anti-h-α-Syn, biotinylated anti-rat IgG (1:200, ref.: BA-9401, Vector Laboratories, Burlingame, CA, USA) for anti-DAT, and biotinylated anti-rabbit IgG (1:200; ref.: BA-1000, Vector Laboratories) for anti-TH according to the manufacturer's instructions. The color reaction was performed thorugh incubation with diaminobenzidine tetrahydrochloride (DAB) (ref.: D5905-50TAB, Sigma-

Aldrich) solution. Sections were mounted and embedded in Entellan (Electron Microscopy Sciences, Hatfield, PA, USA).

In addition, primary antibodies included mouse anti-NET (1:1000, ref.: NET05-2 clone 2-3B2scD7, Mab Technologies, Stone Mountain, GA, USA). Slides were washed multiple times with PBS and incubated with fluorescently labeled secondary antibody A555 anti-mouse IgG (1:500, ref.: A-21427, Life Technologies) for 2 h at room temperature. Immunofluorescent slides were treated for 10 min with Hoechst dye (1:10,000) before the final PBS wash and cover-slipping with Fluoromont Aqueous Mounting Medium (Sigma-Aldrich, F4680).

The number of TH-positive cells and h-α-Syn-positive cells and their intracellular densities in the SNc/VTA and LC were assessed in sections corresponding to different antero-posterior levels −2.70 to −3.80 mm and −5.34 to −5.80 mm from the bregma, respectively using ImageJ software (v1.51s, NIH, Bethesda, MD, USA). All labeled cells with its nucleus within the counting frame were bilaterally counted in six consecutive SNc/VTA and three consecutive LC sections, and three different microscope fields were analyzed in each section. In addition, the intensity of h-α-Syn labelling in the CPu and mPFC, as well as the DAT density in SNc/VTA and CPu, and NET density in LC and mPFC were quantified in four consecutive sections corresponding to different antero-posterior levels (mm from bregma): 2.34 to 1.70 for mPFC, 1.70 to 0.02 for CPu, −2.70 to −3.80 for the SNc/VTA and −5.34 to −5.80 for LC, respectively, using ImageJ software (v1.51s).

4.6. Confocal Fluorescence Microscopy

Mice were sacrificed 24 h after intracerebroventricular Alexa-488 labelled IND-1233-ASO administration, and their brains were extracted and processed for immunofluorescence. Brain sections were rinsed with PBS/Triton 0.2%, incubated with normal serum from the secondary antibody host and treated with primary antibody rabbit anti-TH (1:1250; ref.: AB112, Abcam). Sections were then incubated overnight at 4 °C, rinsed and treated with secondary Alexa555-conjugated antibody (donkey anti-rabbit; 1:500; ref.: A-31572, Life Technologies) for 2 h. After subsequent washes, the sections were dehydrated, and mounted in the anti-fading agent Prolong Gold with DAPI (Life Technologies). DAPI, Alexa488 and Alexa555 images were acquired sequentially using a Leica TCS SP5 laser scanning confocal microscope (Leica Microsystems Heidelberg GmbH, Manheim, Germany) with excitation at 405, 488 nm and 553 nm laser line, respectively. Images were obtained at 400Hz in a 1024 × 1024 pixels format and were composed using ImageJ software (v1.51s).

4.7. In Vivo Microdialysis

Extracellular DA and DOPAC concentrations in the nigrostriatal pathway were measured by in vivo microdialysis as described elsewhere [34,36]. One concentric dialysis probe (Cuprophan membrane; 6000 Da molecular weight cut-off; 2 mm-long) was implanted in the mouse CPu (antero-posterior 0.5, medial-lateral −1.7 and dorsal-ventral −4.5, in mm) [60]. Experiments were performed 24–48 h after surgery in freely moving mice. In addition, the transgenic A30P*A53T*α-Syn mice treated with IND-1233-ASO or a vehicle (intracerebroventricular using osmotic mini-pumps) also had a guide cannula (CMA 7, ref.: CMAP000138, Harvard Apparatus, Holliston, MA, USA) implanted into the CPu. A dummy cannula was inserted into the guide cannula to avoid contamination, and this was fixed with screws. The day prior to the microdialysis experiments, the dummy cannula was removed and replaced with a 2 mm long microdialysis probe (CMA 7 microdialysis probe, ref.; CMAP000083, Harvard Apparatus). Microdialysis experiments were performed by an experimenter who was blinded to mouse treatments. DA and DOPAC levels in dialysate samples were analyzed using HPLC coupled with electrochemical detection (+0.7 V, Waters 2465, Milford, MA, USA), with 3-fmol detection limit. The mobile phase containing 0.15 M $NaH_2PO_4.H_2O$, 0.9 mM PICB8, 0.5 mM EDTA (pH 2.8 adjusted with orthophosphoric acid), and 10% methanol was pumped at 1 mL/min (Waters 515 HPLC pump). DA and DOPAC

were separated on a 2.6 µm particle size C18 column (7.5 × 0.46 cm, Kinetex, Phenomenex, Torrance, CA, USA) at 28 °C.

All reagents used were of analytical grade and were obtained from Merck (Darmstadt). DA hydrochloride, DOPAC acid, (–)-quinpirole hydrochloride, and nomifensine maleate were sourced from Sigma-Aldrich-RBI. D-amphetamine sulphate and veratridine were purchased from Tocris. To assess the local drug effects, compounds were dissolved in artificial cerebrospinal fluid (in mM: NaCl, 125; KCl, 2.5; $CaCl_2$, 1.26 and $MgCl_2$, 1.18) and administered by reverse dialysis at the stated concentrations (uncorrected for membrane recovery).

4.8. Behavioral Testing

Behavioral analyses were performed in non-Tg and A30P*A53T*α-Syn mice with intervals of 1–7 days between tests. Different behavioral paradigms were used to evaluate motor and cognitive functions as well as anxiety- and depressive phenotype. All tests were performed between 10:00 and 15:00 h by an experimenter who was blinded to mouse treatments. On the test day, mice were placed in a dimly illuminated behavioral room and were left undisturbed for at least 1 h before testing [33,36].

Open field test. Motor activity was measured in four Plexiglas open field boxes (35 × 35 × 40 cm) that were indirectly illuminated (25–40 lux) to avoid reflection and shadows. The floor of the open field boxes was covered with an interchangeable opaque plastic base that was replaced for each animal. Motor activity was recorded for 15 min by a camera connected to a computer (Video-track, Viewpoint, Lyon, France) [62]. The following variables were measured: horizontal locomotor and exploratory activity, defined as the total distance moved in cm including fast/large (speed > 10.5 cm/s) and slow/short movements (speed 3–10.5 cm/s), as well as the activation time including the mean speed (cm/s) and resting time (s), and the number of rearings.

Cylinder test. Mice were tested for motor asymmetry in the cylinder test. Each mouse was placed in an acrylic cylinder (diameter, 15 cm; height, 27 cm), and the total number of left and right forepaw touches performed, as well as the number of rearings in 5 min was counted. Behavioural equipment was cleaned with water after each test session to avoid olfactory cues.

Dark-light box test. The apparatus consisted of two glass boxes (27 × 21 cm) with an interconnecting grey plastic tunnel (7 × 10 cm). One of these boxes was painted in black and was weakly lit with a red 25-W bulb (42 lux). The other box was lit with a 60-W desk lamp (400 lux) placed 30 cm above the box, which provided the unique laboratory illumination condition. At the beginning of the test, mice were placed individually in the middle of the dark area facing away from the opening, and were videotaped for 5 min. The following variables were recorded: (a) time spent in the lit box, (b) the latency of the initial movement from the dark to the lit box, and (c) the number of entries in the lit box. A mouse was considered to enter the new area when all four legs were in this area. The floor of each box was cleaned between the mice.

Tail suspension test. Mice were suspended 30 cm above the floor by adhesive tape placed approximately 1 cm from the tip of the tail. Sessions were videotaped for 6 min and the immobility time was measured (Smart, Panlab, Cornellà, Spain).

Novelty object recognition test. Mice were placed into an open field box of Plexiglas (40 × 35 × 16 cm) with a soured of illumination (60 lux) in the center of the box. Two objects of identical shape were used as familiar objects. During the habituation period, the mice could freely explore the open field box without objects for 10 min on two consecutive days. In the acquisition test, the two identical objects were placed separately in the center of the open field and the mice explored it for 10 min. To minimize the presence of olfactory traces, the objects and the open field were cleaned with water between each trial. Twenty-four hours after the acquisition test, one of the familiar objects was replaced with a new object, and the amount of time spend exploring both objects (familiar and novel) was recorded for

a period of 10 min. Exploration of an object was defined as pointing the nose at an object at a distance of <1 cm and/or touching it.

4.9. Statistical Analysis

All values are expressed as the mean ± standard error of the mean (SEM). Statistical comparisons were performed using GraphPad Prism 8.01 (GraphPad software, Inc., San Diego, CA, USA) using the appropriate statistical tests, as indicated in each figure legend. Outlier values were identified by the Grubbs' test (i.e., Extreme Student zed Deviate, ESD, method) using GraphPad Prism software and excluded from the analysis when applicable. Differences among means were analyzed by either 1- or 2-way analysis of variance (ANOVA) or the two-tailed Student's *t*-test, as appropriate. When ANOVA showed significant differences, pairwise comparisons between means were subjected to Tukey's post hoc test or Sidak's multiple comparisons test, as appropriate. Differences were considered significant at $p < 0.05$.

Supplementary Materials: Supplementary materials can be found at https://www.mdpi.com/1422-0067/22/6/2939/s1.

Author Contributions: Conceptualization and supervision of the research, A.B. Design of the conjugated oligonucleotides, F.A., A.M., R.R. and A.B. Methodology: R.P.-C., D.A.-A. and R.R.-A. performed behavioral and microdialysis experiments; V.C.-S. and L.M.-R. performed immunohistochemistry experiments; M.T.-L. performed confocal microscopy experiments; R.P.-C., V.P. and E.R.-B. performed in situ hybridization experiments; L.C. performed DA and DOPAC determinations using HPLC. Writing, A.B. with all 12 authors providing imput. Funding acquisition, R.R. and A.B. All authors have read and agreed to the published version of the manuscript.

Funding: This study was supported by grants SAF2016-75797-R, PID2019-105136RB-100, Retos-Colaboración Subprogram RTC-2015-3309-1, Ministry of Economy and Competitiveness (MINECO) and European Regional Development Fund (ERDF), UE; and CB/07/09/0034 Center for Networked Biomedical Research on Mental Health (CIBERSAM).

Institutional Review Board Statement: The study was conducted according to the guidelines of the Declaration of Helsinki, and approved by Ethical Committee of Animal Experimentation of the University of Barcelona (protocol codes 9628/9832, approved on April 2017/November 2017, expiration date April 2023/March 2023).

Informed Consent Statement: Not applicable.

Data Availability Statement: The data presented in this study area available on request from the corresponding author. The data are not publicly available due to privacy.

Acknowledgments: We thank M. Calvo and E. Coll for outstanding technical support in the confocal microscopy unit (CCiT-UB). We thank to the Coordenação de Aperfeiçõamento de Nivel Superior (CAPES- PDSE: 19/2016 88881.135527/2016-01), Brazil, for their financial support via a scholarship awarded to V.C.-S. We also thank to JAE-Intro Program, CSIC (JAEINT_20_02116), Spain, for their financial support via a scholarship awarded to M.T.-L.

Conflicts of Interest: R. Revilla, A. Montefeltro, F. Artigas, and A. Bortolozzi are the authors of the patent WO/2011/131693 issued for the siRNA and ASO molecules and the targeting approach related to this work. R. Revilla is board members of nLife Therapeutics S.L. A. Montefeltro is a stockholder of nLife Therapeutics S.L. The rest of the authors declare no competing interests.

References

1. Braak, H.; Del Tredici, K.; Bohl, J.; Bratzke, H.; Braak, E. Pathological changes in the parahippocampal region in select non-Alzheimer's dementias. *Ann. N. Y. Acad. Sci.* **2000**, *911*, 221–239. [CrossRef]
2. Reeve, A.; Simcox, E.; Turnbull, D. Ageing and Parkinson's disease: Why is advancing age the biggest risk factor? *Ageing Res. Rev.* **2014**, *14*, 19–30. [CrossRef]
3. Braak, H.; Gai, W.P.; Del Tredici, K. Idiopathic Parkinson's disease: Possible routes by which vulnerable neuronal types may be subject to neuroinvasion by an unknown pathogen. *J. Neural Transm.* **2003**, *110*, 517–536. [CrossRef]

4. Li, J.Y.; Englund, E.; Holton, J.L.; Soulet, D.; Hagell, P.; Lees, A.J.; Lashley, T.; Quinn, N.P.; Rehncrona, S.; Björklund, A.; et al. Lewy bodies in grafted neurons in subjects with Parkinson's disease suggest host-to-graft disease propagation. *Nat. Med.* **2008**, *14*, 501–503. [CrossRef]
5. Desplats, P.; Lee, H.J.; Bae, E.-J.; Patrick, C.; Rockenstein, E.; Crews, L.; Spencer, B.; Masliah, E.; Lee, S.-J. Inclusion formation and neuronal cell death through neuron-to-neuron transmission of -synuclein. *Proc. Natl. Acad. Sci. USA* **2009**, *106*, 13010–13015. [CrossRef]
6. Kordower, J.H.; Brundin, P. Propagation of host disease to grafted neurons: Accumulating evidence. *Exp. Neurol.* **2009**, *220*, 224–225. [CrossRef] [PubMed]
7. Kish, S.J.; Tong, J.; Hornykiewicz, O.; Rajput, A.; Chang, L.J.; Guttman, M.; Furukawa, Y. Preferential loss of serotonin markers in caudate versus putamen in Parkinson's disease. *Brain* **2007**, *131*, 120–131. [CrossRef]
8. Wilson, H.; Dervenoulas, G.; Pagano, G.; Koros, C.; Yousaf, T.; Picillo, M.; Polychronis, S.; Simitsi, A.; Giordano, B.; Chappell, Z.; et al. Serotonergic pathology and disease burden in the premotor and motor phase of A53T α-synuclein parkinsonism: A cross-sectional study. *Lancet Neurol.* **2019**, *18*, 748–759. [CrossRef]
9. Polymeropoulos, M.H.; Lavedan, C.; Leroy, E.; Ide, S.E.; Dehejia, A.; Dutra, A.; Pike, B.; Root, H.; Rubenstein, J.; Boyer, R.; et al. Mutation in the alpha-synuclein gene identified in families with Parkinson's disease. *Science* **1997**, *276*, 2045–2047. [CrossRef]
10. Krüger, R.; Kuhn, W.; Müller, T.; Woitalla, D.; Graeber, M.; Kösel, S.; Przuntek, H.; Epplen, J.T.; Schöls, L.; Riess, O. Ala30Pro mutation in the gene encoding alpha-synuclein in Parkinson's disease. *Nat. Genet.* **1998**, *18*, 106–108. [CrossRef] [PubMed]
11. George, J.M.; Clayton, D.F. Songbirds, synelfin, and neurodegenerative disease. *Neurosci. News* **1998**, *1*, 12–17.
12. Murphy, D.D.; Rueter, S.M.; Trojanowski, J.Q.; Lee, V.M.Y. Synucleins Are Developmentally Expressed, and α-Synuclein Regulates the Size of the Presynaptic Vesicular Pool in Primary Hippocampal Neurons. *J. Neurosci.* **2000**, *20*, 3214–3220. [CrossRef] [PubMed]
13. Scott, D.; Roy, S. α-Synuclein inhibits intersynaptic vesicle mobility and maintains recycling-pool homeostasis. *J. Neurosci.* **2012**, *32*, 10129–10135. [CrossRef] [PubMed]
14. Gispert, S.; Del Turco, D.; Garrett, L.; Chen, A.; Bernard, D.J.; Hamm-Clement, J.; Korf, H.W.; Deller, T.; Braak, H.; Auburger, G.; et al. Transgenic mice expressing mutant A53T human alpha-synuclein show neuronal dysfunction in the absence of ag-gregate formation. *Mol. Cell Neurosci.* **2003**, *24*, 419–429. [CrossRef]
15. Giasson, B.I.; Duda, J.E.; Quinn, S.M.; Zhang, B.; Trojanowski, J.Q.; Lee, V.M.-Y. Neuronal α-Synucleinopathy with Severe Movement Disorder in Mice Expressing A53T Human α-Synuclein. *Neuron* **2002**, *34*, 521–533. [CrossRef]
16. Emmer, K.L.; Waxman, E.A.; Covy, J.P.; Giasson, B.I. E46K Human α-Synuclein Transgenic Mice Develop Lewy-like and Tau Pathology Associated with Age-dependent, Detrimental Motor Impairment. *J. Biol. Chem.* **2011**, *286*, 35104–35118. [CrossRef]
17. Ikeda, M.; Kawarabayashi, T.; Harigaya, Y.; Sasaki, A.; Yamada, S.; Matsubara, E.; Murakami, T.; Tanaka, Y.; Kurata, T.; Wuhua, X.; et al. Motor impairment and aberrant production of neurochemicals in human α-synuclein A30P+A53T transgenic mice with α-synuclein pathology. *Brain Res.* **2009**, *1250*, 232–241. [CrossRef] [PubMed]
18. Lee, M.K.; Stirling, W.; Xu, Y.; Xu, X.; Qui, D.; Mandir, A.S.; Dawson, T.M.; Copeland, N.G.; Jenkins, N.A.; Price, D.L. Human alpha-synuclein-harboring familial Parkinson's disease-linked Ala-53 –> Thr mutation causes neurodegenerative disease with alpha-synuclein aggregation in transgenic mice. *Proc. Natl. Acad. Sci. USA* **2002**, *25*, 8968–8973. [CrossRef]
19. Oaks, A.W.; Frankfurt, M.; Finkelstein, D.I.; Sidhu, A. Age-dependent effects of A53T alpha-synuclein on behavior and do-paminergic function. *PLoS ONE* **2013**, *8*, e60378. [CrossRef]
20. Richfield, E.K.; Thiruchelvam, M.J.; Cory-Slechta, D.A.; Wuertzerc, C.; Gainetdinov, R.R.; Caron, M.G.; Di Monte, D.A.; Federoff, H.J. Behavioral and Neurochemical Effects of Wild-Type and Mutated Human α-Synuclein in Transgenic Mice. *Exp. Neurol.* **2002**, *175*, 35–48. [CrossRef]
21. Thiruchelvam, M.J.; Powers, J.M.; Cory-Slechta, D.A.; Richfield, E.K. Risk factors for dopaminergic neuron loss in human α-synuclein transgenic mice. *Eur. J. Neurosci.* **2004**, *19*, 845–854. [CrossRef]
22. Kilpeläinen, T.; Julku, U.H.; Svarcbahs, R.; Myöhänen, T.T. Behavioural and dopaminergic changes in double mutated human A30P*A53T alpha-synuclein transgenic mouse model of Parkinson's disease. *Sci. Rep.* **2019**, *9*, 17382. [CrossRef]
23. Sardi, S.P.; Cedarbaum, J.M.; Brundin, P. Targeted Therapies for Parkinson's Disease: From Genetics to the Clinic. *Mov. Disord.* **2018**, *33*, 684–696. [CrossRef] [PubMed]
24. Lewis, J.; Melrose, H.; Bumcrot, D.; Hope, A.; Zehr, C.; Lincoln, S.; Braithwaite, A.; Heather, M.; Ogholikhan, S.; Hinkle, K.; et al. In vivo silencing of alpha-synuclein using naked siRNA. *Mol. Neurodegener.* **2008**, *3*, 19. [CrossRef]
25. Junn, E.; Lee, K.W.; Jeong, B.S.; Chan, T.W.; Im, J.Y.; Mouradian, M.M. Repression of -synuclein expression and toxicity by microRNA-7. *Proc. Natl. Acad. Sci. USA* **2009**, *106*, 13052–13057. [CrossRef] [PubMed]
26. McCormack, A.L.; Mak, S.K.; Henderson, J.M.; Bumcrot, D.; Farrer, M.J.; Di Monte, D.A. Alpha-synuclein suppression by targeted small interfering RNA in the primate substantia nigra. *PLoS ONE* **2010**, *5*, e12122. [CrossRef] [PubMed]
27. Zharikov, A.; Bai, Q.; De Miranda, B.R.; Van Laar, A.; Greenamyre, J.T.; Burton, E.A. Long-term RNAi knockdown of α-synuclein in the adult rat substantia nigra without neurodegeneration. *Neurobiol. Dis.* **2019**, *125*, 146–153. [CrossRef]
28. Cole, T.; Paumier, K.; Zhao, H.; Weinhofen, A.; Kordasiewicz, H.; Swyze, E. Snca targeted antisense oligonucleotides mediate progression of pathological deposition in alpha synuclein rodent transmission models of Parkinson's disease. *Neurology* **2016**, *86*, P6.239.

29. Helmschrodt, C.; Höbel, S.; Schöniger, S.; Bauer, A.; Bonicelli, J.; Gringmuth, M.; Fietz, S.A.; Aigner, A.; Richter, A.; Richter, F. Polyethylenimine Nanoparticle-Mediated siRNA Delivery to Reduce α-Synuclein Expression in a Model of Parkinson's Disease. *Mol. Ther. Nucleic Acids* **2017**, *9*, 57–68. [CrossRef]
30. Nakamori, M.; Junn, E.; Mochizuki, H.; Mouradian, M.M. Nucleic acid-based therapeutics for Parkinson's disease. *Neutherapeutics* **2019**, *16*, 287. [CrossRef]
31. Spencer, B.; Trinh, I.; Rockenstein, E.; Mante, M.; Florio, J.; Adame, A.; El-Agnaf, O.M.A.; Kim, C.; Masliah, E.; Rissman, R.A. Systemic peptide mediated delivery of a siRNA targeting a-synuclein in the CNS ameliorates the neurodegenerative process in a transgenic model of Lewy body disease. *Neurobiol. Dis.* **2019**, *127*, 163–177. [CrossRef] [PubMed]
32. Bortolozzi, A.; Castañé, A.; Semakova, J.; Santana, N.; Alvarado, G.; Cortés, R.; Ferrés-Coy, A.; Fernández, G.; Carmona, M.C.; Toth, M.; et al. Selective siRNA-mediated suppression of 5-HT1A autoreceptors evokes strong anti-depressant-like effects. *Mol. Psychiatry* **2012**, *17*, 612–623. [CrossRef]
33. Ferrés-Coy, A.; Galofré, M.; Pilar-Cuéllar, F.; Vidal, R.; Paz, V.; Ruiz-Bronchal, E.; Campa, L.; Pazos, A.; Caso, J.R.; Leza, J.C.; et al. Therapeutic antidepressant potential of a conjugated siRNA silencing the serotonin transporter after intranasal administration. *Mol. Psychiatry* **2016**, *21*, 328–338. [CrossRef]
34. Alarcón-Arís, D.; Recasens, A.; Galofré, M.; Carballo-Carbajal, I.; Zacchi, N.; Ruiz-Bronchal, E.; Pavia-Collado, R.; Chica, R.; Ferrés-Coy, A.; Santos, M.; et al. Selective α-synuclein knockdown in monoamine neurons by intranasal oligonucleotide de-livery: Potential therapy for Parkinson's disease. *Mol. Ther.* **2018**, *26*, 550–567. [CrossRef] [PubMed]
35. Fullana, M.N.; Ferrés-Coy, A.; Ortega, J.E.; Ruiz-Bronchal, E.; Paz, V.; Meana, J.J.; Artigas, F.; Bortolozzi, A. Selective Knockdown of TASK3 Potassium Channel in Monoamine Neurons: A New Therapeutic Approach for Depression. *Mol. Neurobiol.* **2018**, *56*, 3038–3052. [CrossRef]
36. Alarcón-Arís, D.; Pavia-Collado, R.; Miquel-Rio, L.; Coppola-Segovia, V.; Ferrés-Coy, A.; Ruiz-Bronchal, E.; Galofré, M.; Paz, V.; Campa, L.; Revilla, R.; et al. Anti-α-synuclein ASO delivered to monoamine neurons prevents α-synuclein accumulation in a Parkinson's disease-like mouse model and in monkeys. *EBioMedicine* **2020**, *59*, 102944. [CrossRef] [PubMed]
37. Fernagut, P.-O.; Chesselet, M.-F. Alpha-synuclein and transgenic mouse models. *Neurobiol. Dis.* **2004**, *17*, 123–130. [CrossRef] [PubMed]
38. Lengyel, K.; Pieschl, R.; Strong, T.; Molski, T.; Mattson, G.; Lodge, N.J.; Li, Y.-W. Ex vivo assessment of binding site occupancy of monoamine reuptake inhibitors: Methodology and biological significance. *Neuropharmacology* **2008**, *55*, 63–70. [CrossRef]
39. Javitch, J.; Strittmatter, S.; Snyder, S. Differential visualization of dopamine and norepinephrine uptake sites in rat brain using [3H]mazindol autoradiography. *J. Neurosci.* **1985**, *5*, 1513–1521. [CrossRef] [PubMed]
40. Oaks, A.W.; Sidhu, A. Synuclein modulation of monoamine transporters. *FEBS Lett.* **2011**, *585*, 1001–1006. [CrossRef]
41. Nishina, K.; Piao, W.; Yoshida-Tanaka, K.; Sujino, Y.; Nishina, T.; Yamamoto, T.; Nitta, K.; Yoshioka, K.; Kuwahara, H.; Yasuhara, H.; et al. DNA/RNA heteroduplex oligonucleotide for highly efficient gene silencing. *Nat. Commun.* **2015**, *6*, 7969. [CrossRef] [PubMed]
42. Gorbatyuk, O.S.; Li, S.; Nash, K.; Gorbatyuk, M.; Lewin, A.S.; Sullivan, L.F.; Mandel, R.J.; Chen, W.; Meyers, C.; Manfredsson, F.P.; et al. In Vivo RNAi-Mediated α-Synuclein Silencing Induces Nigrostriatal Degeneration. *Mol. Ther.* **2010**, *18*, 1450–1457. [CrossRef]
43. Khodr, C.E.; Sapru, M.K.; Pedapati, J.; Han, Y.; West, N.C.; Kells, A.P.; Bankiewicz, K.S.; Bohn, M.C. An α-synuclein AAV gene silencing vector ameliorates a behavioral deficit in a rat model of Parkinson's disease, but displays toxicity in dopamine neurons. *Brain Res.* **2011**, *1395*, 94–107. [CrossRef] [PubMed]
44. Collier, T.J.; Redmond, D.E., Jr.; Steece-Collier, K.; Lipton, J.W.; Manfredsson, F.P. Is alpha-synuclein loss-of-function a con-tributor to parkinsonian pathology? Evidence from non-human primates. *Front. Neurosci.* **2016**, *10*, 12. [CrossRef] [PubMed]
45. Benskey, M.J.; Sellnow, R.C.; Sandoval, I.M.; Sortwell, C.E.; Lipton, J.W.; Manfredsson, F.P. Silencing Alpha Synuclein in Mature Nigral Neurons Results in Rapid Neuroinflammation and Subsequent Toxicity. *Front. Mol. Neurosci.* **2018**, *11*, 36. [CrossRef]
46. Hardee, C.L.; Arévalo-Soliz, L.M.; Hornstein, B.D.; Zechiedrich, L. Advances in non-viral DNA vectors for gene therapy. *Genes* **2017**, *8*, 65. [CrossRef]
47. Imbert, M.; Dias-Florencio, G.; Goyenvalle, A. Viral Vector-Mediated Antisense Therapy for Genetic Diseases. *Genes* **2017**, *8*, 51. [CrossRef] [PubMed]
48. Nyamay'Antu, A.; Dumont, M.; Kedinger, V.; Erbacher, P. Non-Viral Vector Mediated Gene Delivery: The Outsider to Watch Out For in Gene Therapy. *Cell Gene Ther. Insights* **2019**, *5*, 51–57. [CrossRef]
49. Smith, C.E.; Zain, R. Therapeutic Oligonucleotides: State of the Art. *Annu. Rev. Pharmacol. Toxicol.* **2019**, *59*, 605–630. [CrossRef]
50. Juliano, R.L. The delivery of therapeutic oligonucleotides. *Nucleic Acids Res.* **2016**, *44*, 6518–6548. [CrossRef]
51. Doxakis, E. Therapeutic antisense oligonucleotides for movement disorders. *Med. Res. Rev.* **2020**, 1–33. [CrossRef]
52. Nakagawa, O.; Ming, X.; Huang, L.; Juliano, R.L. Targeted Intracellular Delivery of Antisense Oligonucleotides via Conjugation with Small-Molecule Ligands. *J. Am. Chem. Soc.* **2010**, *132*, 8848–8849. [CrossRef]
53. Willibald, J.; Harder, J.; Sparrer, K.; Conzelmann, K.-K.; Carell, T. Click-Modified Anandamide siRNA Enables Delivery and Gene Silencing in Neuronal and Immune Cells. *J. Am. Chem. Soc.* **2012**, *134*, 12330–12333. [CrossRef] [PubMed]
54. Kurz, A.; Double, K.L.; Lastres-Becker, I.; Tozzi, A.; Tantucci, M.; Bockhart, V.; Bonin, M.; García-Arencibia, M.; Nuber, S.; Schlaudraff, F.; et al. A53T-Alpha-Synuclein Overexpression Impairs Dopamine Signaling and Striatal Synaptic Plasticity in Old Mice. *PLoS ONE* **2010**, *5*, e11464. [CrossRef] [PubMed]

55. Abeliovich, A.; Schmitz, Y.; Fariñas, I.; Choi-Lundberg, D.; Ho, W.H.; Castillo, P.E.; Shinsky, N.; Verdugo, J.M.G.; Armanini, M.; Ryan, A.; et al. Mice Lacking α-Synuclein Display Functional Deficits in the Nigrostriatal Dopamine System. *Neuron* **2000**, *25*, 239–252. [CrossRef]
56. Sidhu, A.; Wersinger, C.; Vernier, P. Does α-synuclein modulate dopaminergic synaptic content and tone at the synapse? *FASEB J.* **2004**, *18*, 637–647. [CrossRef] [PubMed]
57. Wersinger, C.; Prou, D.; Vernier, P.; Niznik, H.B.; Sidhu, A. Mutations in the lipid-binding domain of α-synuclein confer overlapping, yet distinct, functional properties in the regulation of dopamine transporter activity. *Mol. Cell. Neurosci.* **2003**, *24*, 91–105. [CrossRef]
58. Lotharius, J.; Brundin, P. Pathogenesis of Parkinson's disease: Dopamine, vesicles and alpha-synuclein. *Nat. Rev. Neurosci.* **2002**, *3*, 932–942. [CrossRef]
59. Lotharius, J.; Barg, S.; Wiekop, P.; Lundberg, C.; Raymon, H.K.; Brundin, P. Effect of Mutant α-Synuclein on Dopamine Homeostasis in a New Human Mesencephalic Cell Line. *J. Biol. Chem.* **2002**, *277*, 38884–38894. [CrossRef]
60. Franklin, K.B.J.; Paxinos, G. *The Mouse Brain in Stereotaxic Coordinates*, 3rd ed.; Academic Press: San Diego, CA, USA, 2008; pp. 1–256.
61. Morton, D.B.; Griffiths, P.H. Guidelines on the recognition of pain, distress and discomfort in experimental animals and an hypothesis for assessment. *Vet. Rec.* **1985**, *116*, 431–436. [CrossRef]
62. Li, Y.; Lium, W.; Oo, T.F.; Wang, L.; Tang, Y.; Jackson-Lewis, V.; Zhou, C.; Geghman, K.; Bogdanov, M.; Przedborski, S.; et al. Mutant LRRK2(R1441G) BAC transgenic mice recapitulate cardinal features of Parkinson's disease. *Nat. Neurosci.* **2009**, *12*, 826–828. [CrossRef] [PubMed]

International Journal of
Molecular Sciences

MDPI

Article

SERS-Based Colloidal Aptasensors for Quantitative Determination of Influenza Virus

Dmitry Gribanyov [1], Gleb Zhdanov [2], Andrei Olenin [2], Georgii Lisichkin [2], Alexandra Gambaryan [3], Vladimir Kukushkin [1,*] and Elena Zavyalova [2,*]

1 Institute of Solid State Physics of Russian Academy of Science, 142432 Chernogolovka, Russia; digrib@gmail.com
2 Chemistry Department, Lomonosov Moscow State University, 119991 Moscow, Russia; gleb.zhdanov@chemistry.msu.ru (G.Z.); ayolenin@yandex.ru (A.O.); lisich@petrol.chem.msu.ru (G.L.)
3 Chumakov Federal Scientific Center for Research and Development of Immune and Biological Products RAS, 108819 Moscow, Russia; al.gambaryan@gmail.com
* Correspondence: kukushvi@mail.ru (V.K.); zlenka2006@gmail.com (E.Z.)

Abstract: Development of sensitive techniques for rapid detection of viruses is on a high demand. Surface-enhanced Raman spectroscopy (SERS) is an appropriate tool for new techniques due to its high sensitivity. DNA aptamers are short structured oligonucleotides that can provide specificity for SERS biosensors. Existing SERS-based aptasensors for rapid virus detection had several disadvantages. Some of them lacked possibility of quantitative determination, while others had sophisticated and expensive implementation. In this paper, we provide a new approach that combines rapid specific detection and the possibility of quantitative determination of viruses using the example of influenza A virus.

Keywords: aptamer; aptasensor; influenza; nanoparticles; SERS; virus detection

Citation: Gribanyov, D.; Zhdanov, G.; Olenin, A.; Lisichkin, G.; Gambaryan, A.; Kukushkin, V.; Zavyalova, E. SERS-Based Colloidal Aptasensors for Quantitative Determination of Influenza Virus. *Int. J. Mol. Sci.* **2021**, *22*, 1842. https://doi.org/10.3390/ijms22041842

Academic Editors: Salvador F. Aliño and Luis Sendra
Received: 12 January 2021
Accepted: 9 February 2021
Published: 12 February 2021

1. Introduction

Viral pandemics cause serious damage to both public health and economics. Most viral pandemics have been caused by influenza A viruses. The most dangerous influenza pandemic was in 1918–1920 ("spanish flu", H1N1 subtype); the latest influenza pandemic was in 2009–2010 ("swine flu", H1N1 subtype). In 2019, a new strain of coronavirus caused a potent outbreak with relatively high percentage of deaths ("COVID-19", SARS-CoV-2 strain). One more significant pandemic was caused by human immunodeficiency virus (HIV, mainly HIV-1 strain); this pandemic has been the most long-lasting, and it has caused the highest number of deaths among recent viral pandemics [1].

Recurrent pandemics make us face the problem of the absence of affordable, rapid and precise diagnostic tools. Polymerase chain reaction (PCR) is a contemporary "gold standard" due to high sensitivity and accuracy [2,3]. PCR can be used both for qualitative and quantitative estimation of viral genomes. However, PCR requires several hours to perform 30–40 cycles. Several attempts have been made to create rapid PCR within small portable devices; their robustness and accuracy are to be studied in the near future [4]. Antibody-based assays have been used for rapid diagnostics of influenza A, HIV and other viruses. These assays include techniques with detection of enzymatic activity, fluorescence or chemiluminescence [5,6]; most of them require an advanced laboratory setting and several hours for an execution. Among them, lateral flow immunochromatographic assays (LFIA) are rapid and are the simplest in performance necessary for practical usage, but they provide only qualitative estimations [7–11]. Their limit of detection (LOD) is higher by 3–4 orders compared to PCR techniques, being more than 10^6 viral particles per mL (VP/mL) [7–10]. A number of extremely sensitive techniques have been developed, but they have not been optimized for routine usage because of long-lasting sophisticated

sample preparation and/or usage of expensive high-technology equipment [3,12–15]. The development of simple, rapid and sensitive techniques for virus determination is in progress [3].

Biosensors with aptamers as recognition elements are of particular interest for virus determination due to their specificity, sensitivity and availability of aptamer functionalization with a variety of labels [3,16]. In our previous work, a SERS-based aptasensor for qualitative determination of influenza viruses had an intermediate limit of detection; the LOD was 10^4 viral particles per sample, which is 10-fold higher compared to PCR and 100-fold lower compared to antibody-based strips [17]. Specificity was achieved due to DNA aptamer RHA0385 to hemagglutinin (HA, surface protein of influenza virus); this aptamer binds different strains of influenza A with nearly the same affinity (K_D = 2–5 nM [18]), providing a possibility of strain-independent detection of the virus [17]. Surface-enhanced Raman spectroscopy (SERS) provided the high sensitivity of the technique; SERS-active surfaces were created by the deposition of silver nanoparticles on the silica substrates. The overall duration of the analysis was less than 15 min. However, the dependence of an analytical signal from a viral load had a complex shape that did not allow quantitative determination of the viruses [17].

In this paper, we describe a novel SERS-based aptasensor for quantitative determination of influenza A viruses that matches the requirements for further practical implementation. Colloidal silver nanoparticles (AgNP) were used instead of solid-state substrates. Colloidal AgNP have several advantages, including the following: (1) simple and cheap one-pot synthesis without the use of high-technology equipment [19]; (2) an analytical signal that has predominantly monotonous concentration dependence [20]; (3) colloidal AgNP are surrounded by an aqueous homogenous environment that decreases heterogeneity in distribution of substances. The combination of SERS on colloidal AgNP and specific recognition of viruses by aptamers can provide a simple, cheap and rapid technique for the quantitative determination of viruses.

2. Materials and Methods

Inorganic salts and buffer solutions were purchased from Sigma-Aldrich (St. Louis, MO, USA) and MP Biomedicals (Illkirch-Graffenstaden, France). The following modified oligonucleotides were used: RHA0385-SH (5′-HS-$(CH_2)_6$-TTGGGGTTATTTTGGGAGGGC GGGGGTT-3′) from Synthol (Moscow, Russia) and RHA0385-BDPFL (5′-BODIPY FL-TTGGGGTTATTTTGGGAGGGCGGGGGTT-3′) and BV42-BDPFL (5′-Bodipy FL-AACG CTCACTCCCCCAAGAAGAACCCCCCCCCCCC-CCCCCCCCCCAGTGAGCGTT) from Lumiprobe (Moscow, Russia).

Influenza viruses and allantoic fluid were provided by the Chumakov Federal Scientific Center for Research and Development of Immune and Biological Products of the Russian Academy of Sciences. The following influenza strains were studied: A/chicken/Kurgan/3654-at/2005 (H5N1, influenza A virus) and B/Victoria/2/1987 (influenza B virus). Virus stocks were propagated in the allantoic cavity of 10-day-old embryonated specific pathogen free chicken eggs. Eggs were incubated at 37 °C, cooled at 4 °C 48 h post-infection and harvested 16 h later. The study design was approved by the Ethics Committee of the Chumakov Institute of Poliomyelitis and Viral Encephalitides, Moscow, Russia (Approval #4 from 2 December 2014). Viruses were inactivated via the addition of 0.05% (*v*/*v*) glutaric aldehyde, preserved via the addition of 0.03% (*w*/*v*) NaN_3 and stored at +4 °C.

2.1. Aptamer Preparation

Aptamers are to be properly folded to exhibit the functional activity. The aptamer RHA0385-SH was folded at 2 μM concentration in 10 mM KCl. Aptamers RHA0385-BDPFL and BV42-BDPFL were folded at 2 μM concentration in 10 mM KCl and 140 mM NaCl. The folding process was carried out in the following way: the solution was heated at 95 °C for 5 min and cooled at room temperature.

2.2. Preparation and Characterization of Citrate-Stabilized Silver Nanoparticles (AgNP-Citr)

The $AgNO_3$ solution (10 mM, 3 mL) was mixed with sodium citrate solution (19 mM, 29 mL). This solution was mixed with fresh solution of $NaBH_4$ (26 mM, 34 µL). The reaction mixture was mixed for 30 min using a magnetic stirrer. These nanoparticles (AgNP-Citr) were characterized by several techniques.

The absorption spectrum of AgNP-Citr peaked with a maximum at 396 nm and a width at half-height of 68 nm (Figure S1). AgNP-Citr had a mean diameter of 5 nm (Figure S2A); the AgNP-Citr diameter was estimated by dynamic light scattering using Zetasizer Nano ZS with a He-Ne laser with a wavelength of 633 nm (Malvern Instruments, Worcestershire, UK). The diameter was determined independently using transmission electron microscope Leo 912 AB Omega (Leo, Oberkochen, Germany) with accelerating voltage 100 kV. One to two microliters of AgNP-Citr were applied onto formvar-treated copper mesh with 3 mm diameter. The estimated AgNP diameter was 4 nm.

ZetasizerNano ZS (Malvern, Worcestershire, UK) was used to characterize ζ-potential that was -40 ± 2 mV (Figure S2B). This value corresponds to AgNP-Citr that are stable against spontaneous aggregation. The state of Ag in nanoparticles was estimated using X-ray phase diffractometer Dron-3 (NPP Burevestnik, Saint Petersburg, Russia) with CuKα (λ = 1.54 Å) anode emission. The peaks corresponded to Ag crystal lattice (Figure S3).

2.3. Preparation of Silver Nanoparticles According to Leopold and Lendl (AgNP-LL)

Silver nanoparticles (AgNP-LL) were prepared according to the technique described earlier by Leopold and Lendl [21]. One hundred eighty microliters of 167 mM solution of $NH_2OH{\cdot}HCl$ and 120 µL of 500 mM solution of NaOH were mixed with 18.7 mL of water. Then 1 mL of 20 mM $AgNO_3$ solution was added. The reaction mixture was mixed for 1 h by a magnetic stirrer at room temperature. AgNP-LL with citrate were obtained by treatment of 12 mL of AgNP-LL with 80 µL of 65 mM solution of sodium citrate. Both types of AgNP were used 3–4 days after preparation. The mean size of these AgNP and their modifications with RHA0385-SH and citrate was nearly 10 nm according to dynamic light scattering performed using ZetasizerNano ZS (Malvern, Worcestershire, UK) (Figure S4A,B). The ζ-potential was -44 ± 6 mV (Figure S4C), as measured by ZetasizerNano ZS (Malvern, Worcestershire, UK).

2.4. Characterization of Influenza Viruses

The functional activity of the influenza viruses was estimated by hemagglutination assay. One hundred microliters of 0.5% chicken red blood cells in 140 mM NaCl were placed in V-bottom 96-well plates (Greiner, Kremsmünster, Austria). Viruses were aliquoted with 2-fold dilution (the final volume of mixture was 200 µL). Hemagglutination was estimated after 30 min of incubation. The absence of red dots was interpreted as hemagglutination. The sample with minimal viral content that caused hemagglutination was assigned to contain 1 HAU (hemagglutination unit) viral titer. An example of the hemagglutination assay for an influenza A virus is shown in Figure S5. Viral loads in viral particles per mL (VP/mL) were estimated from hemagglutination units (HAU/mL) based on correlations published earlier (1 HAU ~ 5×10^7) [22].

2.5. Determination of Influenza Viruses Using Different Nanoparticles

AgNP-Citr. AgNP-Citr were incubated with 20 nM solution of RHA0385-SH for 1 h at 37 °C. Then, 480 µL of modified AgNP were mixed with 5 µL of 2 µM solution of RHA0385-BDPFL, 15 µL of 5 M solution of NaCl and 250 µL of influenza A virus (or influenza B virus, or allantoic fluid) diluted in 15 mM PBSK (15 mM phosphate buffer pH 7.2, 150 mM NaCl, 15 mM KCl). The mixture was incubated for 10 min; then, SERS spectra were recorded for 200 ms with 25 repeats using handheld Raman analyzer RaPort (Enhanced Spectrometry, San Jose, CA, USA) with a laser excitation wavelength of 532 nm and a power of 30 mW.The experimental series had the following differences in setup:

(1a) The viral load was increased sequentially in the same AgNP sample. This setup was used in this series only.
(1b) Different viral loads were achieved in different AgNP samples. Other details were the same as in 1a series.
(1c) The setup was the same as in 1b series except for the type of aptamer. BV42-BDPFL was used instead of RHA0385-BDPFL.

AgNP-LL treated with a thiol-modified aptamer and citrate. AgNP were incubated with 40 nM solution of RHA0385-SH for 1 h at 37 °C. The resulted AgNP were modified with sodium citrate solution for 2 h (the final citrate concentration was 450 μM). Then, 196 μL of modified AgNP was mixed with 4 μL of 2 μM solution of RHA0385-BDPFL, 50 μL of 5× concentrated PBS and 250 μL of influenza A or influenza B viruses diluted in 10 mM PBSK (10 mM phosphate buffer pH 7.2, 150 mM NaCl, 20 mM KCl). The mixture was incubated for 10 min; then SERS spectra were recorded for 400 ms with 25 repeats using handheld Raman analyzer RaPort (Enhanced Spectrometry, San Jose, CA, USA) with a laser excitation wavelength of 532 nm and a power of 30 mW. This series is marked as 2a.

AgNP-LL treated with citrate. One hundred ninety-six microliters of AgNP-LL was mixed with 4 μL of 2 μM solution of RHA0385-BDPFL, 50 μL of 5× concentrated PBS and 250 μL of influenza A or influenza B viruses diluted in 10 mM PBSK (10 mM phosphate buffer pH 7.2, 150 mM NaCl, 20 mM KCl). The mixture was incubated for 10 min; then SERS spectra were recorded for 400 ms with 25 repeats using handheld Raman analyzer RaPort (Enhanced Spectrometry, San Jose, CA, USA) with a laser excitation wavelength of 532 nm and a power of 30 mW. The differences were as follows:

(2b) AgNP were incubated with 40 nM solution of RHA0385-SH for 1 h at 37 °C before the experiment described above.
(2c) The setup without any modifications was used.

A brief description of all experimental series is provided in Table 1.

Table 1. A brief description of components in different experimental series.

Type of AgNP	**AgNP-Citr**			**AgNP-LL**		
Setup	1a	1b	1c	2a	2b	2c
Reagents	Concentrations					
Ag^+	0.3 mM	0.3 mM	0.3 mM	0.4 mM	0.4 mM	0.4 mM
RHA0385-SH	20 nM	20 nM	20 nM	40 nM	40 nM	-
Citrate	-	-	-	450 μM	450 μM	450 μM
RHA0385-BDPFL	13 nM	13 nM	-	16 nM	16 nM	16 nM
BV42-BDPFL	-	-	13 nM	-	-	-

3. Results

3.1. Setup of Aptasensors for Influenza Virus Determination

Colloidal AgNP were tested as a basis for creation of aptasensor for virus determination. Two types of DNA aptamers to influenza hemagglutinin were used. Aptamer RHA0385 [23] was shown to recognize a wide variety of influenza A strains [17,18]; aptamer BV42 [24] had the same ability (unpublished data). The setup of the aptasensor was similar to our previous solid-state aptasensor [17]. It consumed primary aptamers for functionalization of silver and secondary aptamers to provide an analytical signal.

AgNP were functionalized with thiol-modified aptamer RHA0385. Then AgNP were mixed with aptamers conjugated to SERS-active label and were aggregated by increasing ionic strength. Viral particles of A/chicken/Kurgan/3654-at/2005 (H5N1, influenza A virus) and B/Victoria/2/1987 (influenza B virus) were added to the AgNP aggregates in different content.

BODIPY FL was chosen as SERS-active label due to low fluorescence and high SERS intensity. AgNP aggregates provide SERS spectra of BODIPY FL (Figure 1A) that is similar to SERS spectrum of BODIPY FL onto solid-state substrate [17]. The position of peaks was the same both in colloidal and solid-state sensors, but the ratio of intensities at small and large Raman shifts was different for solid-state substrates and colloidal SERS substrates. (Figure 1A). This is due to the different plasmon absorption contours of colloidal silver particles and solid-state SERS substrates.

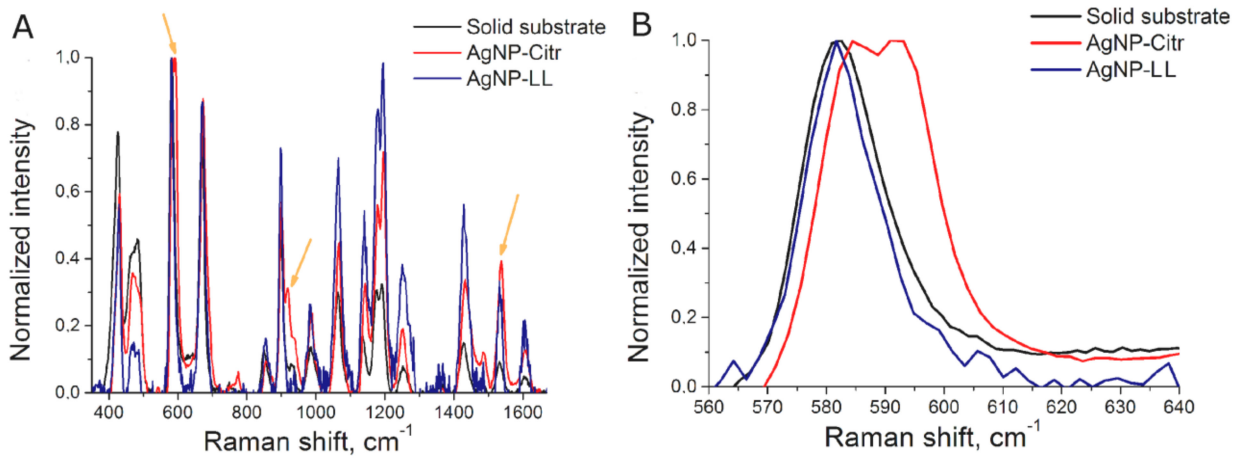

Figure 1. Surface-enhanced Raman spectroscopy (SERS) spectra of BODIPY FL dye onto solid substrate, AgNP-Citr aggregates and AgNP-LL aggregates (**A**). The peaks used for further consideration (**B**).

The spectrum of the BODIPY FL-labeled aptamer onto AgNP-Citr aggregates had several additional peaks compared to AgNP-LL aggregates and solid-state sensors (Figure 1A, Table S1); the peak with the highest intensity is shown in Figure 1B (the peak at 591 cm^{-1}). This peak was attributed to BODIPY FL, as it was absent in the spectra of AgNP alone and AgNP with the thiol-modified aptamer (Figure S6). SERS spectra of the same substance differ on various AgNP if the substance forms different complexes with the surface. For example, peaks of citrate are different depending on the AgNP parameters [25,26]. Indeed, SERS spectra of citrate onto AgNP-LL aggregates did not match completely with previously published spectra (Figure S6C). One of the possible explanations for 591 cm^{-1} peak emergence is the following: AgNP-Citr had an extremely small size that is comparable with the size of the aptamer; if one molecule of the BODIPY FL-modified aptamer is trapped between several small AgNP, polarizability of some chemical bond is changed providing a new peak in the spectrum. The SERS signal intensities at 585 cm^{-1} and 595 cm^{-1} (BODIPY FL) were used to estimate the efficiency of aptasensors with AgNP-Citr. The value 595 cm^{-1} for the peak at 591 cm^{-1} was chosen to minimize the contribution of the nearby peak at 585 cm^{-1}. The peaks at 585 cm^{-1} (BODIPY FL) and 611 cm^{-1} (citrate peak) were used to estimate the efficiency of aptasensors with AgNP-LL. It should be noted that the majority of modern Raman spectrometers have sufficient resolution to distinguish nearby peaks at 585 cm^{-1} and 591 cm^{-1}. For example, RaPort spectrometer has resolution of 4 cm^{-1} in this part of the spectral range.

Several schemes for aptasensor setup were used. Generally, AgNP were functionalized with a thiol-modified aptamer, mixed with a labeled aptamer in buffered saline. The resulted aggregates were mixed with viruses, and SERS spectra were measured (Figure 2). Specific interaction with the virus provided higher SERS signals than non-specific interactions with components of allantoic fluid or influenza B virus. A detailed description of the experiments is provided in the Materials and Methods section and summarized in Table 1. SERS signal from BODIPY FL appeared only when the dye was trapped between several AgNP. In other cases, only high fluorescence was detected.

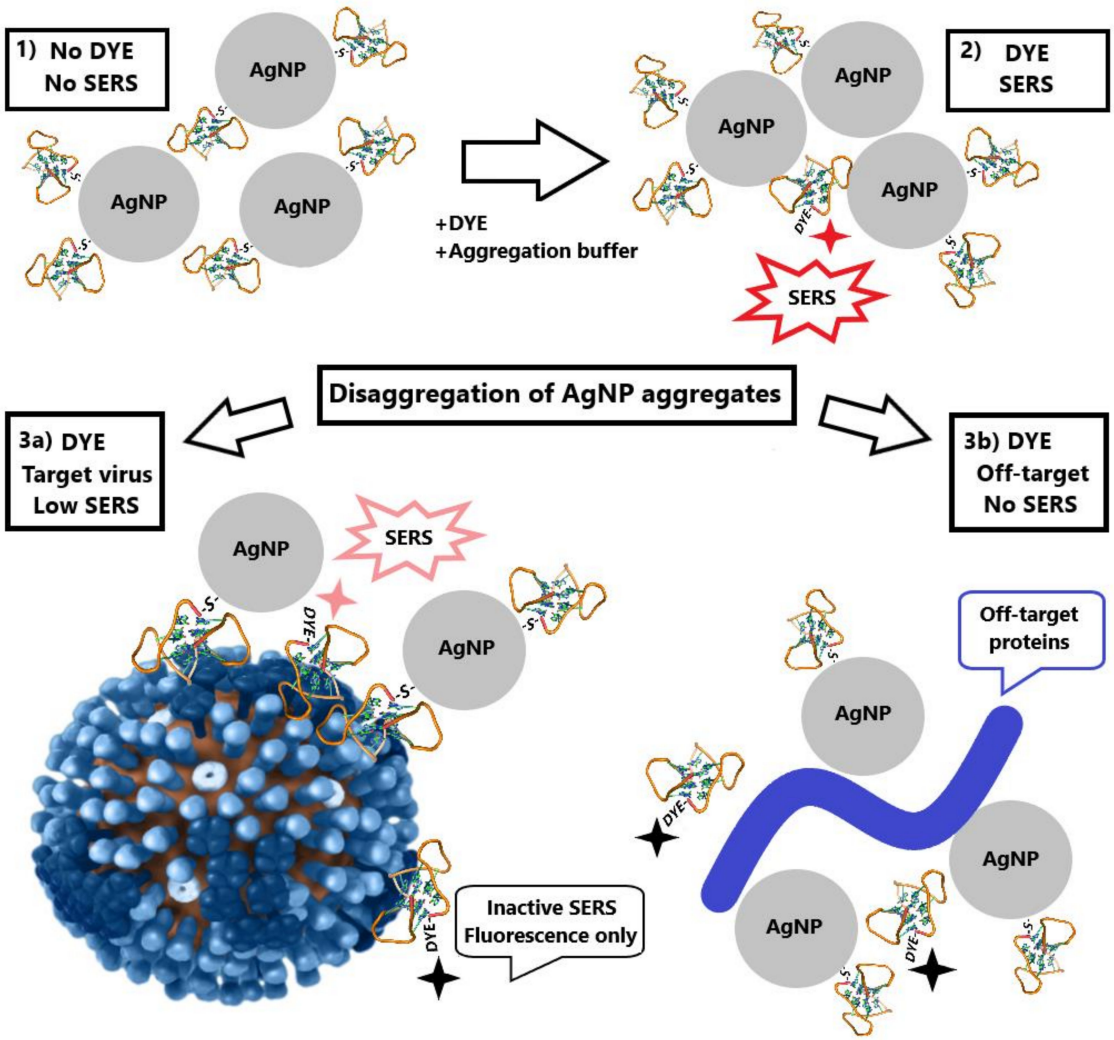

Figure 2. Schematic representation of aptasensor setup. Aptamer-functionalized AgNP (1) were mixed with a labeled aptamer in buffered saline providing AgNP aggregates (2). The aggregates were mixed with target viruses (3a) resulting in weaker SERS signals or with off-target biologicals (3b) losing SERS effect due to the elimination of the labeled aptamer from AgNP aggregates. The picture for influenza A virus was derived from the Public Health Image Library (ID:19013).

3.2. Determination of Influenza Virus with AgNP-Citr

Firstly, we performed subsequent addition of aliquots of the virus to the same samples of AgNP-Citr (setup 1a). Allantoic fluid decreased drastically the intensity of SERS signal due to non-specific interactions with AgNP, whereas samples with influenza A viruses had slightly diminished signals. As the quantity of AgNP was the same in subsequent samples, monotonous dependence was expected. However, the considerable scatter of points was observed for BODIPY FL peaks (Figure 3A and Figure S7). Next, we used relative SERS signal intensities; namely, the newly emerged peak (intensity at 595 cm^{-1} was used) was normalized to the 585 cm^{-1} peak from the label. The dependence became much more smooth (Figure 3B and Figure S8).

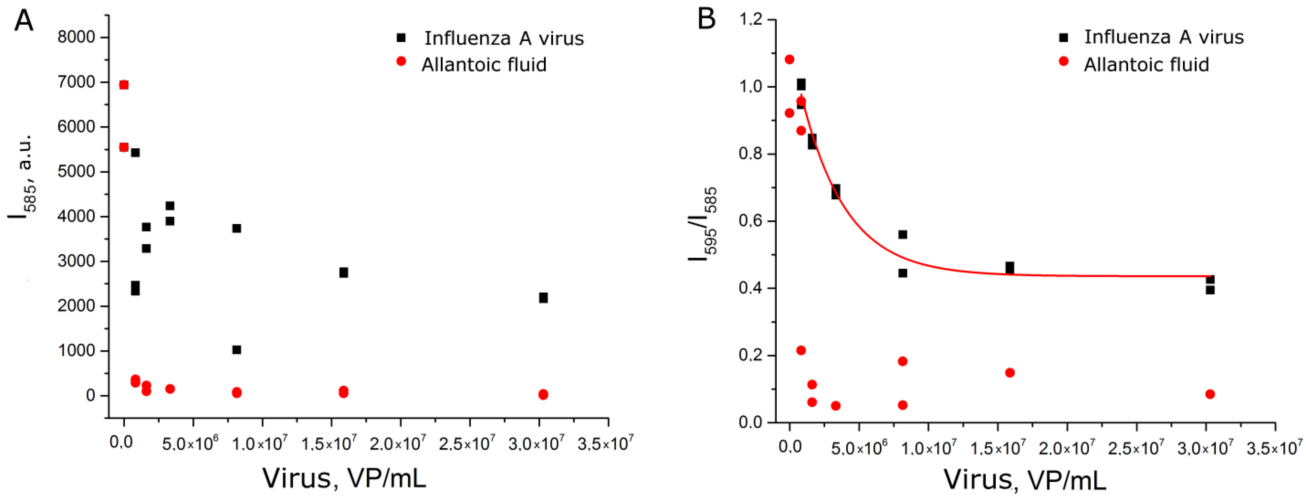

Figure 3. Concentration dependencies of absolute SERS signal intensity of the label (**A**) and relative SERS signal intensity of BODIPY FL peaks (**B**) for influenza virus and allantoic fluid. Allantoic fluid was diluted identically to influenza A virus.

The dynamic range of the curve was between 1×10^6 and 1×10^7 VP/mL (Figure S9); the range for reliable quantitative determination of influenza A virus was 1×10^6–3×10^7 VP/mL (the upper limit of detection was not reached in the series). Here the peak from the labeled aptamer trapped between several small AgNP was normalized to the regular BODIPY FL peak. The resulting relative value was used as an analytical signal; the procedure diminished the low reproducibility of aggregation.

The experiments with setup 1b reproduced setup 1a, but each sample was prepared independently. Nevertheless, the dependence of relative SERS signal intensity from the viral load was reproduced (Figure 4A). Samples with influenza A virus had significantly higher signal intensity than allantoic fluid and off-target influenza B virus. The reproducibility of the curves can be illustrated by the match within the error of curvatures (Table S2).

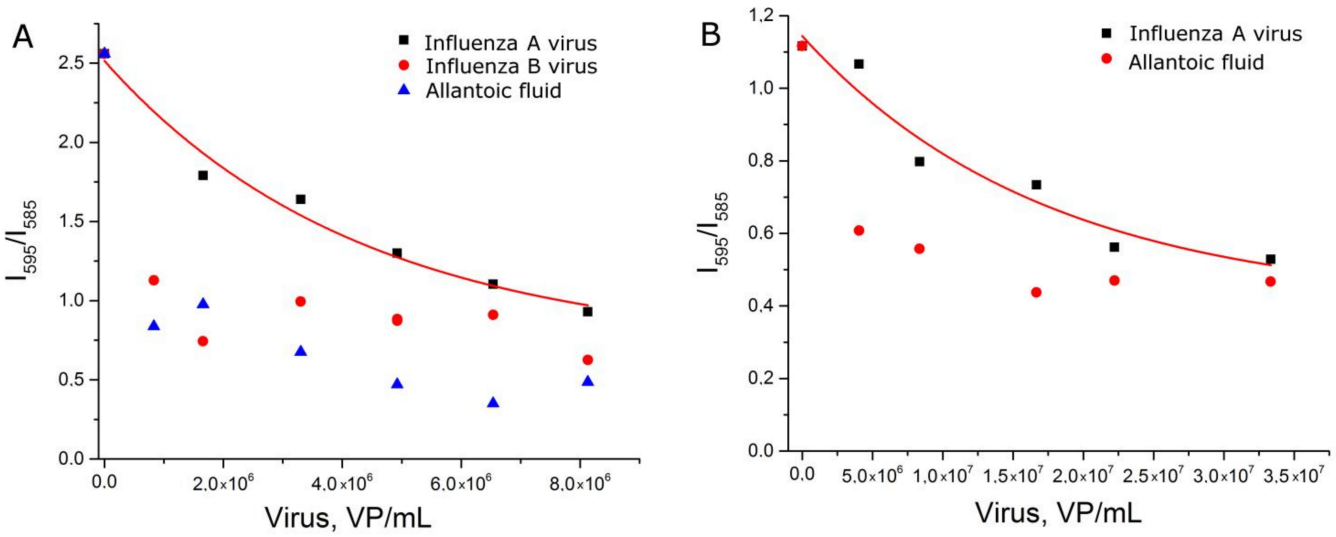

Figure 4. Concentration dependencies of relative SERS signal intensities of the labeled aptamer in experimental setups 1b (**A**) and 1c (**B**). Allantoic fluid was diluted identically to influenza A virus. Fittings with exponential functions are provided (see Table S2 for details).

Next, we tested another BODIPY FL-labeled aptamer to hemagglutinin. Aptamer BV42 has putative i-motif structure [27] and inhibits hemagglutinin function with IC_{50} = 8 nM [24]. Its inhibitory activity is comparable to activity of the RHA0385 aptamer [28]. Thiol-

modified RHA0385 and BODIPY FL-labeled BV42 aptamers were used in the experimental setup 1c. Replacement of the aptamer decreased discrepancy between samples with influenza A virus and control samples (Figure 4B). The exponential fit of the curve differed from those of setups 1b and 1c (Table S2). The dynamic range (5×10^6–2×10^7 VP/mL) was narrower and shifted to higher viral loads compared to the setup with BODIPY FL-labeled RHA0385. Thus, the type of aptamer affects the aptasensor characteristics.

3.3. Determination of Influenza Virus with AgNP-LL

One more AgNP type was tested. AgNP were optimized exactly for SERS measurements by Leopold and Lendl [21], having the mean particle diameter of 10 nm (Figure S4). AgNP-LL were incubated with citrate in order to imitate the surface of AgNP-Citr.

First, AgNP-LL were functionalized with a thiol-modified aptamer with subsequent incubation in a sodium citrate solution (setup 2a). These AgNP provided peaks of citrate spectrum (Figure S6) that were supposed to be useful as an internal standard. However, the relative peak intensity had no dependence on virus content (Figure S10). Absolute values of SERS signal intensity of BODIPY FL were revealed to be a relevant parameter which was dependent on influenza virus content (Figure 5A). The dynamic range of the curve was between 2×10^5 and 2×10^6 VP/mL, which corresponds to the highest sensitivity among the different setups.

Second, the order of AgNP modification was changed. AgNP-LL were incubated with citrate and subsequently functionalized with the thiol-modified aptamer (setup 2b). The dynamic range was extremely narrow (Figure 5B). This setup cannot be used for virus quantification.

Third, AgNP-LL were incubated with citrate without further functionalization with the aptamer (setup 2c). In this case, the curve was of a good quality with the dynamic range between 6×10^5 and 3×10^6 VP/mL. This setup was less efficient compared to setup 2a, which illuminates the role of functionalization of AgNP with aptamers for assay sensitivity.

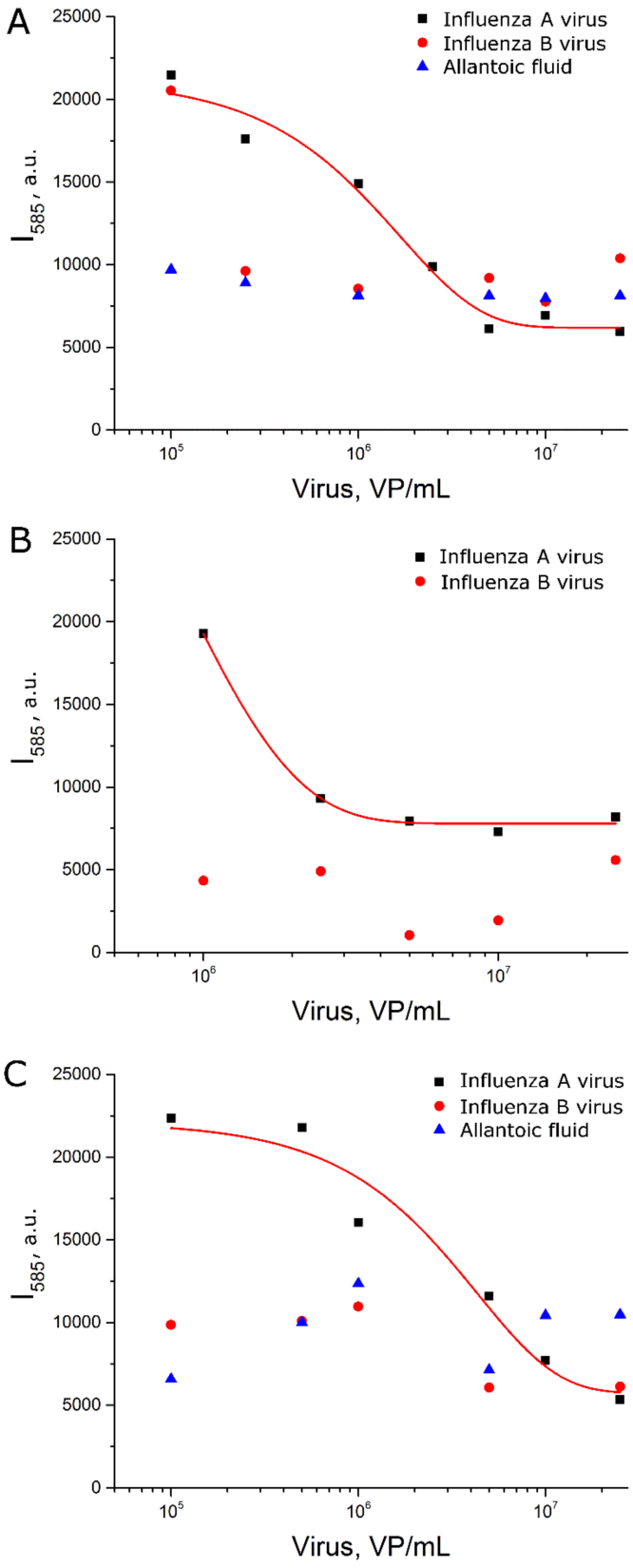

Figure 5. Concentration dependencies of SERS signal intensity of BODIPY FL for experimental setup 2a (**A**), 2b (**B**) and 2c (**C**). Allantoic fluid was diluted identically to influenza A virus. Fittings with exponential functions are provided (see Table S2 for details).

4. Discussion

A wide variety of SERS-based techniques was developed to detect viruses. Most of them consumed antisense oligonucleotides (ASO) to capture viral genomes. This field has been reviewed in detail in our recent work [3]. In general, ASO-based techniques have lower limits of detection if the virus genome is DNA because of higher stability of DNA duplexes compared to RNA/DNA duplexes [29,30]. Influenza has an RNA genome; and a comparison between assays with genome capture and surface protein capture revealed the latter ones to be an unambiguously better choice for highly sensitive assays [12,17,30]. Surface proteins can be captured by either antibodies or aptamers. Aptamers have advantages due to a relatively small size and a variety of modifications that can be introduced site-specifically during chemical synthesis [3].

SERS-based assays with the highest performance consume solid nanostructured substrates with complex surfaces [3]. For example, aptamer-covered multilayer substrates made up of polyethylene naphthalate, gold, perfluorodecanethiol and one more gold layer were used to detect influenza A virus with a limit of detection of nearly 100 pfu/mL (10^4 VP/mL [30]) [13]. This technique was shown to be useful for virus quantitation, as opposed to another aptamer-based technique with a similar limit of detection that was useful for qualitative analysis only [17]. Both techniques consume solid substrates made up using advanced equipment to provide metal deposition in a controlled and reproducible manner.

Contrary to solid substrates, nanoparticles can be synthesized in a "one pot" manner at room temperature. Many techniques have been described that provide good reproducibility of AgNP size, shape and ζ-potential [21,31,32]. Here we used two types of AgNP with simple formulations: the first one was citrate stabilized with a mean diameter of 4 nm; the second one was chloride stabilized with mean diameter 10 nm. The assay setup comprised aggregation of aptamer-functionalized AgNP in the presence of a labeled aptamer with subsequent disruption of aggregates by viruses and other biological molecules. The efficiency of disintegration of AgNP aggregates differed in the presence of aptamer-targeted and aptamer-off-targeted viruses. Supposed mechanisms include AgNP organization onto the viral particles with preservation of SERS signal and the removal of the labeled aptamer from proximity to AgNP due to non-specific interactions of AgNP with biological molecules (Figure 2).

Absolute SERS signal intensity of the label was successfully used as an analytical signal in the case of AgNP-LL but not AgNP-Citr. In the case of AgNP-Citr, the relative SERS signal can be used as a reproducible analytical signal. Relative intensity of the specific peak from the complex of the BODIPY FL-modified aptamer with AgNP-Citr was used. Non-specific interactions of biological molecules with AgNP surface with partial destruction of the complex between the BODIPY FL-modified aptamer and AgNP-Citr citrate ions can be proposed as a possible mechanism that explains the higher rate of decrease of the analytical signal. It is interesting to study the polarization of peaks at 585 cm^{-1} and 591 cm^{-1} of BODIPY FL in order to increase the dynamic range for detection of the influenza virus. The particular Raman peak could be amplified by excitation with parallel polarization or cross-polarization [33].

Usage of an internal standard was shown to be a potent approach for a wide range of analytes including ions, low-molecular compounds, exosomes and whole bacterial cells [34–38]. Some approaches utilize a signal from molecules entrapped in AgNP as a standard [34,38]. If the analyte is a cell, several membrane components can be used to normalize the signal from the label, enhancing accuracy and reproducibility of the assay [35]. In other approaches, several types of AgNP were used simultaneously; some of AgNP were used as an internal standard for other target-bound AgNP [36]. Our assay with AgNP-Citr did not require additional compound due to peculiarities of the interaction between labeled the aptamer and these particular types of AgNP.

AgNP-LL provided more reproducible SERS signal; and thus, the results for absolute SERS signal intensity on AgNP-LL were nearly of the same quality as relative SERS signal intensity on AgNP-Citr. We tried to use citrate as an internal standard for AgNP-LL, but

the reproducibility of citrate adsorption and desorption was very low. Possibly, it was due to a layer of chloride ions adsorbed onto AgNP-LL. Both AgNP-Citr and AgNP-LL preparation techniques are simple and consume affordable chemicals. The simplicity and the low cost make these AgNP very attractive for a practical implementation.

Several SERS-based techniques with lower LOD and wider dynamic range have been described, but all of them consume much more sophisticated procedures for preparation of SERS-active structures and/or sample preparation [39]. For example, antibody-modified AgNP allowed detection of as low as 100 VP/mL with dynamic range over 10^7 VP/mL, but the sample preparation requires nearly 2 h with usage of adsorption onto nitrocellulose membrane [39]. Another antibody-based assay had a dynamic range over 4×10^5–10^9 VP/mL with setup duration more than 3.5 h for step-by-step adsorption of the assay components [12]. The aptasensor with similar characteristics allowed determination of 10^4–10^6 VP/mL; the experimental setup was rather quick (>10 min) but needed a sophisticated multilayer substrate [13]. Our aptasensor had LOD 2×10^5 VP/mL and a dynamic range of 2×10^5–2×10^6 VP/mL; however, the time of the assay was below 15 min, and the AgNP preparation was very simple.

Considering further development of nanoparticle-based aptasensors for rapid diagnostics, there are several possible ways to improve the setups described. The first way is to reverse the concentration dependence of the analytical signal, i.e., to get the increase of SERS intensity with the increase of virus content. This technique allows the increase of the difference between samples with and without the target; FRET-based techniques are good examples of this approach [40,41]. The second way is to increase the affinity of the aptamers to the virus, which results in better sensitivity of the assay. The example with two different aptamers to hemagglutinin in this article (Figure 4) clearly indicates that affinity is a key determinant. We also speculate that highly affine aptamers could provide broader dynamic range of the aptasensors.

5. Conclusions

A new approach was developed combining rapid specific detection and a possibility for quantitative determination of viruses using the example of influenza A virus. Specificity was provided by aptamers to influenza hemagglutinin, whereas sensitivity was provided by a SERS-based technique. The proposed technique can be classified as a rapid diagnostic test due to a short time of analysis (below 15 min) and simple sample preparation (the assay is homogeneous). AgNP with the simplest preparation and high stability were chosen. Absolute and relative SERS signal intensities could be used as an analytical signal. The optimal aptasensor had LOD of 2×10^5 VP/mL and a dynamic range of 2×10^5–2×10^6 VP/mL.

Supplementary Materials: The following are available online at https://www.mdpi.com/1422-0067/22/4/1842/s1.

Author Contributions: Conceptualization, V.K. and E.Z.; methodology, A.O., G.L., D.G. and A.G.; formal analysis, E.Z. and D.G.; writing—original draft preparation, E.Z., D.G. and G.Z.; writing—review and editing, V.K. and E.Z.; funding acquisition, E.Z. All authors have read and agreed to the published version of the manuscript.

Funding: This research was supported by the Russian Science Foundation (grant number 18-74-10019).

Institutional Review Board Statement: The study was conducted according to the guidelines of the Declaration of Helsinki, and approved by the Ethics Committee of the Chumakov Institute of Poliomyelitis and Viral Encephalitides, Moscow, Russia (Approval #4 from 2 December 2014).

Informed Consent Statement: Not applicable.

Data Availability Statement: The data presented in this study are available on request from the corresponding author. The data are not publicly available due to privacy.

Conflicts of Interest: The authors declare no conflict of interest. The funders had no role in the design of the study; in the collection, analyses, or interpretation of data; in the writing of the manuscript; or in the decision to publish the results.

Abbreviations

AgNP-Citr	Citrate stabilized silver nanoparticles
AgNP-LL	Silver nanoparticles synthesized according to Leopold and Lendl
ASO	Antisense oligonucleotides
FRET	Fluorescence resonance energy transfer
HxNy	Abbreviation of influenza subtype, namely, hemagglutinin subtype x (1 or 5) and neuraminidase subtype y (1)
HA	Hemagglutinin
HAU	Hemagglutination unit
HIV	Human immunodeficiency virus
pfu	Plaque forming unit
PCR	Polymerase chain reaction
LFIA	Lateral flow immunochromatographic assays
LOD	Limit of detection
SERS	Surface-enhanced Raman spectroscopy
VP	Viral particle

References

1. Morens, D.M.; Fauci, A.S. Emerging pandemic diseases: How we got to COVID-19. *Cell* **2020**, *182*, 1077–1092. [CrossRef]
2. Mahony, J.B.; Petrich, A.; Smieja, M. Molecular diagnosis of respiratory virus infections. *Crit. Rev. Clin. Lab. Sci.* **2011**, *48*, 217–249. [CrossRef] [PubMed]
3. Ambartsumyan, O.; Gribanyov, D.; Kukushkin, V.; Kopylov, A.; Zavyalova, E. SERS-based biosensors for virus determination with oligonucleotides as recognition elements. *Int. J. Mol. Sci.* **2020**, *21*, 3373. [CrossRef]
4. Muraoka, M.; Tanoi, Y.; Tada, T.; Tabata, A.; Mizukoshi, M.; Kawaguchi, O. Direct detection of Dengue viruses without extraction of RNA on the mobile real-time PCR device. *MedRxiv* **2020**. [CrossRef]
5. Ho, H.-T.; Qian, H.-L.; He, F.; Meng, T.; Szyporta, M.; Prabhu, N.; Prabakaran, M.; Chan, K.-P.; Kwang, J. Rapid detection of H5N1 subtype influenza viruses by antigen capture enzyme-linked immunosorbent assay using H5- and N1-specific mono-clonal antibodies. *Clin. Vaccine Immunol.* **2009**, *16*, 726–732. [CrossRef] [PubMed]
6. Noh, J.Y.; Yoon, S.-W.; Kim, Y.; Van Lo, T.; Ahn, M.-J.; Jung, M.-C.; Le, T.B.; Na, W.; Song, D.; Le, V.P.; et al. Pipetting-based immunoassay for point-of-care testing: Application for detection of the influenza A virus. *Sci. Rep.* **2019**, *9*, 16661. [CrossRef] [PubMed]
7. Anderson, C.E.; Holstein, C.A.; Strauch, E.-M.; Bennett, S.; Chevalier, A.; Nelson, J.; Fu, E.; Baker, D.; Yager, P. Rapid diagnostic assay for intact influenza virus using a high affinity hemagglutinin binding protein. *Anal. Chem.* **2017**, *89*, 6608–6615. [CrossRef]
8. Chan, K.-H.; To, K.K.W.; Chan, J.F.W.; Li, C.P.Y.; Chen, H.; Yuen, K.-Y. Analytical sensitivity of seven point-of-care Influenza virus detection tests and two molecular tests for detection of avian origin H7N9 and swine origin H3N2 variant Influenza A viruses. *J. Clin. Microbiol.* **2013**, *51*, 3160–3161. [CrossRef] [PubMed]
9. Keitel, K.; Wagner, N.; Lacroix, L.E.; Manzano, S.; Gervaix, A. Performance characteristics of a rapid immunochromatographic assay for detection of pandemic influenza A (H1N1) virus in children. *Eur. J. Pediatr.* **2010**, *170*, 511–517. [CrossRef]
10. Peters, T.R.; Blakeney, E.; Vannoy, L.; Poehling, K.A. Evaluation of the limit of detection of the BD Veritor™ system flu A + B test and two rapid influenza detection tests for influenza virus. *Diagn. Microbiol. Infect. Dis.* **2013**, *75*, 200–202. [CrossRef]
11. Ran, B.; Xianyu, Y.; Dong, M.; Chen, Y.; Qian, Z.; Jiang, X. Bioorthogonal reaction-mediated ELISAusing peroxide test strip as signal readout for point-of-care testing. *Anal. Chem.* **2017**, *89*, 6113–6119. [CrossRef] [PubMed]
12. Moon, J.; Yi, S.Y.; Hwang, A.; Eom, G.; Sim, J.; Jeong, J.; Lim, E.-K.; Chung, B.H.; Kim, B.; Jung, J.; et al. Facile and sensitive detection of influenza viruses using SERS antibody probes. *RSC Adv.* **2016**, *6*, 84415–84419. [CrossRef]
13. Chen, H.; Park, S.-G.; Choi, N.; Moon, J.-I.; Dang, H.; Das, A.; Lee, S.; Kim, D.-G.; Chen, L.; Choo, J. SERS imaging-based ap-tasensor for ultrasensitive and reproducible detection of influenza virus A. *Biosens. Bioelectron.* **2020**, *167*, 112496. [CrossRef] [PubMed]
14. Diba, F.S.; Kim, S.; Lee, H.J. Amperometric bioaffinity sensing platform for avian influenza virus proteins with aptamer modified gold nanoparticles on carbon chips. *Biosens. Bioelectron.* **2015**, *72*, 355–361. [CrossRef]
15. Wang, R.; Xu, L.; Li, Y. Bio-nanogate controlled enzymatic reaction for virus sensing. *Biosens. Bioelectron.* **2015**, *67*, 400–407. [CrossRef] [PubMed]
16. Kieboom, C.H.; Beek, S.L.; Mészáros, T.; Gyurcsányi, R.E.; Ferwerda, G.; Jonge, M.I. Aptasensors for viral diagnostics. *Trends Anal. Chem.* **2015**, *74*, 58–67. [CrossRef]

17. Kukushkin, V.I.; Ivanov, N.M.; Novoseltseva, A.A.; Gambaryan, A.S.; Yaminsky, I.V.; Kopylov, A.M.; Zavyalova, E.G. Highly sensitive detection of influenza virus with SERS aptasensor. *PLoS ONE* **2019**, *14*, e0216247. [CrossRef]
18. Novoseltseva, A.A.; Ivanov, N.M.; Novikov, R.A.; Tkachev, Y.V.; Bunin, D.A.; Gambaryan, A.S.; Tashlitsky, V.N.; Arutyunyan, A.M.; Kopylov, A.M.; Zavyalova, E.G. Structural and functional aspects of G-quadruplex aptamers which bind a broad range of Influenza A viruses. *Biomolecules* **2020**, *10*, 119. [CrossRef]
19. Leopold, N.; Chiş, V.; Mircescu, N.E.; Marişca, O.T.; Buja, O.M.; Leopold, L.F.; Socaciu, C.; Braicu, C.; Irimie, A.; Berindan-Neagoe, I. One step synthesis of SERS active colloidal gold nanoparticles by reduction with polyethylene glycol. *Colloids Surf. A Physicochem. Eng. Asp.* **2013**, *436*, 133–138. [CrossRef]
20. Akanny, E.; Bonhommé, A.; Commun, C.; Doleans-Jordheim, A.; Bessueille, F.; Bourgeois, S.; Bordes, C. Development of un-coated near-spherical gold nanoparticles for the label-free quantification of Lactobacillus rhamnosus GG by surface-enhanced Raman spectroscopy. *Anal. Bioanal. Chem.* **2019**, *411*, 5563–5576. [CrossRef]
21. Leopold, N.; Lendl, B. A new method for fast preparation of highly surface-enhanced Raman scattering (SERS) active silver colloids at room temperature by reduction of silver nitrate with hydroxylamine hydrochloride. *J. Phys. Chem. B* **2003**, *107*, 5723–5727. [CrossRef]
22. Kramberger, P.; Ciringer, M.; Štrancar, A.; Peterka, M. Evaluation of nanoparticle tracking analysis for total virus particle determination. *Virol. J.* **2012**, *9*, 265. [CrossRef] [PubMed]
23. Shiratori, I.; Akitomi, J.; Boltz, D.A.; Horii, K.; Furuichi, M.; Waga, I. Selection of DNA aptamers that bind to influenza A viruses with high affinity and broad subtype specificity. *Biochem. Biophys. Res. Commun.* **2014**, *443*, 37–41. [CrossRef]
24. Musafia, B.; Oren-Banaroya, R.; Noiman, S. Designing anti-influenza aptamers: Novel quantitative structure activity relation-ship approach gives insights into aptamer—virus interaction. *PLoS ONE* **2014**, *9*, e97696. [CrossRef]
25. Pattanayak, S.; Swarnkar, A.; Priyam, A.; Bhalerao, G.M. Citrate–hydrazine hydrogen-bonding driven single-step synthesis of tunable near-IR plasmonic, anisotropic silver nanocrystals: Implications for SERS spectroscopy of inorganic oxoanions. *Dalton Trans.* **2014**, *43*, 11826–11833. [CrossRef] [PubMed]
26. Zhang, Y.; Wang, F.; Yin, H.; Hong, M. Nonuniform distribution of capping ligands promoting aggregation of silver nanopar-ticles for use as a substrate for SERS. *Adv. Nanopart.* **2013**, *02*, 104–111. [CrossRef]
27. Zavyalova, E.; Kopylov, A. G-quadruplexes and i-motifs as scaffolds for molecular engineering of DNA aptamers. In *G-Quadruplex Structures, Formation and Roles in Biology*; Santos, H., Ed.; Nova Publishers: New York, NY, USA, 2016; pp. 53–80.
28. Zavyalova, E.; Kopylov, A. Aptamers to hemagglutinin: A novel tool for influenza virus recognition and neutralization. *Curr. Pharm. Des.* **2016**, *22*, 4835–4853. [CrossRef]
29. Zengin, A.; Tamer, U.; Caykara, T. SERS detection of hepatitis B virus DNA in a temperature-responsive sandwich-hybridization assay: SERS detection of HBV DNA. *J. Raman Spectrosc.* **2017**, *48*, 668–672. [CrossRef]
30. Pang, Y.; Wang, J.; Xiao, R.; Wang, S. SERS molecular sentinel for the RNA genetic marker of PB1-F2 protein in highly pathogenic avian influenza (HPAI) virus. *Biosens. Bioelectron.* **2014**, *61*, 460–465. [CrossRef] [PubMed]
31. Mikac, L.; Ivanda, M.; Gotić, M.; Mihelj, T.; Horvat, L. Synthesis and characterization of silver colloidal nanoparticles with different coatings for SERS application. *J. Nanoparticle Res.* **2014**, *16*, 1–13. [CrossRef]
32. Krutyakov, Y.A.; Kudrinskiy, A.A.; Olenin, A.Y.; Lisichkin, G.V. Synthesis and properties of silver nanoparticles: Advances and prospects. *Russ. Chem. Rev.* **2008**, *77*, 233–257. [CrossRef]
33. Lan, Y.; Zondode, M.; Deng, H.; Yan, J.-A.; Ndaw, M.; Lisfi, A.; Wang, C.; Pan, Y.-L. Basic concepts and recent advances of crystallographic orientation determination of graphene by raman spectroscopy. *Crystals* **2018**, *8*, 375. [CrossRef]
34. Wu, Y.; Jiang, T.; Wu, Z.; Yu, R. Internal standard-based SERS aptasensor for ultrasensitive quantitative detection of Ag+ ion. *Talanta* **2018**, *185*, 30–36. [CrossRef] [PubMed]
35. Liu, J.; Hong, Z.; Yang, W.; Liu, C.; Lu, Z.; Wu, L.; Foda, M.F.; Yang, Z.; Han, H.; Zhao, Y. Bacteria inspired internal standard SERS substrate for quantitative detection. *ACS Appl. Bio Mater.* **2020**. [CrossRef]
36. Wang, Z.; Zong, S.; Wang, Y.; Li, N.; Li, L.; Lu, J.; Wang, Z.; Chen, B.; Cui, Y. Screening and multiple detection of cancer exosomes using an SERS-based method. *Nanoscale* **2018**, *10*, 9053–9062. [CrossRef]
37. Goodacre, R.; Graham, D.; Faulds, K. Recent developments in quantitative SERS: Moving towards absolute quantification. *Trends Anal. Chem.* **2018**, *102*, 359–368. [CrossRef]
38. Shen, W.; Lin, X.; Jiang, C.; Li, C.; Lin, H.; Huang, J.; Wang, S.; Liu, G.; Yan, X.; Zhong, Q.; et al. Reliable quantitative SERS analysis facilitated by core-shell nanoparticles with embedded internal standards. *Angew. Chem. Int. Ed.* **2015**, *54*, 7308–7312. [CrossRef]
39. Lin, Y.-J.; Wu, C.-Y.; Li, T.; Hsiao, P.-W.; Chang, D.-K. A rapid and sensitive early diagnosis of Influenza virus subtype via surface enhanced raman scattering. *J. Biosens. Bioelectron.* **2014**, *5*, 1–5. [CrossRef]
40. Nasirian, V.; Chabok, A.; Barati, A.; Rafienia, M.; Arabi, M.S.; Shamsipur, M. Ultrasensitive aflatoxin B1 assay based on FRET from aptamer labelled fluorescent polymer dots to silver nanoparticles labeled with complementary DNA. *Microchim. Acta* **2017**, *184*, 4655–4662. [CrossRef]
41. Li, G.; Zeng, J.; Liu, H.; Ding, P.; Liang, J.; Nie, X.; Zhou, Z. A fluorometric aptamer nanoprobe for alpha-fetoprotein by ex-ploiting the FRET between 5-carboxyfluorescein and palladium nanoparticles. *Microchim. Acta.* **2019**, *186*, 314. [CrossRef]

International Journal of
Molecular Sciences

MDPI

Review

Epigenetic Targets for Oligonucleotide Therapies of Pulmonary Arterial Hypertension

William Gerthoffer

Department of Pharmacology, Reno School of Medicine, University of Nevada, Reno, NV 89557, USA; wgerthoffer@med.unr.edu; Tel.: +1-775-229-3028

Received: 2 November 2020; Accepted: 30 November 2020; Published: 3 December 2020

Abstract: Arterial wall remodeling underlies increased pulmonary vascular resistance and right heart failure in pulmonary arterial hypertension (PAH). None of the established vasodilator drug therapies for PAH prevents or reverse established arterial wall thickening, stiffening, and hypercontractility. Therefore, new approaches are needed to achieve long-acting prevention and reversal of occlusive pulmonary vascular remodeling. Several promising new drug classes are emerging from a better understanding of pulmonary vascular gene expression programs. In this review, potential epigenetic targets for small molecules and oligonucleotides will be described. Most are in preclinical studies aimed at modifying the growth of vascular wall cells in vitro or normalizing vascular remodeling in PAH animal models. Initial success with lung-directed delivery of oligonucleotides targeting microRNAs suggests other epigenetic mechanisms might also be suitable drug targets. Those targets include DNA methylation, proteins of the chromatin remodeling machinery, and long noncoding RNAs, all of which act as epigenetic regulators of vascular wall structure and function. The progress in testing small molecules and oligonucleotide-based drugs in PAH models is summarized.

Keywords: DNA methylation; histone code; microRNA; nanoparticles; noncoding RNA; pulmonary arterial hypertension

1. Introduction

The set of proteins expressed and the abundance of proteins in cells of the vascular wall is a complex function of transcription, translation, and regulation of protein lifespan. In addition to the heritable protein-coding sequences in DNA, there are epigenetic processes in somatic cells that modify gene expression within a generation to define the somatic epitype (Figure 1) [1]. In this way, the normal gene expression programs and pathological gene expression programs are modulated during development and during adaptation to variations of cellular and organ homeostasis. Diseases that change the extracellular milieu will trigger changes in phenotype in part by activating epigenetic processes. For example, DNA methylation typically inhibits transcription, thus silencing genes not expressed in a given tissue under a given set of conditions. DNA methylation occurs at CpG islands, often in promoters of protein-coding genes. Posttranslational modifications of histones act in tandem with DNA methylation to either repress or permit transcription by opening chromatin to allow access of the transcriptional machinery. Transcription produces several species of protein-coding (mRNA, some circRNAs) and noncoding RNAs (miRNA, lncRNA, circRNAs) that can modulate transcription, mRNA processing, and mRNA stability. The net effect of these epigenetic processes is to regulate protein abundance, which is the defining molecular component of phenotype. Epigenetic processes are highly conserved, occurring in all the cells of the pulmonary circulation. This suggests vascular arteriopathy of pulmonary artery hypertension might respond to drugs that alter one or more epigenetic process. However, there is significant heterogeneity of DNA methylation patterns, histone marks, and noncoding RNA expression patterns among cell types.

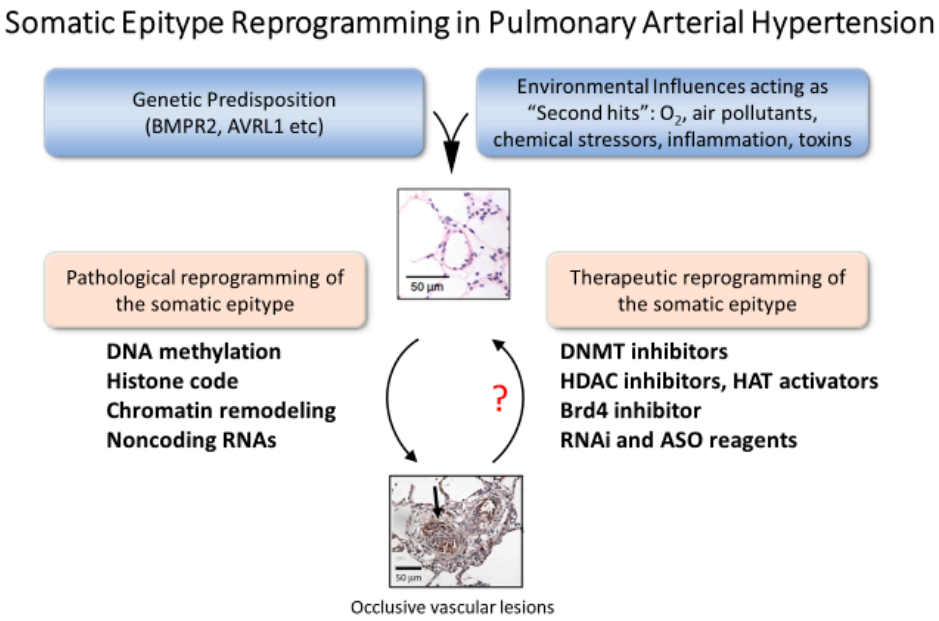

Figure 1. Somatic epitype reprogramming as a therapeutic strategy in PAH. Vascular wall cells involved vascular remodeling are all potential targets for novel epigenetic therapies. Both inflammatory and structural cells of the vascular wall contribute to remodeling in pulmonary hypertension. The therapeutic goal is to modify gene expression programs to reverse and prevent occlusive lesions. The contributions of epigenetic processes to the function of each cell type in the lung is a topic of intense interest and rapid progress in lung cell biology.

Epigenetic therapies could be developed that are effective with tolerable off-target effects. To establish appropriate drug targets, the timing and the necessity for particular epigenetic adaptations in developing pulmonary hypertension need to be defined. Many new drug targets have been described in preclinical studies which are summarized in this review and in several recent reviews of the same topic [2–6]. The premise is that drugs antagonizing both causative and adaptive epigenetic events will prevent disease progression and allow vascular wall repair, thus favoring a return to normal vascular structure. Drug therapy begins well after PAH has developed, often after several years of onset of symptoms. This means new drugs must reverse vascular remodeling to become clinically useful. Several aspects of pulmonary vascular remodeling are of particular interest in this regard—vascular wall thickening, formation of occlusive lesions, and vascular pruning. In this review, some of the landmark studies of epigenetic modifiers in PAH are described along with some more recent work on chromatin remodeling, including BET proteins and noncoding RNAs. Novel oligonucleotide tools and therapeutics are emerging from this very exciting new work. The reader should consult earlier reviews for a general appreciation of advances in epigenetic therapy in other organ systems [7–10].

Targeting epigenetic mechanisms is appealing because enzymatically catalyzed reactions are often reversible, and the enzymes are targets for small molecules and oligonucleotide drugs. This is in sharp contrast to mutations in genomic and mitochondrial DNA, which are not routinely correctable in a clinical setting, although remarkable advances in gene editing technology have created new opportunities that are advancing rapidly [11]. This review will describe recent progress in preclinical studies of small molecule and oligonucleotide modifiers with the goal of focusing on new therapeutic approaches that may add to current treatments of PAH.

2. Pulmonary Vascular Remodeling in PAH

Pulmonary arterial hypertension (WHO Group I) is a rare, progressive pulmonary vascular disease characterized by elevated pulmonary artery pressure (>25 mm Hg), dyspnea, exercise intolerance, and ultimately right heart failure. In the USA, it is more common in women than men (3–5:1) and in

Caucasians (85%) compared to African-Americans (12%) and Hispanics (<3%) [12]. The pathological vascular remodeling in PAH is the result of increased proliferation and decreased apoptosis of vascular wall cells, including smooth muscle, endothelial cells, fibroblasts, and immune cells. Vascular wall hypertrophy is associated with increased inward migration of progenitor cells and immune cells, as well as altered autophagy and cell differentiation. These processes are the subject of intense research to understand basic pulmonary vascular wall cell biology and to identify novel targets for drug development [13–15]. In addition to identifying novel inhibitors of cell signaling, noncoding RNAs (miRNA and long noncoding RNAs) have undergone intense scrutiny as molecular targets for anti-remodeling therapy [16]. In addition, early evidence of changes in DNA methylation [17] and histone marks [18] in pulmonary hypertension stimulated an active search for targets for new therapies [19,20].

There are several issues to address when developing therapies to reprogram the somatic epitype in order to prevent or reverse vascular remodeling. Which processes in which cells should be targeted (Figure 2)? What are the epigenetic drivers of pulmonary remodeling vs. the adaptive responses to disease (Figure 2)? Perhaps most importantly, are there unique targets that produce disease-specific effects such as regulation of bone morphogenetic protein receptor 2 (*BMPR2*) expression and function in subjects with familial PAH? In pulmonary vascular remodeling and repair, the druggable targets include enzymes that catalyze DNA methylation and demethylation, enzymes of DNA repair pathways, enzymes that catalyze histone posttranslational modifications, and noncoding RNAs. Most studies described below are early-stage preclinical trials arranged by biochemical and molecular classes.

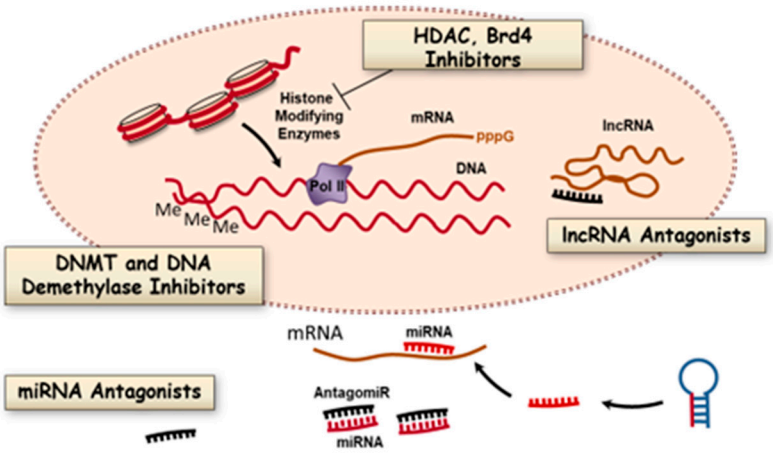

Figure 2. Epigenetic processes that are potential targets for modifying pulmonary vascular remodeling in PAH. There are multiple biochemical processes that promote arteriopathy in PAH by altering gene expression programs in vascular wall cells. These processes are valid therapeutic targets for small molecule inhibitors of DNA methylation and histone modifications and other elements of chromatin remodeling machinery. In addition, oligonucleotide antagonists of short and long noncoding RNAs (miRNAs, lncRNAs) are also potential new classes of antiremodeling drugs.

3. Epigenetic Targets for Novel Therapy of PAH

3.1. DNA Methylation and Inhibitors

One of the major determinants of whether a gene is transcribed is methylation of DNA, typically but not exclusively in CpG islands in promoter regions (Figure 2). DNA methylation is catalyzed by DNA methyltransferase (DNMT) and removed by demethylases. These classes of enzymes have been studied extensively in cancer chemotherapy [21], but less thoroughly in PAH. Although the data on DNA methylation patterns in lung diseases other than lung cancer are less extensive, some interesting patterns have emerged that are relevant to PAH. A landmark study by Archer and coworkers

reported DNA methylation patterns in the superoxide dismutase gene in vascular smooth muscle cells in the Fawn hooded rat model of PAH [17]. Aside from this study, there is no direct evidence for changes in DNA methylation or hydroxymethylation and gene expression in endothelial cells, immune cells, or fibroblasts in PAH. However other studies of related conditions might be relevant to future work. For example, increased methylation of the granulysin gene (*GLYN*) occurs in peripheral blood monocytes of human subjects with pulmonary veno-occlusive disease, but not in patients with PAH [22]. The authors concluded that *GLYN* genes in several T-cell populations (cytotoxic, natural killer and natural killer-like T cells) were not altered in PAH. This suggests some disease-restricted effects on immune cell gene silencing that offer selective targets for drugs altering DNA methylation. Further work in PAH samples is required to find analogous PAH-restricted methylation patterns.

Methylation of the *BMPR2* promoter in scleroderma patients is another relevant observation [23]. Patients with scleroderma may be predisposed to PAH due to *BMPR2* promoter methylation and reduced BMPR2 expression. Later studies of *BMPR2* silencing by DNA methylation in PAH patients are mixed. One study of peripheral blood cell DNA reported no methylation of the *BMPR2* promoter [24], but a more recent study did find increased methylation and reduced expression of BMPR2 protein in heritable PAH [25]. Several mutations of the Tet-methylcytosine-dioxygenase-2 (*TET2)* gene coding for a DNA demethylase have been reported in humans with PAH. Furthermore, *TET2* knockout mice develop a mild form of PAH [26]. These later studies support the significance of dynamic changes in DNA methylation and suggest additional genes might be worth investigating. For example, there is no information on DNA 5mC and 5hmC methylation status of proinflammatory genes in humans with PAH. There is significant infiltration of immune cells into occlusive vascular lesions in humans and in animal models of PAH, but no knowledge of inflammatory gene silencing by DNA modifications. This seems likely given that a genome-wide association study (GWAS) of systemic hypertension found several loci where DNA methylation patterns were associated with hypertension [27]. Similar genome-wide serial DNA methylation studies could be conducted in models of severe PAH models to establish patterns of altered 5mC and 5hmC patterns. Such a study in humans would be challenging due to the low prevalence of PAH and the inability to conduct a longitudinal study of diseased arterial tissue. Despite these limitations, the loci identified in human studies of systemic hypertension might serve as a guide to studies in animal models of severe PAH.

The timing of a therapeutic intervention that reduces DNA methylation will be important to establish. If changes in DNA methylation occur prior to diagnosis (drivers) the damage may be difficult to reverse versus ongoing DNA methylation during the progression of the disease (adaptive responses). It is not clear whether DNA methylation can be selectively modulated with drugs, but there is some reason for optimism. De novo DNA methylation is dynamic and reversible by the action of demethylases. Blocking DNMT activity might be effective in allowing vascular repair, as shown by Archer and coworkers using 5-azacytidine in a rat model of PAH [17]. This study has an important limitation in that 5-azacytidine has pharmacological effects in addition to DNMT inhibition [28]. More selective agents must be developed, preferably with some lung-restricted distribution to minimize off-target effects. Targeting DNA methylation machinery with oligonucleotide-based drugs is an approach tested in cell systems and with knockout mouse models. Several oligonucleotides targeting elements of DNA methylation have been tested as treatments of neurological diseases. Targets include DNMTs 1 and 3 a/b and Tett1 [29–31]. However, similar studies have not been attempted in animal models of pulmonary hypertension. Delivery of oligonucleotides to lung tissues is well established as described below, which suggests that altering the DNA methylation/demethylation machinery might be achievable.

3.2. Histone Modifications and Inhibitors

3.2.1. Histone Deacetylases

Post-translational modifications of histones control chromatin structure by charge effects and by recruiting additional chromatin remodeling enzymes [32]. In general, lysine acetylation of the histone

tails permits transcription. Deacetylation is restrictive, but the effects vary with the particular gene being regulated. Histone acetylation is catalyzed by histone acetyltransferases (HATs) and histone deacetylation by a large family of protein deacetylases (HDACs and sirtuins). Histone marks are modified during normal development and often in disease. The roles in development and diseases have been explored in detail using numerous small molecule inhibitors of protein acetylases and methylases that catalyze histone modification [33]. Several of these have been tested as drugs to modify vascular remodeling, as described in more detail below. Methylation of histones can also be either permissive or restrictive depending upon the methylated residue. Two of the best-studied examples are H3K4 di/tri-methylation, which is permissive, and H3K9 di/tri-methylation, which is restrictive. Histone methylation is catalyzed by histone lysine or arginine methyltransferases. Histone demethylases catalyze the reverse reactions. Some serine residues on histones are phosphorylated, but this topic is less well developed compared to histone methylation and acetylation. There is also emerging evidence for modification of glutamine 5 in histone 3 (H3Q5) with serotonin and dopamine in neuronal tissues, but there is no evidence yet of these interesting modifications in vascular wall cells [34,35]. Disease-restricted alterations in the histone code are the results of changes in activity, chromatin binding, or expression of histone-modifying enzymes. Imbalances in the activity of these enzymes and resulting changes in open versus closed chromatin states are associated with numerous diseases, including pulmonary arterial hypertension (see Figure 2 above).

A growing set of pharmacological studies implicate histone acetylation in PAH by virtue of the effects of HDAC inhibitors on vascular remodeling and cardiac function. Detailed progress at the molecular level is somewhat limited by the modest understanding of exactly which genes to focus on. Some of the earliest evidence supporting HDACs in pulmonary hypertension is from a study of the bovine model of hypoxic pulmonary hypertension [36]. Apicidin, a class I HDAC inhibitor, reduced proinflammatory gene expression in pulmonary adventitial fibroblasts from chronically hypoxic calves. SAHA, a broad spectrum HDAC inhibitor, reduced fibroblast induced migration of monocytes, suggesting that HDACs support vascular inflammation and that HDAC inhibitors can be anti-inflammatory drugs in treating PAH. This begs the question of whether HDAC expression and activity is altered in humans with PAH. In humans with heritable PAH, increased expression of HDACs 1, 4, and 5 was observed, as was a predicted increase in H3 and H4 acetylation [37]. In the same study, valproic acid and SAHA prevented vascular remodeling in a hypoxic rat model.

Inhibiting HDACs in PAH might be beneficial in part because it alters ROS production. In macrophages and THP-1 cells, HDAC inhibitors reduced NOX 1, 2, and 4 expression of macrophages and THP-1 cells by reducing Pol II and p300 HAT loading on *NOX* gene promoters [38]. H3K4me3 and H3K9ac histone marks were also reduced by HDAC inhibition in lung fibroblasts. In pulmonary endothelial cells, there is evidence for HDAC4 and HDAC5 regulating Mef2 activity, which participates in a signaling cascade that influences cell migration and proliferation [20]. The class IIa HDAC inhibitor MC1568 reversed signs of PAH in several rat models, suggesting HDACs 4 and 5 contributed to pulmonary artery endothelial dysfunction. This result is part of an increasing set of studies of HDAC inhibitors in rat models that suggest HDAC inhibitors have beneficial prevention and reversal effects [20,37]. Some of these effects are mediated by nuclear HDACs, but there is also evidence for nonnuclear HDAC6 acting on substrates other than histones to affect pulmonary vascular remodeling [39]. Studies of multiple HDAC inhibitors in multiple PAH models suggest that regulation of proinflammatory genes, pro-growth genes, and promigratory signaling genes are regulated by histone modifications that may well initiate and promote arteriopathy and control PAH severity. Further preclinical studies and mechanistic studies are needed to refine the use of HDAC inhibitors with a goal of identifying the HDAC isoforms to target for the most effective therapy of PAH. In contrast to the significant literature on small molecule HDAC inhibitors in animal models of PAH, there are few studies of oligonucleotides targeting HDACs in vascular tissues.

3.2.2. Histone Acetyltransferases

There are only a few studies of histone acetyltransferases in PAH. It is known that histone acetyltransferase activity is higher in lung tissue of PAH patients [40], but it is less clear that increased histone acetylation promotes inflammation, proliferation, cell migration, or cell survival in the arterial wall. It appears some of the benefits of prostacyclin therapy may be due to modifying histone marks and reducing inflammation. Iloprost decreased secretion of several pro-inflammatory proteins (IL-8, CCL2, RANTES and TNFα) in activated human monocytes [41]. Reduced cytokine production correlated with decreased STAT1 phosphorylation and with decreased localization of the p300 HAT at the STAT1 promoter. This is an interesting observation, but more information is needed to define the proinflammatory genes sensitive to HAT inhibitors and to establish the therapeutic significance of HAT inhibitors for reversing arteriopathy of PAH.

3.2.3. Histone Methylation

Methylation of histones has a cooperative effect with DNA methylation to favor heterochromatin formation and gene repression [42]. During embryonic development, SET histone methyltransferases catalyze H3K9 trimethylation, which enhances DNA methylation by DNMT3a and DNMT3b enzymes [42]. When somatic cells undergo reprogramming during neoplastic transformation, changes in DNA methylation of pluripotency genes are guided in part by histone demethylation. This suggests changes in histone H3K9 methylation might influence vascular remodeling and perivascular inflammation in PAH. To address this question, a recent study investigated the influence of the Nuclear receptor binding SET domain 2 (NSD2) histone methyltransferase. NSD2 is upregulated in some cancers and cancer models where it promotes somatic reprogramming and transformation [43]. In the monocrotaline rat model, knockdown of NSD2 with shRNA reduced H3K36 dimethylation and antagonized pulmonary arterial remodeling, normalized pulmonary artery pressure, and normalized right ventricular dysfunction [44]. Metabolomic analysis suggested NSD2 regulates genes controlling autophagy, carbohydrate metabolism, transporters, and protein synthesis. This is a novel role for histone methylation in PAH that provides an interesting new target for drug therapy. There are a number of small-molecule NSD2 inhibitors in development as anticancer chemotherapy, but no oligonucleotide-based drugs have been reported in human studies. Both approaches might be useful for knocking down NSD2 in vivo in PAH models, although the transfer of cancer chemotherapy approaches to PAH is not always a useful therapeutic strategy. Further preclinical development of NSD2 inhibitors in PAH models is required to address safety and efficacy in nonneoplastic diseases.

3.3. Bromodomain Proteins

Bromodomain-containing proteins bind acetylated lysine residues on histones and function as transcriptional coactivators in the histone code "reader" machinery [45,46]. Vascular remodeling in PAH depends on changes in the transcription of multiple pathways in multiple cell types. One the most important transcriptional regulators is NFkB, particularly for genes expressed during vascular inflammation. NFkB-regulated genes are also dynamically controlled in normal human pulmonary vascular endothelial cells, as shown by cell cycle arrest induced by the BET inhibitor JQ1 [40]. JQ1 increased expression of proteins p19INK4D and p21CIP1 and reduced expression of cyclin-dependent protein kinases. JQ1 treatment also increased HAT activity, presumably due to reducing the association of BET proteins with HATs in histone reader/writer complexes. BET inhibition also inhibits the proliferation of pulmonary artery vascular smooth muscle cells [47]. In both endothelium and smooth muscle cells, BRD4 was the proposed target of JQ1. It appears that BET inhibitors used in a rescue strategy have significant beneficial anti-inflammatory effects in animal models of PAH [48], which is the rationale for a phase 2 clinical trial of apabetalone, an orally available BRD4 inhibitor (ClinicalTrials.gov Identifier: NCT03655704). Recent reports of cardiac toxicity temper

enthusiasm for broad-spectrum BET inhibitors [49]. Isoform-selective drugs and lung-restricted delivery might be necessary to minimize adverse effects on non-targeted organs [48].

In contrast to the significant literature on small molecule inhibitors of histone remodeling in PAH animal models, there is a lack of studies of oligonucleotides targeting HDACs, HATs, or BET proteins in vascular tissues. Although there are numerous antisense oligonucleotides available to modify chromatin remodeling machinery in vitro, there are few or no preclinical drug development studies of PAH models. Drug delivery and tissue specificity are two important problems slowing the development of new oligonucleotide drugs. These two issues have been addressed to some extent by recent studies of oligonucleotides targeting microRNAs in animal models of PAH.

3.4. MicroRNAs

Several classes of noncoding RNAs regulate gene expression and protein abundance to fine-tune cell phenotypes in conditions of health and disease (Figure 3). MicroRNAs, long noncoding RNAs, and circular RNAs are all modulators of steps in the flow of genetic sequence information from genomic DNA to mRNA and to proteins. Transcription of mRNA depends on the synthesis of adequate numbers of ribosomes. Ribosome biogenesis requires a variety of small nucleolar RNAs that are structural elements of ribosomes, as well as small nuclear RNAs that participate in mRNA splicing and processing of mature mRNA. Once processed and associated with ribosomes, mature mRNAs are translated to peptides by complex biochemical machinery subject to extensive regulation. MicroRNAs fine-tune the output of gene expression programs by modulating translation, thus varying protein abundance and cell phenotype.

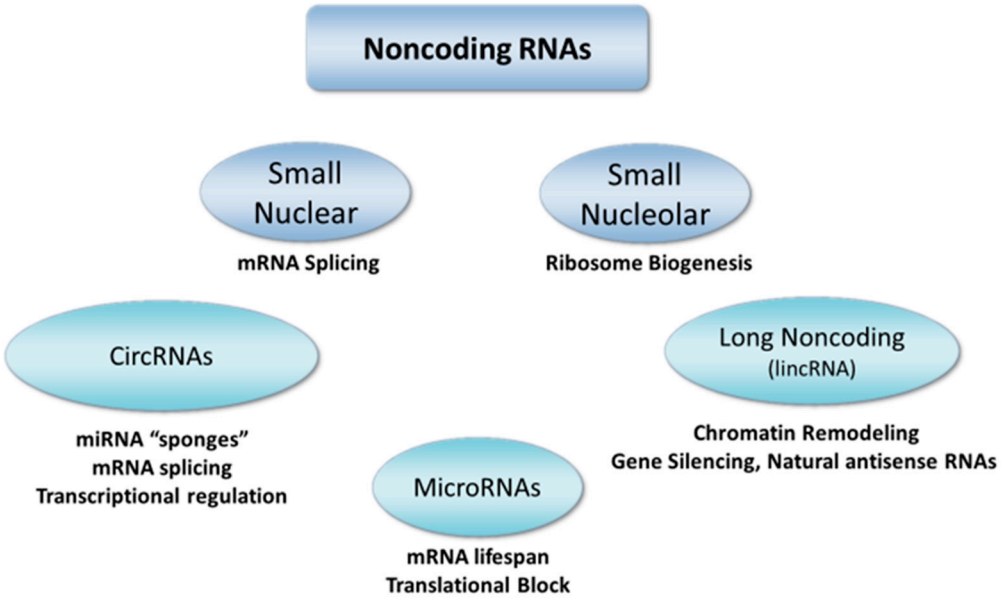

Figure 3. Classes of noncoding RNAs. Cell growth, organ development, and pathological remodeling all depend on dynamic changes in the expression of noncoding RNAs. MicroRNAs are the best-established class of noncoding RNAs with important roles in regulating the translation of proteins that remodel the pulmonary vasculature. Long noncoding RNAs are also modified during the development of PAH, but their functions are less clear. Circular RNAs are emerging as collaborators with the other classes of RNAs to regulate mRNA production, transcription, and gene silence via interactions with miRNAs. miRNAs, long noncoding RNAs, and circular RNAs are all potentially targetable molecules using lung-directed delivery of oligonucleotide antagonists and mimics.

Numerous correlative studies of miRNA expression in vascular tissue from humans have defined altered miRNA expression patterns in PAH. The miR-17~92 cluster, MiR-21, miR-145, and miR-204 were the first miRNAs associated with PAH [50–54] (Table 1). Similar lists of miRNAs altered in animal

models have also been assembled and are described in prior reviews [4,55,56]. Early correlative studies stimulated preclinical translational studies designed to normalize miRNA expression and to halt or reverse the progression of PAH. There is now substantial proof of the efficacy of RNAi-based therapies targeting miRNAs in PAH. Preclinical prevention trials in animal models of PAH have described the roles of miR-204 [52], miR-17 [57], miR-21 [58], miR-20a [59], miR-145 [53,60], miR-223 [61], miR-424, and miR-503 [62] in PAH pathology.

Table 1. Noncoding RNA targets in pulmonary arterial hypertension.

miRNAs	Long Noncoding RNAs
let-7f/miR-22/30 [51]	CASC2 [63]
miR-17/92 cluster [50,57]	H19 [64]
miR-21 [51]	Hoxaas3 [65]
miR-23b/130a/191/451/1246 3 [66]	HOXB1, CBL, GDF7, RND1 [67]
miR-124 [68]	LnRPT [69,70]
miR-143 [54]	MALAT1 [71], [72]
miR-145 [53]	Tug1 [73]
miR-204 [52]	UCA1 [74]
miR-206 [75]	
miR-322/451 [51]	
miR-424/503 [62]	

One limitation of initial studies of miRNA mimics and antagonists is that none used intravenous therapy to achieve lung-directed delivery. They also used prevention protocols rather than a rescue protocol to reverse severe occlusive vascular remodeling. This limitation is relevant to drug therapy because humans are diagnosed with PAH after it is well established, not prior to the development of arteriopathy and cardiac dysfunction. A later reversal study [60] employing a pegylated cationic lipid nanoparticle (Therasilence) delivered intravenously showed that a miR-145 antagonist could ameliorate many pathological features of established PAH in the Sugen/hypoxia rat model of severe PAH (Figure 4A). The miR-145 antisense oligonucleotide was a locked nucleic acid/DNA mixmer that achieved high levels in lung tissues (Figure 4B). AntimiR-145 treatment partially reversed vascular wall thickening (Figure 4C). Right ventricular systolic pressure was reduced, and there was a modest reduction of perivascular inflammation. Similar anti-inflammatory effects were reported in another reversal study by Gubrij et al. [61] using a miR-223 antagonist in the monocrotaline rat model of PAH. The studies summarized in Table 1 include both prevention trials and reversal trials in animal models showing that therapeutic oligonucleotides targeting microRNAs can be delivered to the lung via the airway or from the vascular compartment to ameliorate vascular inflammation, vascular medial thickening, and occlusive vascular lesions in PAH.

One question that remains unanswered is which cell types should be targeted in treating PAH with oligonucleotide drugs? Many mechanistic studies of miRNAs in pulmonary artery remodeling have focused on endothelial cells and vascular smooth muscle cells. However, some miRNAs associated with PAH in humans (miR-145, miR-155, miR-21 and the miR-17~92 cluster) also regulate inflammation and immune cell biology. For example, IL-6 upregulates expression of the miR-17~92 cluster, which targets BMPR2, suggesting that inflammation exacerbates PAH by inhibiting BMPR2 signaling. MiR-145 is known to regulate cell fate during early embryogenesis and is a master regulator of smooth muscle contractile phenotype. It also regulates the immune response by promoting M1 to M2 macrophage polarization [76] and Th2 cell development in the airways and thoracic lymph nodes [77]. MiR-21 is pro-inflammatory in mouse models of severe asthma [78]. MiR-124 silences MCP1 expression in adventitial fibroblasts, which probably influences the extent of vascular inflammation [79]. Future

translational studies of miRNA antagonists could be designed to target multiple protein networks known to mediate vascular wall remodeling and perivascular inflammation. MicroRNA antagonists and mimics with combined vasodilating, anti-inflammatory, and anti-remodeling effects would constitute a novel class of therapy to complement and improve the efficacy of current vasodilator therapy. However, early-phase clinical trials have not yet been conducted on human subjects. One limitation is the complexity of drug delivery to the lungs. Complexing oligonucleotide drugs with carriers such as lipid nanoparticles or carbohydrate polymers clearly works in preclinical animal models. However, the delivery system may have pharmacological effects unrelated to the oligonucleotide target, which adds significant barriers to regulatory approval for use in humans.

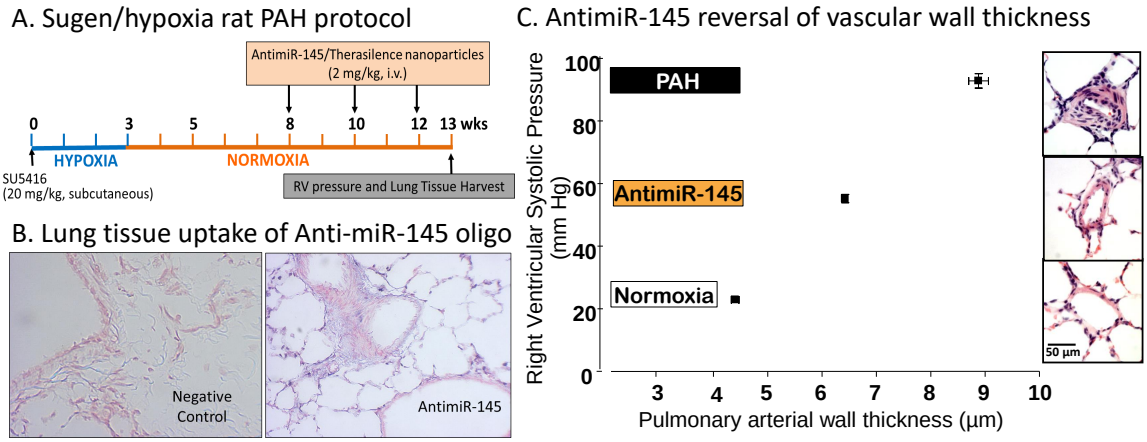

Figure 4. A rat model of severe PAH employed treatment with Sugen5416 followed by a period of hypoxia. Right ventricular systolic pressure (RVSP) increased to >90 mmHg at 13 weeks (**A**). Lung tissue uptake of the antimiR-145 antisense oligonucleotide was assessed by in situ hybridization (**B**), blue staining). (**C**) shows a positive correlation of RVSP with vessel wall thickness in small pulmonary arteries (50–200 μm dia.). AntimiR-145 treatment partially reversed both wall thickening and RVSP. Data are replotted from McLendon et al. [60].

3.5. Long Noncoding RNAs

Long RNAs (>200nt) not translated to proteins (lncRNA) are transcribed from a variety of sites in the nuclear genome. There are lncRNAs from enhancer sequences of protein-coding genes (eRNAs) [80], RNAs from intergenic, multiexomic regions (lincRNAs) [81], and from noncoding strands of protein-coding genes (naturally occurring antisense transcripts, NATs) [82,83] (see Figure 5). The term long noncoding RNAs (lncRNA) will refer to all RNAs > 200 nt that do not code for proteins. The functions of most long noncoding RNAs are still being defined. Some are thought to serve as adapter molecules able to bind proteins, DNA, and other RNAs. This versatile set of binding reactions underlies some of the functions of lncRNAs which include: Regulation of transcription by controlling gene looping [80,84], regulation of mRNA splicing [85], regulation of mRNA lifespan [63,86], and organization of gene neighborhoods [87] (Figure 5). Recent work in various PAH models describe the influence of lncRNAs on microRNA function [73,88], on scaffolding functions [67], and on vascular cell proliferation and differentiation [63–65,74] (Table 1). Collectively, these studies strongly suggest lncRNAs are valuable targets for further translational drug development.

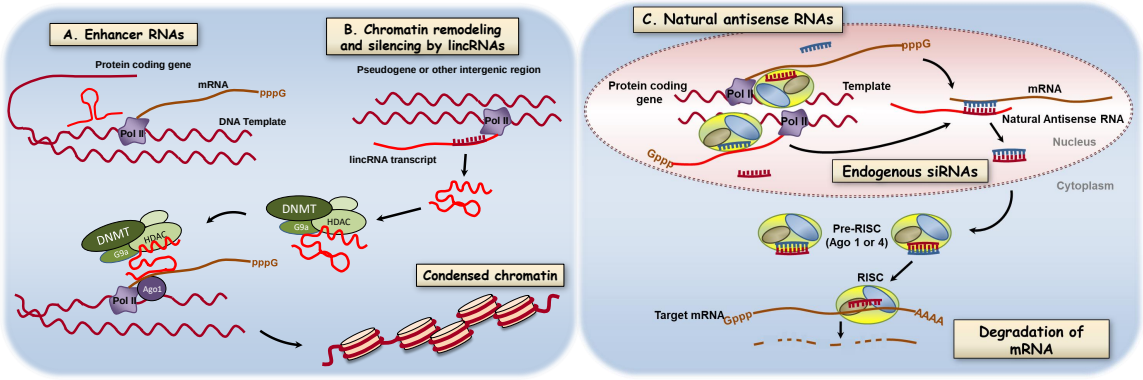

Figure 5. Regulation of gene expression by long noncoding RNAs. Long nonprotein coding RNAs are transcribed from a variety of genomic loci including enhancer sequences (eRNAs), intergenic, multiexomic sequences (lincRNAs), and noncoding strands of protein-coding genes (naturally occurring antisense transcripts. Shown here are two of the emerging mechanisms by which lncRNAs modify gene expression and protein abundance. (**A**) Binding of RNAs coded in enhancer regions to effect DNA looping. (**B**) lncRNA serving as an adapter molecule in chromatin remodeling via DNA methylation and histone modifications. A salient feature of lncRNAs is the potential to bind chromatin remodeling proteins, DNA, and in some cases other RNAs. (**C**) Some long noncoding RNAs are processed to endogenous siRNAs that regulate transcription or regulate translation by altering mRNA decay. Some long noncoding RNAs also modify mRNA splicing (not shown). Targeting new oligonucleotide drugs to lncRNA function will require identification of key lncRNAs in lung diseases and defining the contribution of these mechanisms to pathology. Reproduced from Comer et al. [55] with permission from Elsevier.

Although recent observational studies reveal the association between lncRNAs and PAH, it will be important to determine what strategies are used to modify lncRNA expression and function in the pulmonary circulation. Antisense oligonucleotides ("antagoNATs") that inactivate lncRNAs in cells and in animal models of disease have been proposed [89] and used effectively in several of the recent studies of PAH cited above. The response to a lncRNA antagonist may be to increase protein expression if the lncRNA is a repressor of gene expression, or to reduce protein expression if the lncRNA is an enhancer. For example, inhibiting the function of MALAT1 reduces endothelial cell differentiation in vitro [90]. A MALAT1 antagonist active in vivo might reduce occlusive lesions in pulmonary arterial hypertension or inhibit airway epithelial cell proliferation. This notion is supported by the fact that polymorphisms in the *MALAT1* gene have been described in humans with essential hypertension [72]. MALAT1 reduced miR-539-3p and miR-485-3p levels and increased expression of BMP receptor type 2. The authors suggested low plasma levels of MALAT1 correlated with increased miRNA expression and reduced BMPR2 expression, conditions associated with PAH. Other lncRNAs might be targeted by oligonucleotides to inhibit lncRNAs that act as "sponges" for miRNAs. In this use case, the drugs would increase the expression of proteins repressed by the miRNA binding partners. The lncRNAs and proteins targeted might be proteins with anti-inflammatory effects [91], antiproliferative effects, or antimigratory effects. Another interesting strategy that remains untested is to disrupt lncRNA function with small molecules that bind to RNA secondary structure or disrupt the tertiary structure of ribonucleoprotein complexes [92].

4. Summary and Future Directions

The prospect of modifying epigenetic processes to alter the interaction of genes and the environment in pulmonary vascular cells is exciting and important. The premise is that cell phenotype and vessel architecture are determined by reversible biochemical processes acting on the genetic substrate. This is the mechanistic basis for several anticancer drugs that modify the epigenetic processes described in this review. In cancer chemotherapy, single epigenetic modifying drugs and combination therapies that

include epigenetic modifiers are effective in some cases, but ideal drug regimens are still being defined. Successful epigenetic reprogramming in lung cancer chemotherapy is very encouraging and highly relevant to epigenetic therapy for PAH [93,94]. If normal control of cell proliferation, cell survival, and tissue boundaries is compromised, then vascular tissue growth might be reversible with drugs that reestablish normal epigenetic processes, normal cell phenotype, and normal tissue architecture. However, treating a nonneoplastic lung disease such as PAH with oligonucleotide drugs targeting epigenetic mechanisms is a relatively new enterprise. Repurposing anticancer drugs in PAH has produced mixed results but the idea that epigenetic reprogramming can be affected with drugs is worth pursuing. Most work is in vitro or in early preclinical stages. Recent progress in early-stage clinical trials is summarized in several reviews [95,96].

There are still significant gaps in knowledge that limit the development of epigenetic modifying oligonucleotide drugs. We need better descriptions of which miRNAs, lncRNAs, circRNAs, histone modifications, and DNA methylation sites are present at the single-cell level in PAH. We also need important longitudinal studies of epigenetic features in individual pulmonary vascular wall cells and in key genes controlling cell phenotype [2]. Serial genome-wide assays are needed to define which epigenetic events are causes and which are consequences of the disease. This would be analogous to GWAS studies of genomic DNA sequences, the key difference being that epigenetic modifications are dynamic and reversible. Therefore, longitudinal data similar to data used to validated prognostic biomarkers are needed to establish the best targets and the best timing of dosing. The function of the epigenetic marks and the pathways regulated then need to be validated in both human samples and in multiple clinically relevant animal models. Once high-value targets are identified, candidate drugs must be validated in preclinical animal trials and ultimately in initial clinical trials to establish efficacy, lung-directed delivery, and off-target effects. Potential adverse effects of oligonucleotide therapies that would appear in phase 2 clinical trials are difficult to predict. They will depend on the targets and on pharmacologic effects unrelated to the targets. For example, targeting conserved DNA and histone-modifying enzymes with broad-spectrum drugs that are widely distributed can disrupt organ function well beyond the lungs—e.g., in the bone marrow, heart, liver, kidneys or nervous system. Small oligonucleotides are also perceived by the immune system as damage-associated or pathogen-associated molecular patterns which can activate the innate immune response to deleterious effect [97,98]. Managing the off-target effects of oligonucleotide drugs is a challenge that needs to be overcome. However, if effective and safe oligonucleotides can be delivered preferentially to the lungs, they could become important adjuncts to vasodilator therapies that could act as true disease-modifying therapies.

Author Contributions: W.G. conceived of the topic and wrote the manuscript. All authors have read and agreed to the published version of the manuscript.

Funding: This publication was made possible by a grant from the National Institute of General Medical Sciences (GM103440) from the National Institutes of Health.

Conflicts of Interest: The author declares no conflict of interest. The funders had no role in the design of the study; in the collection, analyses, or interpretation of data; in the writing of the manuscript, or in the decision to publish the results.

Abbreviations

DNMT	DNA methyltransferase
HAT	histone acetyltransferase
HDAC	histone deacetylase
lncRNA	long noncoding RNA
MALAT1	metastasis associated lung adenocarcinoma transcript 1
miRNA	microRNA
NSD2	nuclear receptor binding SET domain 2
PAH	pulmonary arterial hypertension
RVSP	right ventricular systolic pressure

References

1. Lahiri, D.K.; Maloney, B. Genes are not our destiny: The somatic epitype bridges between the genotype and the phenotype. *Nat. Rev. Neurosci.* **2006**, *7*, 976. [CrossRef]
2. Chelladurai, P.; Seeger, W.; Pullamsetti, S.S. Epigenetic mechanisms in pulmonary arterial hypertension: The need for global perspectives. *Eur. Respir. Rev.* **2016**, *25*, 135–140. [CrossRef] [PubMed]
3. Luna, R.C.P.; de Oliveira, Y.; Lisboa, J.V.C.; Chaves, T.R.; de Araujo, T.A.M.; de Sousa, E.E.; Miranda Neto, M.; Pirola, L.; Braga, V.A.; de Brito Alves, J.L. Insights on the epigenetic mechanisms underlying pulmonary arterial hypertension. *Braz. J. Med. Biol. Res.* **2018**, *51*, e7437. [CrossRef] [PubMed]
4. Wang, Y.; Yan, L.; Zhang, Z.; Prado, E.; Fu, L.; Xu, X.; Du, L. Epigenetic Regulation and Its Therapeutic Potential in Pulmonary Hypertension. *Front. Pharmacol.* **2018**, *9*, 241. [CrossRef] [PubMed]
5. Chelladurai, P.; Boucherat, O.; Stenmark, K.; Kracht, M.; Seeger, W.; Bauer, U.M.; Bonnet, S.; Pullamsetti, S.S. Targeting histone acetylation in pulmonary hypertension and right ventricular hypertrophy. *Br. J. Pharmacol.* **2019**. [CrossRef]
6. Humbert, M.; Guignabert, C.; Bonnet, S.; Dorfmuller, P.; Klinger, J.R.; Nicolls, M.R.; Olschewski, A.J.; Pullamsetti, S.S.; Schermuly, R.T.; Stenmark, K.R.; et al. Pathology and pathobiology of pulmonary hypertension: State of the art and research perspectives. *Eur. Respir. J.* **2019**, *53*, 1801887. [CrossRef]
7. Dhanak, D.; Jackson, P. Development and Classes of Epigenetic Drugs for Cancer. *Biochem. Biophys. Res. Commun.* **2014**, *455*, 58–69. [CrossRef]
8. Haldar, S.M.; McKinsey, T.A. BET-ting on chromatin-based therapeutics for heart failure. *J. Mol. Cell Cardiol.* **2014**, *74C*, 98–102. [CrossRef]
9. Natarajan, R. Drugs targeting epigenetic histone acetylation in vascular smooth muscle cells for restenosis and atherosclerosis. *Arter. Thromb. Vasc. Biol.* **2011**, *31*, 725–727. [CrossRef]
10. Tao, H.; Shi, K.H.; Yang, J.J.; Huang, C.; Zhan, H.Y.; Li, J. Histone deacetylases in cardiac fibrosis: Current perspectives for therapy. *Cell Signal.* **2014**, *26*, 521–527. [CrossRef]
11. Doudna, J.A. The promise and challenge of therapeutic genome editing. *Nature* **2020**, *578*, 229–236. [CrossRef] [PubMed]
12. Prins, K.W.; Thenappan, T. World Health Organization Group I Pulmonary Hypertension: Epidemiology and Pathophysiology. *Cardiol. Clin.* **2016**, *34*, 363–374. [CrossRef] [PubMed]
13. Morrell, N.W.; Archer, S.L.; Defelice, A.; Evans, S.; Fiszman, M.; Martin, T.; Saulnier, M.; Rabinovitch, M.; Schermuly, R.; Stewart, D.; et al. Anticipated classes of new medications and molecular targets for pulmonary arterial hypertension. *Pulm. Circ.* **2013**, *3*, 226–244. [CrossRef] [PubMed]
14. Tuder, R.M.; Archer, S.L.; Dorfmuller, P.; Erzurum, S.C.; Guignabert, C.; Michelakis, E.; Rabinovitch, M.; Schermuly, R.; Stenmark, K.R.; Morrell, N.W. Relevant issues in the pathology and pathobiology of pulmonary hypertension. *J. Am. Coll. Cardiol.* **2013**, *62* (Suppl. 25), D4–D12. [CrossRef]
15. Stratton, M.S.; Farina, F.M.; Elia, L. Epigenetics and vascular diseases. *J. Mol. Cell. Cardiol.* **2019**, *133*, 148–163. [CrossRef]
16. White, K.; Loscalzo, J.; Chan, S.Y. Holding our breath: The emerging and anticipated roles of microRNA in pulmonary hypertension. *Pulm. Circ.* **2012**, *2*, 278–290. [CrossRef]
17. Archer, S.L.; Marsboom, G.; Kim, G.H.; Zhang, H.J.; Toth, P.T.; Svensson, E.C.; Dyck, J.R.; Gomberg-Maitland, M.; Thebaud, B.; Husain, A.N.; et al. Epigenetic attenuation of mitochondrial superoxide dismutase 2 in pulmonary arterial hypertension: A basis for excessive cell proliferation and a new therapeutic target. *Circulation* **2010**, *121*, 2661–2671. [CrossRef]
18. Xu, X.F.; Ma, X.L.; Shen, Z.; Wu, X.L.; Cheng, F.; Du, L.Z. Epigenetic regulation of the endothelial nitric oxide synthase gene in persistent pulmonary hypertension of the newborn rat. *J. Hypertens.* **2010**, *28*, 2227–2235. [CrossRef]
19. Pullamsetti, S.S.; Perros, F.; Chelladurai, P.; Yuan, J.; Stenmark, K. Transcription factors, transcriptional coregulators, and epigenetic modulation in the control of pulmonary vascular cell phenotype: Therapeutic implications for pulmonary hypertension (2015 Grover Conference series). *Pulm. Circ.* **2016**, *6*, 448–464. [CrossRef]
20. Kim, J.D.; Lee, A.; Choi, J.; Park, Y.; Kang, H.; Chang, W.; Lee, M.S.; Kim, J. Epigenetic modulation as a therapeutic approach for pulmonary arterial hypertension. *Exp. Mol. Med.* **2015**, *47*, e175. [CrossRef]

21. Gros, C.; Fahy, J.; Halby, L.; Dufau, I.; Erdmann, A.; Gregoire, J.M.; Ausseil, F.; Vispe, S.; Arimondo, P.B. DNA methylation inhibitors in cancer: Recent and future approaches. *Biochimie* **2012**, *94*, 2280–2296. [CrossRef] [PubMed]
22. Perros, F.; Cohen-Kaminsky, S.; Gambaryan, N.; Girerd, B.; Raymond, N.; Klingelschmitt, I.; Huertas, A.; Mercier, O.; Fadel, E.; Simonneau, G.; et al. Cytotoxic cells and granulysin in pulmonary arterial hypertension and pulmonary veno-occlusive disease. *Am. J. Respir. Crit. Care Med.* **2013**, *187*, 189–196. [CrossRef] [PubMed]
23. Wang, Y.; Kahaleh, B. Epigenetic repression of bone morphogenetic protein receptor II expression in scleroderma. *J. Cell. Mol. Med.* **2013**, *17*, 1291–1299. [CrossRef] [PubMed]
24. Pousada, G.; Baloira, A.; Valverde, D. Methylation Analysis of the BMPR2 Gene Promoter Region in Patients With Pulmonary Arterial Hypertension. *Arch. Bronconeumol.* **2016**, *52*, 293–298. [CrossRef] [PubMed]
25. Liu, D.; Yan, Y.; Chen, J.W.; Yuan, P.; Wang, X.J.; Jiang, R.; Wang, L.; Zhao, Q.H.; Wu, W.H.; Simonneau, G.; et al. Hypermethylation of BMPR2 Promoter Occurs in Patients with Heritable Pulmonary Arterial Hypertension and Inhibits BMPR2 Expression. *Am. J. Respir. Crit. Care Med.* **2017**, *196*, 925–928. [CrossRef] [PubMed]
26. Potus, F.; Pauciulo, M.W.; Cook, E.K.; Zhu, N.; Hsieh, A.; Welch, C.L.; Shen, Y.; Tian, L.; Lima, P.; Mewburn, J.; et al. Novel Mutations and Decreased Expression of the Epigenetic Regulator TET2 in Pulmonary Arterial Hypertension. *Circulation* **2020**, *141*, 1986–2000. [CrossRef]
27. Kato, N.; Loh, M.; Takeuchi, F.; Verweij, N.; Wang, X.; Zhang, W.; Kelly, T.N.; Saleheen, D.; Lehne, B.; Mateo Leach, I.; et al. Trans-ancestry genome-wide association study identifies 12 genetic loci influencing blood pressure and implicates a role for DNA methylation. *Nat. Genet.* **2015**, *47*, 1282–1293. [CrossRef]
28. Pechalrieu, D.; Etievant, C.; Arimondo, P.B. DNA methyltransferase inhibitors in cancer: From pharmacology to translational studies. *Biochem. Pharmacol.* **2017**, *129*, 1–13. [CrossRef]
29. Rudenko, A.; Dawlaty, M.M.; Seo, J.; Cheng, A.W.; Meng, J.; Le, T.; Faull, K.F.; Jaenisch, R.; Tsai, L.H. Tet1 is critical for neuronal activity-regulated gene expression and memory extinction. *Neuron* **2013**, *79*, 1109–1122. [CrossRef]
30. Feng, J.; Zhou, Y.; Campbell, S.L.; Le, T.; Li, E.; Sweatt, J.D.; Silva, A.J.; Fan, G. Dnmt1 and Dnmt3a maintain DNA methylation and regulate synaptic function in adult forebrain neurons. *Nat. Neurosci.* **2010**, *13*, 423–430. [CrossRef]
31. Southwell, A.L.; Skotte, N.H.; Bennett, C.F.; Hayden, M.R. Antisense oligonucleotide therapeutics for inherited neurodegenerative diseases. *Trends Mol. Med.* **2012**, *18*, 634–643. [CrossRef] [PubMed]
32. Bannister, A.J.; Kouzarides, T. Regulation of chromatin by histone modifications. *Cell Res.* **2011**, *21*, 381–395. [CrossRef] [PubMed]
33. Rodríguez-Paredes, M.; Esteller, M. Cancer epigenetics reaches mainstream oncology. *Nat. Med.* **2011**, *17*, 330–339. [CrossRef] [PubMed]
34. Fu, L.; Zhang, L. Serotonylation: A novel histone H3 marker. *Signal Transduct. Target. Ther.* **2019**, *4*, 15. [CrossRef] [PubMed]
35. Lepack, A.E.; Werner, C.T.; Stewart, A.F.; Fulton, S.L.; Zhong, P.; Farrelly, L.A.; Smith, A.C.W.; Ramakrishnan, A.; Lyu, Y.; Bastle, R.M.; et al. Dopaminylation of histone H3 in ventral tegmental area regulates cocaine seeking. *Science* **2020**, *368*, 197–201. [CrossRef] [PubMed]
36. Li, M.; Riddle, S.R.; Frid, M.G.; El Kasmi, K.C.; McKinsey, T.A.; Sokol, R.J.; Strassheim, D.; Meyrick, B.; Yeager, M.E.; Flockton, A.R.; et al. Emergence of fibroblasts with a proinflammatory epigenetically altered phenotype in severe hypoxic pulmonary hypertension. *J. Immunol.* **2011**, *187*, 2711–2722. [CrossRef] [PubMed]
37. Zhao, L.; Chen, C.N.; Hajji, N.; Oliver, E.; Cotroneo, E.; Wharton, J.; Wang, D.; Li, M.; McKinsey, T.A.; Stenmark, K.R.; et al. Histone deacetylation inhibition in pulmonary hypertension: Therapeutic potential of valproic acid and suberoylanilide hydroxamic acid. *Circulation* **2012**, *126*, 455–467. [CrossRef] [PubMed]
38. Chen, F.; Li, X.; Aquadro, E.; Haigh, S.; Zhou, J.; Stepp, D.W.; Weintraub, N.L.; Barman, S.A.; Fulton, D.J. Inhibition of histone deacetylase reduces transcription of NADPH oxidases and ROS production and ameliorates pulmonary arterial hypertension. *Free Radic. Biol. Med.* **2016**, *99*, 167–178. [CrossRef]
39. Boucherat, O.; Chabot, S.; Paulin, R.; Trinh, I.; Bourgeois, A.; Potus, F.; Lampron, M.C.; Lambert, C.; Breuils-Bonnet, S.; Nadeau, V.; et al. HDAC6: A Novel Histone Deacetylase Implicated in Pulmonary Arterial Hypertension. *Sci. Rep.* **2017**, *7*, 4546. [CrossRef]
40. Mumby, S.; Gambaryan, N.; Meng, C.; Perros, F.; Humbert, M.; Wort, S.J.; Adcock, I.M. Bromodomain and extra-terminal protein mimic JQ1 decreases inflammation in human vascular endothelial cells: Implications for pulmonary arterial hypertension. *Respirology* **2017**, *22*, 157–164. [CrossRef]

41. Strassheim, D.; Riddle, S.R.; Burke, D.L.; Geraci, M.W.; Stenmark, K.R. Prostacyclin inhibits IFN-gamma-stimulated cytokine expression by reduced recruitment of CBP/p300 to STAT1 in a SOCS-1-independent manner. *J. Immunol.* **2009**, *183*, 6981–6988. [CrossRef]
42. Cedar, H.; Bergman, Y. Linking DNA methylation and histone modification: Patterns and paradigms. *Nat. Rev. Genet.* **2009**, *10*, 295–304. [CrossRef] [PubMed]
43. Bennett, R.L.; Swaroop, A.; Troche, C.; Licht, J.D. The Role of Nuclear Receptor-Binding SET Domain Family Histone Lysine Methyltransferases in Cancer. *Cold Spring Harb. Perspect. Med.* **2017**, *7*, a026708. [CrossRef] [PubMed]
44. Zhou, X.L.; Liu, Z.B.; Zhu, R.R.; Huang, H.; Xu, Q.R.; Xu, H.; Zeng, L.; Li, Y.Y.; Huang, C.H.; Wu, Q.C.; et al. NSD2 silencing alleviates pulmonary arterial hypertension by inhibiting trehalose metabolism and autophagy. *Clin. Sci.* **2019**, *133*, 1085–1096. [CrossRef] [PubMed]
45. Arrowsmith, C.H.; Bountra, C.; Fish, P.V.; Lee, K.; Schapira, M. Epigenetic protein families: A new frontier for drug discovery. *Nat. Rev. Drug Discov.* **2012**, *11*, 384–400. [CrossRef] [PubMed]
46. Zhang, W.; Prakash, C.; Sum, C.; Gong, Y.; Li, Y.; Kwok, J.J.T.; Thiessen, N.; Pettersson, S.; Jones, S.J.M.; Knapp, S.; et al. Bromodomain-containing protein 4 (BRD4) regulates RNA polymerase II serine 2 phosphorylation in human CD4+ T cells. *J. Biol. Chem.* **2012**, *287*, 43137–43155. [CrossRef] [PubMed]
47. Meloche, J.; Renard, S.; Provencher, S.; Bonnet, S. Anti-inflammatory and immunosuppressive agents in PAH. *Handb. Exp. Pharmacol.* **2013**, *218*, 437–476. [PubMed]
48. Van der Feen, D.E.; Kurakula, K.; Tremblay, E.; Boucherat, O.; Bossers, G.P.; Szulcek, R.; Bourgeois, A.; Lampron, M.C.; Habbout, K.; Martineau, S.; et al. Multicenter Preclinical Validation of BET Inhibition for the Treatment of Pulmonary Arterial Hypertension. *Am. J. Respir. Crit. Care Med.* **2019**, *200*, 910–920. [CrossRef]
49. Piquereau, J.; Boet, A.; Pechoux, C.; Antigny, F.; Lambert, M.; Gressette, M.; Ranchoux, B.; Gambaryan, N.; Domergue, V.; Mumby, S.; et al. The BET Bromodomain Inhibitor I-BET-151 Induces Structural and Functional Alterations of the Heart Mitochondria in Healthy Male Mice and Rats. *Int. J. Mol. Sci.* **2019**, *20*, 1527. [CrossRef]
50. Brock, M.; Trenkmann, M.; Gay, R.E.; Michel, B.A.; Gay, S.; Fischler, M.; Ulrich, S.; Speich, R.; Huber, L.C. Interleukin-6 modulates the expression of the bone morphogenic protein receptor type II through a novel STAT3-microRNA cluster 17/92 pathway. *Circ. Res.* **2009**, *104*, 1184–1191. [CrossRef]
51. Caruso, P.; MacLean, M.R.; Khanin, R.; McClure, J.; Soon, E.; Southgate, M.; MacDonald, R.A.; Greig, J.A.; Robertson, K.E.; Masson, R.; et al. Dynamic changes in lung microRNA profiles during the development of pulmonary hypertension due to chronic hypoxia and monocrotaline. *Arter. Thromb. Vasc. Biol.* **2010**, *30*, 716–723. [CrossRef] [PubMed]
52. Courboulin, A.; Paulin, R.; Giguere, N.J.; Saksouk, N.; Perreault, T.; Meloche, J.; Paquet, E.R.; Biardel, S.; Provencher, S.; Cote, J.; et al. Role for miR-204 in human pulmonary arterial hypertension. *J. Exp. Med.* **2011**, *208*, 535–548. [CrossRef] [PubMed]
53. Caruso, P.; Dempsie, Y.; Stevens, H.C.; McDonald, R.A.; Long, L.; Lu, R.; White, K.; Mair, K.M.; McClure, J.D.; Southwood, M.; et al. A role for miR-145 in pulmonary arterial hypertension: Evidence from mouse models and patient samples. *Circ. Res.* **2012**, *111*, 290–300. [CrossRef]
54. Bockmeyer, C.L.; Maegel, L.; Janciauskiene, S.; Rische, J.; Lehmann, U.; Maus, U.A.; Nickel, N.; Haverich, A.; Hoeper, M.M.; Golpon, H.A.; et al. Plexiform vasculopathy of severe pulmonary arterial hypertension and microRNA expression. *J. Heart Lung Transplant.* **2012**, *31*, 764–772. [CrossRef]
55. Comer, B.S.; Ba, M.; Singer, C.A.; Gerthoffer, W.T. Epigenetic targets for novel therapies of lung diseases. *Pharmacol. Ther.* **2015**, *147*, 91–110. [CrossRef] [PubMed]
56. Boucherat, O.; Potus, F.; Bonnet, S. microRNA and Pulmonary Hypertension. *Adv. Exp. Med. Biol.* **2015**, *888*, 237–252. [PubMed]
57. Pullamsetti, S.S.; Doebele, C.; Fischer, A.; Savai, R.; Kojonazarov, B.; Dahal, B.K.; Ghofrani, H.A.; Weissmann, N.; Grimminger, F.; Bonauer, A.; et al. Inhibition of microRNA-17 improves lung and heart function in experimental pulmonary hypertension. *Am. J. Respir. Crit Care Med.* **2012**, *185*, 409–419. [CrossRef]
58. Parikh, V.N.; Jin, R.C.; Rabello, S.; Gulbahce, N.; White, K.; Hale, A.; Cottrill, K.A.; Shaik, R.S.; Waxman, A.B.; Zhang, Y.Y.; et al. MicroRNA-21 integrates pathogenic signaling to control pulmonary hypertension: Results of a network bioinformatics approach. *Circulation* **2012**, *125*, 1520–1532. [CrossRef]

59. Brock, M.; Samillan, V.J.; Trenkmann, M.; Schwarzwald, C.; Ulrich, S.; Gay, R.E.; Gassmann, M.; Ostergaard, L.; Gay, S.; Speich, R.; et al. AntagomiR directed against miR-20a restores functional BMPR2 signalling and prevents vascular remodelling in hypoxia-induced pulmonary hypertension. *Eur. Heart J.* **2014**, *35*, 3203–3211. [CrossRef]
60. McLendon, J.M.; Joshi, S.R.; Sparks, J.; Matar, M.; Fewell, J.G.; Abe, K.; Oka, M.; McMurtry, I.F.; Gerthoffer, W.T. Lipid nanoparticle delivery of a microRNA-145 inhibitor improves experimental pulmonary hypertension. *J. Control. Release* **2015**, *210*, 67–75. [CrossRef]
61. Gubrij, I.B.; Pangle, A.K.; Pang, L.; Johnson, L.G. Reversal of microRNA dysregulation in an animal model of pulmonary hypertension. *PLoS ONE* **2016**, *11*, e0147827. [CrossRef] [PubMed]
62. Kim, J.; Kang, Y.; Kojima, Y.; Lighthouse, J.K.; Hu, X.; Aldred, M.A.; McLean, D.L.; Park, H.; Comhair, S.A.; Greif, D.M.; et al. An endothelial apelin-FGF link mediated by miR-424 and miR-503 is disrupted in pulmonary arterial hypertension. *Nat. Med.* **2013**, *19*, 74–82. [CrossRef] [PubMed]
63. Gong, J.; Chen, Z.; Chen, Y.; Lv, H.; Lu, H.; Yan, F.; Li, L.; Zhang, W.; Shi, J. Long non-coding RNA CASC2 suppresses pulmonary artery smooth muscle cell proliferation and phenotypic switch in hypoxia-induced pulmonary hypertension. *Respir. Res.* **2019**, *20*, 53. [CrossRef] [PubMed]
64. Su, H.; Xu, X.; Yan, C.; Shi, Y.; Hu, Y.; Dong, L.; Ying, S.; Ying, K.; Zhang, R. LncRNA H19 promotes the proliferation of pulmonary artery smooth muscle cells through AT1R via sponging let-7b in monocrotaline-induced pulmonary arterial hypertension. *Respir. Res.* **2018**, *19*, 254. [CrossRef]
65. Zhang, H.; Liu, Y.; Yan, L.; Wang, S.; Zhang, M.; Ma, C.; Zheng, X.; Chen, H.; Zhu, D. Long noncoding RNA Hoxaas3 contributes to hypoxia-induced pulmonary artery smooth muscle cell proliferation. *Cardiovasc. Res.* **2019**, *115*, 647–657. [CrossRef]
66. Wei, C.; Henderson, H.; Spradley, C.; Li, L.; Kim, I.K.; Kumar, S.; Hong, N.; Arroliga, A.C.; Gupta, S. Circulating miRNAs as potential marker for pulmonary hypertension. *PLoS ONE* **2013**, *8*, e64396. [CrossRef]
67. Chinnappan, M.; Gunewardena, S.; Chalise, P.; Dhillon, N.K. Analysis of lncRNA-miRNA-mRNA Interactions in Hyper-proliferative Human Pulmonary Arterial Smooth Muscle Cells. *Sci. Rep.* **2019**, *9*, 10533. [CrossRef]
68. Kang, K.; Peng, X.; Zhang, X.; Wang, Y.; Zhang, L.; Gao, L.; Weng, T.; Zhang, H.; Ramchandran, R.; Raj, J.U.; et al. MicroRNA-124 suppresses the transactivation of nuclear factor of activated T cells by targeting multiple genes and inhibits the proliferation of pulmonary artery smooth muscle cells. *J. Biol. Chem.* **2013**, *288*, 25414–25427. [CrossRef]
69. Chen, J.; Guo, J.; Cui, X.; Dai, Y.; Tang, Z.; Qu, J.; Raj, J.U.; Hu, Q.; Gou, D. The Long Noncoding RNA LnRPT Is Regulated by PDGF-BB and Modulates the Proliferation of Pulmonary Artery Smooth Muscle Cells. *Am. J. Respir. Cell Mol. Biol.* **2018**, *58*, 181–193. [CrossRef]
70. Oldham, W.M. The Long Noncoding RNA LnRPT Puts the Brakes on Pulmonary Artery Smooth Muscle Cell Proliferation. *Am. J. Respir. Cell Mol. Biol.* **2018**, *58*, 138–139. [CrossRef]
71. Wang, D.; Xu, H.; Wu, B.; Jiang, S.; Pan, H.; Wang, R.; Chen, J. Long noncoding RNA MALAT1 sponges miR1243p.1/KLF5 to promote pulmonary vascular remodeling and cell cycle progression of pulmonary artery hypertension. *Int. J. Mol. Med.* **2019**, *44*, 871–884. [PubMed]
72. Mou, X.; Wang, J.; Wang, L.; Wang, S. Correlation Between Single Nucleotide Polymorphisms of the rs664589 Locus in the Long-Chain Noncoding RNA Lung Adenocarcinoma Metastasis-Associated Gene 1, Hypertension, and Its Mechanism. *Genet. Test. Mol. Biomark.* **2020**, *24*, 120–130. [CrossRef]
73. Yang, L.; Liang, H.; Shen, L.; Guan, Z.; Meng, X. LncRNA Tug1 involves in the pulmonary vascular remodeling in mice with hypoxic pulmonary hypertension via the microRNA-374c-mediated Foxc1. *Life Sci.* **2019**, *237*, 116769. [CrossRef] [PubMed]
74. Zhu, T.T.; Sun, R.L.; Yin, Y.L.; Quan, J.P.; Song, P.; Xu, J.; Zhang, M.X.; Li, P. Long noncoding RNA UCA1 promotes the proliferation of hypoxic human pulmonary artery smooth muscle cells. *Pflug. Arch.* **2019**, *471*, 347–355. [CrossRef] [PubMed]
75. Jalali, S.; Ramanathan, G.K.; Parthasarathy, P.T.; Aljubran, S.; Galam, L.; Yunus, A.; Garcia, S.; Cox, R.R., Jr.; Lockey, R.F.; Kolliputi, N. Mir-206 regulates pulmonary artery smooth muscle cell proliferation and differentiation. *PLoS ONE* **2012**, *7*, e46808. [CrossRef]
76. Freilich, R.W.; Woodbury, M.E.; Ikezu, T. Integrated expression profiles of mRNA and miRNA in polarized primary murine microglia. *PLoS ONE* **2013**, *8*, e79416. [CrossRef]

77. Collison, A.; Mattes, J.; Plank, M.; Foster, P.S. Inhibition of house dust mite-induced allergic airways disease by antagonism of microRNA-145 is comparable to glucocorticoid treatment. *J. Allergy Clin. Immunol.* **2011**, *128*, 160–167. [CrossRef]
78. Kim, R.Y.; Horvat, J.C.; Pinkerton, J.W.; Starkey, M.R.; Essilfie, A.T.; Mayall, J.R.; Nair, P.M.; Hansbro, N.G.; Jones, B.; Haw, T.J.; et al. MicroRNA-21 drives severe, steroid-insensitive experimental asthma by amplifying phosphoinositide 3-kinase-mediated suppression of histone deacetylase 2. *J. Allergy Clin. Immunol.* **2017**, *139*, 519–532. [CrossRef]
79. Wang, D.; Zhang, H.; Li, M.; Frid, M.G.; Flockton, A.R.; McKeon, B.A.; Yeager, M.E.; Fini, M.A.; Morrell, N.W.; Pullamsetti, S.S.; et al. MicroRNA-124 controls the proliferative, migratory, and inflammatory phenotype of pulmonary vascular fibroblasts. *Circ. Res.* **2014**, *114*, 67–78. [CrossRef]
80. Natoli, G.; Andrau, J.C. Noncoding transcription at enhancers: General principles and functional models. *Annu. Rev. Genet.* **2012**, *46*, 1–19. [CrossRef]
81. Ulitsky, I.; Bartel, D.P. lincRNAs: Genomics, evolution, and mechanisms. *Cell* **2013**, *154*, 26–46. [CrossRef] [PubMed]
82. Cabili, M.N.; Trapnell, C.; Goff, L.; Koziol, M.; Tazon-Vega, B.; Regev, A.; Rinn, J.L. Integrative annotation of human large intergenic noncoding RNAs reveals global properties and specific subclasses. *Genes Dev.* **2011**, *25*, 1915–1927. [CrossRef] [PubMed]
83. Rinn, J.L.; Chang, H.Y. Genome regulation by long noncoding RNAs. *Annu. Rev. Biochem.* **2012**, *81*, 145–166. [CrossRef] [PubMed]
84. Rinn, J.L.; Kertesz, M.; Wang, J.K.; Squazzo, S.L.; Xu, X.; Brugmann, S.A.; Goodnough, L.H.; Helms, J.A.; Farnham, P.J.; Segal, E.; et al. Functional demarcation of active and silent chromatin domains in human HOX loci by noncoding RNAs. *Cell* **2007**, *129*, 1311–1323. [CrossRef]
85. Zong, X.; Tripathi, V.; Prasanth, K.V. RNA splicing control: Yet another gene regulatory role for long nuclear noncoding RNAs. *RNA Biol.* **2011**, *8*, 968–977. [CrossRef]
86. Kretz, M.; Siprashvili, Z.; Chu, C.; Webster, D.E.; Zehnder, A.; Qu, K.; Lee, C.S.; Flockhart, R.J.; Groff, A.F.; Chow, J.; et al. Control of somatic tissue differentiation by the long non-coding RNA TINCR. *Nature* **2013**, *493*, 231–235. [CrossRef]
87. Hacisuleyman, E.; Goff, L.A.; Trapnell, C.; Williams, A.; Henao-Mejia, J.; Sun, L.; McClanahan, P.; Hendrickson, D.G.; Sauvageau, M.; Kelley, D.R.; et al. Topological organization of multichromosomal regions by the long intergenic noncoding RNA Firre. *Nat. Struct. Mol. Biol.* **2014**, *21*, 198–206. [CrossRef]
88. Wang, X.; Yan, C.; Xu, X.; Dong, L.; Su, H.; Hu, Y.; Zhang, R.; Ying, K. Long noncoding RNA expression profiles of hypoxic pulmonary hypertension rat model. *Gene* **2016**, *579*, 23–28. [CrossRef]
89. Wahlestedt, C. Targeting long non-coding RNA to therapeutically upregulate gene expression. *Nat. Rev. Drug Discov.* **2013**, *12*, 433–446. [CrossRef]
90. Michalik, K.M.; You, X.; Manavski, Y.; Doddaballapur, A.; Zornig, M.; Braun, T.; John, D.; Ponomareva, Y.; Chen, W.; Uchida, S.; et al. Long noncoding RNA MALAT1 regulates endothelial cell function and vessel growth. *Circ. Res.* **2014**, *114*, 1389–1397. [CrossRef]
91. Hassoun, P.M. Inflammation in chronic thromboembolic pulmonary hypertension: Accomplice or bystander in altered angiogenesis? *Eur. Respir. J.* **2015**, *46*, 303–306. [CrossRef] [PubMed]
92. Li, C.H.; Chen, Y. Targeting long non-coding RNAs in cancers: Progress and prospects. *Int. J. Biochem. Cell Biol.* **2013**, *45*, 1895–1910. [CrossRef] [PubMed]
93. Tuder, R.M.; Marecki, J.C.; Richter, A.; Fijalkowska, I.; Flores, S. Pathology of pulmonary hypertension. *Clin. Chest Med.* **2007**, *28*, 23–42. [CrossRef] [PubMed]
94. Boucherat, O.; Vitry, G.; Trinh, I.; Paulin, R.; Provencher, S.; Bonnet, S. The cancer theory of pulmonary arterial hypertension. *Pulm. Circ.* **2017**, *7*, 285–299. [CrossRef]
95. Sitbon, O.; Gomberg-Maitland, M.; Granton, J.; Lewis, M.I.; Mathai, S.C.; Rainisio, M.; Stockbridge, N.L.; Wilkins, M.R.; Zamanian, R.T.; Rubin, L.J. Clinical trial design and new therapies for pulmonary arterial hypertension. *Eur. Respir. J.* **2019**, *53*, 1801908. [CrossRef]
96. Sommer, N.; Ghofrani, H.A.; Pak, O.; Bonnet, S.; Provencher, S.; Sitbon, O.; Rosenkranz, S.; Hoeper, M.M.; Kiely, D.G. Current and future treatments of pulmonary arterial hypertension. *Br. J. Pharmacol.* **2020**. [CrossRef]

97. Barros, S.A.; Gollob, J.A. Safety profile of RNAi nanomedicines. *Adv. Drug Deliv. Rev.* **2012**, *64*, 1730–1737. [CrossRef]
98. Subhan, M.A.; Torchilin, V.P. siRNA based drug design, quality, delivery and clinical translation. *Nanomedicine* **2020**, *29*, 102239. [CrossRef]

International Journal of
Molecular Sciences

MDPI

Article

Light-Induced Oxidase Activity of DNAzyme-Modified Quantum Dots

Krzysztof Żukowski, Joanna Kosman * and Bernard Juskowiak *

Department of Bioanalytical Chemistry, Faculty of Chemistry, Adam Mickiewicz University, Uniwersytetu Poznanskiego 8, 61-614 Poznan, Poland; krzysztof.zukowski@amu.edu.pl
* Correspondence: kosman@amu.edu.pl (J.K.); juskowia@amu.edu.pl (B.J.)

Received: 21 September 2020; Accepted: 30 October 2020; Published: 1 November 2020

Abstract: Here, we report the synthesis of a quantum dot (QD)-DNA covalent conjugate to be used as an H_2O_2-free DNAzyme system with oxidase activity. Amino-coupling conjugation was carried out between amino-modified oligonucleotides (CatG4-NH_2) and carboxylated quantum dots (CdTe@COOH QDs). The obtained products were characterized by spectroscopic methods (UV-Vis, fluorescence, circular dichroizm (CD), and IR) and the transmission electron microscopy (TEM) technique. A QD-DNA system with a low polydispersity and high stability in aqueous solutions was successfully obtained. The catalytic activity of the QD-DNA conjugate was examined with Amplex Red and ABTS (2,2′-azino-bis(3-ethylbenzothiazoline-6-sulfonate)) indicators using reactive oxygen species (ROS) generated by visible light irradiation. The synthesized QD-DNAzyme exhibited enhanced catalytic activity compared with the reference system (a mixture of QDs and DNAzyme). This proved the assumption that the covalent attachment of DNAzyme to the surface of QD resulted in a beneficial effect on its catalytic activity. The results proved that the QD-DNAzyme system can be used for generation of the signal by light irradiation. The light-induced oxidase activity of the conjugate was demonstrated, proving that the QD-DNAzyme system can be useful for the development of new cellular bioassays, e.g., for the determination of oxygen radical scavengers.

Keywords: quantum dots (QDs); DNAzyme; ROS; Amplex Red; light-induced activity

1. Introduction

Reactive oxygen species (ROS) are oxygen compounds that have a higher reactivity than molecular oxygen in the triplet state. The group of ROS mainly includes superoxide anion radicals ($^{\bullet}O^{2-}$, $^{\bullet}O_2{}^{2-}$), hydroxyl radicals ($^{\bullet}OH$), hydroperoxide radicals ($HO_2{}^{\bullet}$), and oxygen species without an unpaired electron, such as singlet oxygen ($^1O_2$), ozone (O_3), and hydrogen peroxide (H_2O_2) [1–3]. ROS are involved in many cellular processes. These include oxidative-phosphorylation coupling that occurs in mitochondria and provides energy for cell apoptosis or programmed self-destruction of the cells [4–6]. There are many methods employed for obtaining ROS, including biological [7–9], chemical [10,11], and electrochemical [12,13] approaches and methods that use photochemical or photocatalytic reactions [14,15].

Nowadays, semiconductor nanoparticles (NPs), for example, ZnO NP [16–18], TiO_2 NP [19–21], and quantum dots (QDs) [22–24], are used to obtain oxygen free radicals. QDs are semiconductor nanocrystals with sizes ranging from 1 to 10 nm. These inorganic fluorophores are distinguished by a high quantum efficiency, narrow emission bands, a long life time of fluorescence, stability, and resistance to photobleaching [22–24]. The emission wavelength is directly related to the size of these nanoparticles, which gives the possibility to design a nanomaterial with emission at a specific wavelength. QDs can be easily modified, which provides a wide range of applications in medicine and diagnostics [25–27]. Another of their advantages is their semiconductor properties,

which provide a wide range of potential applications of this type of system in the photovoltaic industry [28]. Considering the unique semiconductor properties of QDs, they can be used as efficient reactive oxygen generators. The application of QDs as ROS generators was proposed by the Niemeyer group [29]. They examined CdS QDs functionalized with an adsorbed layer of horseradish peroxidase (HRP) as ROS generators. The free oxygen radicals generated upon light irradiation were involved in the HRP-catalyzed oxidation of an indicator. The Campos-Terán group [30] used similar systems and focused on studying the effect of immobilization of the QD-enzyme on silanized silica for the photocatalytic application of this nanomaterial.

It is unclear whether the switching enzymatic activity of HRP/QDs by light is a unique phenomenon of protein enzymes [28,29], or whether this approach can also be used to design catalysts that comprise DNAzymes with peroxidase activity. Peroxidase-mimicking DNAzymes are promising alternatives to the HRP commonly used in bioanalytics. DNAzymes are based on the G-quadruplex (G4) architecture of some nucleic acids [31]. The planar structure of the G-quartet (part of the G-4 structure) is able to interact with other planar molecules, such as hemin. With the increasing strength of this end-stacking interaction, the peroxidase activity of hemin, being a cofactor in the resulting DNAzyme, also increases [31–33]. The strength of this interaction mainly depends on the topology of the G-quadruplex, which makes it an important factor affecting the DNAzyme catalytic capacity. Generally, the peroxidase activity of DNAzyme is also sensitive to the concentration and type of cations present in solution, the oligonucleotide sequence, and oligonucleotide strand modification. Undoubtedly, DNA-based systems have advantages over protein enzymes, because they are characterized by cheap and easy synthesis and modification, as well as a good stability at a higher temperature (increasing the range of potential applications). Working with nucleic acids also allows for the development of new analytical strategies based on the hybridization phenomenon that occurs between complementary DNA strands or target-aptamer complex formation [33–35].

In this study, we examined the peroxidase activity of G-rich oligonucleotides attached to QDs. This system was designed as an oxidase-mimicking DNAzyme activated by light due to the QD generation of ROS (Figure 1). The DNAzyme-QD conjugate was characterized by spectroscopic methods (UV-Vis, fluorescence, circular dichroizm (CD), and IR) and transmission electron microscopy. The obtained QD-DNAzyme exhibited enhanced photocatalytic activity compared with the reference mixture of QD and DNAzyme. The activity of the QD-DNAzyme conjugate was mediated by light irradiation in the indicator reaction with Amplex Red.

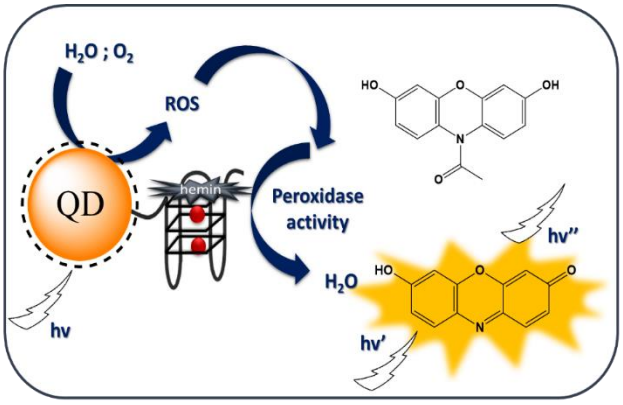

Figure 1. Expected mechanism of the oxidation reaction of the fluorogenic indicator Amplex Red catalyzed by the quantum dot (QD)-DNAzyme conjugate.

2. Results and Discussion

2.1. Design and Synthesis of the QD-DNA Conjugate

It has been proven that CdTe nanoparticles with a diameter of 2.7–3.0 nm possess a band gap of 2.4 eV and, upon visible light irradiation, are able to generate electrons which interact with oxygen and water molecules to form superoxide, hydroxyl radicals, singlet oxygen, and ROS [36]. It is also plausible that these forms of reactive oxygen are able to replace hydrogen peroxide in the oxidation reaction of organic substrates (for example, ABTS or Amplex Red) catalyzed by DNAzyme (scheme in Figure 1). In order to verify this hypothesis we designed a covalent QD-DNA conjugate to bring the DNAzyme closer to the surface of QD, where ROS are expected to be generated. The QD-DNA conjugate was obtained using an amine coupling reaction between carboxyl-functionalized QDs and amino-modified oligonucleotides. 1-Ethyl-3-(3-dimethylamino propyl) carbodiimide hydrochloride (EDC) and N-hydroxysuccinimide (NHS) were used as coupling agents (Figure 2) [37–39].

Figure 2. Scheme of the synthesis of the QD-DNA conjugate using amine coupling between COOH-functionalized quantum dots and amine-modified DNA oligonucleotides.

In order to optimize the conditions of QD-DNA synthesis, the molar ratio of DNA:QD was investigated. The main goal was to obtain the conjugate product with the lowest polydispersity. A series of syntheses with different amounts of DNA equivalents were performed and analyzed using agarose gel electrophoresis (Figure 3). The mobility of the migrated QD band increased with the number of DNA equivalents used for QD-DNA synthesis. The mobility increase of the product can be explained by the successive attachment of anionic oligonucleotides to the nanoparticles that resulted in the more negative charge of the resulting conjugates. No further increase in the band mobility was observed for concentrations of DNA higher than 4 equivalents (Figure 3: lanes 7–10), which suggests saturation of the QD surface with oligonucleotides. The width of this relatively broad band was also unaffected at higher DNA/QD ratios, which proved completion of the coupling reaction with a relatively low polydispersity of the product. The sufficient amount of DNA used in the synthesis was 4–10 equivalents. Therefore, in the synthesis of QD-DNA for further studies, 8 equivalents of oligonucleotide over QDs were used to guarantee QD surface saturation.

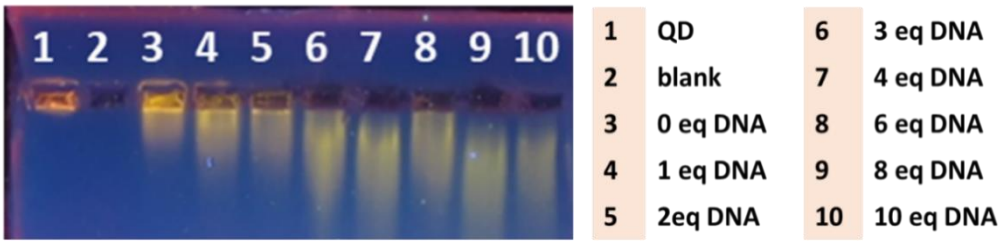

Figure 3. Agarose gel electrophoresis of QDs and QD-DNA conjugates (1% agarose gel, 1 × SB buffer (pH 8.5), 100 V). Stained with thiazole orange aqueous solution. Line 1—freshly prepared QDs alone; 2—DNA alone (blank); 3—QD after the reaction, no DNA was added; 4–10 products of the coupling reaction between QDs and varied concentrations of DNA.

In order to verify whether oligonucleotide molecules were covalently attached to the QD surface, the obtained QD-DNA conjugate was examined by a separation experiment with magnetic particles (Figure S1). Details of this experiment are described in the supplementary material. Briefly, the experiment was based on hybridization between an oligonucleotide (CatG4) covalently attached to QDs and a complementary strand (cCatG4) attached by a biotin–streptavidin interaction to a magnetic particle (Figure S1C). Visualization of the separated product under a UV light illuminator (Figure S1B) showed the bright luminescence of QDs, which proved that the covalent attachment of oligonucleotides to the QD surface was successful.

The information needed for further study of the QD-DNA conjugate was the average number of immobilized oligonucleotides on the surface of the nanoparticles. A direct estimation of the QD content in the QD-DNA conjugate using the fluorescence signal of QDs was hampered by the quenching effect of immobilized oligonucleotides (Figure 4B). Therefore, UV-Vis absorption spectroscopy was exploited for this purpose. The QD and oligonucleotide calibration graphs were plotted using absorption spectra recorded for series of standard solutions containing increasing concentrations of CdTe@COOH QDs or CatG4 oligonucleotides (Figure S2). Since QDs absorb at the same wavelength as CatG4 (Figure 4A), the QD absorption at 350 nm (beyond the DNA absorption band) was selected to quantify the QD concentration and to estimate the contribution of QD absorption to the total absorbance of QD-DNA conjugate at 260 nm. To determine the immobilization efficiency, expressed as a G4/QD molar ratio (number of CatG4 molecules immobilized on a single QD nanoparticle), a simple relationship (1) was used:

$$G4/QD = \frac{A_{260}\varepsilon_{350}^{QD}}{A_{350}\varepsilon_{260}^{G4}} - \frac{\varepsilon_{260}^{QD}}{\varepsilon_{260}^{G4}}, \quad (1)$$

where A_{260} and A_{350} are the absorbance for the *QD-DNA* conjugate, and ε parameters denote molar extinction coefficients for quantum dots (*QD* superscript) and CatG4 (*G4* superscript) at 260 or 350 nm (subscripts). The values of extinction coefficients ($\varepsilon_{350}^{QD} = 7.5 \times 10^4$ M^{-1} cm^{-1}, $\varepsilon_{260}^{QD} = 2.8 \times 10^5$ M^{-1} cm^{-1}, and $\varepsilon_{260}^{G4} = 1.8 \times 10^5$ M^{-1} cm^{-1}) were determined from calibration graphs (Figure S2). The calculated *G4/QD* ratio of 3.15 ± 0.3 indicates that, on average, three CatG4 molecules are immobilized on a single *QD* nanoparticle. This result is reasonable if one considers the surface area of about 25 nm^2 for a single *QD*. The resulting area of 8 nm^2 accessible for a 21-mer oligonucleotide seems to be reasonable for the extended single-stranded DNA adsorbed on the *QD* surface.

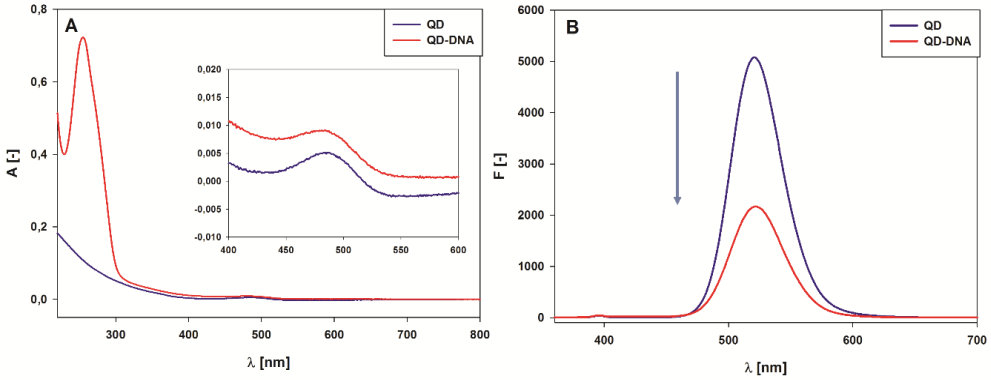

Figure 4. QD and QD-DNA spectral properties: UV-Vis absorption spectra (**A**) and emission spectra with excitation at 350 nm (**B**) in 10 mM Tris-HCl (pH = 8.0), and 1 μM QD and QD-DNA, respectively.

To estimate the size of the nanoparticles and their degree of polydispersity, the obtained products were characterized using transmission electron microscopy (TEM), dynamic light scattering (DLS), and zeta potential measurement (Table 1, Figure 5, Figures S3 and S4, Table S1). The zeta potential values for investigated nanoparticles are shown in Table 1. Three QD-containing systems were compared: Starting CdTe@COOH QDs; the QD-DNA conjugate; and the QD/DNA mixture at a 1:3 molar ratio

that corresponded to the conjugate composition. The high negative value of the zeta potential (Table 1) proves that the covalent attachment of oligonucleotide molecules to the surface of the QDs has a beneficial effect on the stability of nanoparticles in aqueous solution. Transmission electron microscopy (TEM) was applied to characterize the size and polydispersity of the synthesized QD-DNA conjugate (Figure 5A–C). Unmodified CdTe@COOH nanoparticles displayed a dispersed form, as expected for nanoparticles with a surface covered with negatively charged carboxylic groups, which prevent aggregation (Figure 5A). Similar single nanoparticles could be observed for the DNA-modified QDs (Figure 5B). One can conclude that the obtained covalent QD-DNA conjugates are characterized by a high monodispersity (Figure 5B), in contrast to the QDs/DNA mixture (1:3), for which the formation of numerous small aggregates could be observed (Figure 5C). This aggregation may be explained by the more hydrophobic surface of QDs covered by physically adsorbed DNA molecules compared to the QD-DNA covalent conjugates. Size distribution histograms for QDs and the QD-DNA conjugate (Figure S3) indicated that nanoparticles after DNA conjugation retained their original size distribution. Unfortunately, the DLS results concerning the hydrodynamic size of the investigated systems disagreed with the TEM results (Figure S4, Table S1). The high values of hydrodynamic sizes obtained for all investigated systems can be explained by the aggregation of NPs in aqueous solution and possible fluorescence from QDs that contributed to the scattered light. Interestingly, the QD/DNA system exhibited larger aggregates than QDs and QD-DNA conjugates, in good agreement with the TEM results.

Table 1. Values of the zeta potential measured using the dynamic light scattering method.

	Z (mV)	**± ΔZ (mV)**
QD	−41.9	3.85
QD + DNA	−55.0	1.44
QD − DNA	−47.1	4.69

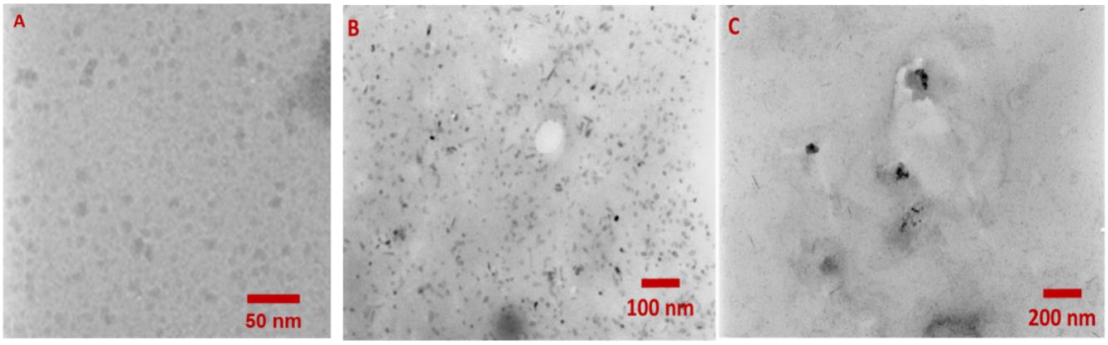

Figure 5. Transmission electron microscopy (TEM) images of nanoparticles: QDs (**A**); QD-DNA (**B**); QD/DNA mixture at a 1:3 molar ratio (**C**).

2.2. Spectroscopic Characterization of the QD-DNA Conjugate

The spectral properties of the QD-DNA conjugate and related systems were studied using UV-Vis absorption spectrophotometry, the fluorescence, and circular dichroizm (CD) spectroscopy. The UV-Vis spectrum of QDs displayed broad absorption, extending from the ultraviolet down to the band edge around 350 nm and a low intensity absorption band at 485 nm (Figure 4A and inset, blue line). In the case of the spectrum of QD-DNA (red line in Figure 4A), an additional absorption band emerged with a maximum at 260 nm, which should be ascribed to the absorption of oligonucleotide molecules immobilized on the surface of nanoparticles. The UV-Vis spectra proved that DNA oligonucleotides were immobilized on the surface of QDs.

As can be seen in Figure 4B, the emission spectrum of QD appeared to be sensitive to the modification of QDs with oligonucleotides. A significant decrease in the fluorescence intensity

was observed for the QD-DNA system compared with unmodified QDs. The reference fluorescence spectrum for the QD/DNA mixture (non-covalent system, 1:3 ratio) also showed a quenching effect of oligonucleotides on the QD fluorescence, but one that was less efficient than for the QD-DNA covalent conjugate.

Fluorescence quenching titration of QDs was performed for three structural forms of CatG4: G-quadruplex (in the presence of K+); random coil conformation (without stabilizing ions); and with dsDNA (CatG4/cCatG4 hybrid). The high values of the Stern–Volmer constants suggested static quenching (Figure S5). All three forms of CatG4 have similar fluorescent quenching abilities (random coiled: $K_{SV} = 6.0 \times 10^4$ M^{-1}, G-quadruplex: $K_{SV} = 4.5 \times 10^4$ M^{-1}, and duplex: $K_{SV} = 8.9 \times 10^4$ M^{-1}). The double-stranded form of DNA is able to quench fluorescence almost two times more efficiently than single-stranded oligonucleotides, but one should consider that dsDNA possesses two times more nucleobases than G4 and ssDNA forms of CatG4. Therefore, we assumed that this quenching was caused by the physical adsorption of DNA nucleobases on the surface of QDs, followed by a photoinduced electron transfer between QDs and nucleobases. Both forms of G-quadruplex and random coiled oligonucleotides quenched QD fluorescence, with a subtle difference showing that the G-quadruplex structure quenched the fluorescence less effectively. This difference also confirms that the process of the attachment of oligonucleotides to QDs was carried out successfully. The Zeng research group [40] noticed a similar effect for carboxyl-modified CdSe/ZnS 525QDs, which were quenched after the covalent conjugation of amino-modified oligonucleotides.

It was also important to clarify whether the oligonucleotides on the QDs were able to form G-quadruplexes upon the addition of KCl. For this purpose, the CD spectra were analyzed. Figure 6A shows the CD spectra of the QD-DNA conjugate in the absence and presence of 10 mM KCl. This concentration of KCl is sufficient to transform unfolded CatG4 into a G-quadruplex structure [31–34]. Weak CD bands are present in the spectrum without KCl, which proves the lack of G-quadruplex assemblies on the QD surface (blue line). On the contrary, the CD spectrum in the presence of KCl (red line, Figure 6A) shows a strong negative band at 240 nm and positive band at 260 nm, proving the formation of a parallel G-quadruplex structure typical for the CatG4 sequence in the presence of potassium ions. For comparison, Figure 6C shows the CD spectra of QD alone and with added DNA (1:3 molar ratio, no KCl), as well as in the presence of 10 mM KCl. The band that appears at 265 nm after the addition of KCl also proves the formation of the G-quadruplex structure in this system. Another interesting observation was the increase in QD fluorescence when potassium ions were added to the system containing QD and DNA (Figure 6B,D). This effect agrees with the slightly lower K_{SV} value obtained for G4 DNA quenching (Figure S5). The random coil oligonucleotide can probably lay on QDs and more strongly interact with the QD surface than the G-quadruplex structure.

The QD effect on the G-quadruplex structure stability was further investigated by titration of the G-quadruplex solution in 10 mM KCl with QDs (Figure S6). As shown in the titration plot (Figure 7), an increase in the QD concentration resulted in a moderate drop of the intensity of CD signals. This observation proved the modest destabilizing effect of QDs on the G-quadruplex structure of CatG4 oligonucleotides. Equilibrium in the system was reached immediately, since the CD spectra recorded within 1 h after the last QD addition revealed negligible spectral changes (Figure 7). The mechanism behind the decrease of CD signals probably involves competition between two processes: K^+-stabilized G-quadruplex formation and the adsorption of an unstructured layer of oligonucleotides on the QD surface. The different behavior of the QD-DNA conjugate and QD/DNA system suggests the importance of the covalent immobilization of CatG4 for G-quadruplex structure formation on the QD surface.

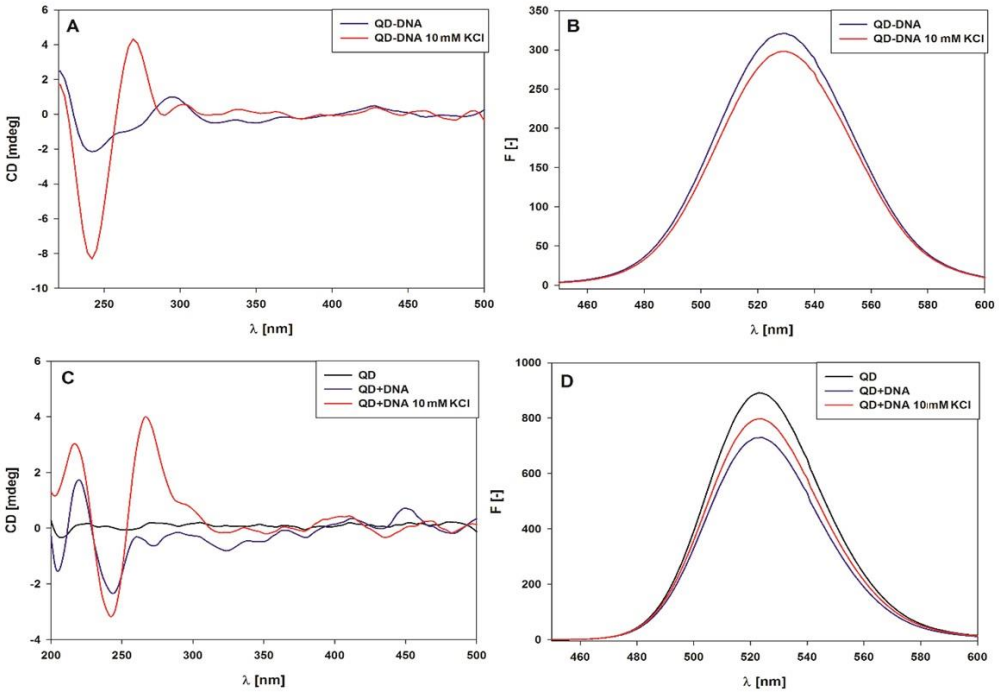

Figure 6. Circular dichroizm (CD) and fluorescence spectra of 1 μM QD-DNA (**A**,**B**) before (blue line) and after the addition of KCl at a 10 mM concentration (red line) and the spectra of 1 μM QD (**C**,**D**) before (black line) and after the addition of DNA at a 1:3 molar ratio (blue line) and the addition of KCl at a 10 mM concentration (red line).

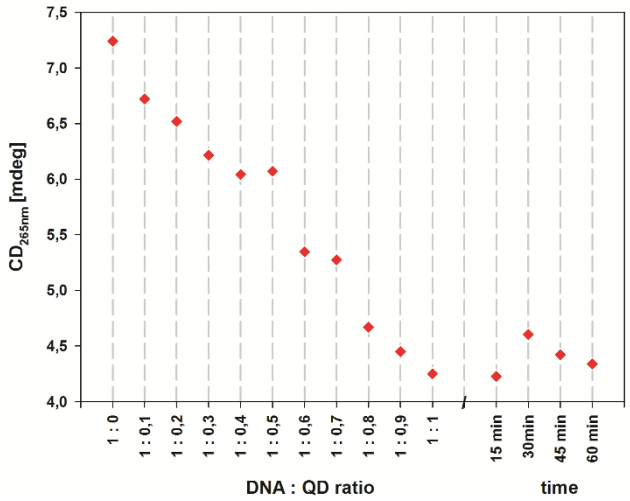

Figure 7. Scatter plot showing CD signal changes at 265 nm for 1 μM CatG4 in 10 mM KCl titrated with QDs. Additionally, after titration, the CD signal was subsequently recorded at intervals of 15 min.

2.3. Peroxidase Activity of the QD-DNA Conjugate

All peroxidase activity experiments were carried out for the systems that contained hemin at a 1:1 ratio to G4 DNA. The association of hemin changed the QD-DNA conjugate into a QD-DNAzyme catalyst. Two substrates for the catalytic reaction were studied: A colorimetric indicator called ABTS and a fluorogenic one known as Amplex Red. The reaction was preceded by sample irradiation with light (λ = 350 nm) for 5 min, in order to produce free oxygen radicals, which could then oxidize substrates in the DNAzyme catalyzed reaction (Figure 1). Initial experiments were carried out with the colorimetric substrate ABTS and typical experimental results are shown in Figure S8. Unexpectedly,

a decrease in absorbance in the broad spectral range from 400 to 870 nm, including the absorption band at 414 nm, was observed. ABTS is known as a radical producing substrate and in an aqueous solution, a small fraction of the colored radical form $ABTS^{+\bullet}$ exists in equilibrium with the colorless ABTS molecules. Typically, in catalyzed reactions with hydrogen peroxide, an increase in absorption bands at 414 nm is observed as a result of the increase in the concentration of the $ABTS^{+\bullet}$ radical form. The observed decrease in the absorption band of the radical with catalytic reaction progress suggests that recombination and quenching processes occur between ROS produced by QD irradiation and the radicals formed by ABTS oxidation. As shown in Figure S8B, the QD-DNA conjugates caused less rapid bleaching in the $ABTS^{+\bullet}$ absorption bands compared with systems containing unmodified QDs (DNA/QD). Nemeyer et al. [29] reported similar results for the oxidation of ABTS catalyzed by HRP/CdS QDs. However, in their system, the oxidation of ABTS produced initially colorful products, followed by a decrease in absorbance at around 414 nm. They explained the observed effect by the further oxidation of $ABTS^{+\bullet}$ to the colorless $ABTS^{2+}$ product. DNAzymes usually display lower activity than HRP. Therefore, we could not observe such an initial absorbance increase. Another reason for the lower activity of QD-DNAzyme compared with that for the QD/HRP system stems from the different method of QD irradiation, as well as the different type of QDs, used by Nemeyer et al. (CdS produces a higher number of ROS than CdTe QDs) [41].

The activity of DNAzyme on the QD surface was then examined using the oxidation reaction of the fluorogenic substrate Amplex Red. Progression of the reaction can be easily followed, since the product of the reaction—resorufin—exhibits strong fluorescence. Moreover, contrary to $ABTS^{+\bullet}$, resorufin is not a radical product, so should remain stable in the experimental conditions. The initial rates of Amplex Red oxidation were determined from the first 5 min of the reaction and the results for different systems are shown in Figure 8.

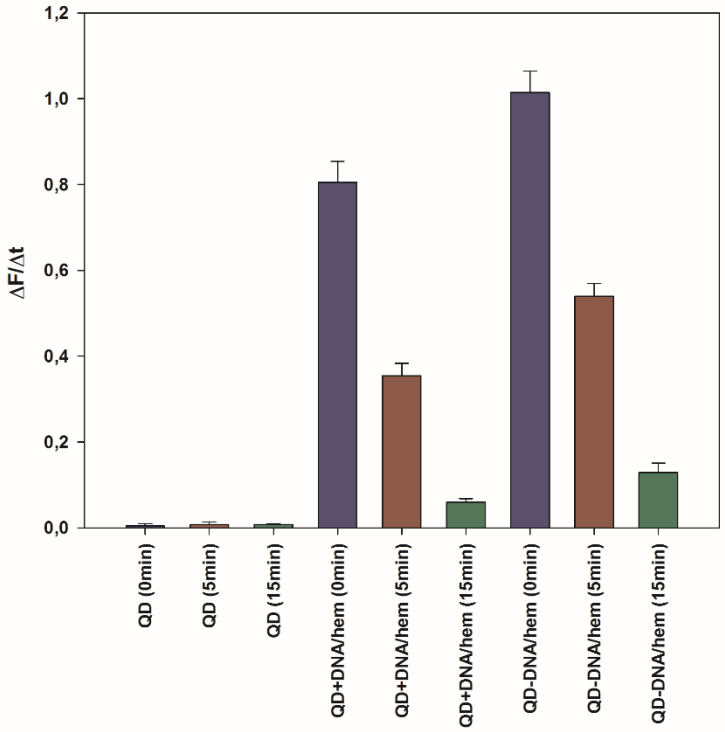

Figure 8. Relative oxidase activity for studied systems with Amplex Red substrate in 10 mM Tris-HCl (pH = 8.0). Conditions: 10 mM KCl; 33 nM QD-DNA or QDs; 100 nM DNA; 100 nM hemin; 5 μM Amplex Red; 1.1% DMSO. Samples were deaerated with Ar purging (0, 5, and 15 min) and irradiated with 350 nm light for 15 min prior to Amplex Red addition.

As can be noticed, the QD-DNAzyme system exhibited higher activity towards the Amplex Red oxidation than the QD/DNAzyme mixture. It is also clear that there was no oxidation of the organic substrate in the reference systems without DNAzyme (buffer and QDs). In the case of deoxygenated solutions (5 or 15 min Ar purging and 15 min of irradiation by monochromatic light at 350 nm), the progression of resorufin production decreased dramatically for all investigated systems, in accordance with the reduced amount of generated ROS. This drop in catalytic activity was the most evident for extensively deoxygenated solutions (15 min Ar purging). The observed residual activity may be due to the production of hydroxyl radicals, together with ROS. The oxidation of Amplex Red was also performed for QD-DNAzyme systems with and without light irradiation, which produced ROS (Figure 9). In this experimental setup, the QD-DNAzyme/Amplex Red system was placed in the spectrofluorimeter and the sample was irradiated with light sequentially, through 350 and 450 nm long-pass filters at regular time intervals of 5 min. The fluorescence at 590 nm was monitored to follow the resorufin production. In both filter modes, resorufin could be excited, but only with irradiation through the 350 nm filter were QDs able to generate ROS. As can be seen in Figure 9 (trace A), the initial irradiation through a 450 nm filter did not enhance fluorescence, and even caused a fluorescence decrease. On the contrary, replacement of the 450 nm filter with the 350 nm one induced a noticeable increase in the fluorescence signal of resorufin. Subsequent replacement with the 450 nm filter again resulted in a horizontal run of the fluorescence signal, followed by a further increase in fluorescence after filter replacement. A reference experiment was carried out with Amplex Red in the absence of the QD-DNAzyme conjugate, which proved that the observed fluorescence changes were not caused by the photooxidation of Amplex Red (Figure 9, trace B). To confirm that the increase of recorded fluorescence was due to resorufin production, we recorded the fluorescence spectra of the system before and after 15 min irradiation through 450 and 350 nm filters, respectively. The spectra shown in Figure S9 confirmed that resorufin was the product of the catalytic reaction, which could be mediated by light. Undoubtedly, the short wavelength light (350 nm long-pass filter) induced the catalytic activity of DNAzyme due to the QD generation of ROS in the system.

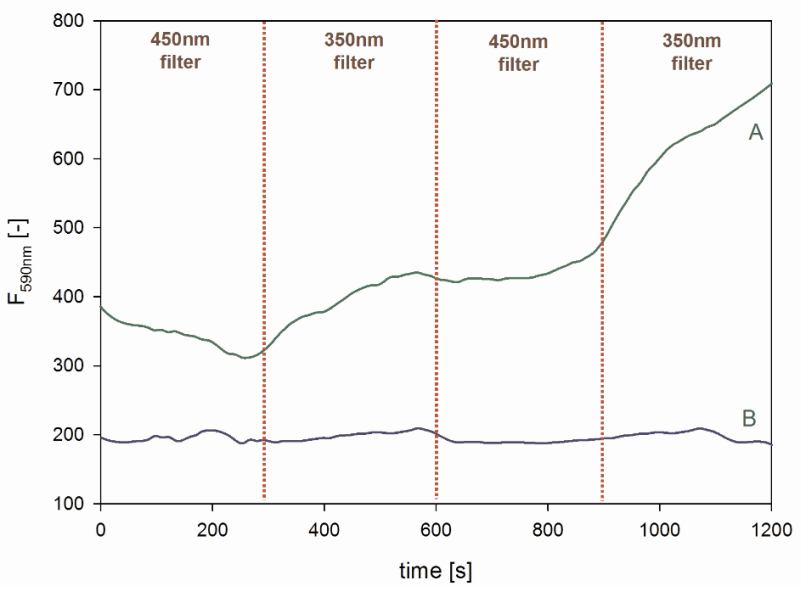

Figure 9. Light triggered the activity of QD-DNAzyme in the catalytic oxidation of Amplex Red (Trace (**A**)). Trace (**B**) represents the reference experiment without QD-DNAzyme. Fluorescence traces represent generation of the Amplex Red oxidation product (resorufin). The reaction system contained 33 nM QD-DNA, 100 nM hemin (100 nM DNAzyme), and 5 μM Amplex Red in 10 mM KCl.

These results prove that DNAzyme can catalyze the reaction between the indicator and ROS produced by QD light irradiation. The QD-DNAzyme system can be used for the development of assays

for ROS scavengers (e.g., mannitol and sodium azide). This reaction system can also be exploited as a novel indicator reaction for DNAzyme-related study and used for the development of new biosensors and aptasensors for DNA and other analytes. We proved that the immobilization of DNA on QDs increases the activity of DNAzyme. Furthermore, this approach can be applied, for example, in the assessment of various QDs' toxicity caused by the generation of ROS, especially in cellular conditions. The obtained results also present prospects for further research on covalent QD-DNA systems.

3. Materials and Methods

3.1. Materials

Studies were performed using CdTe@COOH QDs (Sigma Aldrich) and amino-modified oligonucleotide CatG4-NH2 (H2N-C6H12-5′-TGGGTAGGGCGGGTTGGGAAA-3′) purchased from Genomed (Poland). The oligonucleotide was HPLC-purified and its concentration was quantified by UV-Vis spectroscopy at 85 °C, with the following extinction coefficients at 260 nm: A = 15400; T = 8700; G = 11500; and C = 7400 (M^{-1} cm) [42]. Amplex Red (10-acetyl-3,7-dihydroxyphenoxazine), ABTS (2,2′-azino-bis(3-ethylbenzothiazoline-6-sulfonate)), 1-ethyl-3-(3-dimethylaminopropyl) carbodiimide hydrochloride (EDC), N-hydroxysuccinimide (NHS), and hemin were purchased from Sigma-Aldrich and used without any further purification. Hemin and Amplex Red were dissolved in DMSO and stored in a freezer (−30 °C).

3.2. Synthesis and Purification of QD-DNA Conjugates

QD-DNA conjugates were obtained using an amine coupling reaction between carboxylic group-coated QDs (CdTe@COOH) and amino-modified oligonucleotides based on the CatG4 sequence (H_2N-C_6H_{12}-5′-TGG GTA GGG CGG GTT GGG AAA-3′). This reaction was promoted by EDC and NHS addition. The first step included 15 min incubation of modified QDs (1 equivalent; 2 nmol; 85.6 μL 23.4 μM) with freshly prepared NHS (200 equivalents; 400 nmol; 10 μL 40 mM) and EDC (400 equivalents; 800 nmol; 20 μL 40 mM) in 10 mM Tris-HCl buffer (pH = 8.0). The concentration of DNA was optimized and the experiments were performed using 1–10 equivalents of CatG4 oligonucleotide, with 8 equivalents being determined as an optimal ratio of DNA to QD. The final reaction with 8 equivalents of amino-modified oligonucleotide (16 nmol; 41.2 μL 388.3 μM) was carried out by incubation of the reaction mixture for 45 min on a magnetic stirrer (25 °C).The total volume of the reaction medium was 200 μL. The crude product of the amine coupling of DNA to the QDs was purified using 10 kDa cut-off centrifugal filter units (Amicon Ultra, Merck, Germany). For the experiments involving microscopic characterization and zeta potential measurements, the synthesis scale was 10 times higher.

3.3. Determination of the Size of Nanoparticles and their Zeta Potential

TEM images were collected using a JEM-1200EX transmission electron microscope (JEOL, Peabody, MA, USA). Prior to the visualization, the samples were applied to the copper/carbon TEM grids and allowed to evaporate. Measurements of the zeta potential and DLS experiments were conducted with a Nano ZS Zetasizer (Malvern, UK) equipped with an He-Ne laser of 633 nm using 23 μM aqueous solution of QDs alone, QD-DNA conjugate, and QDs with the addition of DNA at a 1:3 molar ratio. Parameters for the above experiments were material (CdTe) RI = 1.47, water RI = 1.330, and a viscosity of water equal to 0.8872 at 25 °C.

3.4. Spectroscopic Characterization of QD and QD-DNA Systems

QD and QD-DNA were characterized by UV-Vis, fluorescence, CD, and IR spectroscopy. Absorption spectra were recorded in the 220–800 nm range using a Jasco V-750 (Tokyo, Japan) spectrophotometer in 10 mm pathlength quartz cuvettes. Emission spectra were recorded with a Jasco FP-8200 spectrofluorimeter (Tokyo, Japan) in the range of 360 to 700 nm at a 350 nm excitation

wavelength, using emission and excitation slits of 5 nm with a medium sensitivity of the detector. CD spectra were recorded using a Jasco J-1500 spectropolarimeter (Tokyo, Japan) in the spectral range from 220 to 500 nm at a rate of 200 nm/min and a number of accumulations equal to 3. The Jasco J-1500 spectropolarimeter, Jasco V-750 spectrophotometer, and FP-8200 spectrofluorimeter were equipped with Peltier temperature control accessories and all of the experiments were performed at 25 °C. IR spectra were recorded for aqueous solutions of QD and QD-DNA at 84 μM concentration using an ALPHA FT-IR spectrometer in a CaF_2 cell.

3.5. Gel Electrophoresis

The electrophoresis experiment was performed in 1% agarose gel in 1 × SB buffer (pH = 8.50) for 45 min with a 100 V (10 V/cm) voltage using a B1A electrophoresis system model (Owl Separation Systems Llc., Portsmouth, NH, USA). After the electrophoresis process, gel was stained with thiazole orange and visualized using UV Transiluminator (Cleaver Scientific, Rugby, UK).

3.6. Activity Measurements

Measurements of DNAzyme activity against the generated ROS were carried out in 10 mm quartz cuvettes using the Jasco spectrofluorimeter, FP-8200 with a Peltier-type temperature accessory (irradiation and Amplex Red reaction measurements), and the Jasco V-750 spectrophotometer (ABTS reaction measurements). The samples containing QDs and other reagents were deoxygenated under argon for 0–15 min and then irradiated in a spectrofluorimeter at a wavelength of 350 nm with an excitation slit of 10 nm. A suitable indicator (fluorogenic—Amplex Red or colorimetric—ABTS) was added directly before the activity measurement started. Reactions with 5 μM Amplex Red indicator were carried out for samples containing 0.033 μM QD-DNA or QDs and 0.1 μM DNA for a reference QD/DNA system (the average ratio of DNA to QD of 3:1 was found in the QD-DNA conjugate). Reaction progression was monitored at λem = 590 nm with excitation at 560 nm. Experiments with ABTS indicator were carried out, with samples containing 0.167 μM QDs or QD-DNA, 0.5 μM DNA if needed, and 1 mM ABTS. Absorbance changes were monitored at 415 nm. In all cases, measurements were made in Tris-HCl buffer pH = 8.0 and 10 mM KCl, at a temp. of 25 °C. The concentration of hemin corresponded to the amount of G4-DNA at a 1:1 molar ratio.

3.7. Light-Induced Switching of Peroxidase Activity

In total, 33 nM QD-DNAzyme and 100 nM hemin in Tris-HCl buffer pH 8.0 were mixed in a quartz cell. Amplex Red stock solution was added to this such that the final concentration was 5 μM. The cell was placed in the spectrofluorimeter and the sample was irradiated with light sequentially through 350 and 450 nm long-pass filters at regular time intervals. The fluorescence at 590 nm was monitored to follow resorufin production. In both filter modes, resorufin was excited, but only with irradiation at the 350 nm filter did QDs generate ROS. A reference experiment was carried out with Amplex Red in the absence of the QD-DNAzyme conjugate.

4. Conclusions

The QD-DNA conjugate was successfully obtained by amino coupling, using EDC and NHS as a coupling reagents. The average number of immobilized oligonucleotide molecules on the surface of the nanoparticle was three, as proved by the spectroscopic method. It was also proven that the modification of QDs with DNA had a beneficial effect on the stability of the system in aqueous solutions. The obtained QD-DNA product was used as a DNAzyme system with oxidative activity triggered by light. This approach was based on the assumption that free oxygen radicals can be generated by QDs under the influence of light. The light-directed oxidative activity of the QD-DNAzyme conjugate was confirmed by oxidation of the fluorogenic Amplex Red indicator. There is a general lack of means for controlling and triggering the enzymatic activity of peroxidase-mimicking DNAzymes, for example, cellular applications are hampered because of the harsh reaction conditions due to the presence

of H_2O_2, which makes the realization of in vivo applications of DNAzymes difficult. Taking into account the possibility to control the activity of the QD-based catalyst systems, we foresee applications of this light-switchable catalyst in biocatalysis, biosensing, and the design of novel cellular assays. The obtained results also present prospects for further research on covalent QD-DNAzyme systems (additional information Figure S7)

Supplementary Materials: The following are available online at http://www.mdpi.com/1422-0067/21/21/8190/s1, Figure S1: Visualization of magnetic particles experiment in Vis light (A) and under illumination with UV 254 nm (B). The reaction scheme of this experiment is shown in panel (C)., Figure S2: CdTe@COOH QD and CatG4-NH_2 calibration plots for absorbance measured at 260 nm for DNA (A), QD (B) and at 350 nm for QD (C) in 10 mM Tris-HCl (pH = 8,0)., Figure S3: Size distribution obtain by TEM for QD (A) and QD-DNA conjugate (B)., Figure S4: Size distribution obtained with DLS technique for QD (A), QD-DNA (B) and QD+DNA 1:3 molar ratio (C). Zeta potential distribution for QD (D), QD-DNA (E), QD+DNA 1:3 molar ratio (F)., Figure S5: Stern-Volmer plots showing quenching of CdTe@COOH QDs fluorescence at 525 nm against DNA concentration. (A) G-quadruplex (CatG4 in 10 mM KCl), (B) ds DNA (CatG4/cCatG4 in 10 mM KCl), (C) ssDNA (CatG4 without KCl). 1 μM QDs in 10 mM Tris-HCl (pH = 8,0) was excited at 350 nm., Figure S6: Circular dichroism spectra of 1 μM CatG4 G-quadruplex (GQ) solution in 10 mM KCl titrated with QDs., Figure S7: Dependence of the fluorescence intensity of 1 μM QDs upon sequential titration with CatG4 and its complementary strand cCatG4., Figure S8: (A) Absorption spectra for QD-DNAzyme catalyzed oxidation of ABTS recorded at 0 - 1050 s, (B) Activity for studied systems with ABTS substrate in 10 mM Tris-HCl (pH = 8,0); 10 mM KCl; 167 nM QD-DNA or QD/500 nM DNA, 500 nM hemin; 1 mM ABTS, 0.1% DMSO. Activity was expressed by observing changes in absorbance at 415 nm with time ($\Delta A_{415\,nm}/\Delta t$) and the irradiation time is 15 min using monochromatic light at 350 nm., Figure S9: Fluorescence spectra of resorufin produced by QD-DNAzyme catalyzed oxidation of Amplex Red, recorded before (black line), and after 15 min irradiation using 450 nm filter (red line) or 350 nm filter (green line). Emission spectra with excitation at 560 nm (Conditions: 10 mM Tris-HCl (pH = 8,0); 10 mM KCl; 33 nM QD-DNA (100 nM G-quadruplex), 100 nM hemin; 5 μM Amplex Red, 1,1% DMSO).

Author Contributions: K.Ż., J.K., and B.J. conceived and designed the experiments; K.Ż. performed the experiments; all of the authors analyzed the data; K.Ż. and J.K. contributed reagents/materials/analysis tools; K.Ż. and J.K. prepared the manuscript; B.J. revised the manuscript. All authors have read and agreed to the published version of the manuscript.

Funding: This research was funded by National Science Center of Poland grant number 2013/M/10/ST4/00490.

Conflicts of Interest: The authors declare no conflict of interest.

References

1. Halliwell, B. Reactive Species and Antioxidants. Redox Biology Is a Fundamental Theme of Aerobic Life. *Plant Physiol.* **2006**, *141*, 312–322. [CrossRef] [PubMed]
2. Halliwell, B.; Gutteridge, J.M.C. Oxygen Toxicity, Oxygen Radicals, Transition Metals and Disease. *Biochem. J.* **1984**, *219*, 1–14. [CrossRef] [PubMed]
3. Hayyan, M.; Hashim, M.A.; AlNashef, I.M. Superoxide Ion: Generation and Chemical Implications. *Chem. Rev.* **2016**, *116*, 3029–3085. [CrossRef] [PubMed]
4. Kroemer, G.; Zamzami, N.; Susin, S.A. Mitochondrial Control of Apoptosis. *Immunol. Today* **1997**, *18*, 44–51. [CrossRef]
5. Marzo, I. Bax and Adenine Nucleotide Translocator Cooperate in the Mitochondrial Control of Apoptosis. *Science* **1998**, *281*, 2027–2031. [CrossRef]
6. Murphy, M.P. How Mitochondria Produce Reactive Oxygen Species. *Biochem. J.* **2009**, *417*, 1–13. [CrossRef]
7. Liu, H.; Qu, X.; Kim, E.; Lei, M.; Dai, K.; Tan, X.; Xu, M.; Li, J.; Liu, Y.; Shi, X.; et al. Bio-Inspired Redox-Cycling Antimicrobial Film for Sustained Generation of Reactive Oxygen Species. *Biomaterials* **2018**, *162*, 109–122. [CrossRef]
8. Del Río, L.A.; López-Huertas, E. ROS Generation in Peroxisomes and Its Role in Cell Signaling. *Plant Cell Physiol.* **2016**, *57*, 1364–1376. [CrossRef]
9. Cai, P.-J.; Xiao, X.; He, Y.-R.; Li, W.-W.; Zang, G.-L.; Sheng, G.-P.; Hon-Wah Lam, M.; Yu, L.; Yu, H.-Q. Reactive Oxygen Species (ROS) Generated by Cyanobacteria Act as an Electron Acceptor in the Biocathode of a Bio-Electrochemical System. *Biosens. Bioelectron.* **2013**, *39*, 306–310. [CrossRef]
10. Walling, C. Fenton's Reagent Revisited. *Acc. Chem. Res.* **1975**, *8*, 125–131. [CrossRef]
11. Zepp, R.G.; Faust, B.C.; Hoign, J. Hydroxyl Radical Formation in Aqueous Reactions (PH 3-8) of Iron(I1) with Hydrogen Peroxide: The Photo-Fenton Reaction. *Environ. Sci. Technol.* **1992**, *26*, 313–319. [CrossRef]

12. Katsounaros, I.; Cherevko, S.; Zeradjanin, A.R.; Mayrhofer, K.J.J. Oxygen Electrochemistry as a Cornerstone for Sustainable Energy Conversion. *Angew. Chem. Int. Ed.* **2014**, *53*, 102–121. [CrossRef] [PubMed]
13. Katsounaros, I.; Schneider, W.B.; Meier, J.C.; Benedikt, U.; Biedermann, P.U.; Cuesta, A.; Auer, A.A.; Mayrhofer, K.J.J. The Impact of Spectator Species on the Interaction of H2O2 with Platinum—Implications for the Oxygen Reduction Reaction Pathways. *Phys. Chem. Chem. Phys.* **2013**, *15*, 8058. [CrossRef] [PubMed]
14. Surib, N.A.; Kuila, A.; Saravanan, P.; Sim, L.C.; Leong, K.H. A Ligand Strategic Approach with Cu-MOF for Enhanced Solar Light Photocatalysis. *New J. Chem.* **2018**, *42*, 11124–11130. [CrossRef]
15. Liao, Y.; Brame, J.; Que, W.; Xiu, Z.; Xie, H.; Li, Q.; Fabian, M.; Alvarez, P.J. Photocatalytic Generation of Multiple ROS Types Using Low-Temperature Crystallized Anodic TiO2 Nanotube Arrays. *J. Hazard. Mater.* **2013**, *260*, 434–441. [CrossRef] [PubMed]
16. Yin, H.; Casey, P.S.; McCall, M.J.; Fenech, M. Effects of Surface Chemistry on Cytotoxicity, Genotoxicity, and the Generation of Reactive Oxygen Species Induced by ZnO Nanoparticles. *Langmuir* **2010**, *26*, 15399–15408. [CrossRef]
17. Lipovsky, A.; Tzitrinovich, Z.; Friedmann, H.; Applerot, G.; Gedanken, A.; Lubart, R. EPR Study of Visible Light-Induced ROS Generation by Nanoparticles of ZnO. *J. Phys. Chem. C* **2009**, *113*, 15997–16001. [CrossRef]
18. Sirelkhatim, A.; Mahmud, S.; Seeni, A.; Kaus, N.H.M.; Ann, L.C.; Bakhori, S.K.M.; Hasan, H.; Mohamad, D. Review on Zinc Oxide Nanoparticles: Antibacterial Activity and Toxicity Mechanism. *Nano-Micro Lett.* **2015**, *7*, 219–242. [CrossRef]
19. Brzicova, T.; Sikorova, J.; Milcova, A.; Vrbova, K.; Klema, J.; Pikal, P.; Lubovska, Z.; Philimonenko, V.; Franco, F.; Topinka, J.; et al. Nano-TiO_2 Stability in Medium and Size as Important Factors of Toxicity in Macrophage-like Cells. *Toxicol. In Vitro* **2019**, *54*, 178–188. [CrossRef]
20. Chen, L.; Hu, C.; Guo, Y.; Shi, Q.; Zhou, B. TiO2 Nanoparticles and BPA Are Combined to Impair the Development of Offspring Zebrafish after Parental Coexposure. *Chemosphere* **2019**, *217*, 732–741. [CrossRef]
21. Aliakbari, F.; Haji Hosseinali, S.; KhaliliSarokhalil, Z.; Shahpasand, K.; Akbar Saboury, A.; Akhtari, K.; Falahati, M. Reactive Oxygen Species Generated by Titanium Oxide Nanoparticles Stimulate the Hemoglobin Denaturation and Cytotoxicity against Human Lymphocyte Cell. *J. Biomol. Struct. Dyn.* **2019**, *37*, 4875–4881. [CrossRef] [PubMed]
22. Blaškovičová, J.; Sochr, J.; Koutsogiannis, A.; Diamantidou, D.; Kopel, P.; Adam, V.; Labuda, J. Detection of ROS Generated by UV-C Irradiation of CdS Quantum Dots and Their Effect on Damage to Chromosomal and Plasmid DNA. *Electroanalysis* **2018**, *30*, 698–704. [CrossRef]
23. Dou, X.; Zhang, Q.; Shah, S.N.A.; Khan, M.; Uchiyama, K.; Lin, J.-M. MoS_2 -Quantum Dot Triggered Reactive Oxygen Species Generation and Depletion: Responsible for Enhanced Chemiluminescence. *Chem. Sci.* **2019**, *10*, 497–500. [CrossRef] [PubMed]
24. Ribeiro, D.S.M.; Frigerio, C.; Santos, J.L.M.; Prior, J.A.V. Photoactivation by Visible Light of CdTe Quantum Dots for Inline Generation of Reactive Oxygen Species in an Automated Multipumping Flow System. *Anal. Chim. Acta* **2012**, *735*, 69–75. [CrossRef]
25. Chan, W.C.W.; Maxwell, D.J.; Gao, X.; Bailey, R.E.; Han, M.; Nie, S. Luminescent Quantum Dots for Multiplexed Biological Detection and Imaging. *Curr. Opin. Biotechnol.* **2002**, *13*, 40–46. [CrossRef]
26. Biju, V.; Itoh, T.; Anas, A.; Sujith, A.; Ishikawa, M. Semiconductor Quantum Dots and Metal Nanoparticles: Syntheses, Optical Properties, and Biological Applications. *Anal. Bioanal. Chem.* **2008**, *391*, 2469–2495. [CrossRef]
27. Jamieson, T.; Bakhshi, R.; Petrova, D.; Pocock, R.; Imani, M.; Seifalian, A.M. Biological Applications of Quantum Dots. *Biomaterials* **2007**, *28*, 4717–4732. [CrossRef]
28. Nozik, A.J.; Beard, M.C.; Luther, J.M.; Law, M.; Ellingson, R.J.; Johnson, J.C. Semiconductor Quantum Dots and Quantum Dot Arrays and Applications of Multiple Exciton Generation to Third-Generation Photovoltaic Solar Cells. *Chem. Rev.* **2010**, *110*, 6873–6890. [CrossRef]
29. Fruk, L.; Rajendran, V.; Spengler, M.; Niemeyer, C.M. Light-Induced Triggering of Peroxidase Activity Using Quantum Dots. *ChemBioChem* **2007**, *8*, 2195–2198. [CrossRef]
30. Iñarritu, I.; Torres, E.; Topete, A.; Campos-Terán, J. Immobilization Effects on the Photocatalytic Activity of CdS Quantum Dots-Horseradish Peroxidase Hybrid Nanomaterials. *J. Colloid Interface Sci.* **2017**, *506*, 36–45. [CrossRef]
31. Travascio, P.; Li, Y.; Sen, D. DNA-Enhanced Peroxidase Activity of a DNA Aptamer-Hemin Complex. *Chem. Biol.* **1998**, *5*, 505–517. [CrossRef]

32. Kong, D.-M.; Yang, W.; Wu, J.; Li, C.-X.; Shen, H.-X. Structure–Function Study of Peroxidase-like G-Quadruplex-Hemin Complexes. *Analyst* **2010**, *135*, 321–326. [CrossRef] [PubMed]
33. Kosman, J.; Juskowiak, B. Peroxidase-Mimicking DNAzymes for Biosensing Applications: A Review. *Anal. Chim. Acta* **2011**, *707*, 7–17. [CrossRef] [PubMed]
34. Kosman, J.; Żukowski, K.; Juskowiak, B. Comparison of Characteristics and DNAzyme Activity of G4–Hemin Conjugates Obtained via Two Hemin Attachment Methods. *Molecules* **2018**, *23*, 1400. [CrossRef]
35. Wang, F.; Lu, C.-H.; Willner, I. From Cascaded Catalytic Nucleic Acids to Enzyme−DNA Nanostructures: Controlling Reactivity, Sensing, Logic Operations, and Assembly of Complex Structures. *Chem. Rev.* **2014**, *114*, 2881–2941. [CrossRef] [PubMed]
36. Goodman, S.M.; Levy, M.; Li, F.-F.; Ding, Y.; Courtney, C.M.; Chowdhury, P.P.; Erbse, A.; Chatterjee, A.; Nagpal, P. Designing Superoxide-Generating Quantum Dots for Selective Light-Activated Nanotherapy. *Front. Chem.* **2018**, *6*, 46. [CrossRef]
37. Pong, B.-K.; Trout, B.L.; Lee, J.-Y. Preparation of DNA-Functionalised CdSe/ZnS Quantum Dots. Available online: https://dspace.mit.edu/handle/1721.1/35870 (accessed on 1 January 2017).
38. Karakoti, A.S.; Shukla, R.; Shanker, R.; Singh, S. Surface Functionalization of Quantum Dots for Biological Applications. *Adv. Colloid Interface Sci.* **2015**, *215*, 28–45. [CrossRef]
39. Lišková, M.; Voráčová, I.; Klepárník, K.; Hezinová, V.; Přikryl, J.; Foret, F. Conjugation Reactions in the Preparations of Quantum Dot-Based Immunoluminescent Probes for Analysis of Proteins by Capillary Electrophoresis. *Anal. Bioanal. Chem.* **2011**, *400*, 369–379. [CrossRef]
40. Kubota, Y.; Motosa, Y.; Shigemune, Y.; Fujisaki, Y. Fluorescence quenching of 10-methylacrjdinium chloride by nucleotides. *Photochem. Photobiol.* **1979**, *29*, 1099–1106. [CrossRef]
41. Torimura, M.; Kurata, S.; Yamada, K.; Yokomaku, T.; Kamagata, Y.; Kanagawa, T.; Kurane, R. Fluorescence-Quenching Phenomenon by Photoinduced Electron Transfer between a Fluorescent Dye and a Nucleotide Base. *Anal. Sci.* **2001**, *17*, 155–160. [CrossRef]
42. Fasman, G.D. *Handbook of Biochemistry and Molecular Biology, Volume 1: Nucleic Acids*, 3rd ed.; CRC Press: Boca Raton, FL, USA, 1975.

MDPI
St. Alban-Anlage 66
4052 Basel
Switzerland
Tel. +41 61 683 77 34
Fax +41 61 302 89 18
www.mdpi.com

International Journal of Molecular Sciences Editorial Office
E-mail: ijms@mdpi.com
www.mdpi.com/journal/ijms

MDPI
St. Alban-Anlage 66
4052 Basel
Switzerland

Tel: +41 61 683 77 34
Fax: +41 61 302 89 18

www.mdpi.com

ISBN 978-3-0365-3056-7